Alma Mater Studiorum – Università di Bologna

DOTTORATO DI RICERCA IN

Chimica

Ciclo XXXV

Settore Concorsuale: 03/C1 CHIMICA ORGANICA

Settore Scientifico Disciplinare: CHIM06 CHIMICA ORGANICA

SYNTHESIS, CHARACTERIZATION AND POTENTIAL APPLICATIONS OF NOVEL METAL-ORGANIC FRAMEWORKS

Presentata da: Francesca Gambassi

Coordinatore Dottorato Luca Prodi

Supervisore Daniele Nanni

Co-supervisori Christian Serre
Barbara Ballarin
Maria Cristina Cassani

Esame finale anno 2023

Abstract

The research work described in this thesis concerns the synthesis, characterization, and applications of two kinds of metal-organic frameworks (MOFs), Copper based MOF (Cu-MOF) and zirconium based MOF (Zr-MOF) functionalized with new linkers.

The common thread of this research project can be summarized in three work phases:

first, the synthesis and characterization of new organic linkers is described, followed by the presentation of the different optimization conditions for the MOFs synthesis.

Second, the new materials were fully characterized using several complementary techniques, such as infrared (ATR-FTIR) and Raman spectroscopy, X-ray powder diffraction spectroscopy (PXRD), scanning electron microscopy (SEM), X-ray photoelectron spectroscopy (XPS), atomic absorption spectroscopy (AAS) as well as thermal and surface area measurements.

Final, to obtain a complete work the possible environmental applications of the new materials were explored.

The same type of project path was followed and implemented for the six months spent at the Institut des Matériaux Poreux (IMAP) at Ecole normale supérieure (ENS), PSL in Paris.

The thesis organization and the content of each chapter can be summarized as follows:

Chapter 1. General Introduction on the topic of Metal Organic Frameworks, followed by an overview on the synthesis and properties of these materials, with a special focus on copper and zirconium based MOF.

Chapter 2. The synthesis of the new linker **H_2YBDC** and of the new Cu-MOF **Cu-YBDC** is fully described as well their thoroughly characterization, in particular the synchrotron X-ray diffraction analysis that revealed an unexpected structure of this MOF.

Chapter 3. The reactivity of **Cu-YBD** towards $HAuCl_4$ was studied through a detailed XPS study, to confirm the possibility of the propargylcarbamate functionalities of reducing Au(III) to Au(0) without the aid of electrochemical devices.

Chapter 4. The possible environmental applications of the new **Cu-YBDC** MOF in the field of water remediation were investigated, exploring its properties in two kinds of possible future use, as sensor for water pollutants or adsorbent for organic dyes.

Chapter 5. The new organic ligand abbreviated as **H_2YL_{80}**, was designed, synthesized and fully characterized. Different reaction conditions have been studied with $Cu(NO_3)_2 \cdot 2.5H_2O$ as reagent, in order to obtain a new Cu-based MOF.

Chapter 6. The synthesis of a new zirconium chiral metal–organic framework **R*MOF** and a new chiral linker is described. The novel material was prepared using the synthetic route of the known MIP-206 and was fully characterized. Moreover, the chiral properties of this new material were tested with preliminary enantiomeric separative application.

Table of Contents

CHAPTER 1

1 GENERAL INTRODUCTION

1.1 Context of the work

In past studies, the research group I worked with showed that a propargylcarbamate [-N(H)C(O)OCH$_2$C≡CH] group anchored on different oxide supports (SiO_2, Al_2O_3, TiO_2, Fe_3O_4) is capable of straightforwardly reducing Au(III) to Au(0), yielding supported gold nanoparticles (AuNPs) without the addition of any external reducing and/or stabilizing agent (Figure 1.1).[1,2]

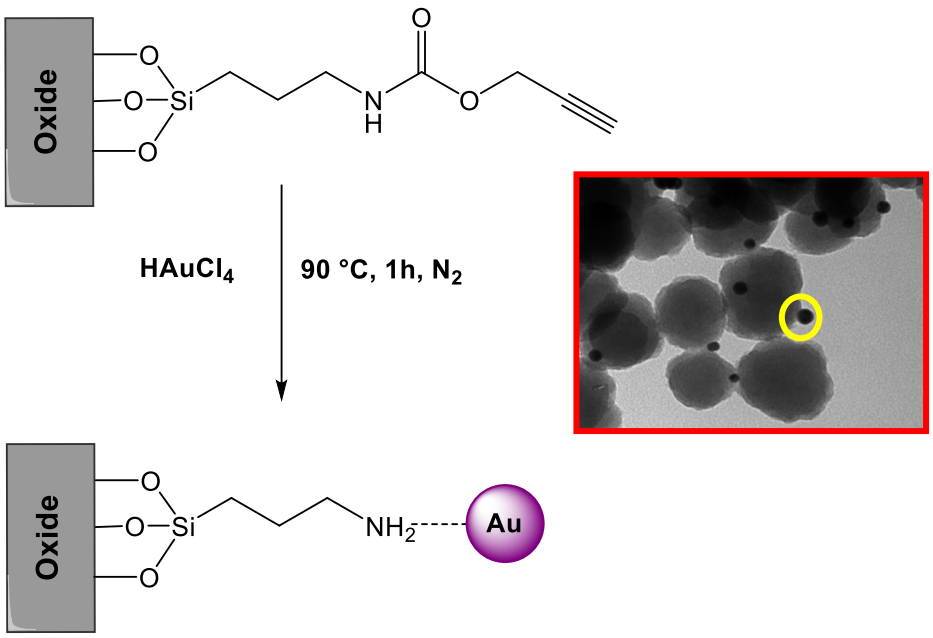

Figure 1.1: Alkyne-modified oxide supports and TEM image of AuNPs supported on functionalized Nanosilica.[1]

The first paper[3] reporting the use of this molecule was about functionalization of nanosilica spherical particles (**Figure 1.1**). The average size of AuNPs synthetized by the functionalized silica was reported to be 11 nm, way lower than the size of AuNPs synthesized using similar systems, e.g. PEI-functionalized silica nanoparticles (40-100 nm).[3] In order to show the higher catalytic activity of AuNPs synthesized using the new molecule supported on silica, this nanomaterial was used as a heterogeneous catalyst for 4-nitrophenol reduction[2] and alkyne hydroamination.[1]

Based on these results the research group envisaged that the versatility demonstrated by the propargylcarbamate residue could be further exploited by anchoring it to different solid supports other than oxides, for example within alkynyl-derivatized Metal Organic Frameworks (MOFs). Indeed, the isolation of a metal-organic framework starting from a suitably functionalized organic linker (Figure 1.2**, Chapter 2**) would ensure an even, dense, and possibly highly symmetric distribution of the reactive alkyne moiety in the material. Additionally, the material porosity and the presence of the metal nodes could affect the reactivity of the alkyne and induce different effects on the ensuing gold nanoparticles, than when the alkyne is attached onto the oxidic surfaces cited above.

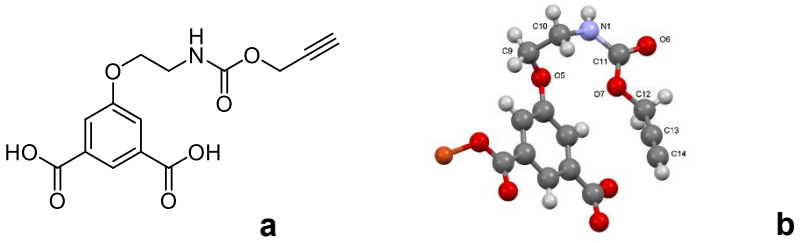

Figure 1.2: Chemical structure (**a**) and XRD simulation (**b**) of **1,3-H2YBDC.**

Based on this starting plan, we decided to explore the MOF world and, in particular, to test the possibility of creating novel functionalized MOFs suitable for generating and supporting metal NPs, possibly capable of being used as heterogeneous catalysts. Taking into account the results previously obtained with alkynyl moieties, our first goal was the synthesis of new organic linkers such as that reported in Figure 1.2.

1.2 Objectives

The first aim of this work has been to show how the linker 1,3-H_2YBDC and the MOF named [Cu(1,3-YBDC)]**.**xH_2O were synthesized, focusing on the chemical and electro-chemical characterization of the material. The characterization of this compound was performed using several complementary techniques such as infrared (ATR-FTIR) and Raman spectroscopy, X-ray powder diffraction spectroscopy (PXRD), scanning electron microscopy (SEM), X-ray photoelectron spectroscopy (XPS), atomic absorption spectroscopy (AAS), as well as thermal and surface area measurements.

Successively, the Cu-MOF was treated with $HAuCl_4$ in order to study the ability of the propargylcarbamate functionality to capture and reduce the Au(III) ions. The overall amount of gold retained by the Cu-MOF/Au was determined through AAS while the amount of gold and its oxidation state on the surface of the MOF was studied by XPS.

A glassy carbon electrode was modified with the Cu-MOF with the purpose to evaluate the nitrite sensing capabilities of the modified electrode. The electro-chemical characterization of the newly synthetized MOF was performed using cyclic voltammetry (CV) and electrochemical impedance spectroscopy (EIS) while its performance toward nitrite oxidation was evaluated through cyclic voltammetry (CV) and chronoamperometry.

Moreover, the possible application of [Cu(1,3-YBDC)] $\cdot xH_2O$ as an adsorbent material for dyes is explored. The adsorption of dyes is currently a topic of great interest in the field of wastewaters treatments and MOFs, thanks to their unique structures and properties, are among the materials that are receiving the greatest attention in that scope.

The second aim of this work has been the design, synthesis, and characterization of a new organic ligand, named H_2YL_{80}, (where Y stands for the pendant alkyne and L_{80} indicates the similarity of the aromatic moiety of the ligand with the one of the ligand H_3L_{80} found in the literature)[4] and the corresponding Cu-[YL80] MOF. The new organic linker maintains the propargylcarbamate functionality and the two carboxylic acid groups of 1,3-H_2YBDC but provides a larger spacer between the carboxylic acid groups by adding two benzene rings on the aromatic moiety of the molecule (**Figure 1.3**). This new design of the ligand was chosen envisaging that the larger, more rigid, and more hindered spacer could prevent the coordination of the propargylcarbamate chains to the Cu(II) ions. This behaviour was found to be the main responsible for the very low material porosity in [Cu(1,3-YBDC)]$\cdot xH_2O$ and its absence or limitation could achieve a higher porosity in the new MOF.

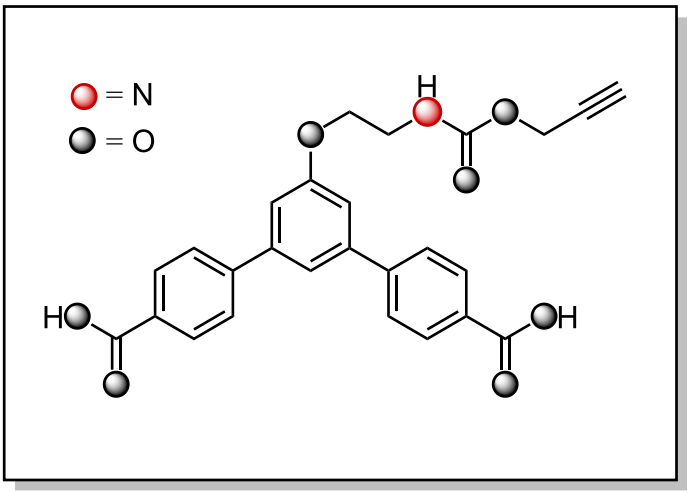

Figure 1.3: Chemical structure of the new H_2YL_{80} ligand.

Moreover, following the same research line of exploring the synthesis of new functionalized linkers for new MOFs with particular properties and applications, the synthesis of a new chiral linker has been realized. The idea was to use the usual 1,3-dicarboxylic functionality to attain a bidentate linker for the metal node or cluster. An additional functionality on the aromatic ring was exploited to stick a chiral residue with low steric hindrance, in order to avoid the constriction of the pores and the decrease of SSA in the new synthetized MOF. Following this reasoning the proposed linker was identified in (*S*)-5-(2-methylbutoxy)isophtalic acid.

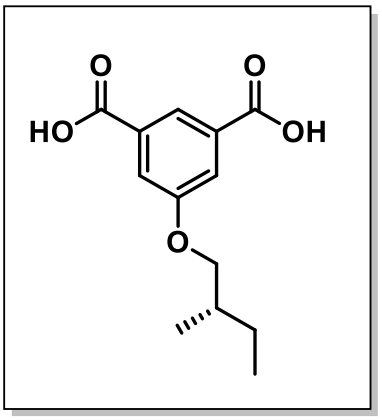

(*S*)-5-(2-methylbutoxy)isophthalic acid

1.3 Introduction to Metal Organic Frameworks

1.3.1. Definition of MOFs

Metal Organic Frameworks are a class of porous, crystalline materials characterized by organic ligands that act as linkers between metal centers (nodes), forming 3D structures. Metal centers can be metal ions or metallic clusters.

1.3.2 The research field of Metal Organic Frameworks

Nowadays the chemistry of the so-called Metal Organic Frameworks (MOFs) represents a vast research field, thanks to the large type of possible structures that can be synthesized and defined as MOFs, as well as the numerous possible applications of these interesting, versatile materials.[5]

Although the study of their properties, syntheses and structural characteristics is considered a relatively new topic, the history of MOFs dates back to more than 50 years ago. In 1965, Tomic reported coordination polymers constructed using di- and tetratopic carboxylic acid linkers coordinated to di-, tri-, or tetravalent metals. The thermal stabilities of these polymers were studied and correlated to the valency of the metal used as well as the number of possible coordination sites on the linker. The emergent properties of the materials that would later be known as metal-organic frameworks (MOFs) was just beginning to be understood.

Nearly 25 years later, Hoskins and Robson proposed that a wide range of scaffold-like materials with infinite 3D frameworks could be accessible, tunable, and potentially useful. Hoskins and Robson predicted also that materials with large empty cavities and low densities should be attainable while maintaining high thermal, chemical, and mechanical stability. A few years later, Yaghi et al. reported the hydrothermal synthesis of a 3D crystalline $Cu(4,4'\text{-bpy})1.5*NO_3(H_2O)_{1.25}$ as an extended network having extended channel systems and they coined the term Metal Organic Frameworks.[6]

Since then, MOFs have become an extremely vibrant topic, with hundreds of papers published every year dealing with newly discovered structures (**Figure 1.4**) and applications for those materials.

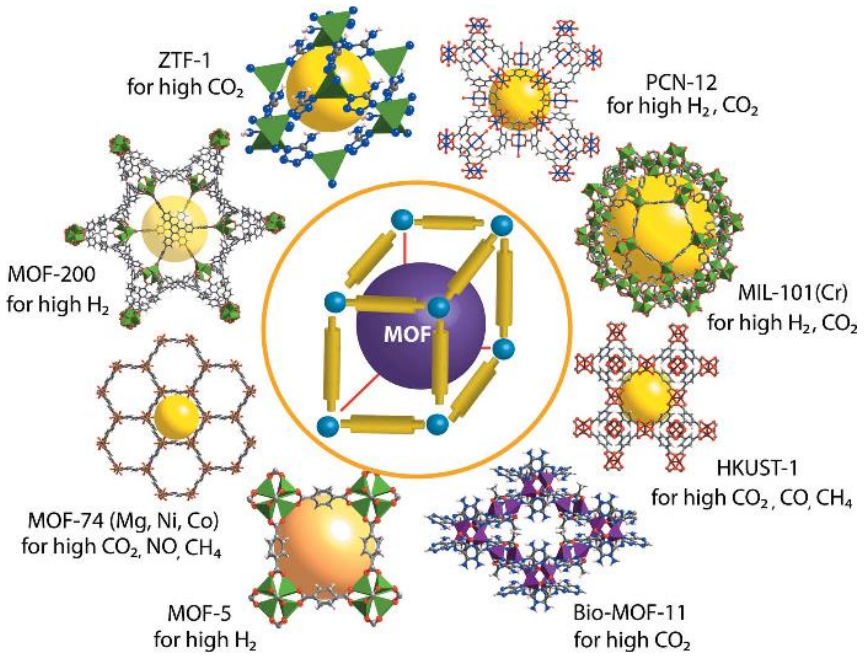

Figure 1.4: Schematic representation of important reported MOFs and their applications.[7]

For example, the use of MOFs for methane gas storage has just begun to be explored by Kitagawa et al: they synthesized two new coordination compounds with 4,4'-bipyridildisulfide as ligand and Mn an Cd as metal ions. Each metal ion in these compounds is linked by the two bridging ligands to make up a one-dimensional structure with large cavities. Assembled structures of these compounds contain microchannels for molecules of solvent (two of ethanol and two of water). Although the channels have enough space for small molecules, the dried compound shows no methane adsorption property because this pore structure is not retained after removal of the guest molecules.[8] In 1999 Yaghi et al. reported MOF-5, the first framework that demonstrated permanent porosity and avoided structural collapse when guest solvent molecules were removed from its pores. The synthesis of a metal organic framework which remains crystalline is achieved by borrowing ideas from metal carboxylate cluster chemistry, where an organic dicarboxylate linker is used in a reaction that gives supertetrahedric clusters when capped with monocarboxylates. The rigid and divergent character of the added linker allows the articulation of the clusters into a three-dimensional framework resulting in a structure with higher apparent surface area and pore volume than most porous crystalline zeolites.[9]

Not long after that, the use of computational predictions and rational design by Férey et al. led to the synthesis of a highly stable MOF with very large pores and high surface area. They created a crystal structure for porous chromium terephthalate, MIL-101 (**Figure 1.5**),

with very large pore sizes and surface area. Its zeotype cubic structure has a giant cell volume (approximately 702,000 cubic angstroms), a hierarchy of extra-large pore sizes (approximately 30 to 34 angstroms), and a Langmuir surface area for N_2 of approximately 5900 ± 300 m^2/g. Besides the usual properties of porous compounds, this solid has potential as a nanomold for monodisperse nanomaterials.[10]

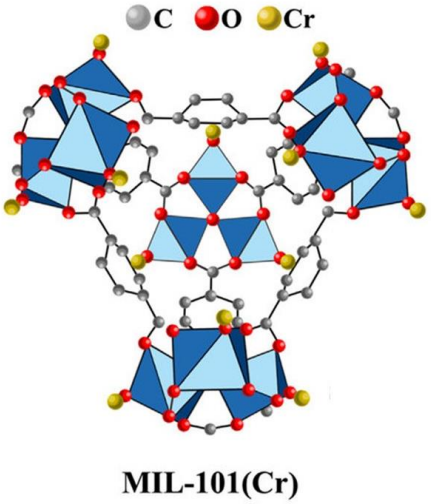

Figure 1.5. Schematic representation of MIL-101.

These first key studies have highlighted the great importance of microporous solids such as zeolites in adsorption, ion exchange, and selective catalysis. Their main attraction derives from their ability to reversibly bind molecules and ions within their extended channels. The major research efforts have focused on the use of the molecular building block approach to generate similar materials with organic structures 3-D, both metal-organic and inorganic. The strategies for the construction of these solids have respectively used hydrogen-bond interactions, metal-ligand coordination, and group metal copolymerization reaction to connect their molecular components. It has been discovered that several such structures exhibit desirable zeolitic properties such as stability and microporosity of the structure, exchange of guest, and selective catalytic activity.

Today there are thousands of MOF structures in the Cambridge Structural Database, including frameworks with densities as low as 0.13 g/cm^3, pre volumes up to 90 % free volume, and Brunauer Emmet Teller (BET) areas greater than 6000 m^2/g.[11] These materials are attractive to scientist in academia and industry alike because of their diverse and tunable porosities and such proprieties have proven to be useful in a wide range of applications, including gas storage, gas separations, catalysis, electrochromic and chemical sensing.

1.3.3 MOFs in Industry

It is a quite common belief that large-scale production of MOFs would be prohibitively expensive, due to the need of complex materials, peculiar solvents, and reaction conditions. It is also often pointed out that MOFs, being composed in large percentages of organic material, cannot have the necessary stability (thermal, chemical or structural) for any industrial or commercial application. Both affirmations represent though a narrow and incomplete comprehension of the topic. First, the stability of the MOFs depends on their structure, hence it can be improved through the choice of the appropriate combination of organic linker and metal ions. Most importantly, the required stability of a MOF depends strictly on the application the material is designed for. For example, the thermal stability required to MOFs used in gas adsorption or gas separation is way lower than the one necessary for the MOFs used in catalysis.

Regarding the price issues, while it is true that expensive technologies are employed in the synthesis, the end price is also heavily dependent on many other factors dealing with productionscale, market value, and the specific application in question.[12] To support this last statement, it can be brought up that from 2011 to 2019, the number of annual patents filing related to the field of MOFs has increased from 78 to 665 (more than 9 times), and that around 50% of the patents come from the private sector, demonstrating that the foundations for a future large-scale commercialization of MOFs are solid and tangible. The chemical company BASF, for example, took an interest in MOFs and struck up a collaboration with Omar Yaghi, currently at the University of California, Berkeley. As a result of this partnership, BASF developed a MOF-based natural gas storage system which, since 2013, has been tested in a fleet of demonstration vehicles (**Figure 1.6**). Although economic pressures may not currently favour methane fuels, indications are that this technology is getting very close to the market.

Figure 1.6. Omar M. Yaghi in a pilot automobile with a MOF-filled natural gas tank developed by BASF.

Moreover, NuMat Technologies - a company spun out of Northwestern University – developed a system representing the first commercial product that uses MOFs, named ION-X, a sub-atmospheric dopant gas delivery system designed for ion implantation for the storage of hazardous gases as arsine, phosphine, and boron trifluoride.[13]

Therefore companies, both small start-ups and larger groups, are already producing MOFs in ton scale quantities for various applications, from gas storage to battery materials. Indeed, research has since developed to the point where there is now a broad array of exciting candidates for implementation in real-world systems.

1.4 Composition, structure, and properties of MOFs

This class of porous materials is very attractive on account of their relative simplicity and increasing predictability in their construction. The reversible nature of coordination bonds between the organic linkers and metal ions renders MOFs highly ordered crystalline materials, which, in turn, usually results in high surface areas and pore volumes.

MOFs are a top growing division of novel inorganic-organic materials as they combine the two often-separated disciplines of chemistry, organic and inorganic. In fact, they are made by linking inorganic and organic building units through coordination bonds. The inorganic units can be metal ions or clusters and the total lattice composed by the linkers and the ions (or clusters) is usually designated as Secondary Building Units (SBUs), that are molecular complexes, in which ligand coordination modes and metal coordination environments are utilized to incorporate these fragments into extended networks through multidentate ligands.[14]

Eddaoudi M. et al, found first that multidentate linkers such as carboxylates allow for the formation of more rigid frameworks due to their ability to aggregate metal ions into M−O−C clusters that are referred to as secondary building units (SBUs, **Figure 1.7b**).[15]

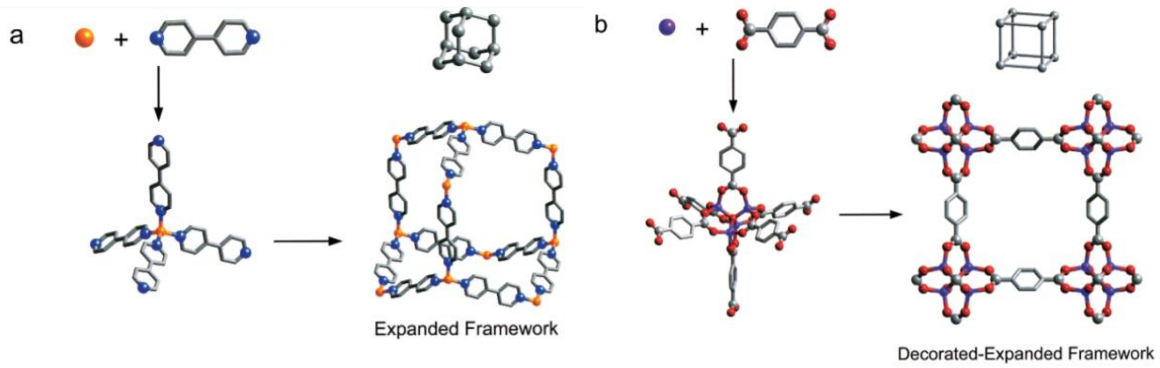

Figure 1.7. Assembly of MOFs by the copolymerization of metal ions with organic linkers to give (a) flexible metal−bipyridine structures with expanded diamond topology and (b) rigid metal−carboxylate clusters that can be linked by benzene "struts" to form rigid extended frameworks in which the M−O−C core (SBU) of each cluster acts as a large octahedron decorating a 6-connected vertex in a cube. All hydrogen atoms have been omitted for clarity. (In (a), M, orange; C, gray, N, blue; in (b), M, purple; O, red; C, gray.)

The SBUs are sufficiently rigid because the metal ions are locked into their positions by the carboxylates; thus, instead of having one metal ion at a network vertex (as is the case in M-

BPY compounds), the SBUs serve as large rigid vertices that can be joined by rigid organic links to produce extended frameworks of high structural stability.

To appreciate the impact of SBUs on pore size and porosity of frameworks, it is instructive to compare two strategies developed for the construction of highly porous frameworks. (**a**) The use of long links that increase the spacing between vertices in net yields void space proportional to the length of the linker (**Figure 1.7a**). This means that a bond is replaced by a sequence of bonds (a process so-called *expansion*). Although in principle such expanded structures provide for large pores, in practice they are often found to be highly interpenetrated and to have low porosity. (**b**) In contrast, replacement of a vertex of a framework net by a group of vertices, a process termed *decoration*, results in open structures with high rigidity and without a tendency to interpenetrate (**Figure 1.7b**). In fact, when such networks are interpenetrating, optimal pore volume may be achieved as described below.

An increasing number of assembled frameworks have as components polytopic groupings of linkers such as 1,3,5-benzenetribenzoate (BTB), which in themselves may act to decorate a vertex in an assembly. Polytopic links can thus be employed both to decorate and to expand a net. It is worth noting that the sizes of rings (or pore size) and voids in nets can be significantly increased with decoration, augmentation, or a combination thereof.

The SBUs have long been fundamental concepts in zeolite chemistry, and now draw considerable attention as a firm basis of synthetic strategies for constructing high-dimensional coordination polymers. Ideally, by judiciously selecting SBUs and linkers, MOFs can be tailor made as matrixes with controlled pore size, shape and functionality for specific applications. To achieve framework design, a high degree of predictability must be integrated prior to synthesis.

In reality, it is hard to realize even a well-educated design, especially when extending it to more complicated cases (for example, polytopic linkers), not to mention that the other factors (temperature, solvent, substrate composition/concentration) would also affect the product crystallinity and morphology.

But summarizing the concept, metal-organic frameworks (MOFs), can be defined as structure constituted by transition metal ions or cluster of metal ion occupying nodal positions in a crystalline framework that are held in place by bi- or multipodal rigid organic linkers. These rigid organic ligands are fundamental because the structure and function of metal-organic framework can be tuned via linker design, in particular adjustments of linker geometry, length, ratio, and functional-group can tune the size, shape, and internal surface property of a MOF for a targeted application.

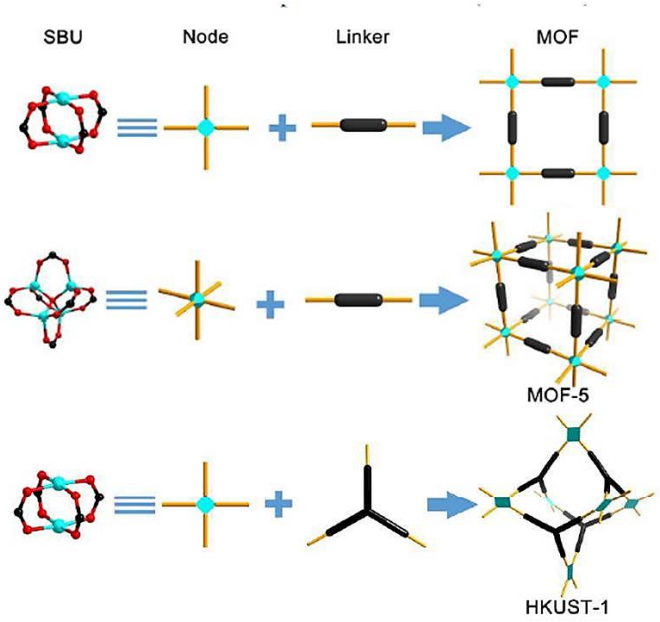

Figure 1.8. Graphic illustration of the construction of some representative coordination polymers/MOFs from SBUs and rigid linkers.

So, the term 'MOF' was originally used in a relatively narrow sense, with SBUs as polyatomic clusters built entirely with strong covalent bonds. Once the synthesis of the SBU is established, it could be used to direct the assembly of ordered frameworks with rigid organic linkers; thus, it is highly possible to predict the chemistry of the yielded crystalline materials. This approach, proposed by Yaghi and co-workers as "reticular synthesis", has triggered systematic investigation of diverse properties of MOFs with pore metrics varied and functionalized.[16] In other words, on the premise of forming SBUs with fixed linking geometries, the MOF structure in the assembly procedures can be anticipated with predesigned linkers (primarily regarding those with rigid and robust geometries). The orientation of organic linkers will result in the construction of MOFs with predetermined structural topologies. Overall, it is the combination of both SBUs (as connectors) and the type of organic ligands (as linkers) that determines the final framework topology (**Figure 1.8**). Linkers can be categorized as ditopic, tritopic, tetratopic, hexatopic, octatopic, mixed, desymmetrized, metallo, and *N*-heterocyclic linkers.

1.4.1 The linker-metal bond and the framework structure

As already said, MOFs are the resulting combination of two different building units, respectively the organic linkers and the inorganic components, often referred to as Secondary

Building Units (SBUs). The organic linkers are characterized by the presence of binding groups, such as carboxylates (by far the most common), phospates, pyrazolates, ecc.

Seeing that the crystallinity of the MOFs is tightly related to the reversibility of the bonds between the linker and the metal ions/clusters, it follows that an enhance of the strength of said bonds leads to encreasing difficulties in the crystallization of the MOFs (**Figure 1.9**).[17]

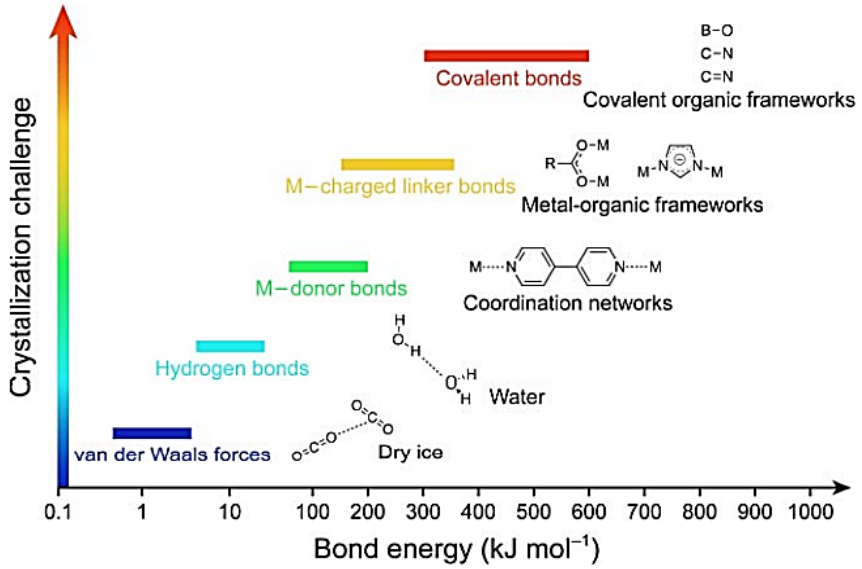

Figure 1.9: Comparison of the strength of different types of interactions ranging from weak (blue and cyan, van der Waals forces, and hydrogen bonding), to intermediate (green, metal–donor bonds), to strong (yellow and red, metal-charged linker and covalent bonds, respectively). The challenge in crystallizing extended structures based on these interactions increases with increasing bond strength.[15]

On the other hand, too weak metal-linker bonds may have negative consequences on the chemical and architectural stability of the products. This problem has been quite common until the first half of the 1990s, when neutral donor linkers were used to prepare coordination networks. The turning point was the replacement of neutral linkers with charged chelating ones. As mentioned earlier, the most common class of ligands consists of carboxylate-based ligands, which provide four advantages over neutral donor linkers: (i) the charged carboxylates neutralize the positive charges of the metal nodes, thus allowing for the formation of neutral frameworks and obviating the need for counter ions; (ii) their chelating ability provides more structural rigidity and directionality; (iii) they favour the formation of polynuclear clusters (SBUs) with a fixed overall coordination geometry and connectivity;

(iv) the strong bonding between the linkers and the metal centres of the SBUs results in MOFs with high thermal, mechanical, and chemical stability.

1.4.2 Ditopic carboxylate linkers

Ditopic carboxylate linkers have been well studied since the beginning of MOF investigations, due partly to their readily accessibility and perhaps to their easily perceivable structures in combination with different SBUs. The in-situ aggregation of metal ions into M-O-C metal clusters/SBUs depends on the reaction conditions; the same starting materials (metal salts and organic linkers) could lead to different crystal structures. For example the reaction between zinc nitrate [$Zn(NO_3)_2$] and terephtalate (bdc) gives crystalline MOF-5 [$Zn_4O(bdc)_3$] under solvothermal conditions; however, slow vapor diffusion at room temperature of triethylamine/ toluene into *N,N'*-dimethylformamide (DMF) / toluene solution containing a mixture of $Zn(NO_3)_2$/H_2bdc yields colourless prism-shaped crystals Zn(bdc)(DMF)(H_2O). In this structure, the SBU is a square planar dizinc paddle-wheel unit instead of an octahedral $Zn_4O(CO_2)_6$ cluster in MOF-5. By linking square planar building units and linear ditopic linkers, it is evident that the Zn(bdc)(DMF)(H_2O) structure is a two dimensional (2D) sheet as opposed to the three dimensional (3D) network in MOF-5 structure.

Generally speaking, twisted angles of linear dicarboxylates plays a crucial role in determining both the dimensionality and topology of the final network structure. Substituents with varied bulkiness could be introduced to adjust the dihedral angle, while linker length might not necessarily a prerequisite for topological control. It should be pointed out that a 90° dihedral angle does not guarantee that the two carboxylates are perpendicular to each other. For example, 2,2'-dihydroxy-1,1'-binaphthalene-5,5'- dicarboxylate (5,5'-bda) was used to synthesize a chiral MOF with $Cu(NO_3)_2$ under solvothermal conditions. Although the two phenyl rings bearing the carboxylates are almost perpendicular to each other, hydrogens at the 4 and 4' positions force the two carboxylates to twist and adopt a nearly coplanar conformation. As a result, a 2D sheet [Cu_2(5,5'-bda)$_2$] containing dicopper paddlewheel SBUs was formed.

It can be concluded that a linear linker with two carboxylates predisposed at right angle would reticulate the squares as desired to produce a MOF with NbO-type structure (**Figure 1.10**). The structure of *NbO* is related to the NaCl-type structure in an interesting way, namely the Nb atoms are located in the center of each face but not at the origin and O atoms are located in the middle of each edge but not in the center of the cell, according to the Reticular Chemistry Structure Resource (RCSR).[16]

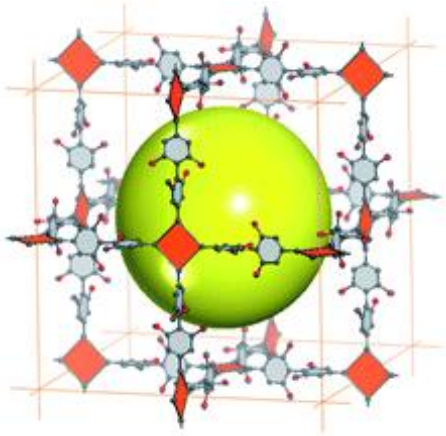

Figure 1.10. Example of *NbO*-type framework crystal structure of a porous MOF (KUMOF-1).

At higher temperature the *NbO* type structure might not form because the right-angle conformation would not be very predominating; thermodynamic factors have to be taken into consideration when predicting the possible structures of the final product.

1.5 Methods of synthesis

A crucial aspect in the study of MOFs is the variety of synthetic methods that can be used to obtain these materials. In most cases, the use of different methods or reaction conditions on the same starting materials can lead to different products.

The most common method, so much so that is commonly referred to as "conventional synthesis", consists in carrying out the reaction by conventional electrical heating (Figure 1.11). For this method, two different sub-categories can be defined: solvothermal synthesis, where the reaction is performed at autogenous pressure, in a closed vessel, above the boiling point of the solvent, and no solvothermal, where the reaction takes place at ambient pressure under the boiling point of the solvent. The most important parameters are the initial concentration of the reactants and the solvent used, which determines the range of temperature that can be employed.

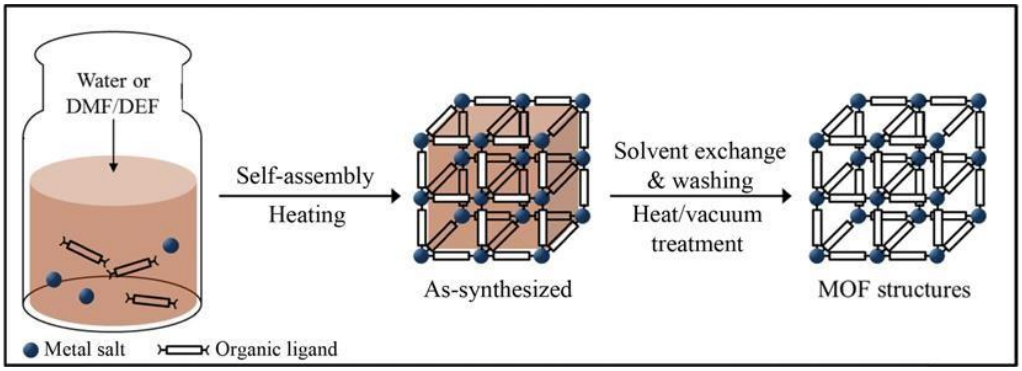

Figure 1.11. Conventional synthesis of MOFs.[18]

There are many methods that fall under the category of "non-conventional synthesis". Among the most common ones we can find microwave-assisted synthesis (where the microwaves are used to heat the reaction mixtures), electrochemical synthesis (in which the metal ions are introduced continuously by anodic dissolution rather than being added in the form of salts), mechanochemical synthesis (a solvent-free method in which the reaction is induced by mechanical forces, by grinding the reactants together), sonochemical synthesis (that consists in inserting the reaction mixture inside an ultrasonic bath to provide the necessary energy), and interfacial synthesis (where the reaction takes place at the interface between two different solutions, one containing the metal salt and one containing the organic linker).[18]

1.6 Activation of MOFs

During the synthesis of MOFs, the presence of guest molecules (solvents, ligand excess, etc.) trapped inside the pores is inevitable, leading to a reduction of the porosity and the surface area of the materials. Since permanent porosity is required for MOFs to be considered viable materials, numerous methods have been developed to remove those guest molecules, and thus activate the MOFs. Sometimes the removal of the guest molecules is achieved by simple heating under vacuum, but usually the synthesis of MOFs requires high-boiling solvents, such as *N*,*N*- dimethylformamide (DMF) or dimethyl sulfoxide (DMSO). In those cases, thermal activation could cause significant capillary forces and surface tension which could yield fully or partially collapsed frameworks. Hence, before applying thermal activation, it is common practice to perform a solvent-exchange routine, by soaking the MOF in a low-boiling solvent. The process of activating the MOFs by heating under vacuum is also known as "conventional activation".

Following the logic of avoiding high surface tension and operating under milder conditions, the use of supercritical CO_2 to activate the MOFs represents a valid alternative to conventional activation. The process consists in the exchanging of the solvent molecules with liquid CO_2, below its critical temperature (31 °C) and above its critical pressure (73 bar). Then, the evaporation of CO_2 is carried out in its supercritical state, by depressurizing the CO_2 above its critical temperature, which drastically minimizes the surface tension that would normally ensue during a conventional liquid-gas transition phase.

Similarly, to supercritical CO_2 drying, another technique that avoids the liquid-gas transition phase is freeze drying. In this case, the initial solvent is exchanged with a high-freezing-point solvent (e.g., benzene)[16] and cooled down to its freezing point. Then, the solvent can be removed under vacuum through sublimation, effectively avoiding the surface tension that would happen during liquid-gas transition phase.[19]

1.7 Copper-based Metal Organic Frameworks

The structural diversity of metal-organic frameworks (MOFs) has stimulated research efforts in a variety of interesting areas, from gas storage and detection, to catalysis, and, more recently, also in the field of electroactive materials in device.[20] From the plethora of reported MOFs, some of the highest performing multi application materials feature an array of Cu-Cu paddlewheel secondary buildings units (SBUs). (**Figure 1.12**).

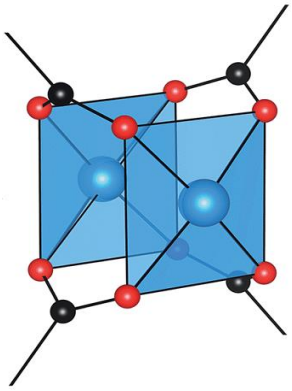

Figure 1.12 Cu···Cu paddlewheel motifs linked by the aromatic tricarboxylate 1,3,5-benzene tricarboxylate (btc). Color scheme: Cu (turquoise); O (black); H (red).

There are many examples of organic-inorganic frameworks featuring this motif, with various porosity and aperture depending on the organic liker selection:

- **HKUST-1**, the most important of materials based on copper (II) ions in combination with BTC (1,3,5-benzene tricarboxylate) as linker, is a highly porous material incorporating a copper 'paddle-wheel' building unit connected by BTC to form a cubic MOF that is particularly notable for its open metal sites (coordinatively unsaturated copper ions); these are available once the guest molecules inside the pores have been thermally removed. HKUST-1 is also the first MOF that has been synthesized by Williams and co-workers as a highly porous metal coordination polymer $[Cu_3(TMA)_2(H_2O)_3]_n$, defined by its inventors a new competitor material for zeolites that are difficult to modify or derivatize in a systematic way.[21]

- **NU-111**, a MOF with a concatenated face-centered-cubic (fcc) lattice, in which the framework nodes consist of Cu-paddlewheels coordinated by the carboxylates of the linkers, which exhibits simultaneously high gravimetric and volumetric methane uptake characteristics.[22]

- **PCN-14**, a microporous metal organic framework, based on an anthracene derivative 5,5'-(9,10-anthracenediyl)di-isophthalate (H4adip), containing nanoscopic cage and exhibiting high methane uptake.[23]

- **NOTT-113**, **NOTT-114** and **NOTT-115**, three isostructural metal organic polyhedral cage-based frameworks with (3,24)-connected topology synthesized by combining hexacarboxylate isophtalate linkers with $[Cu_2(RCOO)_4]$ paddlewheel moieties, and used for H_2 storage.[24]

The most famous copper based MOF, the HKUST-1 is one of the densest porous MOFs: it is a framework composed of an array of 32 Cu---Cu paddlewhees per crystallographic unit cell, connected in three dimensions by 1,3,5-benzenetricarboxylate (btc). Like cupric acetate, this ligand arrangement results in two coordinatively unsaturated Cu sites per paddlewheel which polar molecules can interact with. The paddlewheels are stable in both the coordinatively unsaturated and saturated arrangements. In the original preparation of HKUST-1, $Cu_3(btc)_2$ crystallizes with stoichiometric amounts of water coordinated to each Cu^{2+} ion. Anhydrous (or activated) HKUST-1 is realized by gentle heating under low pressure, resulting in the chemically activated structure with exposed Cu^{2+} sites.

Activated HKUST-1 has demonstrated remarkable gas separation and uptake. It has been shown to be both an ionic and electrical conductor, and an efficient heterogeneous catalyst, despite its pedestrian chemical composition. Both btc and Cu---Cu paddlewheels are not unique to HKUST-1.

Therefore, there are many opportunities for novel Cu based MOFs: the well-defined oxidation and spin states of Cu---Cu motifs is desirable and there is scope for various applications in modified H-KUST analogues. Furthermore, the possibility of tuning properties of Cu-MOFs through rational functionalization of the linking unit and the strength of synthetic approaches for targeting functionalized hybrid materials open in this field a wide range of possibilities to realize a new material with specific uses.

As fas as naming of MOFs is concerned, this may be the moment to insert a brief digression about that. MOFs can be complex in both chemistry and geometry. In attempt to simplify discussions of these frameworks several shorthand naming systems have been devised. The most common is an arbitrary alphanumeric string, often indicating the institution where the material was first isolated (e.g. HKUST-1 as a description of $Cu_3(btc)_2$).

An alternative nomenclature describes the structural topology: in fact, during the past decade, interest has grown tremendously in the design and synthesis of crystalline materials constructed from molecular clusters linked by extended groups of atoms. Most notable are indeed metal-organic frameworks (MOFs), in which polyatomic inorganic metal-containing clusters are joined by polytopic linkers. Although these materials are sometimes referred to as coordination polymers, it is preferable to differentiate them, because MOFs are specifically based on strong linkages that yield robust frameworks. MOFs can be represented as a special kind of graph called a periodic net. Such description dates back to the earliest crystallographic studies but have become much more common recently because thousands of new structures and hundreds of underlying nets have been reported. In the simplest cases (e.g., the structure of diamond), the atoms in the crystal become the vertices of the net, and bonds are the links (edges) that connect them. In the case of MOFs, polyatomic groups act as the vertices and edges of the net. Because of the explosive growth in this area, a need has arisen for a universal system of nomenclature, classification, identification, and retrieval of these topological structures. For this reason, as already mentioned in the previous paragraph, it has been developed a system of symbols for the identification of three periodic nets of interest, and this system is now widely used. This system is based on the underlying methodology of assigning symbols and describe the Reticular Chemistry Structure Resource (RCSR); about 1600 such nets are collected and illustrated in a database that can be searched by symbol, name, keywords, and attributes.

For example, $Cu_3(btc)_2$ crystallizes with a so-called tbo topology in the space group Fm m, which relates to ‘twisted’ boracites (the mineral form of calcium borate). There are many Cu-based MOFs that deviate from the tbo type. For example, Eddaoudi and co-workers reported a Cu-cointaining MOF of type rht, which consists of 12 copper paddlewheels joined by 24 1,3-BDC linkers so that the 5-position of the bent bridging ligand (120° angle) lies exactly on the vertices of the rhombicuboctahedron, and there are further reports including other different topologies.[25]

1.8 Zirconium-based Metal Organic Frameworks

Among the large family of metal–organic frameworks, Zr-based MOFs, which exhibit rich structure types, outstanding stability, intriguing properties and functions, are foreseen as one of the most promising MOF materials for practical applications. Starting from the discovery of $Zr_6(\mu_3\text{-}O)_4(\mu_3\text{-}OH)_4(BDC)_6$ (UiO-66, UiO stands for the University of Oslo), Zr-MOFs have received widespread attention by virtue of their preeminent chemical and physical properties. From then on, the MOFs based on Zr(IV) ions (Zr-MOFs), mostly Zr(IV) carboxylates, ushered in new structural types being reported, diverse strategies being adopted to modify their structures and properties, and various functions and applications being explored.

One key feature of Zr-MOFs is the high oxidation state of Zr(IV) compared with other M(I), M(II), and M(III)-based MOFs (M stands for metal elements). Due to high charge density and bond polarization, there is a strong affinity between Zr(IV) and the carboxylate O atoms in most carboxylate-based Zr-MOFs. Zr(IV) ions and carboxylate ligands are considered hard acids and hard bases, respectively, and their coordination bonds are strong: as a result, most Zr-MOFs are stable in organic solvents and water, and even tolerate acidic aqueous solutions. Zirconium is widely distributed in nature and is found in all biological systems. The rich content and low toxicity of Zr further favor the development and application of Zr-MOFs.

Mostly, Zr-MOFs are constructed by interconnection of polyatomic inorganic Zr-containing clusters and polytopic organic ligands. The structural diversity of the two components and the various ways the two components connect both contribute to the variety of structures in Zr-MOFs.

- **Zr-clusters**: the most important two types of discrete Zr-based clusters observed in reported Zr-MOFs are Zr_6O_8 clusters (Figure 1.12 a) with a variety of coordination environments and Zr_8O_6 clusters (Figure 1.12 b) as a 12-connected node.

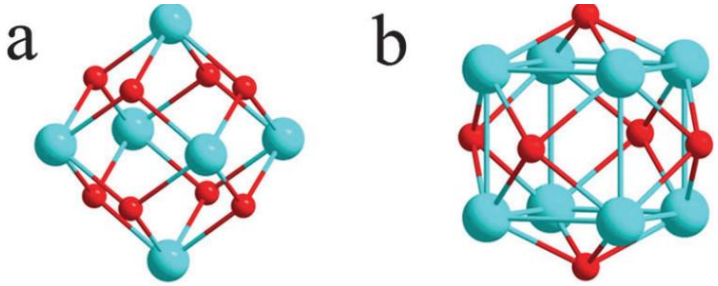

Figure 1.13. Observed Zr-based clusters/cores in Zr-MOFs: (a) Zr_6O_8 cluster, (b) Zr_8O_6 cluster.

The first one, $Zr_6(\mu_3\text{-}O)_4(\mu_3\text{-}OH)_4$ octahedral cluster, is the most commonly observed in Zr-SBUs, in which the six vertices of the octahedron are occupied by Zr(IV) centers. Each Zr(IV) is eight-coordinated by O atoms in a square-antiprismatic coordination geometry. On the contrary, in the $Zr_8(\mu_4\text{-}O)_6$ cubic cluster each Zr atom coordinates with three O atoms from carboxylates and three m4-O atoms, forming a distorted octahedral coordination environment. Eight Zr atoms connecting six m4-O atoms lead to the formation of a cubic cluster based on the Zr arrangement, in which eight vertices are occupied by Zr atoms and six faces are capped by m4-O atoms.

- **Polytopic ligand:** to give a representative example, we can talk about linear dicarboxylate ligands, which have been widely used to build Zr-MOFs. A representative one is terephthalate (BDC_2), which is used for the construction of UiO-66, the first reported Zr-MOF; by increasing length of the used ligands, several isoreticular Zr-MOFs including UiO-67 and UiO-68 were reported early (Figure 1.13).

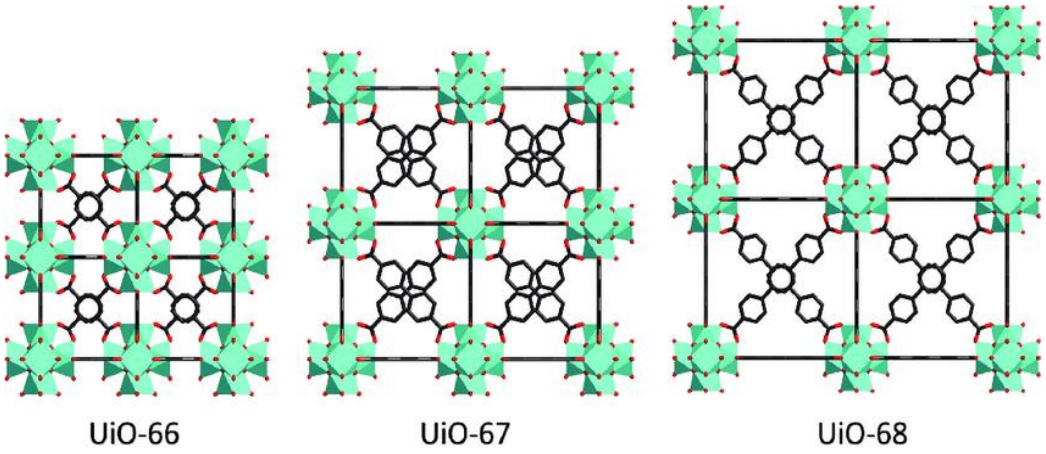

Figure 1.14. UiO-66, UiO-67, and UiO-68 as first examples of Zr-MOF with ditopic ligands.

But there a lot of other polytopic linkers used for Zr-MOFs, as tricarboxylate ligands in MOF-808, reported by Furukawa et al., in which each $Zr_6(\mu_3\text{-}O)_4^{-}(\mu_3\text{-}OH)_4(CO_2)_{12}$ SBU is connected to six BTC_3^{-} ligands, or tetratopic carboxylic ligands that, compared with di- and tricarboxylate ligands, have more coordination sites and rich coordination pattern.

Zr-MOFs based on other SBUs will surely spring up in the future years. In particular, relying on the use of newly selected/designed organic ligands, the structural types of Zr-

MOFs will continuously increase, and more new members of Zr-MOFs with unique properties will emerge and, thanks to their excellent porosity and structural stability, significant efforts have been put into versatile potential applications of Zr-MOFs, including catalysis, molecule adsorption and separation, drug delivery, fluorescence sensing, electrochemistry, porous carrier and so on.

References

(1) Parise, C.; Ballarin, B.; Barreca, D.; Cassani, M. C.; Dambruoso, P.; Nanni, D.; Ragazzini, I.; Boanini, E. Gold Nanoparticles Supported on Functionalized Silica as Catalysts for Alkyne Hydroamination: A Chemico-Physical Insight. *Appl. Surf. Sci.* **2019**, *492*, 45–54. https://doi.org/10.1016/j.apsusc.2019.05.192.

(2) Giorgetti, M.; Aquilanti, G.; Ballarin, B.; Berrettoni, M.; Cassani, M. C.; Fazzini, S.; Nanni, D.; Tonelli, D. Speciation of Gold Nanoparticles by Ex Situ Extended X-Ray Absorption Fine Structure and X-Ray Absorption Near Edge Structure. *Anal. Chem.* **2016**, *88* (13), 6873–6880. https://doi.org/10.1021/acs.analchem.6b01524.

(3) Fazzini, S.; Cassani, M. C.; Ballarin, B.; Boanini, E.; Girardon, J.; Mamede, A.; Mignani, A.; Nanni, D. Novel Synthesis of Gold Nanoparticles Supported on Alkyne-Functionalized Nanosilica. **2014**. https://doi.org/10.1021/JP507637M.

(4) Ghasempour, H.; Wang, K.-Y.; Powell, J. A.; ZareKarizi, F.; Lv, X.-L.; Morsali, A.; Zhou, H.-C. Metal–Organic Frameworks Based on Multicarboxylate Linkers. *Coord. Chem. Rev.* **2021**, *426*, 213542. https://doi.org/10.1016/j.ccr.2020.213542.

(5) Dhakshinamoorthy, A.; Asiri, A. M.; Garcia, H. Metal Organic Frameworks as Versatile Hosts of Au Nanoparticles in Heterogeneous Catalysis. *ACS Catal.* **2017**, *7* (4), 2896–2919. https://doi.org/10.1021/acscatal.6b03386.

(6) Hoskins, B. F.; Robson, R.; Sutherland, E. E. Bis(4-Pyridylethynyl)Mercury. *J. Organomet. Chem.* **1996**, *515* (1), 259–260. https://doi.org/10.1016/0022-328X(96)06185-2.

(7) Lee, Y.-R.; Kim, J.; Ahn, W.-S. Synthesis of Metal-Organic Frameworks: A Mini Review. *Korean J. Chem. Eng.* **2013**, *30* (9), 1667–1680. https://doi.org/10.1007/s11814-013-0140-6.

(8) Jones, J. T. A.; Hasell, T.; Wu, X.; Bacsa, J.; Jelfs, K. E.; Schmidtmann, M.; Chong, S. Y.; Adams, D. J.; Trewin, A.; Schiffman, F.; Cora, F.; Slater, B.; Steiner, A.; Day, G. M.; Cooper, A. I. Modular and Predictable Assembly of Porous Organic Molecular Crystals. *Nature* **2011**, *474* (7351), 367–371. https://doi.org/10.1038/nature10125.

(9) Li, H.; Eddaoudi, M.; O'keeffe, M.; Yaghi, O. Design and Synthesis of an Exceptionally Stable and Highly Porous Metal-Organic Framework. *Nature* **1999**. https://doi.org/10.1038/46248.

(10) Dey, C.; Kundu, T.; Biswal, B. P.; Mallick, A.; Banerjee, R. Crystalline Metal-Organic Frameworks (MOFs): Synthesis, Structure and Function. *Acta Crystallogr. Sect. B Struct. Sci. Cryst. Eng. Mater.* **2014**, *70* (1), 3–10. https://doi.org/10.1107/S2052520613029557.

(11) Furukawa, H.; Ko, N.; Go, Y. B.; Aratani, N.; Choi, S. B.; Choi, E.; Yazaydin, A. Ö.; Snurr, R. Q.; O'Keeffe, M.; Kim, J.; Yaghi, O. M. Ultrahigh Porosity in Metal-Organic Frameworks. *Science* **2010**, *329* (5990), 424–428. https://doi.org/10.1126/science.1192160.

(12) Cordova, K. E.; Yaghi, O. M. The 'Folklore' and Reality of Reticular Chemistry. *Mater. Chem. Front.* **2017**, *1* (7), 1304–1309. https://doi.org/10.1039/C7QM00144D.

(13) Frameworks for Commercial Success. *Nat. Chem.* **2016**, *8* (11), 987–987. https://doi.org/10.1038/nchem.2661.

(14) Ahmad, N.; Chughtai, A. H.; Younus, H. A.; Verpoort, F. Discrete Metal-Carboxylate Self-Assembled Cages: Design, Synthesis and Applications. *Coord. Chem. Rev.* **2014**, *280*, 1–27. https://doi.org/10.1016/j.ccr.2014.07.005.

(15) Kim, J.; Chen, B.; Reineke, T. M.; Li, H.; Eddaoudi, M.; Moler, D. B.; O'Keeffe, M.; Yaghi, O. M. Assembly of Metal−Organic Frameworks from Large Organic and Inorganic Secondary Building Units: New Examples and Simplifying Principles for Complex Structures. *J. Am. Chem. Soc.* **2001**, *123* (34), 8239–8247. https://doi.org/10.1021/ja010825o.

(16) Yaghi, O. M.; O'Keeffe, M.; Ockwig, N. W.; Chae, H. K.; Eddaoudi, M.; Kim, J. Reticular Synthesis and the Design of New Materials. *Nature* **2003**, *423* (6941), 705–714. https://doi.org/10.1038/nature01650.

(17) Rosi, N. L.; Kim, J.; Eddaoudi, M.; Chen, B.; O'Keeffe, M.; Yaghi, O. M. Rod Packings and Metal−Organic Frameworks Constructed from Rod-Shaped Secondary Building Units. *J. Am. Chem. Soc.* **2005**, *127* (5), 1504–1518. https://doi.org/10.1021/ja045123o.

(18) Lee, Y.-R.; Kim, J.; Ahn, W.-S. Synthesis of Metal-Organic Frameworks: A Mini Review. *Korean J. Chem. Eng.* **2013**, *30* (9), 1667–1680. https://doi.org/10.1007/s11814-013-0140-6.

(19) Mondloch, J. E.; Karagiaridi, O.; Farha, O. K.; Hupp, J. T. Activation of Metal–Organic Framework Materials. *CrystEngComm* **2013**, *15* (45), 9258–9264. https://doi.org/10.1039/C3CE41232F.

(20) Cassani, M. C.; Castagnoli, R.; Gambassi, F.; Nanni, D.; Ragazzini, I.; Masciocchi, N.; Boanini, E.; Ballarin, B. A Cu(II)-MOF Based on a Propargyl Carbamate-Functionalized Isophthalate Ligand as Nitrite Electrochemical Sensor. *Sensors* **2021**, *21* (14), 4922. https://doi.org/10.3390/s21144922.

(21) Chui, null; Lo, null; Charmant, null; Orpen, null; Williams, null. A Chemically Functionalizable Nanoporous Material. *Science* **1999**, *283* (5405), 1148–1150. https://doi.org/10.1126/science.283.5405.1148.

(22) Peng, Y.; Srinivas, G.; Wilmer, C. E.; Eryazici, I.; Snurr, R. Q.; Hupp, J. T.; Yildirim, T.; Farha, O. K. Simultaneously High Gravimetric and Volumetric Methane Uptake Characteristics of the Metal-Organic Framework NU-111. *ChemComm* **2013**, *49* (29). https://doi.org/10.1039/c3cc40819a.

(23) Ma, S.; Sun, D.; Simmons, J. M.; Collier, C. D.; Yuan, D.; Zhou, H.-C. Metal-Organic Framework from an Anthracene Derivative Containing Nanoscopic Cages Exhibiting High Methane Uptake. *J. Am. Chem. Soc.* **2008**, *130* (3), 1012–1016. https://doi.org/10.1021/ja0771639.

(24) Yan, Y.; Suyetin, M.; Bichoutskaia, E.; J. Blake, A.; R. Allan, D.; A. Barnett, S.; Schröder, M. Modulating the Packing of [Cu 24 (Isophthalate) 24] Cuboctahedra in a Triazole-Containing Metal–Organic Polyhedral Framework. *Chem. Sci.* **2013**, *4* (4), 1731–1736. https://doi.org/10.1039/C3SC21769H.

(25) Eubank, J. F.; Nouar, F.; Luebke, R.; Cairns, A. J.; Wojtas, L.; Alkordi, M.; Bousquet, T.; Hight, M. R.; Eckert, J.; Embs, J. P.; Georgiev, P. A.; Eddaoudi, M. On Demand: The Singular Rht Net, an Ideal Blueprint for the Construction of a Metal-Organic Framework (Mof) Platform. *Angew. Chem. - Int. Ed.* **2012**, *51* (40), 10099–10103. https://doi.org/10.1002/anie.201201202.

CHAPTER 2

2. SYNTHESIS AND CHARACTERIZATIONS OF 1,3-H2YBDC AND Cu-(1,3-YBDC)

2.1 Aim of the chapter

In this chapter the synthesis in three steps of a new organic linker belonging to the substituted dicarboxylate class, i.e. 5-(2-{[(prop-2-yn-1-yloxy)carbonyl]amino}ethoxy)isophthalic acid (which we have labelled 1,3-H2YBDC, where Y stands for alkYne and BDC for benzene dicarboxylate), bearing a propargyl carbamate residue, is realized. The structure of the intermediates, step 1: **prop-2-yn-1-yl *N*-(2-bromoethyl)carbamate**, step 2: **dimethyl 5-(2-{[(prop-2-yn-1-yloxy)carbonyl]amino}ethoxy) isophthalate (1,3-Me$_2$YBDC)**, and the final product **1,3-H$_2$YBDC**, were investigated by means of complementary characterization techniques such as Esi-MS, NMR, TGA, and IR-ATR analysis. Moreover, the optimized conditions for the synthesis of the novel Cu(II)–MOF, **[Cu(1,3-YBDC)]·*x*H$_2$O** derived from the new linker are discussed. A detailed, comprehensive multi-technique characterization of the new material by means of complementary analytical, structural and imaging tools will be also reported. Part of the work reported in the present chapter has been published in RSC Advances.[1]

2.2 Introduction

Most of the MOFs syntheses typically involve mixing of metal salts (or pre-formed complexes) with a pre-formed organic linker. As denticity and other stereochemical preferences make the different organic ligands prone to the formation of archetypal frameworks (classified by their topology, or, more frequently, by labels referring to some of the most "popular", or efficient, materials), it is not a surprise that specific classes of ligands had received much more attention than others: benzene dicarboxylates (in the form of terephthalates and isophthalates), imidazolates, bis-pyrazolates, and topologically analogues with extended cores.[2]

Thus, a rational design of the network topology, with predictable size and shapes of the pores, has reached its maturity. Jointly with structural prediction, exemplified by the

isoreticular chemistry approach, also thermal inertness, chemical stability in harsh conditions and, to some extent, the functional properties of the prepared MOFs can be rationally outlooked. A seminal article that covers general, modern synthetic strategies to prepare MOFs and discusses their structural diversity and properties with respect to application perspectives has been published by Williams et al.[3]

However, when flexible residues are protruding from the ligand cores, the likely availability of a large "empty space" within the crystal makes prediction capability fail. In these conditions, a systematic study of the sample properties, which heavily depend on the actual "stable" structure, is required. As anticipated, benzene-polycarboxylato ligands are frequent choices for the construction of stable and performing metal–organic networks. One of the most common organic linkers is benzene-1,3,5-tricarboxylic acid (BTC). The related 3D-[Cu_3(- BTC)$_2$(H_2O)$_3$] compound (also called HKUST-1 or Cu–BTC, **Fig.2.1**),[3] one of the most extensively studied 3-dimensional coordination polymers, is a highly porous material (with a specific surface area, SSA, reported to be ca. 690 m^2/g^{-1} in the original paper[3] and much higher than 1500 m^2/g^{-1} in the marketed materials) in which {Cu2} units are coordinated to four carboxylate groups to give the well-known paddle-wheel unit.[4]

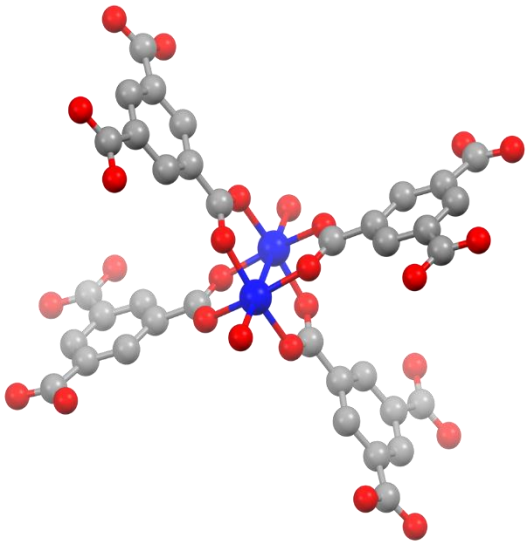

Figure 2.1. Schematic representation of HKUST-1 or Cu-BTC.

Simpler ligands, like benzene-dicarboxylates (BDC), thanks to their structural rigidity (and simultaneous charge balancing effects of M(II) centers), have also been widely employed, as they can bear an additional, pendant and chemically tailored functionality on the benzene ring.[5] In recent years, our research group has shown that a propargyl carbamate

[–N(H)C(O)O–CH_2–CCH] group anchored on different oxide supports (SiO_2, Al_2O_3, TiO_2, Fe_3O_4) is capable of straightforwardly reducing Au(III) to Au(0), yielding supported gold nanoparticles (AuNPs) without the addition of any external reducing and/or stabilizing agent.[6,7]

Based on these results and taking into account that the chemical, structural, and functional behavior of the gold nanoparticles reported above depend on the physico-chemical environment dictated by the support, we envisaged that the versatility demonstrated by the propargyl carbamate residue in generating and stabilizing metal NPs could be further exploited by anchoring it to different solid supports than oxides, for example MOFs. We aimed indeed at synthesizing a new material where distribution of the reactive alkyne moiety could be more even and dense with respect to the previous oxides. Additionally, the material porosity and the presence of the metal nodes could affect the reactivity of the alkyne and induce different effects on the ensuing gold nanoparticles, hence producing novel behaviours as far as the possible applications are concerned.

2.3 Results and discussion

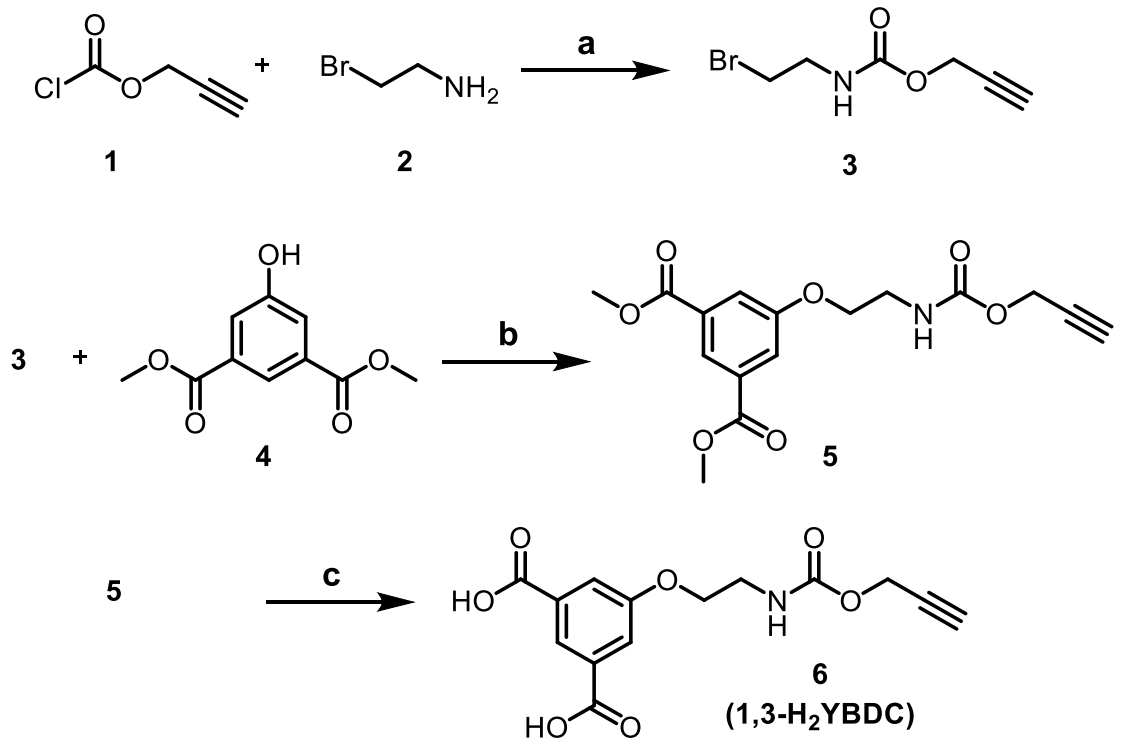

Scheme 2.1. Synthetic steps for 1,3-H2BDC. Reagents and conditions: (a) $NaHCO_3$ (3 eq), THF/H_2O, r.t., overnight; (b) NaI (1.5 eq.), Cs_2CO_3 (1.5 eq.), 2-butanone, 80 °C, overnight; (c) LiOH (2.0 M), THF/MeOH, r.t., 3h.

The novel organic dicarboxylic linker 1,3-H_2YBDC, bearing a propargyl carbamate group, was prepared following the synthetic route depicted in **Scheme 2.1**. The synthesis involves initial condensation of the commercially available chloroformate **1** with bromoamine **2**, yielding carbamate **3**. Crude **3** was then reacted with phenol **4** in the presence of NaI and cesium carbonate to afford arylether **5**, which was subsequently converted into the corresponding dicarboxylic acid **6** by LiOH-promoted hydrolysis, with overall, reproducible yields normally well above 95%.

Figure 2.2 shows the ESI-MS(+) spectra of 1,3-H_2YBDC; the peak at 330 *m/z* is attributed to the pseudomolecular ion $[C_{14}H_{13}NO_7 + Na]^+$.

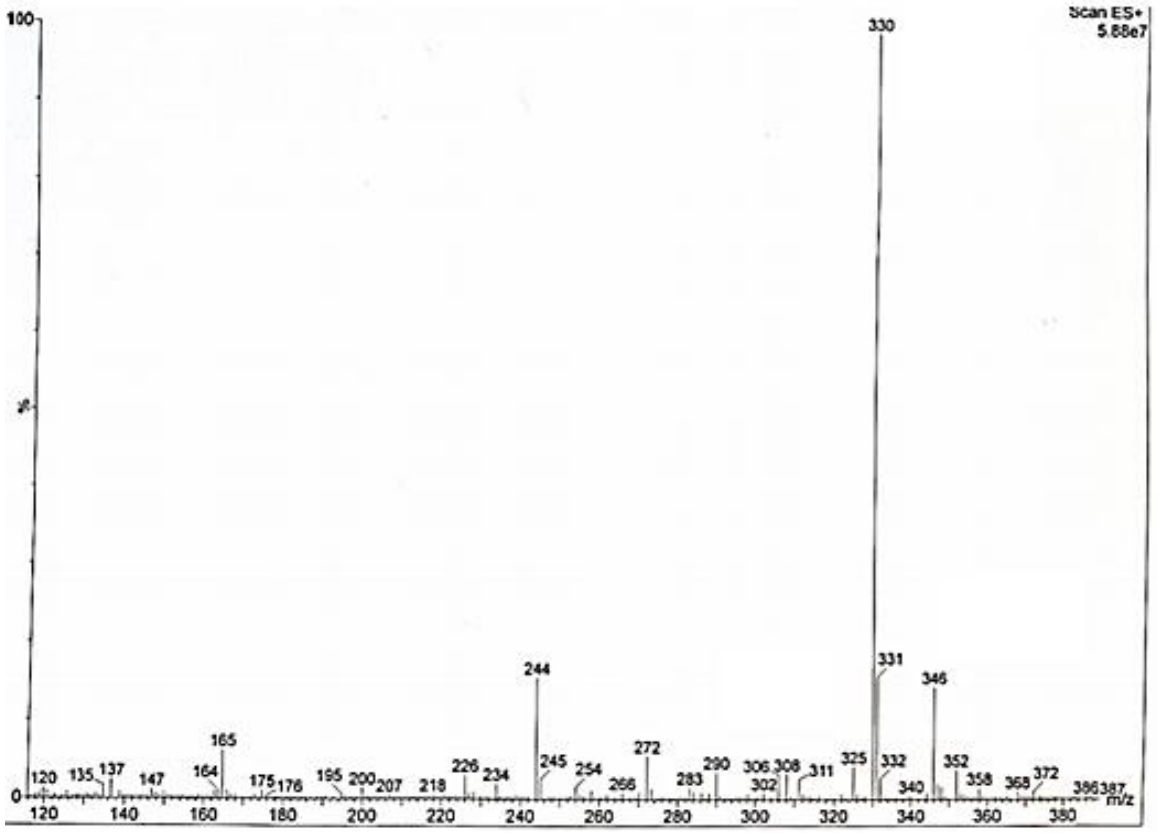

Figure 2.2: ESI-MS(+) spectrum of 1,3-H_2YBDC.

Figure 2.3 shows the ^{1}H-NMR spectra of 1,3-H_2YBDC. In the aromatic region, the Ar-H^1 signal at 8.29 ppm is a triplet and shows a $^4J_{H\text{-}H}$ (1.5 Hz) coupling with the two symmetric Ar-H^2, its integral was set to be unitary. The Ar-H^2 signal at 7.79 ppm is a doublet with a $^4J_{H\text{-}H}$ with Ar-H^1 and an integral slightly more than double that of Ar-H^1. In the aliphatic region of the spectra, the -$OCH_2{}^5C{\equiv}CH$ signal at 4.67 ppm is a doublet that integrates two protons, showing a $^4J_{H\text{-}H}$ (2.4 Hz) coupling with the allylic proton -$C{\equiv}CH^6$. The signals of -$OCH_2{}^3$- and -$CH_2{}^4N(H)$- are located at 4.25 ppm and 3.60 ppm respectively, being -$OCH_2{}^3$- more deshielded due to its proximity to the more electronegative oxygen. They are both triplets, integrating two protons and displaying a $^3J_{H\text{-}H}$ (6.8 Hz) coupling between each other. The signal at 2.95 ppm is attributed to -$C{\equiv}CH^6$, it is a triplet because of its $^4J_{H\text{-}H}$ with the two -$OCH_2{}^5C{\equiv}CH$ protons. Figure 2.4 shows the ^{13}C-NMR spectra of 1,3-H_2YBDC.

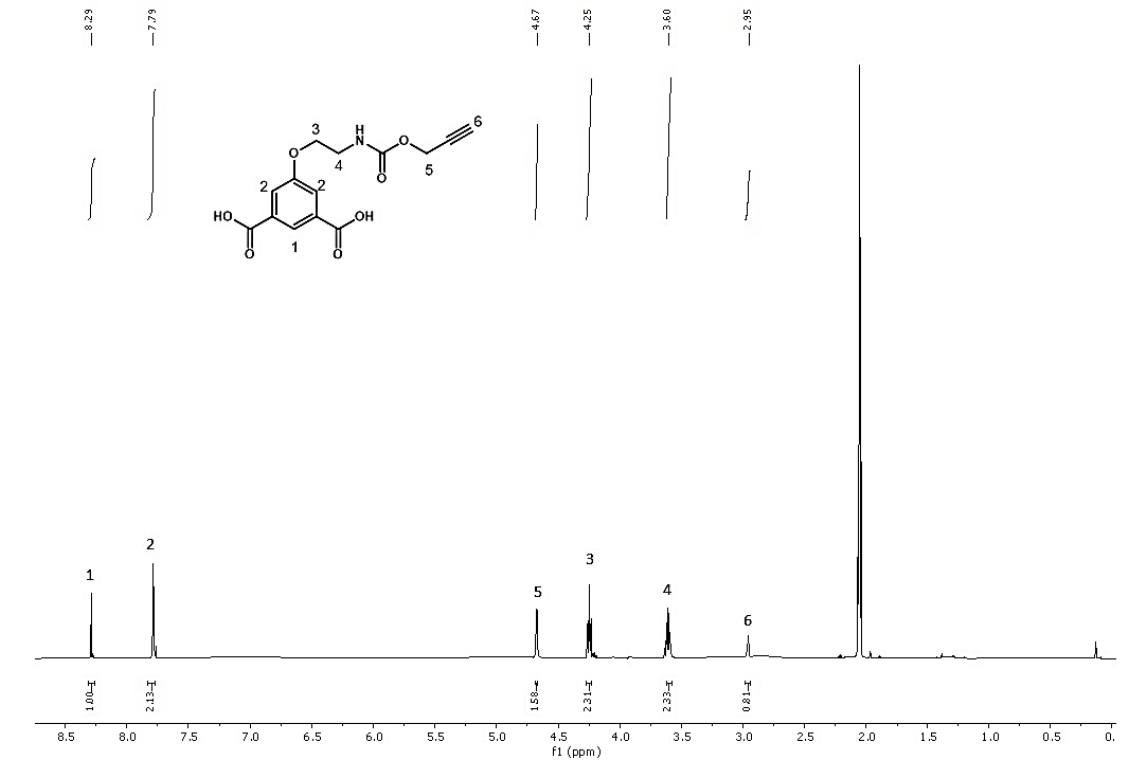

Figure 2.3: ^{1}H-NMR spectrum of 1,3-H_2YBDC.

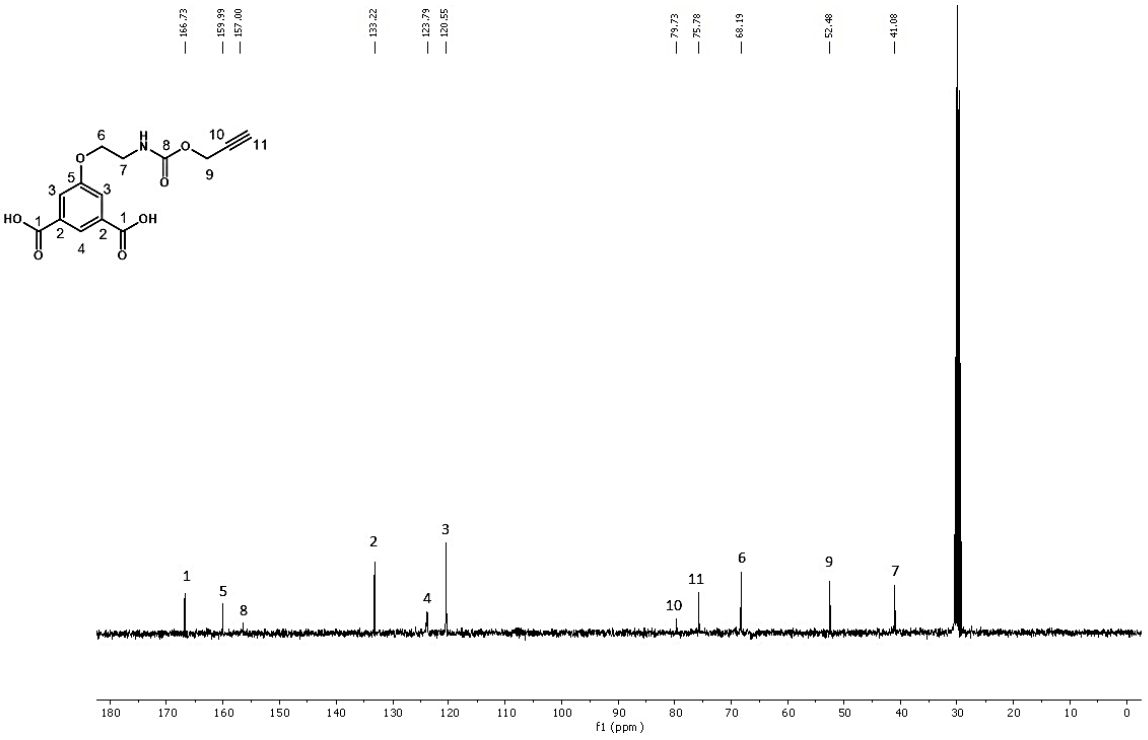

Figure 2.4: ^{13}C-NMR spectrum of 1,3-H_2YBDC.

The IR-ATR spectra of 1,3-H_2YBDC is showed in Figure 2.5. The peak at 3336

cm^{-1} is attributed to the N-H bond stretching and the peak at 3304 cm^{-1} is due to the ≡C-H stretching, both present in the propargylcarbamate residue of 1,3-YBDC. The broad band in the 2800-3200 cm^{-1} region is attributed to the carboxylic acid H-O stretching, while the stetching of both aliphatic and aromatic C-H bonds are responsible for the broad band aroun 3086-2961 cm^{-1}. The peaks at 1737 cm^{-1} and 1687 cm^{-1} are attributed to the stretching of the carboxilate (-C(O)O-) and carbamate (-C(O)NH-) groups, respectively. The bending of the carbammic N-H bond and the stretching of the C-O bond are attributed to the peaks at 1550 cm^{-1} and 1259 cm^{-1}, respectively. Due to the low change in dipole moment caused by the stretching of the alkylic C≡C bond, its peak is barely visible at 2139 cm^{-1}.

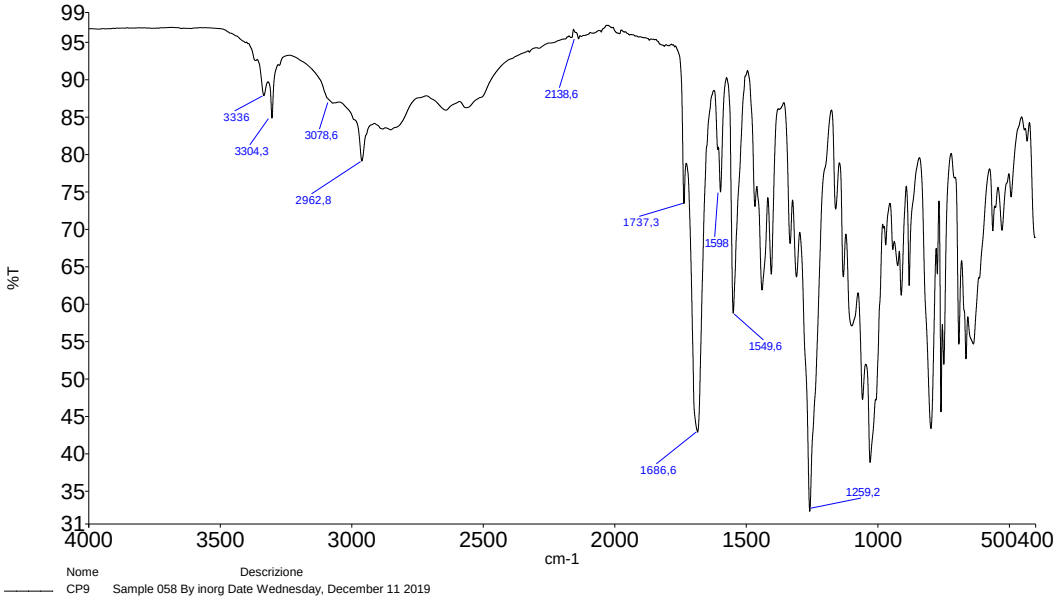

Figure 2.5: IR-ATR spectrum of 1,3-H_2YBDC.

The TGA analysis of the as prepared 1,3-H_2YBDC (Figure 2.6 and Table 2.1) showed a high residue (5%) at 800 °C, indicating the presence of inorganic impurities in the sample deriving from the inorganic salts used in large excesses during the last step of the synthesis.

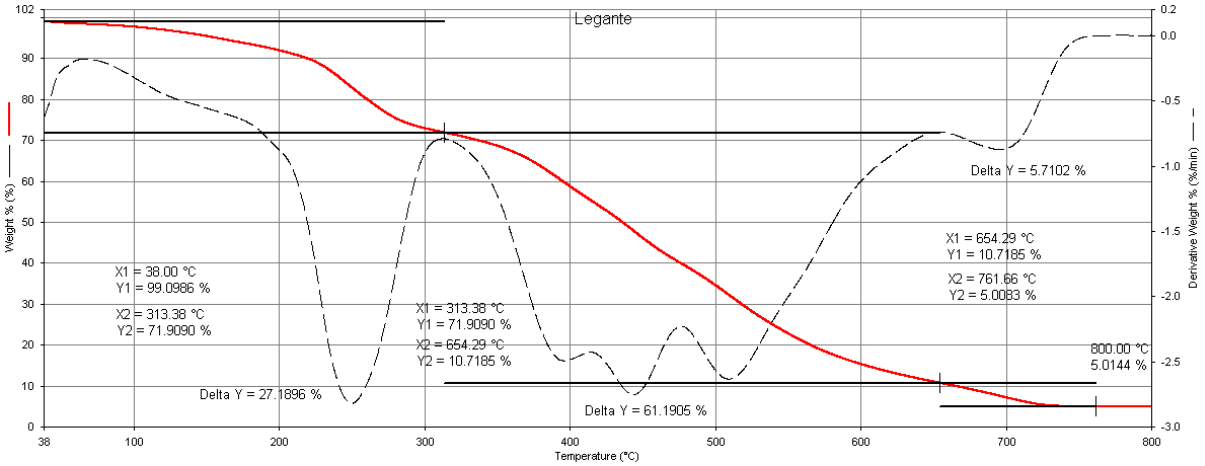

Figure 2.6 TGA curve (continuous red line) and first derivative (dashed line) of the weight loss of 1,3-H_2YBDC.

Table 2.1: TGA table of 1,3-H_2YBDC.

1° loss (%)	*2° loss (%)*	*3° loss (%)*	*Residue (800 °C, %)*
21.2	*61.2*	*5.7*	*5.0*

The presence of LiCl and/or LiOH in the linker could lead to the formation of copper hydroxides and/or copper chlorides impurities within the MOF able to occupy the MOF's pores and in turn lowering its surface area and pore volume. To prevent this, purification of the linker through crystallization became mandatory. The procedure is described in Section 2.3.4. As shown in Table 2.2, after the first crystallization, the melting point of the linker increased from 186-191 °C to 216-217 °C.

Table 2.2: Yields and melting points of the crystallized products.

	Yield (%)	**Melting point (°C)**
First crystallization	29.6	216-217
Second crystallization	8.7	216-217
Third crystallization	11.8	215-217
Fourth crystallization	4.2	187-190

The increased purity was confirmed by the lower % of residue observed in the TGA analysis of the product after the first crystallization. From the fourth crystallization onward 1,3-H_2YBDC showed a lower melting point and a pink colour, probably due to the presence of impurities formed by some decomposition during crystallization. For this reason, it was discarded. The similarity between the ^{1}H-NMR of the as synthetized 1,3-H_2YBDC (Figure 2.3) and that of the recrystallized one (Figure 2.8), suggests that few recrystallization processes do have a beneficial effect on compund purity and do not chemically modify the structure of the molecule. The crystallized 1,3-H_2YBDC was used as the linker for the synthesis of the MOF.

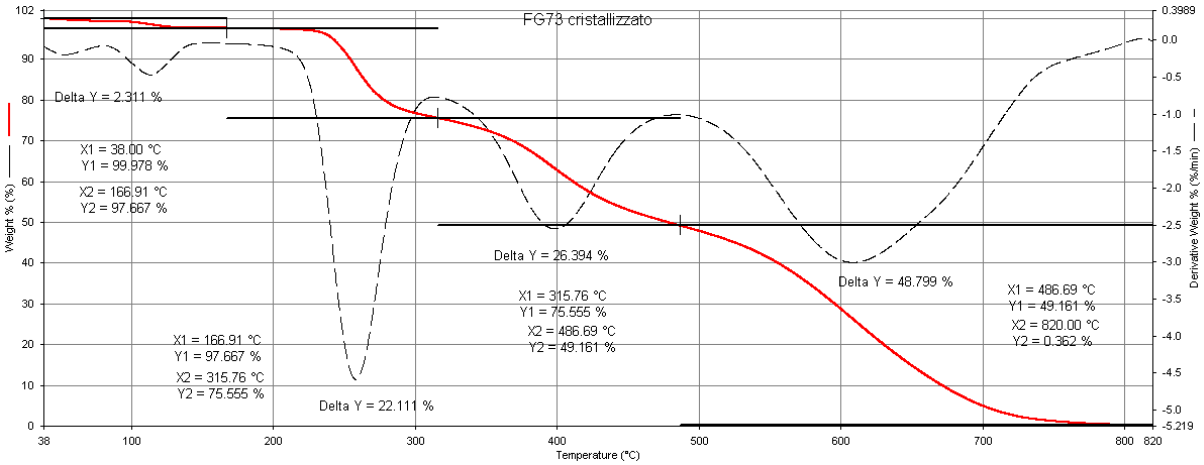

Figure 2.7: TGA curve (continuous red line) and first derivative (dashed line) of the weight loss of 1,3-H_2YBDC from the first crystallization.

Table 2.3: TGA losses of 1,3-H_2YBDC from the first crystallization.

1° loss (%)	2° loss (%)	3° loss (%)	4° loss (%)	Residue (800 °C, %)
2.3	22.1	26.4	48.8	0.4

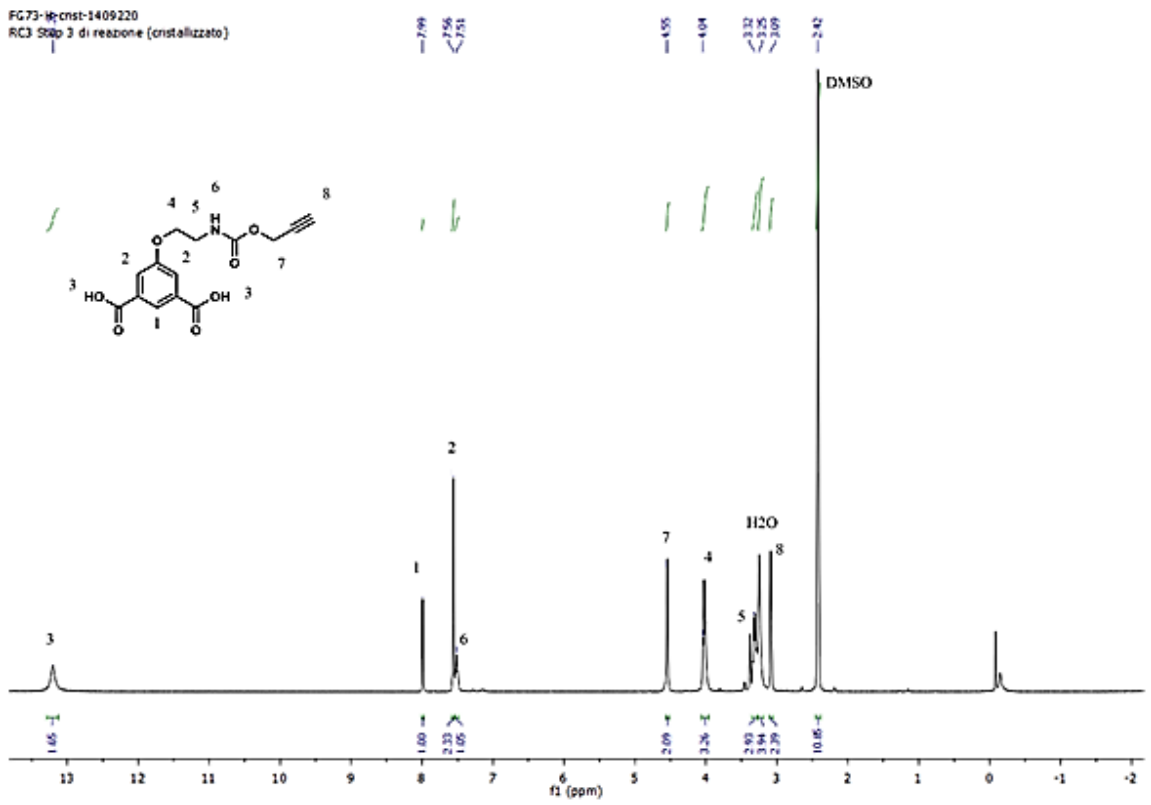

Figure 2.8: ^{1}H-NMR of 1,3-H_2YBDC from the first crystallization.

2.4 [Cu(1,3-YBDC)]·xH_2O synthesis and characterization

2.4.1 Optimization of reaction conditions

As shown in Scheme 2.2, the dicarboxylic linker 1,3-H_2YBDC was reacted with $Cu(NO_3)_2$·2.5H_2O under different reaction conditions. It was found that in refluxing ethanol for 48 h, regardless of the Cu:L molar ratios employed (from 1:1 to 5:1), the yields were erratically ranging between 30 and 60% (based on 1,3-H_2YBDC). As reported by Morris et al.[8] this behaviour is due to the concomitant copper-promoted esterification reaction of the diacid with ethanol and indeed the presence of the diester was confirmed by analysing the reaction supernatant and washings by NMR spectroscopy.

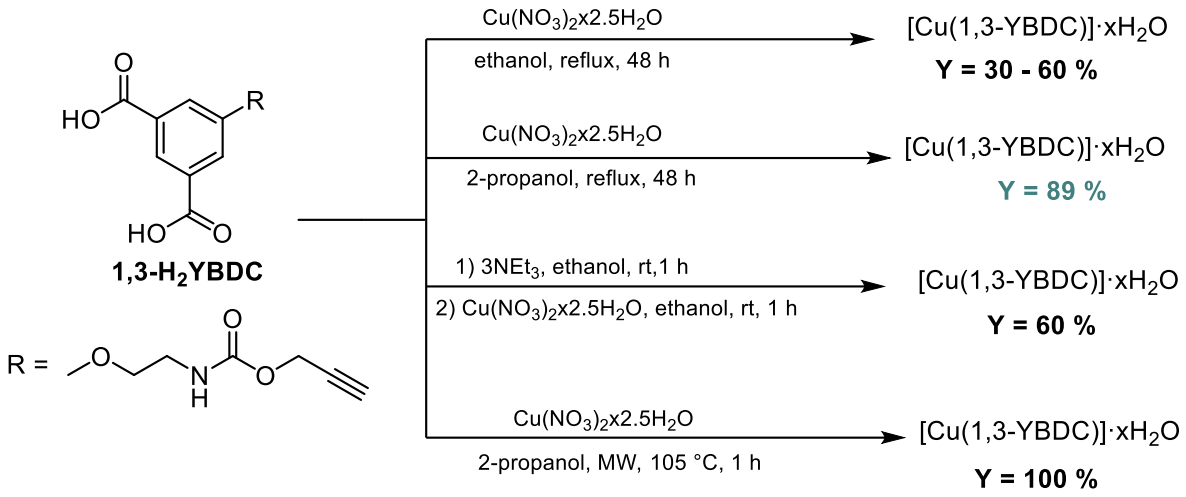

Scheme 2.2: Synthesis of [Cu(1,3-YBDC)]·xH_2O under different conditions.

Figure 2.9: [Cu(1,3-YBDC)]·xH_2O inside its mother liquor (left) and purified MOF after work-up (right).

When 2-propanol is used instead of ethanol, such side reaction is minimized, and the yields were repeatable and always about 90% or higher. Alternatively, the diacid 1,3-H_2YBDC was first reacted with triethylamine in ethanol to give the corresponding triethylammonium salt $[NEt_3H]_2$[1,3-YBDC], which was isolated as a pale, yellow oil that immediately reacted with copper nitrate at room temperature. Regardless of the conditions employed, the final product was always a turquoise polycrystalline powder having formula [Cu(1,3-YBDC)]·xH_2O. All attempts to get X-ray quality single crystals either by carrying out the reaction under hydrothermal conditions using a mixture of water/benzene or layering a solution of $Cu(NO_3)_2$ in ethanol onto a solution of $[NEt_3H]_2$[1,3-YBDC] in $CHCl_3$ failed. Through a microwave-assisted synthesis of [Cu(1,3-YBDC)]·xH_2O in 2-propanol, a turquoise solid was obtained with a very high yield in just one hour.

The screening of the reaction conditions was performed through XRD characterization of the products (Figures 2.10 and 2.11).

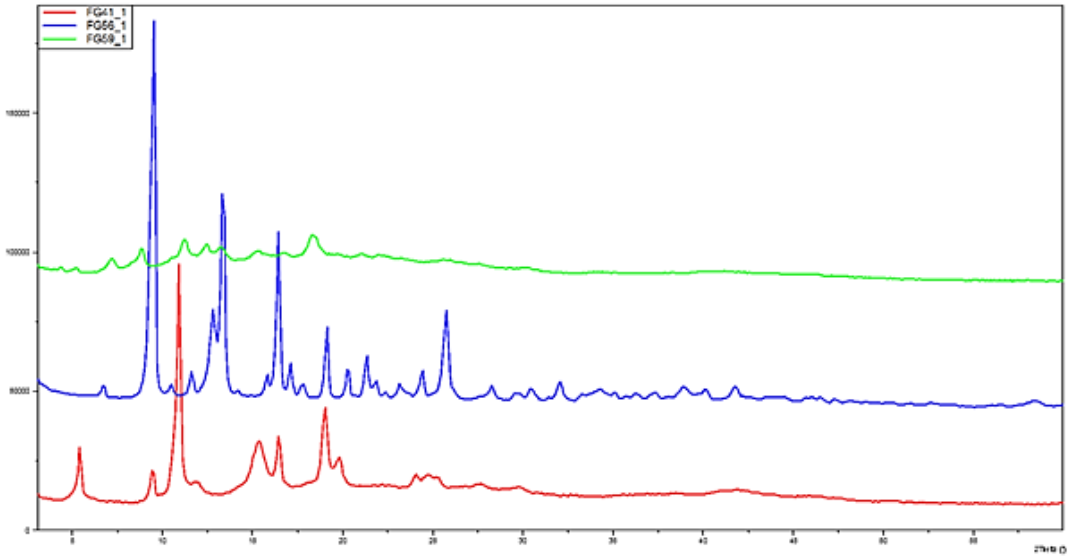

Figure 2.10: XRD patterns of MOF powders from different synthesis: synthesis in ethanol 48 h (red line), synthesis in 2-propanol 48 h (blue line), synthesis in ethanol with trimethylamine (green line).

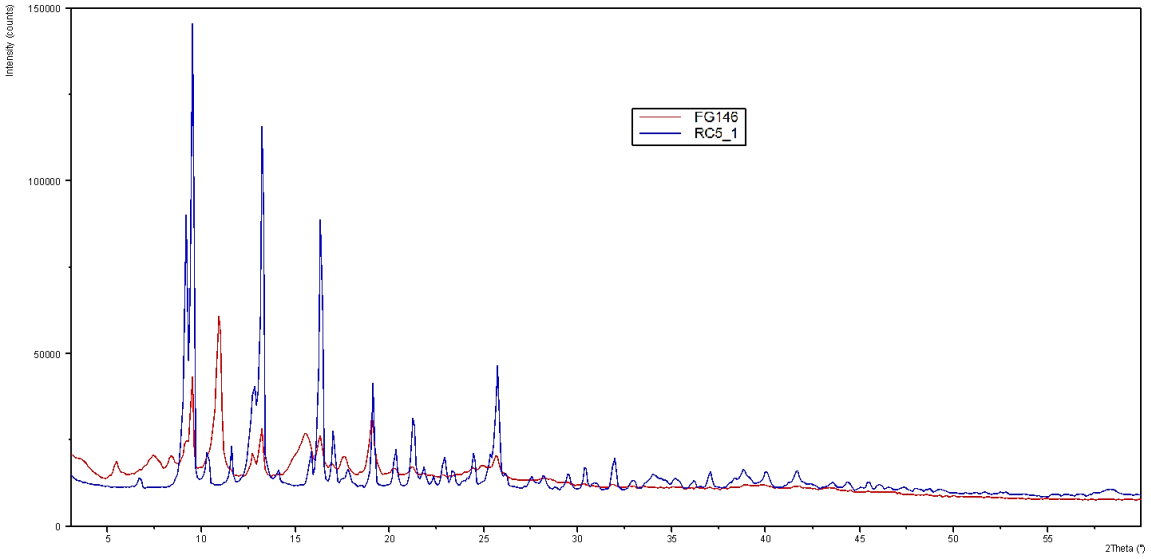

Figure 2.11: XRD patterns of MOF powders from different synthesis: synthesis in 2-propanol 24 h (blue line), microwave assisted synthesis (red line).

The only product that satisfied the crystallinity requirement is the one from the solvothermal synthesis in 2-propanol (Figures 2.10 and 2.11 blue line). The use of ethanol as the solvent for the synthesis (Figure 2.10 red line) led to a low degree of crystallinity. The use of triethylamine as a templating agent (Figure 2.10 green line) in ethanol caused an even

lower degree of crystallinity, as shown by the broadness of the peaks in the XRD spectra. The XRD spectra of the product of the microwave-assisted synthesis also shows broad peaks. Although its XRD spectrum (Figure 3.10 red line) and that of the solvothermal synthesis in 2-propanol product have some peaks in common, the XRD of the microwave-assisted synthesis product shows other peaks indicating the presence of another phase, which is preponderant. By looking at the broadness of the peak at about 15° 2θ, the crystallinity of this new phase also seems to be very low. For all these reasons, 2-propanol was chosen as the solvent for the solvothermal synthesis of [Cu(1,3-YBDC)]·xH_2O.

The screening for the solvent was followed by the screening for the optimal reaction time. The solvothermal synthesis in 2-propanol was carried for 24, 48, 72, and 120 hours. The XRD spectra of the products of these reactions are shown in Figure 2.12.

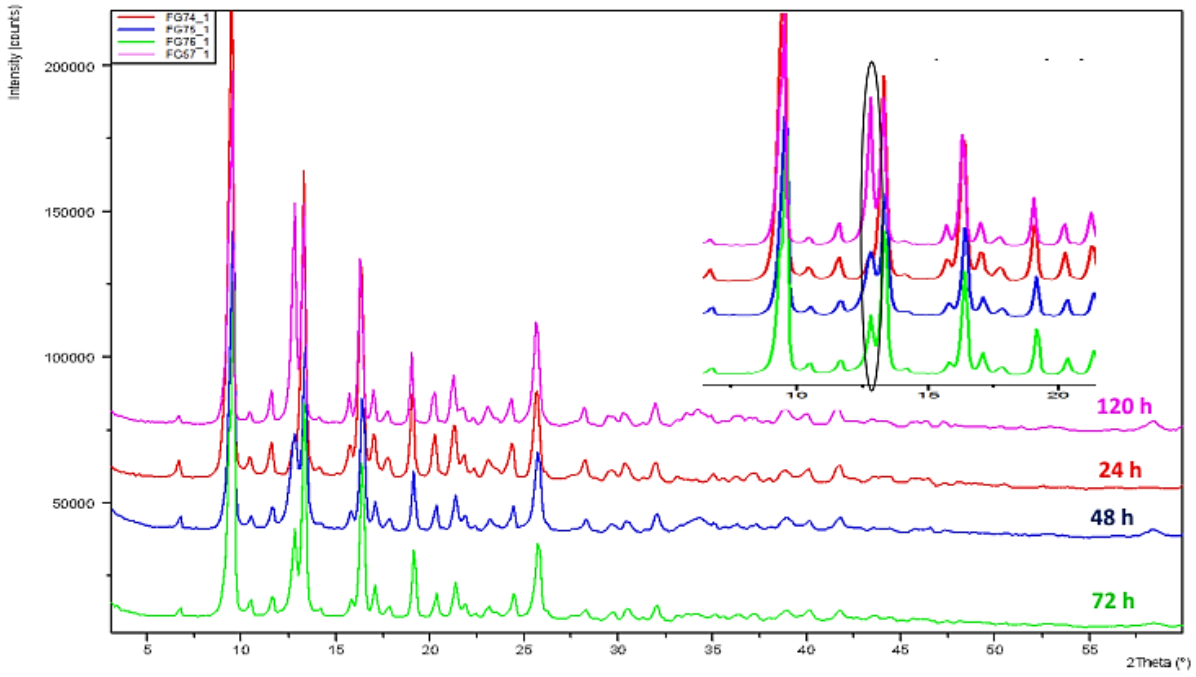

Figure 2.12: XRD patterns of MOF powders from solvothermal synthesis carried in 2-propanol at different reaction times: 24 h (red), 48 h (blue),72 h (green), 120 h (purple).

Increasing the reaction time over 24 hours led to the formation of a new crystalline phase, as evidenced by the peak at about 12.5° 2θ present in the XRD of the products from the reactions carried out for 48h, 72 h, and 120 h. For this reason, 24 hours was chosen as the optimal reaction time for the synthesis of the MOF and all the characterization was carried out on this sample.

2.4.2 Vibrational spectroscopy and thermal characterization

Figure 2.13 shows the IR spectra of the linker (black) and the MOF (red). The very broad band in the 2800-3200 cm^{-1} region, attributed to the carboxylic acid H-O bond stretching and observable in the linker's IR spectra (black), is not present in the MOF's IR spectra (red). This means that the deprotonation of the linker must occur in order for the MOF to form.

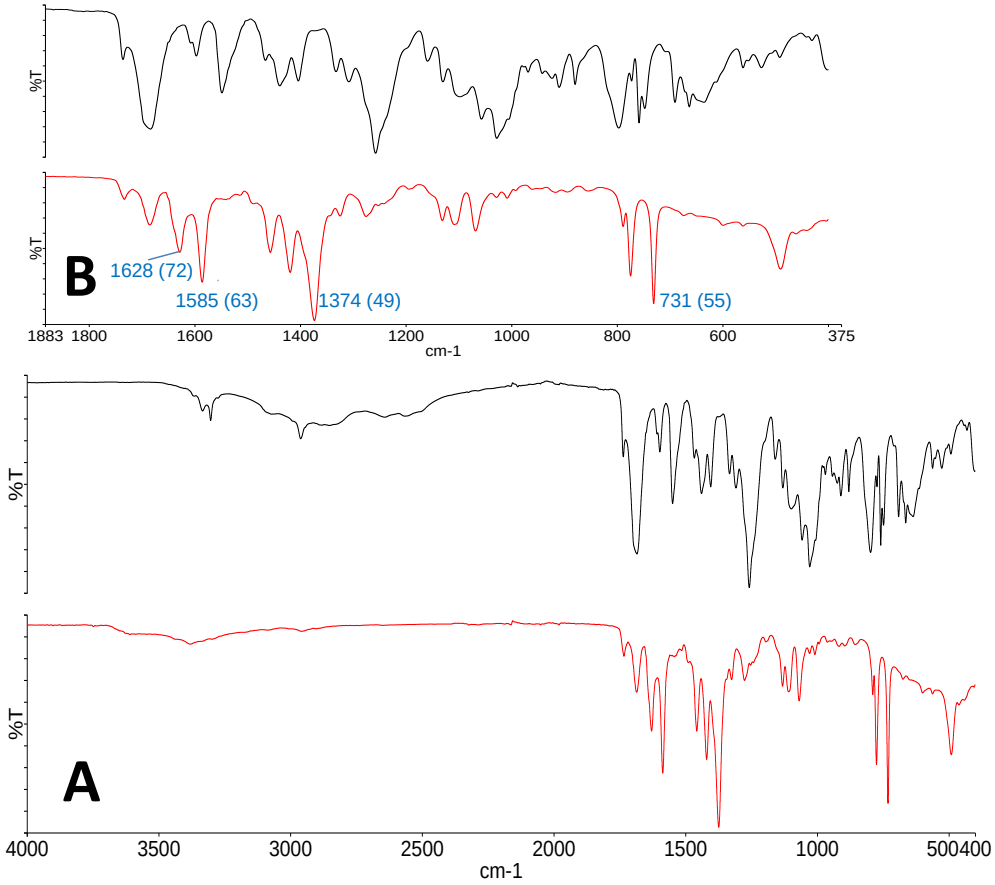

Figure 2.13: (A) ATR-FTIR spectra of 1,3-H2YBDC (black curve) and [Cu(1,3-YBDC)]·xH_2O (red curve); (B) magnification of the 1800-400 cm-1 range (in parentheses the % Transmittance values of the labelled peaks).

The peak at 731 cm^{-1} is attributed to the Cu-O bond.[9] This suggests the coordination of copper with the carboxylate groups of the linker. Because the IR-ATR was always the first analysis performed on the MOF right after its activation, the presence of the 731 cm^{-1} peak in the spectra was used to verify if the MOF synthesis was successful and if the material was worthy of further characterizations. The broad peak at 3000-3500 cm^{-1} in the [Cu(1,3-YBDC)]·xH_2O IR spectra indicates the presence of water inside the MOF structure.[10] This peak is not present in the linker's IR spectra. The presence of water in the MOF could be explained by one or both:

- the adsorption of water from air between the MOF thermal activation and the IR analysis (supported by later shown TGA characterization);
- the presence of weakly bonded water molecules from $Cu(NO_3)_2 \cdot 2.5H_2O$ that are not removed during thermal activation.

The signals at 1605 and 1004 cm^{-1} are associated with the vibrations of the C=C bonds of the benzene ring. In addition, the IR spectrum shows two intense bands at 1585 and 1374 cm^{-1}, particularly diagnostic for the asymmetric and symmetric stretching mode of the carboxylate group (RCO_2^-). The peaks at 3336 cm^{-1} and 3304 cm^{-1} are associated with the vibrations of the ≡C-H and N-H bonds, respectively. These peaks are both presents in the 1,3-YBDX and the $[Cu(1,3\text{-YBDC})] \cdot xH_2O$ IR spectra, although in the second one they are less recognizable due to the presence of water. The peak at 1628 cm^{-1} is attributed to the v(C=O) stretching of the carbamate group. Because of the coordination of this group to the apical position of copper (see the paragraph of Crystallochemical Analysis 2.5.3), the peak is located at a frequency 59 cm^{-1} lower than in the pristine 1,3-H_2YBDC.[11]

Figure 2.14 shows a comparison between the Raman spectra od the linker, the MOF, and copper nitrate. Because of the little change of dipole moment induced by the symmetric stretching of the terminal alkyne group, its peak is not observable in the IR spectra. For this reason, the Raman spectra was used to monitor the alkyne functionality. The peak attributed to the stretching of this group is observable at 2135 cm^{-1}. The presence of this peak in both the linker's and MOF's spectra suggests that, other than deprotonation, no further modification of the linker occurs during the synthesis.

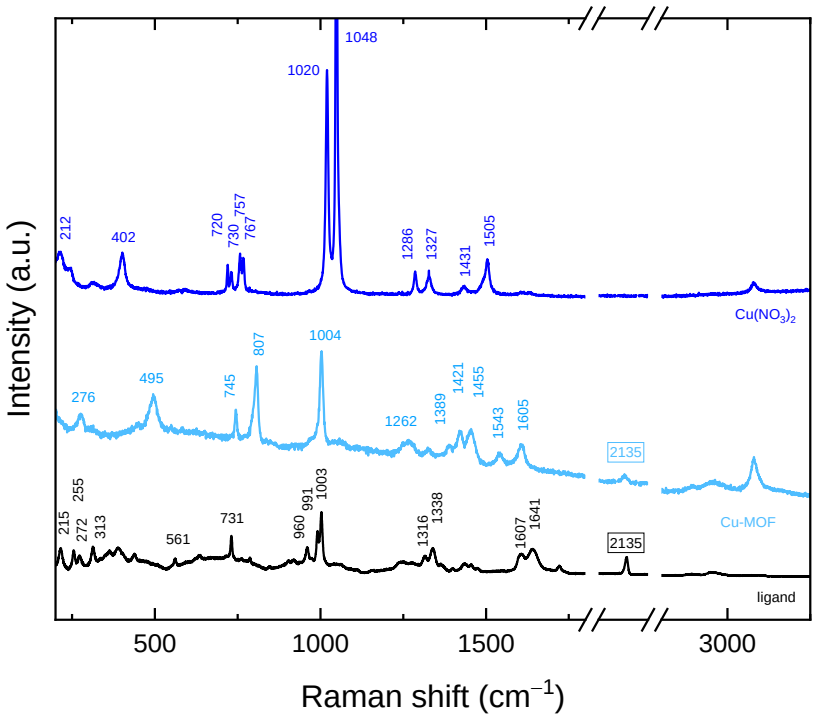

Figure 2.14: Raman spectra of 1,3-H_2YBDC (black), $Cu(NO_3)_2x2.5H_2O$ (blue) and $[Cu(1,3\text{-YBDC})]\cdot xH_2O$.

As mentioned in the introduction, the purpose of the propargylcarbamate group is to give the MOF the ability to synthetize AuNPs. In the proposed mechanism for AuNPs formation shown in scheme 1.1, the alkyne functionality is lost at the end of the process. For this reason, the Raman characterization was also useful to monitor AuNPs formation. In the low frequency range of the Raman spectra, the peaks at 495 and 276 cm^{-1} are assigned to the vibrational stretching modes of equatorial and axial Cu-O bonds respectively.[12] The signals located at 1605 and 1004 cm^{-1} are associated with the benzene ring ν(C=C) stretching modes. The peaks at 807 and 745 cm^{-1} are caused by the out-of-plane δ(C-H) and δ(C=C) ring bending vibrations, respectively.

The elemental analysis of the synthesized sample is in good agreement with the theoretical chemical composition, showing a Cu/N molar ratio of ca. 1 (see the Experimental Part). The TGA characterization was used to investigate the thermal stability of the MOF (Figure 2.15).

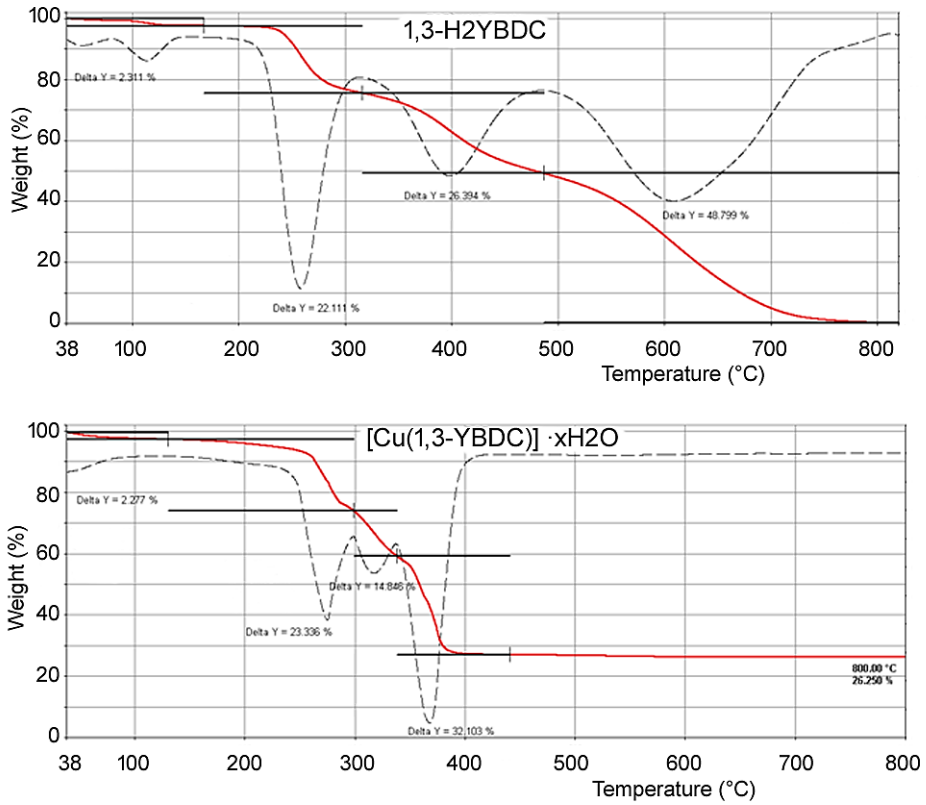

Figure 2.15: TGA curves (continuous red lines) and their first derivatives (dashed lines) for 1,3-H_2YBDC (top) and [Cu(1,3-YBDC)]·xH_2O (bottom).

Table 2.4: TGA losses.

	1° loss (%)	**2° loss (%)**	**3° loss (%)**	**4° loss (%)**	**Residue (800 °C, %)**
1,3-H_2YBDC	2.3	22.1	26.4	48.8	0.4
[Cu(1,3-YBDC)]·xH_2O	2.3	23.9	14.85	32.1	26.5

The first loss (2.3%), from 38 to 100 °C in both samples, could be caused by the evaporation of water absorbed from air by the samples before the TGA analysis.

The TGA plot for 1,3-H_2YBDC (of $C_{14}H_{13}NO_7$ formula, mw 307.25 g mol^{-1}) shows three main weight losses between 200 and 600 °C, due to organic material decomposition, and zero residual weight. The first two steps are interpreted by progressive loss of the propargyl fragments (obs. 48.5%, calc. for $C_6H_8NO_3$ 46.3%). Similarly, the copper-containing product (of $C_{14}H_{11}CuNO_7$ formula, mw 368.79 g mol^{-1}) shows three decomposition steps in the 200-350 °C range (attributed, as above, to the loss of the $C_6H_8NO_3$

residue, obs. 38.2%, calc. 38.5%), terminating at a temperature ca. 150 °C lower than in the pristine organic ligand. Such lower thermal stability of the organic skeleton within the MOF is tentatively attributed to assistance, during decomposition, of redox processes catalysed by Cu(II) ions. Furthermore, a residue of 26 wt% is present at 400 °C, with no significant variation up to 800 °C, which is presumably due to residual CuO. Assuming that all the copper in the MOF retain its oxidation state during the degradation process, only copper (II) oxide, with a stoichiometry of Cu:O = 1:1, will be present in the residue. Because in this oxide copper represents 79.54 % of the weight, it represents 21.07 % of the total weight of the sample used for the TGA analysis. From the AAS characterization the amount of copper inside the MOF is reported to be 18.3%, so the excess residual could be from thermally stable carbonaceous materials.

2.4.3 Crystallochemical analysis

A sample of [Cu(1,3-YBDC)]·xH_2O was sent to the Department of High Technology of the University of Insubria (Como) in order to perform a synchrotron X-ray diffraction analysis. Because no single crystal of the MOF was obtained, the crystal structure was simulated based on XRD data from MOF powder (Figure 2.16).

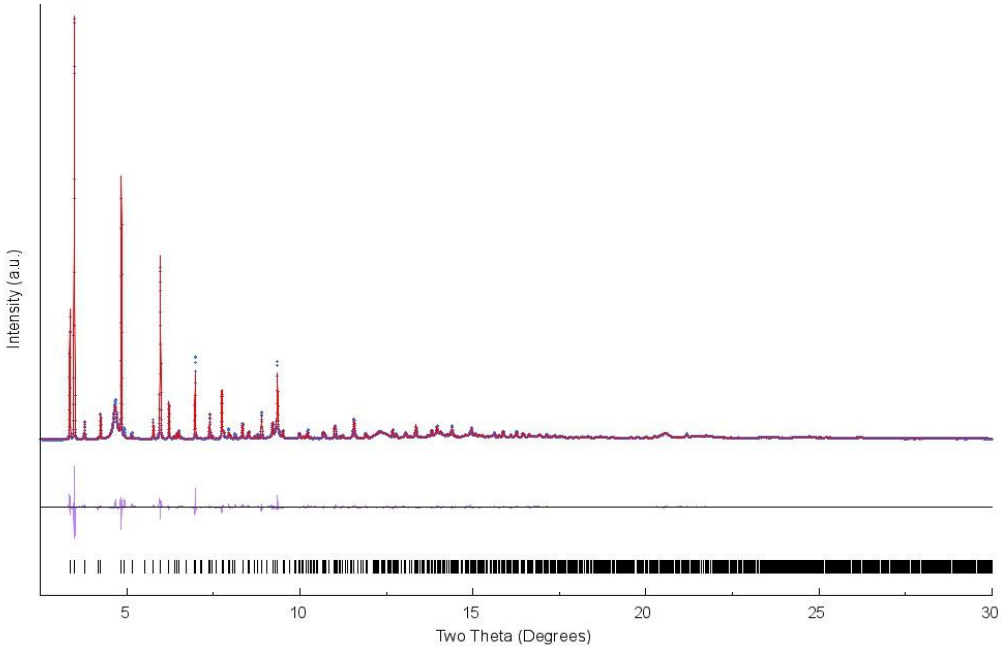

Figure 2.16: Rietveld refinement plot for [Cu(1,3-YBDC)]·xH_2O; Blue trace = observed data; red trace = calculated pattern from the simulated structure. Difference plot in purple; peak markers at the bottom are for [Cu(1,3-YBDC)]·xH_2O.

The structure obtained from the simulation suggests that the solid [Cu(1,3-YBDC)]·xH_2O contains a network of isophthalate anions linked to Cu (II) centres belonging to the paddlewheel dimeric fragments. The apical atom in these fragments is the oxygen of the carbonyl group belonging to the propargylcarbamate residue. This confirms the presence of a coordination between Cu (II) and the carbamate group of the linker. The distance between the two copper atoms in the paddlewheel fragments is calculated to be 2.633 Å. The average Cu-O equatorial bond distance is 2.00 Å. The conformation of the ligand is locked into two different conformations inside the MOF's crystalline phase. In both conformers, the alkyne moieties point directly into the crystal cavities.

Figures 2.17.E and 2.17.F show the complete structure of both conformers, not including the weakly bonded water molecules.

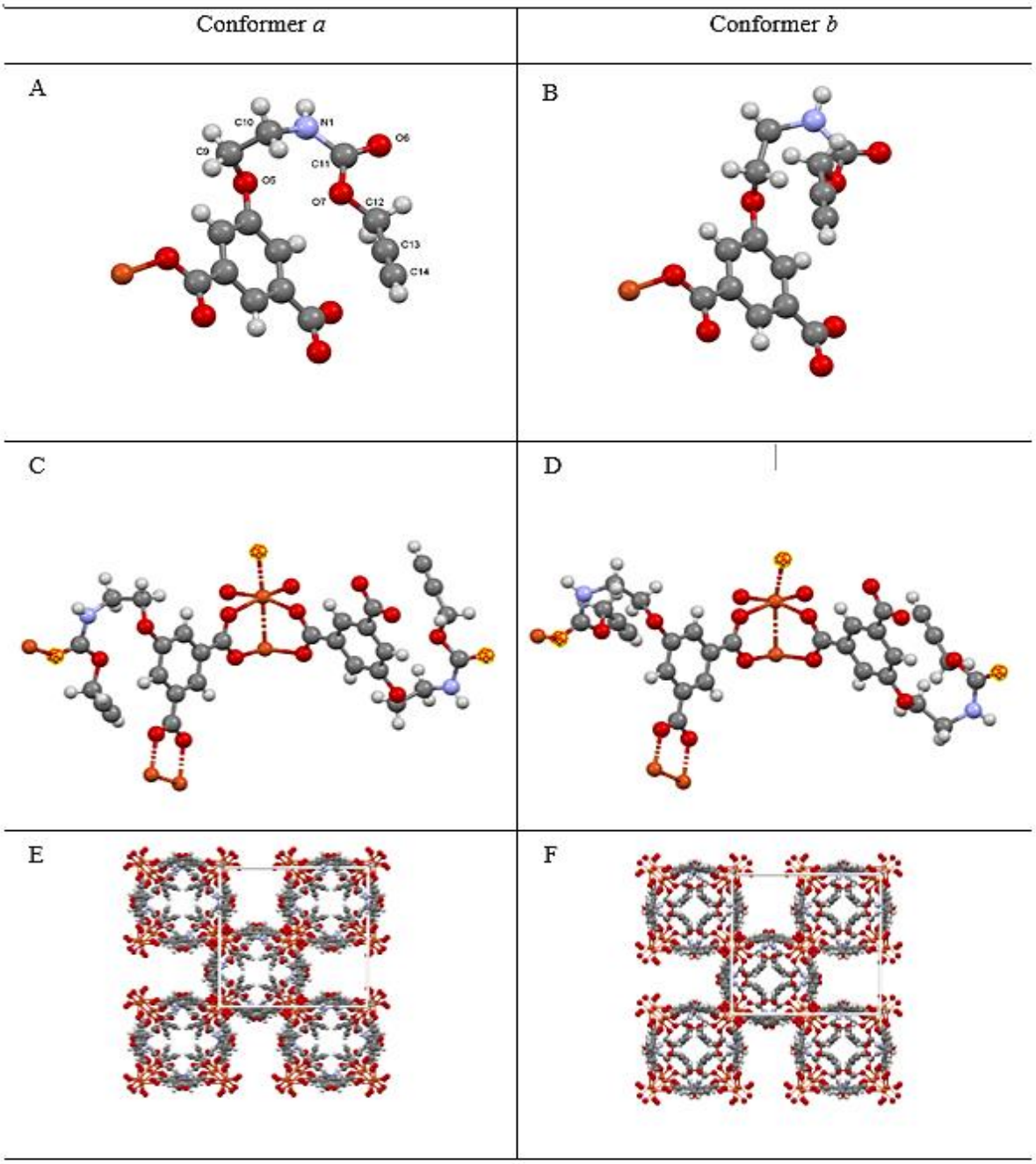

Figure 2.17: (A, B) the two different conformers *a* and *b*; (C, D) paddlewheel fragments arising from the two conformers; (E, F) crystal packing of the two conformers.

The void space inside the MOF structure is reported to be 20% of the volume and is partially occupied by water molecules, possibly disordered and of non-stoichiometric character.

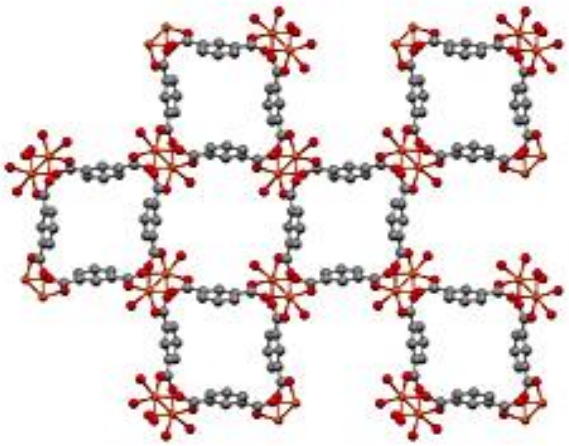

Figure 2.18: crystal packing with omitted hydrogens and propargylcarbamate residues.

The crystalline phase of the MOF is composed by corrugated 2D layers interlinked by the long propargylcarbamate residues through the apical coordination of the carbonyl oxygen with copper. The size of the MOF cavities was reported to be 141 $Å^3$.

However, considering the approximate volume of the tetrachloroaurate anion [the Au(0) precursor, ≈ 142 $Å^3$] and the tabulated size of a single Au atom [≈ 43(2) $Å^3$], the MOF could be used for capturing and anchoring gold species, both inside the material (although to a small extent) and, primarily, on its external surface, due to its dense and even array of protruding propargylcarbamate residues. Taking into account the size of the crystalline domain estimated by the XRD model (of the order of 100 nm for isotropic particles), nearly 2% of the ligands lie on the crystal surface, possibly acting as catalytic sites.

2.4.4 SEM-EDX characterization

The SEM image of the MOF (Figure 2.19) shows the occurrence of interconnected lamellar structures with an average lateral dimension of 2-3 μm and a mean thickness of 200 nm.

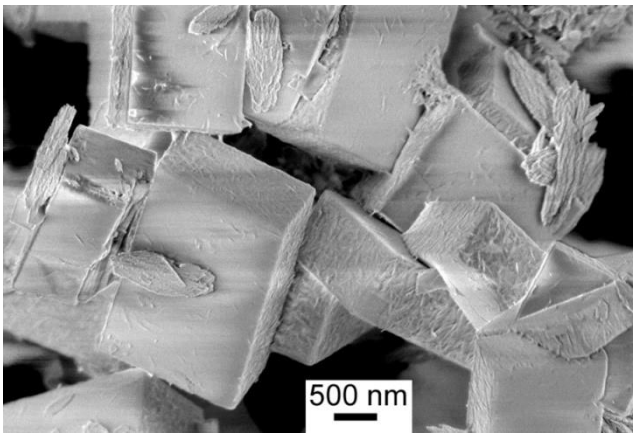

Figure 2.19: SEM image of [Cu(1,3-YBDC)]·xH$_2$O.

Figure 2.20 shows the presence of carbon, oxygen, copper and no other elements in the analyzed region of the sample. Because of the low amount of nitrogen in the sample, its signal is hidden behind the C and O peaks. Figure 2.21 shows the element distribution on the analyzed surface.

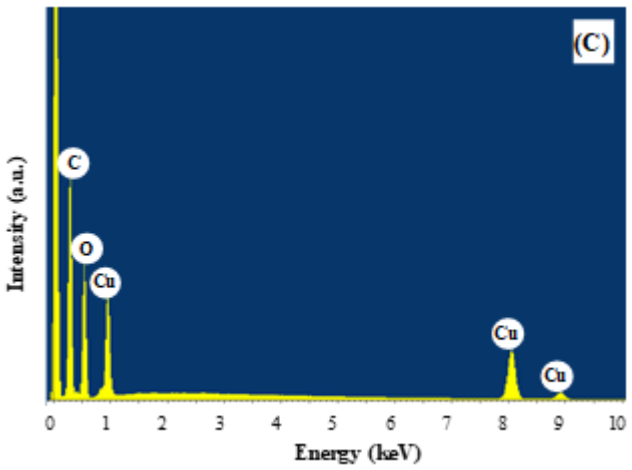

Figure 2.20: EDX spectra of [Cu(1,3-YBDC)]·xH$_2$O.

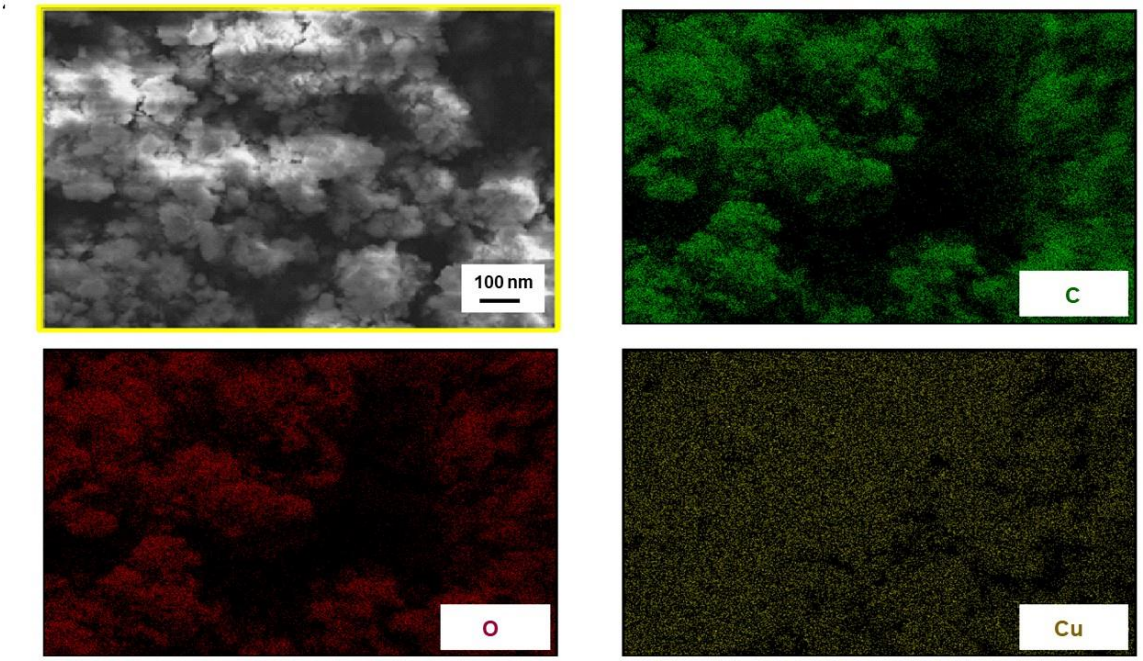

Figure 2.21: C, O and Cu EDXS elemental maps, recorded on the corresponding electron image contained in the yellow box, for [Cu(1,3-YBDC)]·xH_2O specimen.

2.4.5 XPS characterization

The XPS analysis, performed by the Department of Chemical Sciences of Padova University, was used to inspect the elements present on the MOF's surface, their oxidation states and their chemical environments (Figure 2.22).

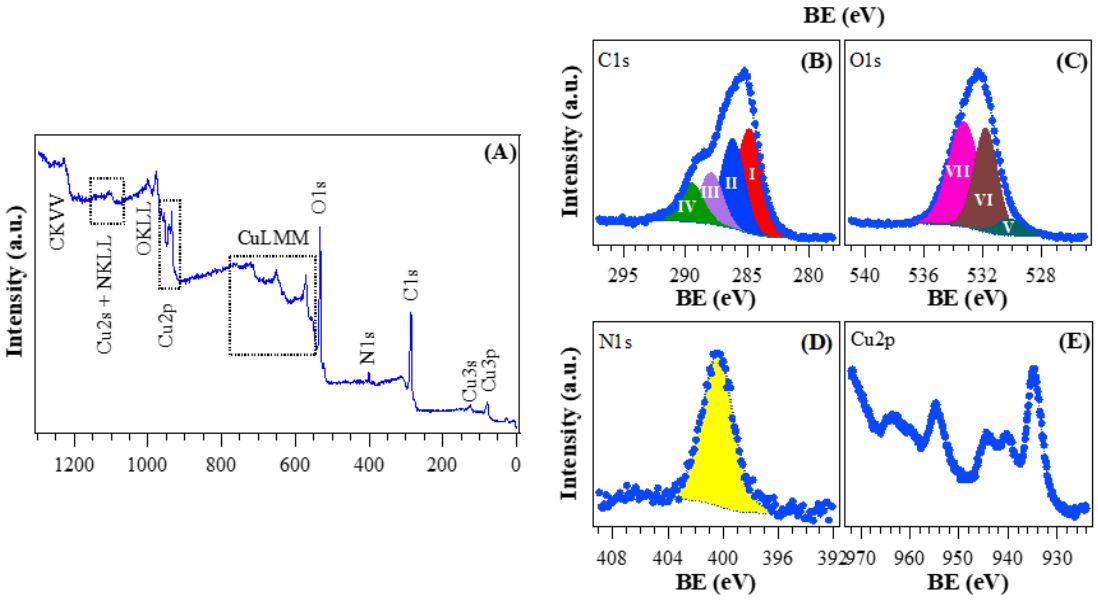

Figure 2.22: XPS analysis for the target [Cu(1,3-YBDC)]·xH_2O specimen:
(A) wide-scan spectrum; (B) C1s, (C) O1s, (D) N1s, (E) Cu2p photoelectron peaks.

The quantitative analysis revealed the presence of C (58.7%), N (5.2%), O (31.3%), and Cu (4.8%) elements on the surface of the MOF (atomic percentages). The C 1s signal can be seen as the superposition of four peaks (Figure 2.22.B), each representing carbon in a different chemical environment (Table 2.5).[14]

Table 2.5: C 1s XPS peaks.

Peak	BE (eV)	Chemical environment	C signal contribution %
C 1s (I)	284.8	C-C	40
C 1s (II)	286.2	C-N/C-O	30
C 1s (III)	287.9	Ar-COOH	20
C 1s (IV)	289.6	-NCOO-	10

The O 1s signal can be seen as the superposition of three peaks (Figure 3.21.C), each representing oxygen in a different chemical environment (Table 3.6).[15]

Table 2.6: O 1s XPS peaks.

Peak	BE (eV)	Chemical environment	O 1s signal contribution %
O 1s (V)	530.2	Cu-O	8
O 1s (VI)	531.8	C-OH	40
O 1s (VII)	533.3	C=O/H_2O	52

The N1s peaks (Figure 2.22.D) showed a single contribution centred at BE = 400.3 eV. The Cu peaks pattern (Figure 2.22.E), with Cu $2p_{3/2}$ and Cu $2p_{1/2}$ at 934.8 eV and 954.7 eV respectively, is a fingerprint of d^9 Cu (II) coming from the metal centers of the MOF and Cu(II) hydroxides.[16]

2.4.6 Surface area and porosity

A sample of [Cu(1,3-YBDC)]·xH_2O was sent to the Institute of Organic Synthesis and Photoreactivity (CNR-ISOF, Bologna) in order to study the surface area and pore volume by

measuring the adsorption isotherm of nitrogen at 77 K (Figure 2.23). The sample was pre-treated at 343 K under vacuum (1×10^{-3} mbar) for 2 h.

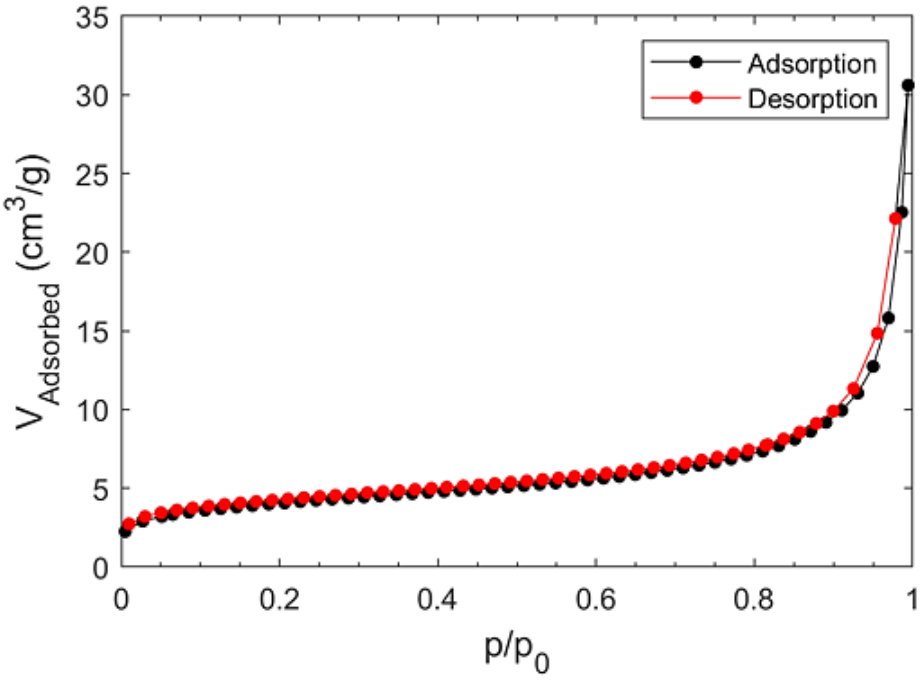

Figure 2.23: Adsorption and desorption isotherm of N_2 at 77 K on [Cu(1,3-YBDC)]·xH_2O.

The data in the low N_2 partial pressure region was fitted with the BET model (R^2 = 0.99986). The BET surface area was calculated to be 14.5 ± 0.8 m^2/g, while the pore volume was 46 mm^3/g. The value obtained for the surface area was way lower than the one that is usually reported for tricarboxylate based MOFs. For example, the surface area of Cu-BTC MOFs is usually over 1000 m^2/g.[17] The main reasons for the low surface area and pore volume are:

- the presence of an extra coordination of Cu with the carbamate group of the linker that is reported to drop the surface area to 100 m^2 and below;[18]
- the presence of trapped water molecules within the structure of the MOF, even after thermal activation and pre-treating, as suggested by the crystallochemical analysis;
- the presence of nanosized copper hydroxides and hydroxonitrates that can lower the channels accessibility.

2.5 Conclusions

In this chapter a copper-based metal–organic framework (MOF) was prepared using a new linker, a 5-substituted isophthalic acid bearing a propargyl carbamate group, intended to provide a terminal alkyne function protruding from the material surface capable to generate supported gold species for potential catalytic applications. The novel material was fully characterized by spectroscopic analyses of different kinds: FTIR, Raman, EDX, and XPS, as well as by thermal and surface area measurements. Synchrotron X-ray diffraction data analysis, in particular, revealed that [Cu(1,3-YBDC)]·xH2O (x ~ 2), contains a complex network of 5-substituted isophthalate anions bound to Cu(II) centers, arranged in pairs within paddlewheel (or "Chinese lantern") fragments of $Cu_2(\mu\text{-}COO)_4(D)_2$ formulation (D being a neutral Lewis base), with a short Cu···Cu distance of 2.633(4) Å. Quite unexpectedly, the apical atom in the paddlewheel structure belongs to the carbamate carbonyl oxygen atom. Such extra coordination by the propargyl carbamate groups drastically reduces the MOF porosity, a feature that was also confirmed by BET measurements. However, the MOF functionality is retained at the external crystal surface where 2% of active terminal alkynes is located.

2.6 Experimental Section

Materials

All reagents and solvents were purchased from commercial vendors and used as received; ultrapure water purified with the Milli-Q plus system (Millipore Co, resistivity over 18 MΩ cm) was used in all cases. The reactions were monitored by thin-layer chromatography (TLC) on highly purified Silica on TLC-PET foils (with fluorescent indicator 254 nm, Fluka). The chemicals 2-bromoethylamine hydrobromide, propargyl chloroformate, dimethyl 5-hydroxyisophthalate, tetrahydrofuran (THF), ethyl acetate, petroleum ether, diethyl ether, butanone, ethanol (EtOH), dichloromethane, deuterated chloroform ($CDCl_3$), sulphuric acid (H_2SO_4, 98%), hydrochloric acid (HCl, 37 wt%), nitric acid (HNO_3, 65 wt%), $NaHCO_3$, magnesium sulphate, and sodium hydroxide (NaOH, 50 wt%) were purchased from Sigma-Aldrich (analytical reagent grade). $HAuCl_4$ was synthetized by dissolving a gold wire (BASF, 99.9999%, 1.4 mm diameter) in hot aqua regia.[19]

Instrumentation

ESI-MS analyses were performed by direct injection of methanol solutions using a WATERS ZQ 4000 mass spectrometer; working temperature: 80 ÷ 100 °C; working concentrations: ca. 10^{-8} g/L; Cone Voltage: 10 ÷ 30 V; working flow: 10 μL/min. The NMR spectra were recorded at 298 K using a Varian MercuryPlus VX 400 (^{1}H, 399.9; ^{13}C, 100.6 MHz); spectra were referenced internally to residual solvent resonances and were recorded at 298 K for characterization purposes; full ^{1}H and ^{13}C NMR assignments were done using standard Varian pulse sequences. Spectra have been edited with the software MestReNova Version: 14.1.0-24037, 2019 MestRelab Research S.L. Abbreviations: s = singlet, d = doublet, t = triplet, m = multiplet, bs = broad singlet. ATR-FTIR analyses were performed with a Perkin Elmer Spectrum Two spectrophotometer, equipped with a Universal ATR accessory, in the range 4000-600 cm^{-1} with a resolution of 0.5 cm^{-1}. The products were directly analysed performing 40 scans. Abbreviations: ν = stretching, δ = bending. Thermogravimetric analyses were carried out using a Perkin Elmer TGA-7. The samples (ca. 10 mg) were heated in a platinum crucible at a rate of 10 °C min^{-1} from 40 °C to 900 °C. Elemental C, H, N analyses were obtained at REDOX s.r.l. (Monza, Italy).

Linker synthesis

Step 1: Synthesis of prop-2-yn-1-yl *N*-(2-bromoethyl)carbamate (3)

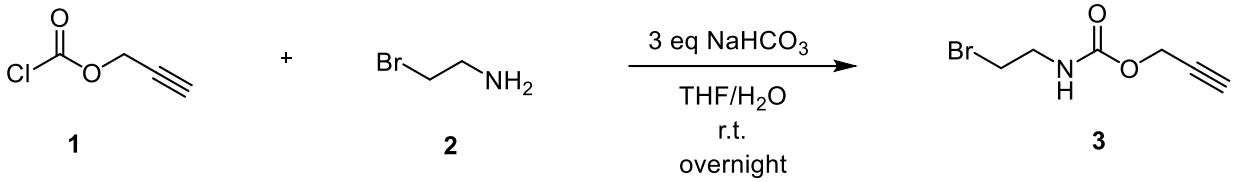

Scheme 2.3: Synthesis of 3.

To a solution of 2-bromoethylamine hydrobromide (2, 17.8 g, 86.9 mmol) in THF/H_2O (214 mL/171 mL), cooled to 0 °C, $NaHCO_3$ (21.9 g, 261 mmol, 3 eq) was added, followed by propargyl chloroformate (1, 10.0 mL, 102.5 mmol, 1.18 eq) added dropwise. The solution was stirred at r.t. overnight. THF was evaporated and the aqueous layer was extracted with ethyl acetate (4 x 20 mL). The organic layer was washed with HCl 1.0 M (2 x 10.0 mL) and brine (2 x 10.0 mL), then dried with $MgSO_4$, filtered, and concentrated in vacuum to obtain a colourless oil (3, 15.5 g, 75.2 mmol, yield 86.5%). The crude material was used without any further purification. Rf1 = 0.54, Rf2 = 0.12, Rf3 = 0.48 (1:2 petroleum ether/Et_2O).

ESI-MS(+) (MeOH, m/z): 228 (100) $[C_6H_8NO_2Br + Na]^+$.

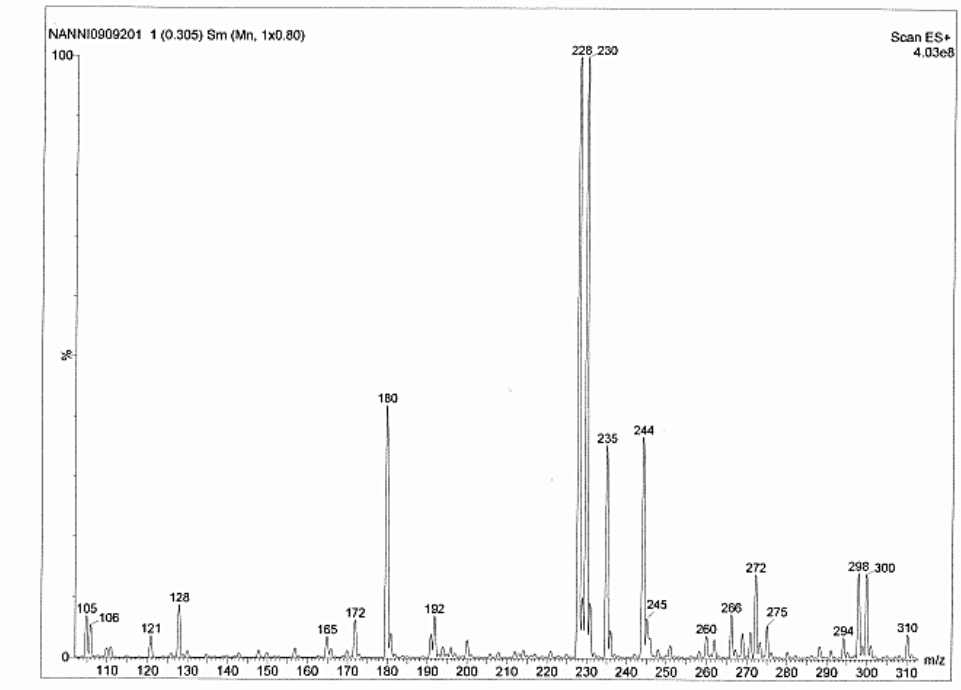

Figure 2.24. ESI-MS(+) spectrum of 3.

^{1}H-NMR (400 MHz, $CDCl_3$): δ 5.51 (bs, 1H, NH**^{3}**), 4.65 (d, $^{4}J_{H,H}$ = 2.4 Hz, 2H, -OCH_2**^{4}**-), 3.55 (m, 2H, -CH_2**^{2}**N(H)-), 3.44 (t, $^{3}J_{H,H}$ = 6.2 Hz, 2H, BrCH_2**^{1}**-), 2.48 (t, $^{4}J_{H,H}$ = 2.4 Hz, 1H, -C≡CH**^{5}**).

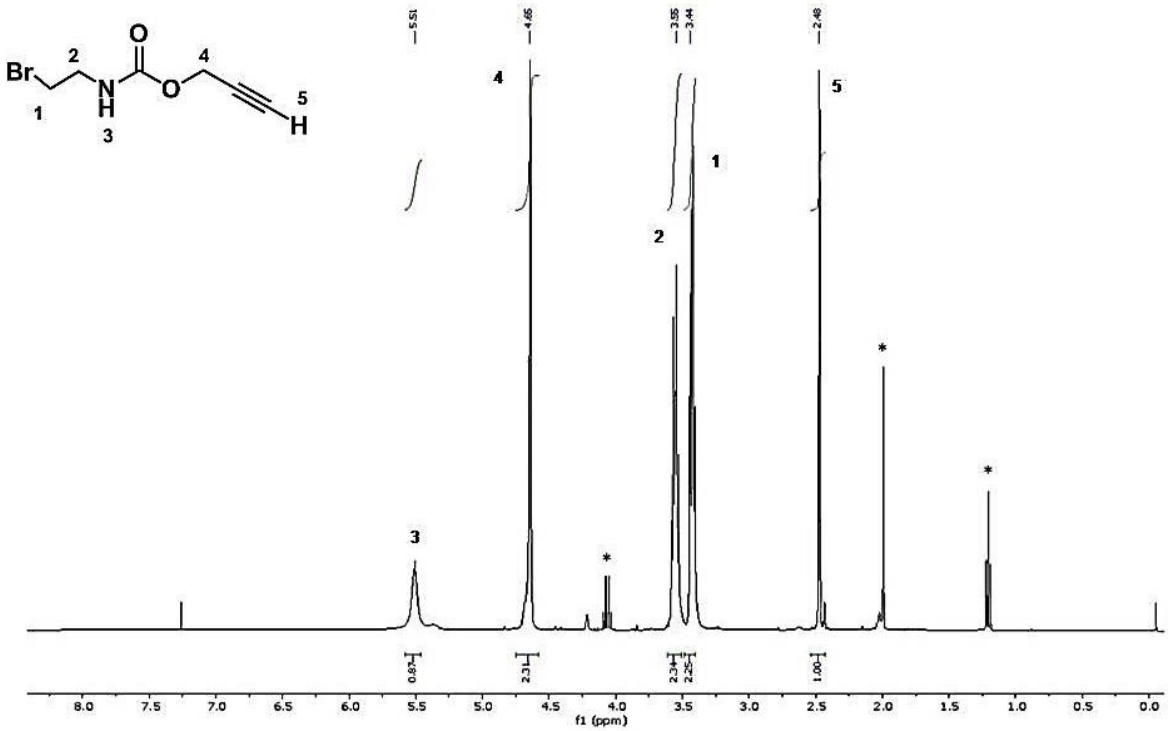

Figure 2.25: ^{1}H-NMR spectrum of **3.** Signal labelled with asterisk is relative to the solvent ethyl acetate.

^{13}C-NMR ($CDCl_3$, 100.6 MHz): δ 155.25 (-NH*C*^{3}(O)O-), 77.97 (-*C*^{5}≡CH), 74.82 (-C≡*C*^{6}H), 52.72 (-O*C*^{4}H_2C≡CH), 42.79 (-*C*^{2}H_2NH-), 32.22 (Br*C*^{1}H_2-) ppm.

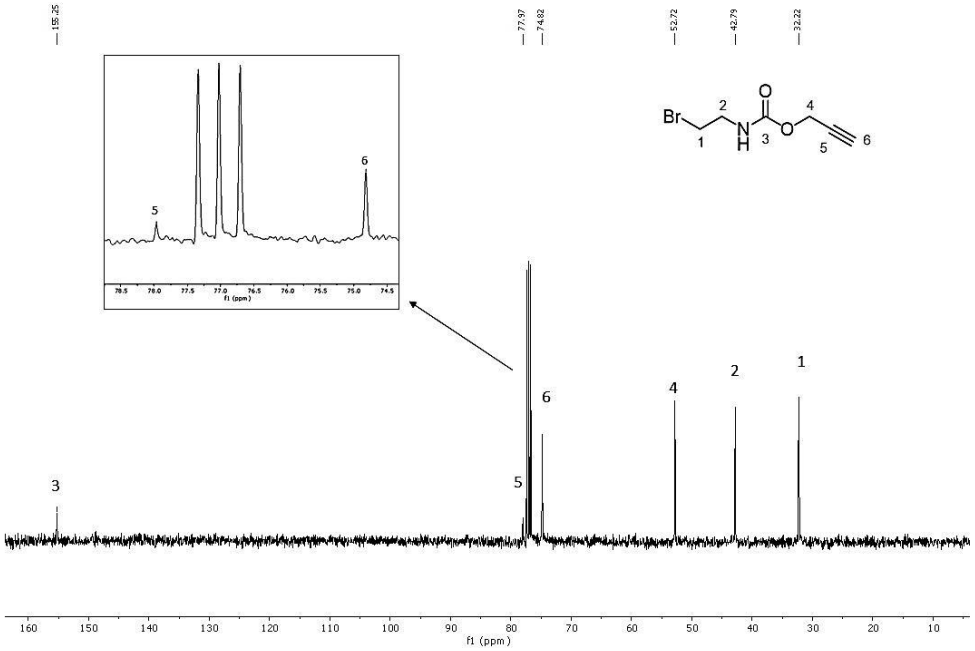

Figure 2.26: ^{13}C-NMR spectrum of **3**.

ATR-FTIR spectra of neat 3 (cm^{-1}): 3331 (ν NH, m), 3293 (ν ≡C-H, m), 2949 (ν C-H aliphatic, w), 2131 (ν -C≡C-, w), 1703 (ν -C(O)NH- carbamate, s), 1520 (δ NH, s), 1245 (ν C-O, s).

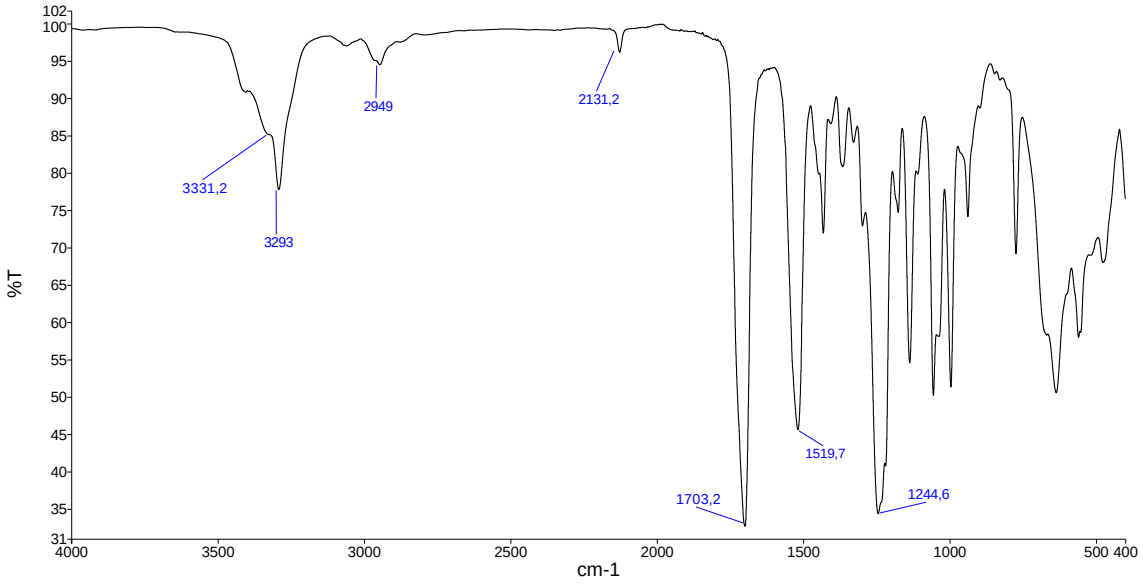

Figure 2.27: IR-ATR spectrum of **3**.

Step 2: Synthesis of dimethyl 5-(2-{[(prop-2-yn-1-yloxy)carbonyl]amino}ethoxy) isophthalate (1,3-Me$_2$YBDC) (5)

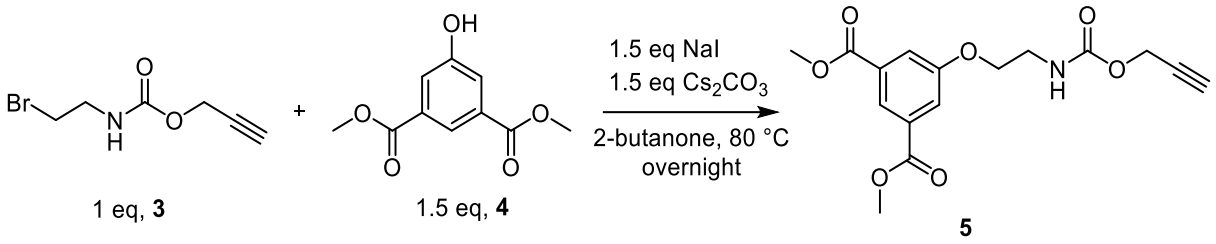

Scheme 2.4: Synthesis of 5.

A solution of prop-2-ynyl *N*-(2-bromoethyl)carbamate (**3**, 3.00 g, 14.6 mmol) in butanone (50 mL) was treated with dimethyl 5-hydroxyisophthalate (**4**, 4.60 g, 21.9 mmol), NaI (3.28 g, 21.9 mmol), and Cs_2CO_3 (7.14 g, 21.9 mmol), and the resulting suspension was vigorously stirred at 80 °C overnight. The cooled reaction mixture was first concentrated under vacuum, then diluted with CH_2Cl_2 (50 mL) and then washed with H_2O and then with NaOH 10% v/v. After drying the organic phase ($MgSO_4$) the solvent was removed to afford **5** as a white solid (4.08 g, 12.19 mmol, 83.5%). Rf3 = 0.48, Rf4 = 0.30, Rf5 = 0.20 (1:2 petroleum ether/Et_2O). M.p. = 99-102 °C. Soluble at r.t. in $CHCl_3$, CH_2Cl_2, THF, Et_2O, soluble in boiling MeOH, EtOH, and i-PrOH.

ESI-MS(+) (MeOH, m/z): 358 (100) $[C_{16}H_{17}NO_7 + Na]^+$.

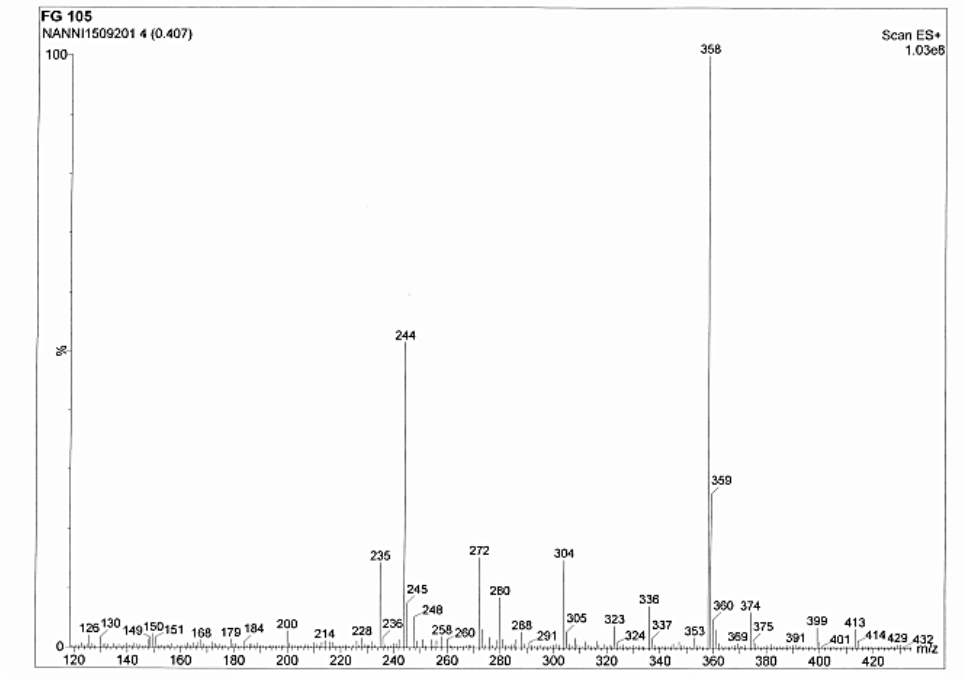

Figure 2.28: ESI-MS(+) spectrum of **5**.

^{1}H-NMR ($CDCl_3$, 399.9 MHz) δ: 8.30 (t, $^{4}J_{H,H}$ =1.9 Hz, 1H, Ar-H**^{2}**), 7.73 (d, $^{4}J_{H,H}$ =1.9 Hz, 2H, Ar-H**^{3}**), 5.24 (bs, 1H, NH**^{6}**), 4.70 (d, $^{4}J_{H,H}$ = 2.4 Hz, 2H, -OCH_2**^{7}**C≡CH), 4.13 (t, $^{3}J_{H,H}$ = 6.8 Hz, 2H, -OCH_2**^{4}**-), 3.94 (s, 6H, OCH_3**^{1}**), 3.63 (m, 2H, -CH_2**^{5}**NH), 2.47 (t, $^{4}J_{H,H}$ = 2.4 Hz, 1H, -C≡CH**^{8}**).

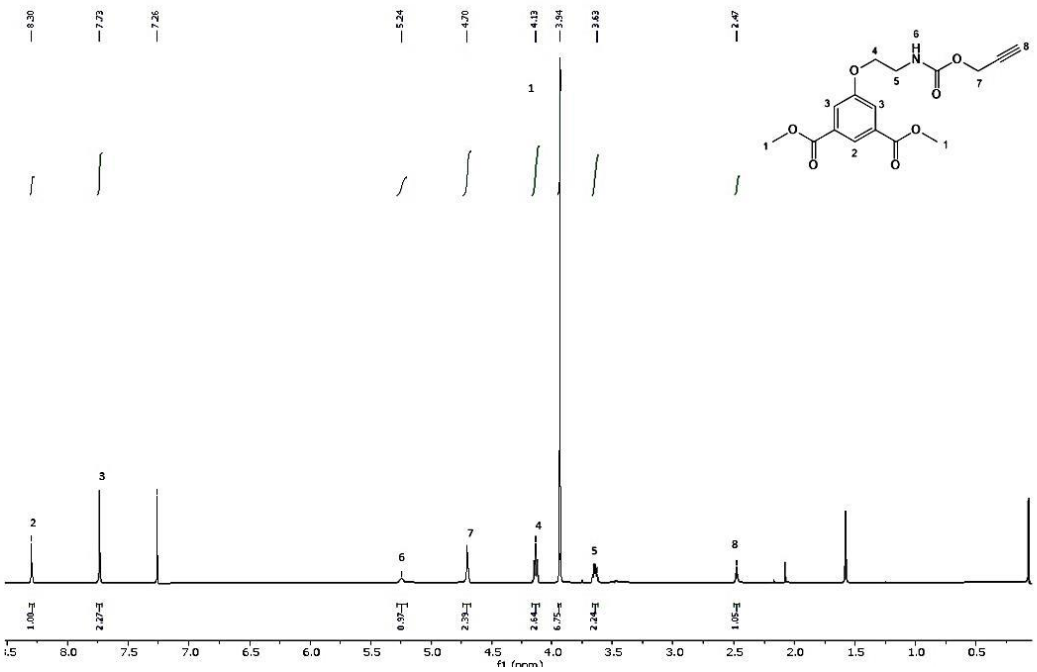

Figure 2.29: ^{1}H-NMR spectrum of **5**.

^{13}C-NMR ($CDCl_3$, 100.6 MHz) δ: 165.90 (Ar-C**^{2}**(O)OMe), 158.43 (ArC**^{6}**O-), 155.44 (-N(H)C**^{9}**(O)O-), 131.81 (Cq, Ar), 123.36 (CH, Ar), 119.67 (CH, Ar), 78.04 (-C**^{11}**≡CH), 74.70 (-C≡C**^{12}**H), 67.35 (-OC**^{7}**H_2-), 52.58 (-OC**^{10}**H_2-C≡CH), 52.40 (-OC**^{1}**H_3), 40.45 (-C**^{8}**H_2N(H)-) ppm.

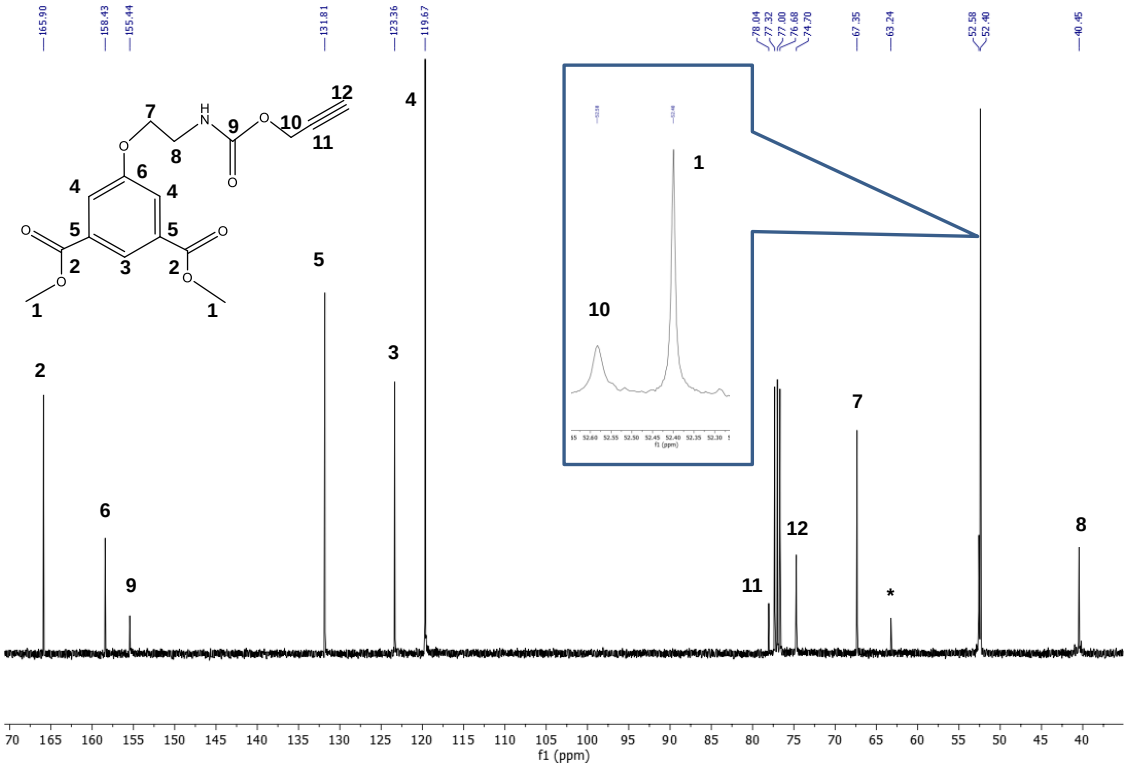

Figure 2.30: ^{13}C-NMR spectrum of **5.** Signal labelled with an asterisk is relative to a solvent impurity.

ATR-FTIR spectrum of neat 5 (cm^{-1}): 3373 cm^{-1} (ν NH, s), 3258 (ν ≡C-H, s), 3078 – 2840 (ν C-H aliphatic and aromatic, m), 2132 (ν -C≡C-, w), 1738 (ν -C(O)O- carboxylate, s), 1714 (ν -C(O)NH- carbamate, vs), 1544 (δ NH, s), 1243 (ν C-O, vs).

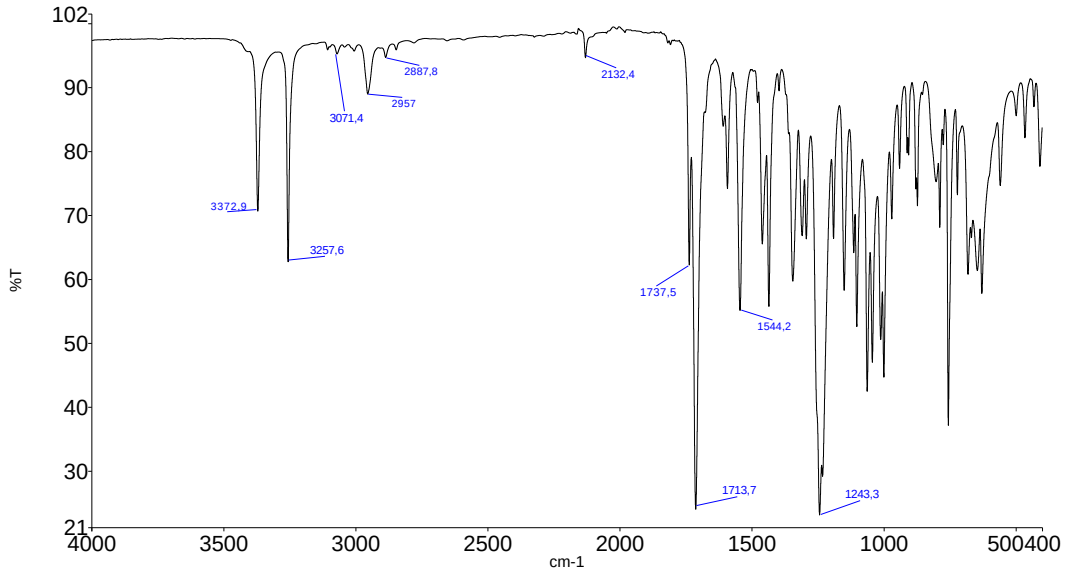

Figure 2.31: IR-ATR spectrum of **5**.

Step 3: Synthesis of 5-(2-{[(prop-2-yn-1-yloxy)carbonyl]amino}ethoxy)isophthalic acid (1,3-H_2YBDC) (6)

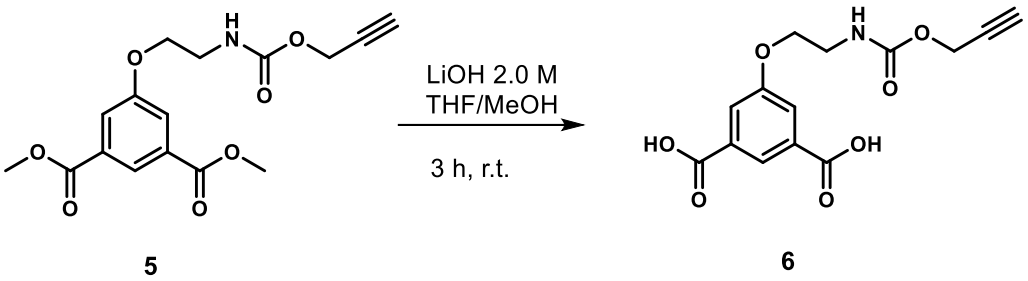

Scheme 2.5: Synthesis of 6.

Dimethyl 5-(2-(((prop-2-yn-1-yloxy)carbonyl)amino)ethoxy)isophthalate (**5**, 2.42 g, 7.20 mmol) was dissolved in a 1:1 v/v mixture of THF/methanol (60 mL) and treated with 18 mL of 2.0 M aqueous solution of LiOH. After stirring for 3 h, the solvents were evaporated and the residue was treated with 1.0 M aqueous HCl (20 mL) and extracted with ethylacetate. The organic phase was dried with $MgSO_4$ and evaporated to obtain the pure desired dicarboxylic acid derivative **6** (2.15 g, 7.00 mmol, yield 97%). M.p.= 186-191 °C (215-217 °C after recrystallization). Soluble at r.t. in ethyl acetate, DMSO, and acetone; soluble in boiling methanol, ethanol, and isopropanol.

ESI-MS(+) (MeOH, m/z): 330 (100) $[C_{14}H_{13}NO_7 + Na]^+$, 308(10) $[C_{14}H_{13}NO_7 + H]^+$.

^{1}H-NMR (acetone-d_6, 399.9 MHz): δ 8.29 (t, $^4J_{H,H}$ =1.5 Hz, 1H, Ar-H**^{1}**), 7.79 (d, $^4J_{H,H}$ =1.5 Hz, 2H, Ar-H**^{2}**), 4.67 (d, $^4J_{H,H}$ = 2.4 Hz, 2H, -OCH_2**^{5}**C≡CH), 4.25 (t, $^3J_{H,H}$ = 6.8 Hz, 2H, -OCH_2**^{3}**-), 3.60 (t, $^3J_{H,H}$ = 6.8 Hz, 2H, -CH_2**^{4}**N(H)-), 2.95 (t, $^4J_{H,H}$ = 2.4 Hz, 1H, -C≡C**H^6**) ppm.

^{13}C-NMR (acetone-d_6, 100.6 MHz) δ: 166.73 (Ar*C*^{1}(O)OH), 159.99 (Ar-*C*^{5}O-), 157.00 (-N(H)*C*^{8}(O)O), 133.22 (Cq, Ar), 123.79 (CH, Ar), 120.55 (CH, Ar), 79.73 (-*C*^{10}≡CH), 75.78 (-C≡*C*^{11}H), 68.19 (-O*C*^{6}H_2-), 52.48 (-O*C*^{9}H_2-C≡CH), 41.08 (-*C*^{7}H_2N(H)-) ppm.

ATR-FTIR spectrum of neat 6 (cm^{-1}): 3336 cm^{-1} (ν NH, s), 3304 (ν ≡C-H, s), 3200 – 2800 (ν -OH, broad), 3086-2961 (ν C-H aliphatic and aromatic, m), 2139 (ν -C≡C-, w), 1737 (ν -C(O)O- carboxylate, s), 1687 (ν -C(O)NH- carbamate, vs), 1550 (δ NH, s), 1259 (ν C-O, vs).

Step 4: 1,3-H_2YBDC crystallization

1,3-H_2YBDC (6, 1.91 g, 5.69 mmol) was dissolved in EtOH (10 mL) at 80 °C. After 1,3-H_2YBDC solubilisation, water (5 mL) was added to the mixture. During cooling in an ice bath, a white precipitate was observed. The solid was separated by filtration and washed with EtOH. The product was placed under vacuum at r.t overnight, while the mother liquor was placed in a freezer at −11 °C overnight to precipitate more linker. The white solid obtained from the mother liquor was filtered following the same procedure as before. The process was repeated three times, monitoring the melting point of the crystallized 1,3-H_2YBDC.

References

(1) Cassani, M. C.; Gambassi, F.; Ballarin, B.; Nanni, D.; Ragazzini, I.; Barreca, D.; Maccato, C.; Guagliardi, A.; Masciocchi, N.; Kovtun, A.; Rubini, K.; Boanini, E. A Cu(II)-MOF Based on a Propargyl Carbamate-Functionalized Isophthalate Ligand. *RSC Adv.* **2021**, *11* (33), 20429–20438. https://doi.org/10.1039/D1RA02686K.

(2) Sachdeva, S.; Pustovarenko, A.; R. Sudhölter, E. J.; Kapteijn, F.; Smet, L. C. P. M. de; Gascon, J. Control of Interpenetration of Copper-Based MOFs on Supported Surfaces by Electrochemical Synthesis. *CrystEngComm* **2016**, *18* (22), 4018–4022. https://doi.org/10.1039/C5CE02462E.

(3) Chui, S. S.-Y; Lo, S. M-F.; Charmant, J. P. H.; Orpen, A. G.; Williams, I. D. A Chemically Functionalizable Nanoporous Material. *Science* **1999**, *283* (5405), 1148–1150. https://doi.org/10.1126/science.283.5405.1148.

(4) Eddaoudi, M.; Kim, J.; Rosi, N.; Vodak, D.; Wachter, J.; O'Keeffe, M.; Yaghi, O. M. Systematic Design of Pore Size and Functionality in Isoreticular MOFs and Their Application in Methane Storage. *Science* **2002**, *295* (5554), 469–472. https://doi.org/10.1126/science.1067208.

(5) Li, H.; Eddaoudi, M.; O'Keeffe, M.; Yaghi, O. M. Design and Synthesis of an Exceptionally Stable and Highly Porous Metal-Organic Framework. *Nature* **1999**, *402* (6759), 276–279. https://doi.org/10.1038/46248.

(6) Ballarin, B.; Barreca, D.; Boanini, E.; Cassani, M. C.; Dambruoso, P.; Massi, A.; Mignani, A.; Nanni, D.; Parise, C.; Zaghi, A. Supported Gold Nanoparticles for Alcohols Oxidation in Continuous-Flow Heterogeneous Systems. *ACS Sustain. Chem. Eng.* **2017**, *5* (6), 4746–4756. https://doi.org/10.1021/acssuschemeng.7b00133.

(7) Parise, C.; Ballarin, B.; Barreca, D.; Cassani, M. C.; Dambruoso, P.; Nanni, D.; Ragazzini, I.; Boanini, E. Gold Nanoparticles Supported on Functionalized Silica as Catalysts for Alkyne Hydroamination: A Chemico-Physical Insight. *Appl. Surf. Sci.* **2019**, *492*, 45–54. https://doi.org/10.1016/j.apsusc.2019.05.192.

(8) Mohideen, M. I. H.; Xiao, B.; Wheatley, P. S.; McKinlay, A. C.; Li, Y.; Slawin, A. M. Z.; Aldous, D. W.; Cessford, N.; Duren, T.; Zhao, X.; Gill, R.; Thomas, K. M.;

Griffin, J. M.; Ashbrook, S. E.; Morris, R. E. Protecting Group and Switchable Pore-Discriminating Adsorption Properties of a Hydrophilic–Hydrophobic Metal–Organic Framework. *Nat. Chem.* **2011**, *3* (4), 304–310. https://doi.org/10.1038/NCHEM.1003.

(9) Jiang, H.-L.; Makal, T. A.; Zhou, H.-C. Interpenetration Control in Metal–Organic Frameworks for Functional Applications. *Coord. Chem. Rev.* **2013**, *257*, 2232-2249. https://doi.org/10.1016/J.CCR.2013.03.017.

(10) Barin, G.; Krungleviciute, V.; Gutov, O.; Hupp, J. T.; Yildirim, T.; Farha, O. K. Defect Creation by Linker Fragmentation in Metal-Organic Frameworks and Its Effects on Gas Uptake Properties. *Inorg. Chem.* **2014**, *53* (13), 6914–6919. https://doi.org/10.1021/ic500722n.

(11) DeCoste, J. B.; Peterson, G. W.; Schindler, B. J.; Killops, K. L.; Browe, M. A.; Mahle, J. J. The Effect of Water Adsorption on the Structure of the Carboxylate Containing Metal–Organic Frameworks Cu-BTC, Mg-MOF-74, and UiO-66. *J. Mater. Chem. A* **2013**, *1* (38), 11922–11932. https://doi.org/10.1039/C3TA12497E.

(12) Prestipino, C.; Regli, L.; Vitillo, J. G.; Bonino, F.; Damin, A.; Lamberti, C.; Zecchina, A.; Solari, P. L.; Kongshaug, K. O.; Bordiga, S. Local Structure of Framework Cu(II) in HKUST-1 Metallorganic Framework: Spectroscopic Characterization upon Activation and Interaction with Adsorbates. *Chem. Mater.* **2006**, *18* (5), 1337–1346. https://doi.org/10.1021/cm052191g.

(13) Hofmann, D. W. M. Fast Estimation of Crystal Densities. *Acta Crystallogr. B* **2002**, *58* (3), 489–493. https://doi.org/10.1107/S0108768101021814.

(14) Wanger, C. D.; Riggs, W. M.; Davis, L. E.; Moulder J. F.; Muilenberg G. E. Handbook of X-Ray Photoelectron Spectroscopy, Perkin-Elmer Corp., Physical Electronics Division, Eden Prairie, Minnesota, USA, 1979. https://doi.org/10.1002/sia.740030412.

(15) Li, X.; Wan, J.; Ma, Y.; Zhao, J. R.; Wang, Y. Mesopores Octahedron GCNOX/Cu2O@C Inhibited Photo-Corrosion as an Efficient Visible-Light Catalyst Derived from Oxidized g-C3N4/HKUST-1 Composite Structure. *Appl. Surf. Sci.* **2020**, *510* (January), 145459. https://doi.org/10.1016/j.apsusc.2020.145459.

(16) Barreca, D.; Carraro, G.; Gasparotto, A. Cu x O - TiO 2 Composites (X=1, 2) Studied by X-Ray Photoelectron Spectroscopy. *Surf. Sci. Spectra* **2009**, *16* (1), 1–12. https://doi.org/10.1116/11.20110101.

(17) Lee, Y. R.; Kim, J.; Ahn, W. S. Synthesis of Metal-Organic Frameworks: A Mini Review. *Korean J. Chem. Eng.* **2013**, *30* (9), 1667–1680. https://doi.org/10.1007/s11814-013-0140-6.

(18) Ghamari Kargar, P.; Aryanejad, S.; Bagherzade, G. Simple Synthesis of the Novel Cu-MOF Catalysts for the Selective Alcohol Oxidation and the Oxidative Cross-coupling of Amines and Alcohols. *Appl. Organomet. Chem.* **2020**, *34* (12), e5965. https://doi.org/10.1002/aoc.5965.

(19) Braurer, G. *Handbook of Preparative Inorganic Chemistry*; Accademic Press: New York, 1963.

CHAPTER 3

3. XPS study of the reactivity of the propargyl carbamate-functionalized Cu(II)-MOF towards chloroauric acid

3.1 Aim of the chapter

In this part of the work I am going to describe the Cu-YBDC functionalization with gold nanoparticles by reaction with $HAuCl_4$ under thermal treatment in methanol and butanol (Scheme 3.1). The resulting systems were investigated by complementary techniques to obtain information on their structure and morphology. In particular, X-ray photoelectron spectroscopy (XPS) was employed to analyze the chemical composition of representative specimens. Wide scan spectra, data obtained by the analysis of the C1s, O1s, N1s, Cu2p, Au4f and CuLMM signals are presented and critically discussed. A good agreement was obtained between the raw data and the performed theoretical fits. The results highlight the reduction of Au(III) to both Au(0) and Au(I), with the latter oxidation state being the predominant one. Overall, the data presented herein may act as useful guidelines for the eventual tailoring of material properties and their possible implementation towards functional applications in heterogeneous catalysis.

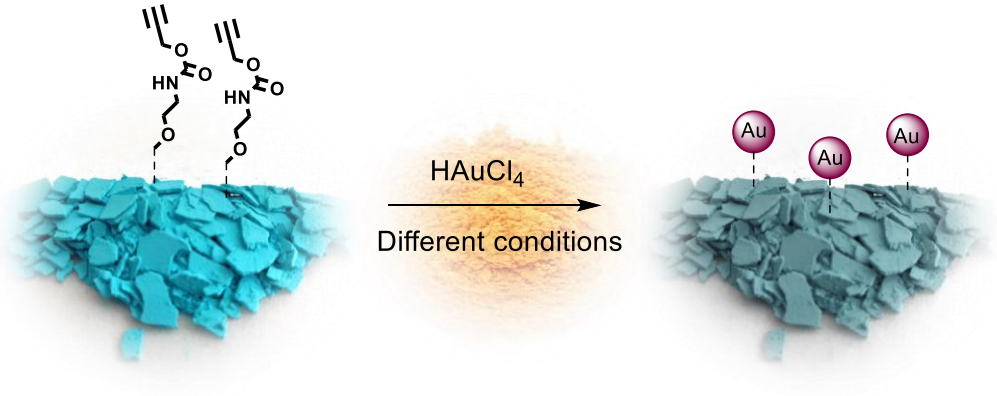

Scheme 3.1. Schematic view of Cu-MOF reactivity with $HAuCl_4$

3.2 Introduction

As already mentioned in the previous chapters, in recent years, our research group has shown that a propargyl carbamate [-N(H)C(O)O-CH_2-C≡CH] group anchored on different oxide supports (SiO_2, Al_2O_3, TiO_2, Fe_3O_4) is capable of straightforwardly reducing Au(III) to Au(0), yielding supported gold nanoparticles (AuNPs) without the addition of any external reducing and/or stabilizing agent.[1,2] This is an important point, since AuNPs are commonly synthesized from Au(III) solutions, typically $HAuCl_4$, in the presence of a strong reductant like $NaBH_4$ and a stabilizing agent. Because of the high stability of Au(0), it is not uncommon to observe Au(III) reduction also by alcohols (especially primary alcohols) or amines in solvothermal conditions.

Although stabilizers have the advantage of stabilizing AuNPs and controlling their size, they bind to low coordination metal sites, reducing their catalytic activity. Furthermore, in the case of NPs synthesis inside a MOF, the use of strong reducing agent such as $NaBH_4$ can damage the framework or bring to the reduction of the metal ions. This is the main drawback of colloidal synthesis of AuNPs.[3] Therefore, the possibility of generating AuNPs on/inside the MOF without using any of those reagents is highly intriguing and could open interesting possibilities.

The group in which I worked during my PhD developed a propargyl carbamate-based functionalization system that proved able to reduce Au(III) to form stabilized AuNPs. The proposed reduction mechanism is shown in Scheme 3.2 in the case of derivatized silica.

The affinity of Au(III) for alkyne groups is exploited to coordinate Au(III) to the propargyl moiety. The activated alkyne group is exposed to nucleophilic attack by the carbamic nitrogen in a 1,3-migration reaction. The following decarboxylation and rearrangement reactions lead to the unsaturated imine D. That imine, as well as its water addition product (e.g. E), can act as a reducing agent for gold species, leading to the formation of AuNPs that can be well stabilized by the presence of the amine nitrogen.[4]

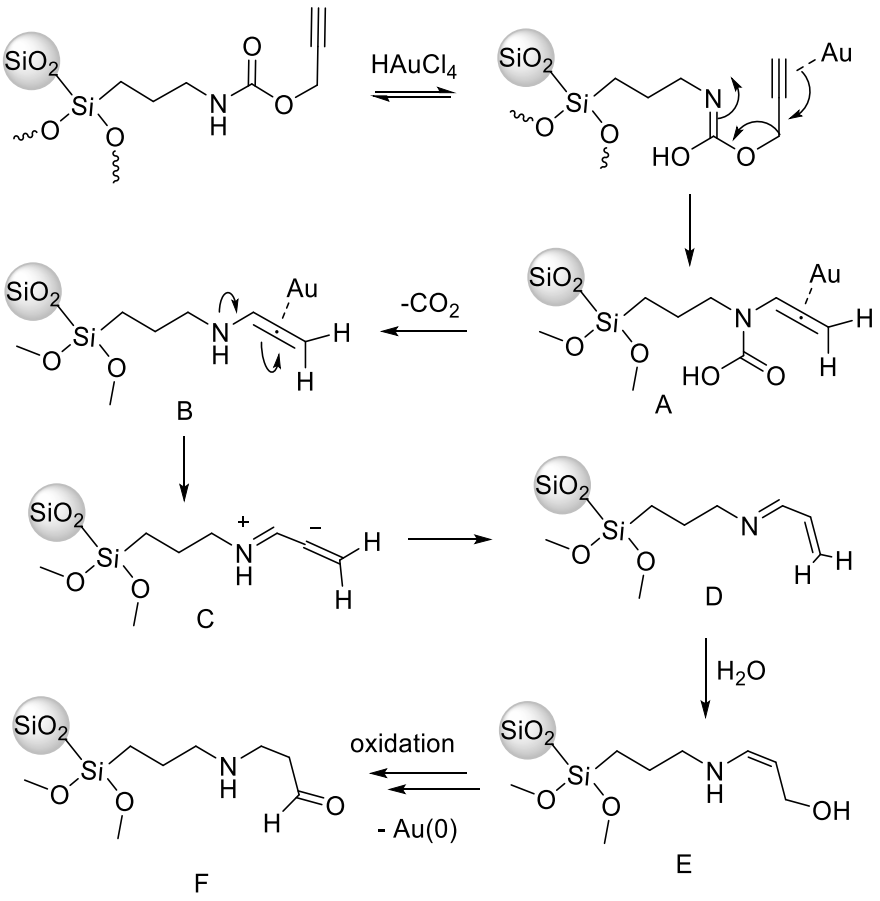

Scheme 3.2: Proposed mechanism for the SiO_2@Yne-mediated reduction of $HAuCl_4$.[1]

Based on these results, we envisaged that the versatility demonstrated by the propargyl carbamate residue could be further exploited by anchoring it to different solid supports other than oxides, for example within alkynyl-derivatized MOFs. In this regard, we showed that the reaction of the novel 5-substituted organic linker 5-(2-{[(prop-2-yn-1-yloxy)carbonyl]-amino}ethoxy)isophthalic acid (labelled 1,3-H_2YBDC, where Y = alkYne and BDC = Benzene DiCarboxylate), bearing a propargyl carbamate substituent, with copper nitrate in refluxing 2-propanol leads to a new copper-based MOF Cu-YBDC in high yields. The novel material was fully characterized by complementary analytical techniques. As explained in **Chapter 2**, Synchrotron X-ray diffraction data revealed that Cu-YBDC contains a complex network of 5-substituted isophthalate anions coordinated to Cu(II) centers belonging to the common paddlewheel dimeric structure with a Cu···Cu distance of 2.633(4) Å. Quite unexpectedly, the apical atom in the paddlewheel structure belongs to the carbonyl atom of the propargyl carbamate functionality, present with two equally populated alternative chain conformations. Such extra-coordination by the propargyl carbamate groups drastically reduces the MOF porosity, as also confirmed by BET measurements.[5]

Despite this evidence suggests that the internal pores of the material are available only to a small extent to host reactive gold species, this material could however stand as an attractive candidate for the generation and anchoring of reduced gold species, at least on the MOF surface, where the relatively dense, even array of propargyl-carbamate residues branching out therefrom could act as binding/reducing sites able to capture Au(III) ions and subsequently form Au(0) clusters.

In this context, the present study focuses on the reactivity of Cu-YBDC with $HAuCl_4$ under thermal treatment in methanol and butanol. X-ray photoelectron spectroscopy (XPS) studies were performed on all the obtained materials using a monochromated AlKα X-ray excitation source. This investigation was carried out in order to gather information on the elemental composition and oxidation states characterizing the elements present on the surface of the investigated materials. All the four samples (*i.e.*, FG130a, FG130b, FG131a, and FG131b) revealed the presence of C, N, O, Cu, and Au atoms on their surface, in agreement with the composition expected for the Au-supported MOF compounds.

3.3 Result and discussion

3.3.1 Reactivity of [Cu(1,3-YBDC)]·xH$_2$O towards HAuCl$_4$

[Cu(1,3-YBDC)]·*x*H$_2$O, here after simply termed Cu-YBDC, was first stirred in a 1.0 mM methanol solution of HAuCl$_4$ at room temperature for 1 h under N$_2$, then the not adsorbed HAuCl$_4$ was separated by centrifugation and the MOF thoroughly washed with methanol. Afterwards, the resulting material was placed in a suitable solvent under reflux to promote the reduction of the adsorbed Au(III). In this way only the Au(III) truly adsorbed on the MOF is reduced (Scheme 3.3).

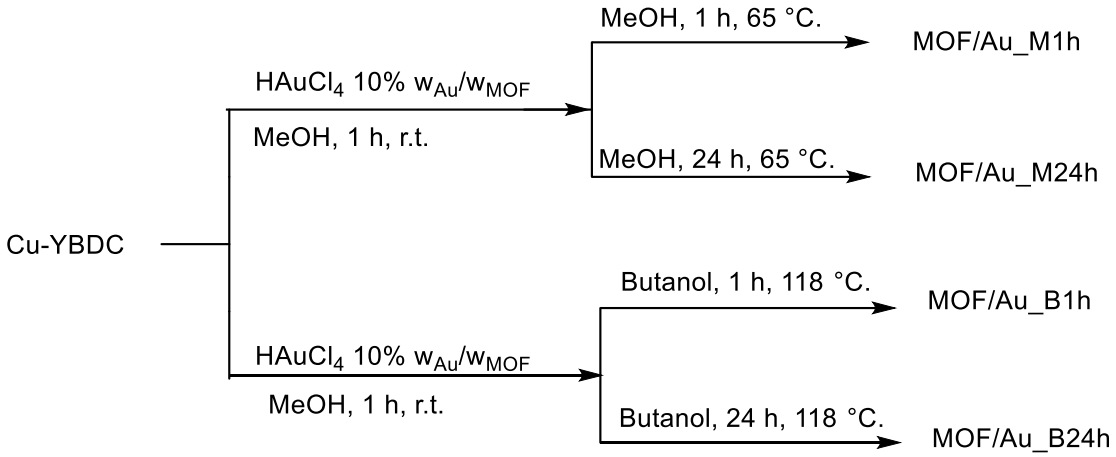

Scheme 3.3*:* [Cu(1,3-YBDC)]·xH$_2$O reactions with HAuCl$_4$.

3.3.2 Determination of Au percentage in the Cu-YBDC/Au MOF through AAS

The samples labelled MOF/Au_M1h (**FG130a**), MOF/Au_M24h (**FG130b**), MOF/Au_B1h (**FG131a**), and MOF/Au_B24h (**FG131b**), were analyzed by AAS to determine the total amount of gold in them (**Table 3.1**).

For this determination the instrument was calibrated using standard solutions at different concentrations (0.1, 0.2, 0.3,0.5, 1, 2, 3, 4 and 6 ppm) obtained by dilution of a mother solution of Au 110 ppm in HCl 0.5 M. The MOF samples were prepared by weighting ca. 10 mg of Cu-[YBDC]/Au MOF in a 25 mL matrass. Each sample was dissolved in hot aqua regia, added dropwise until the solid was completely dissolved, then the matrass was taken to volume with HCl 0.5 M. Considering the volume of the sample, we can calculate the mass of Au present in the solution corresponding to a percentage of Au in the Cu [YBDC]/Au MOF samples.

Table 3.1: Gold content in samples MOF/Au_M1h, MOF/Au_M24h, MOF/Au_B1h, MOF/Au_B24h.

Sample	Weight of the sample (mg)	Abs	Au concentration (ppm)	%Au w/w
MOF/Au_M1h	10.5	0.113	3.48	0.85
MOF/Au_M24h	10.0	0.111	3.46	0.84
MOF/Au_B1h	9.9	0.112	3.47	0.85
MOF/Au_B24h	9.9	0.113	3.48	0.85

The AAS calculations of gold percentage give an important experimental result: there is no significant distinction between the amount of gold in MOF/Au_M1h and MOF/Au_M24h. The same is also true for the couple MOF/Au_B1h and MOF/Au_B24h. This means that the gold retained by the MOF does not leach out in 24 hours, indicating a strong interaction between the MOF surface and gold.

3.3.3 XPS characterization and study

A sample of each reaction product was sent to our collaborator at the Department of Chemical Sciences of Padova University to determine the atomic percentage of gold on the external surface of the MOF and its oxidation state trough XPS analysis. The samples are fixed on an adhesive tape and introduced into the analysis chamber at 298 K and $<10^{-4}$ Pa pressure. The pre-analysis beam exposure was 180 s.

All the four samples (*i.e.*, **FG130a**, **FG130b**, **FG131a**, and **FG131b**) revealed the presence of C, N, O, Cu as major elements and Au as minor element on their surface (see **Figure 3.1**), in agreement with the composition expected for the Au-supported MOF compounds.

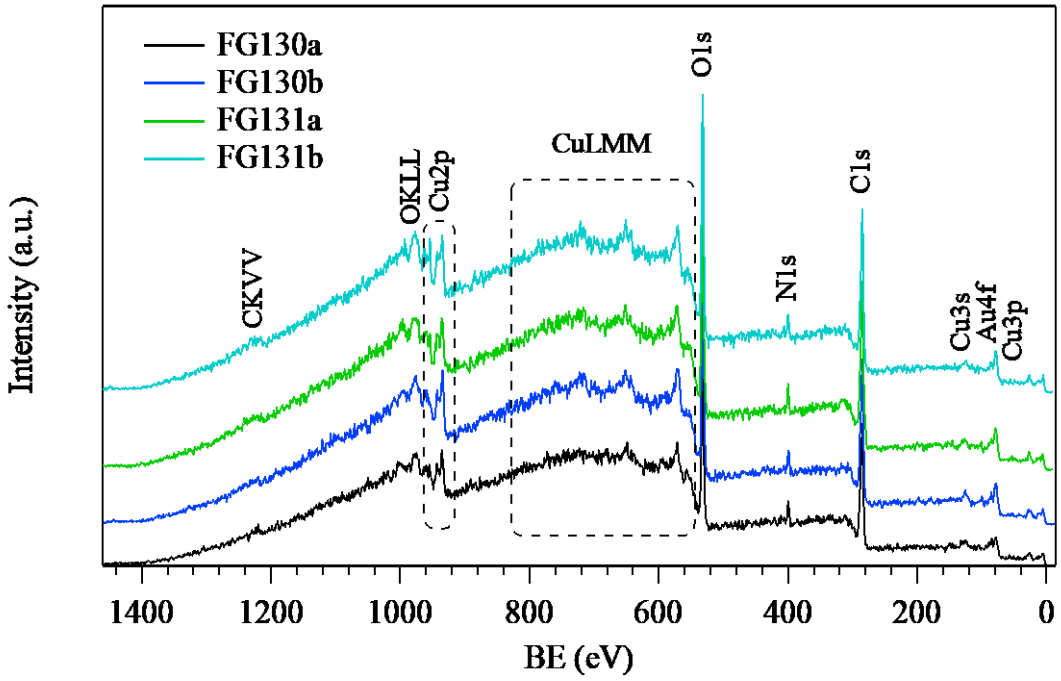

Figure 3.1 Surface XPS wide-scan spectra for all the target specimens.

Results of the surface quantification are summarized in **Table 3.2**. All the samples exhibit a similar C, N and O content. In the case of metals, the **FG130a** and **FG130b** samples revealed a Cu content of *ca*. 2.0 at.%, whereas for **FG131a** and **FG131b** compounds it is *ca*. 1.4 at.%. On the other hand, the Au concentration, which is comprised between 0.12 and 0.06 at.%, decreases in the order **FG130a** > **FG130b** = **FG131a** > **FG131b**.

Table 3.2. Relative composition of the target specimen analyzed by XPS.

Sample	at.% values					
	C	**N**	**O**	**Cu**	**Au**	**Au/Cu**
FG130a	62.76	4.14	31.00	1.97	0.12	0.06
FG130b	62.25	4.72	30.81	2.15	0.08	0.04
FG131a	66.42	3.86	28.27	1.36	0.08	0.06
FG131b	66.57	3.28	28.69	1.41	0.06	0.03

High-resolution spectra of C1s signal reveal the presence of four different components (see Fig 3.2a), which concurrently contribute to this peak and which can be assigned to the MOF scaffold. In detail, C1s signal is the result of the following features: (**I**) BE = 284.8 eV (relative abundance ≈ 42 % of the total C signal), attributed to both adventitious carbon

contaminations and to C-C species; (**II**) BE = 286.0 eV (relative abundance ≈ 30 % of the total C), assigned to C-N and C-O bonds in the ligand skeleton; (**III**) BE = 287.8 eV (relative abundance ≈ 20 % of the total C signal), related to the -COOH functionalities bonded to the aromatic ring; and (**IV**) BE = 289.8 eV (relative abundance ≈ 8 % of the total C signal), assigned to -NCOO- groups present in the ligand lateral chain.[6] Three different peaks are concurring to the overall intensity of the O1s signal (see Fig. 3.2.b), which are: (**V**) BE = 529.8 eV (relative abundance ≈ 7 % of the total O signal), associated to ligand oxygen atoms bonded to copper and/or O in copper oxides [7] (**VI**) BE = 531.5 eV (relative abundance ≈ 45 % of the total O signal), ascribed to C-O single bonds and chemisorbed OH hydroxyl groups;[8,9] and (**VII**) BE = 533.2 eV (relative abundance ≈ 48 % of the total O signal), attributed to the presence of C=O groups in carboxylate functionalities and/or adsorbed water molecules. A single peak signal is determined in the N1s spectra (see Fig. 3.2c), centered at BE = 400.6 eV. This binding energy value indicates that a strong ligand coordination is present between nitrogen atoms and Cu(II) metal centers in the investigated materials.[10]

Important information on the Cu chemical state can be gained by means of a careful evaluation of the copper signals (see Fig. 3.2d-e). Indeed, the calculation of the Auger parameter, which is defined as α_{Cu} = BE($Cu2p_{3/2}$) + KE(CuLMM) (where KE = kinetic energy = 1486.6 - BE), is a useful tool in order to determine the presence of Cu(I) and/or Cu(II) into the investigated materials. In our case, α_{Cu} = 1850.8±0.2 eV, close to the value obtained for pure CuO,[8] thus witnessing that the majority of copper species are in their divalent oxidation state. Indeed, the signal of both $Cu2p_{3/2}$ and $Cu2p_{1/2}$ peaks can be fitted with just one component. In particular, values of BE = 934.6 and 954.3 eV for $Cu2p_{3/2}$ and $Cu2p_{1/2}$ spin-orbit components, respectively, are obtained. These BEs are in agreement with the presence of Cu(II) species into the copper-containing metal-organic framework.[11] A further confirmation of this attribution is given by the presence of intense *shake-up* satellites peaking at BE values ≈ 9.5 eV higher than the main spin-orbit components, which are a finger-print for the predominant presence of d^9 copper (II) centers.[12,13] When only Cu(I) species (d^{10}, a closed-shell system) are present, such satellites are not detected.

A low intensity and broad Au4f signal is detected at its typical BE values (see Fig. 3.2f). The broadening of the peak suggests the presence of Au species with different oxidation states. In particular, it is possible to recognize the presence of: (**VIII**) BE($Au4f_{7/2}$) = 84.0 eV and BE($Au4f_{5/2}$) = 87.8 eV (relative abundance ≈ 23 % of the total Au4f signal), ascribed to Au(0) species; and (**IX**) BE($Au4f_{7/2}$) = 85.8 eV and BE($Au4f_{5/2}$) = 89.6 eV

(relative abundance ≈ 77 % of the total Au4f signal), attributed to oxidized Au(I) species. In particular, the most oxidized gold species are found, in order, in: (i) **FG131b** (81.4 at.% of Au(I)); (ii) **FG131a** (78.7 at.% of Au(I)); (iii) **FG130b** (75.8 at.% of Au(I)); and (iv) **FG130a** (71.9 at.% of Au(I)). In these samples, the Au4f BEs characterizing metallic gold (*i.e.*, peak **VIII**) are in agreement with the typical reference position of Au(0) (*i.e.*, 84.0 eV).[14]

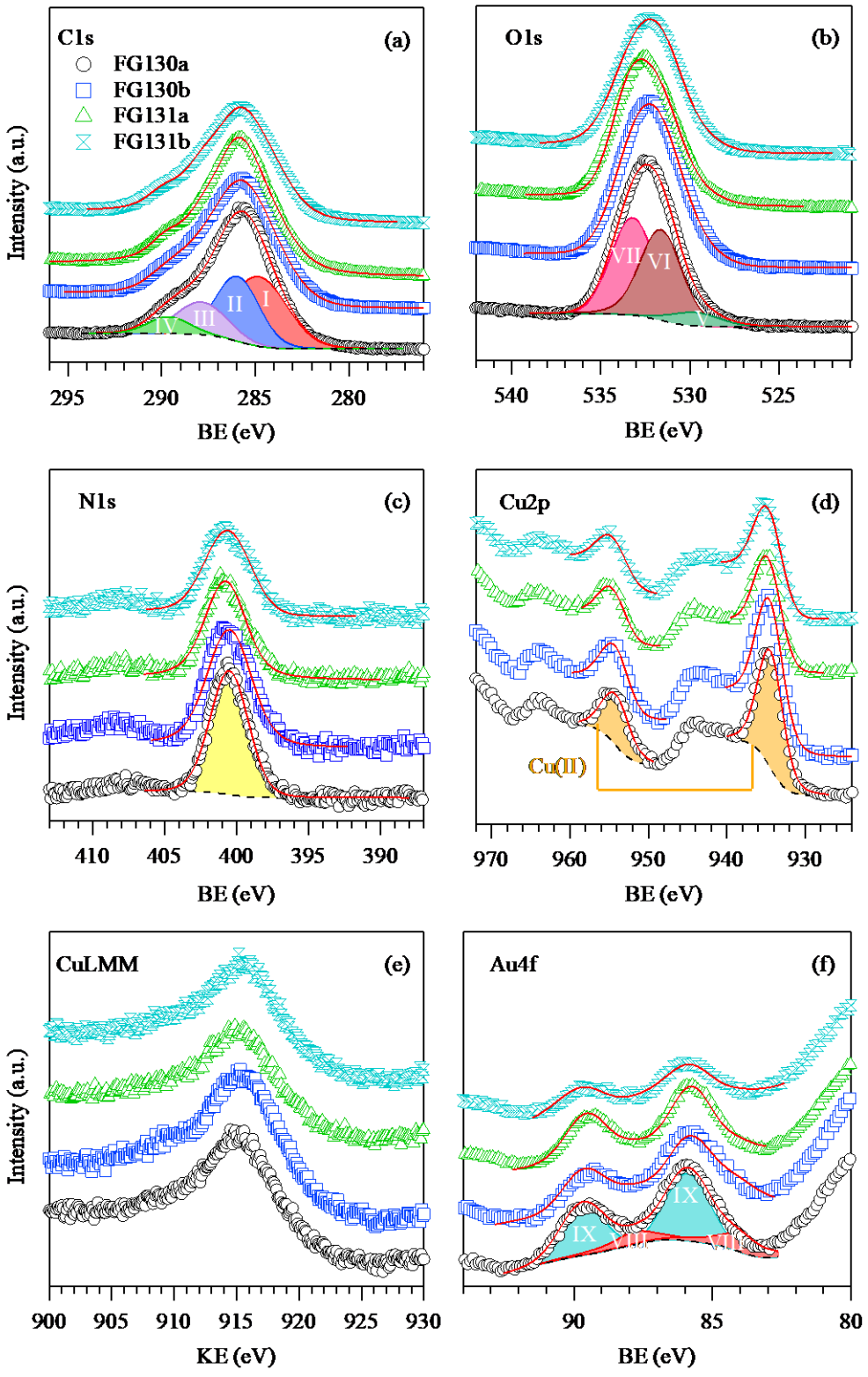

Figure 3.2. Surface XPS analysis for the target specimen: (a) C1s, (b) O1s, (c) N1s, (d) Cu2p, (e) CuLMM, (f) Au4f

3.3.4 Other characterizations

In view of the XPS results discussed above, only the sample FG130a (MeOH, 1h, 65°C) was further fully characterized with four complementary techniques (TGA, XRD, IR-ATR and SEM) and the resulting data compared with the starting Cu-YBDC.

1. The TGA plot for Cu-YBDC (Fig.3.3, mw of $C_{14}H_{11}CuNO_7$ 368.79 g mol^{-1}) shows two decomposition steps in the 200-450 °C range (attributed to the progressive loss of the propargyl fragments $C_6H_8NO_3$ residue, obs. 38.2%, calc. 38.5%), terminating at a temperature ca. 150 °C lower than in the pristine organic ligand.[6] Such lower thermal stability of the organic skeleton within the MOF is tentatively attributed to assistance, during decomposition, of redox process(es) catalyzed by Cu(II) ions. Furthermore, a residue of ≈ 26 wt% is present at 400 °C, with no significant variation up to 800 °C, which is presumably due to residual CuO. As a residual 21.6% only is calculated if the starting material were pure, the excess residue at high T speaks for the presence of carbonaceous residuals and only marginally to Cu-rich contaminants.

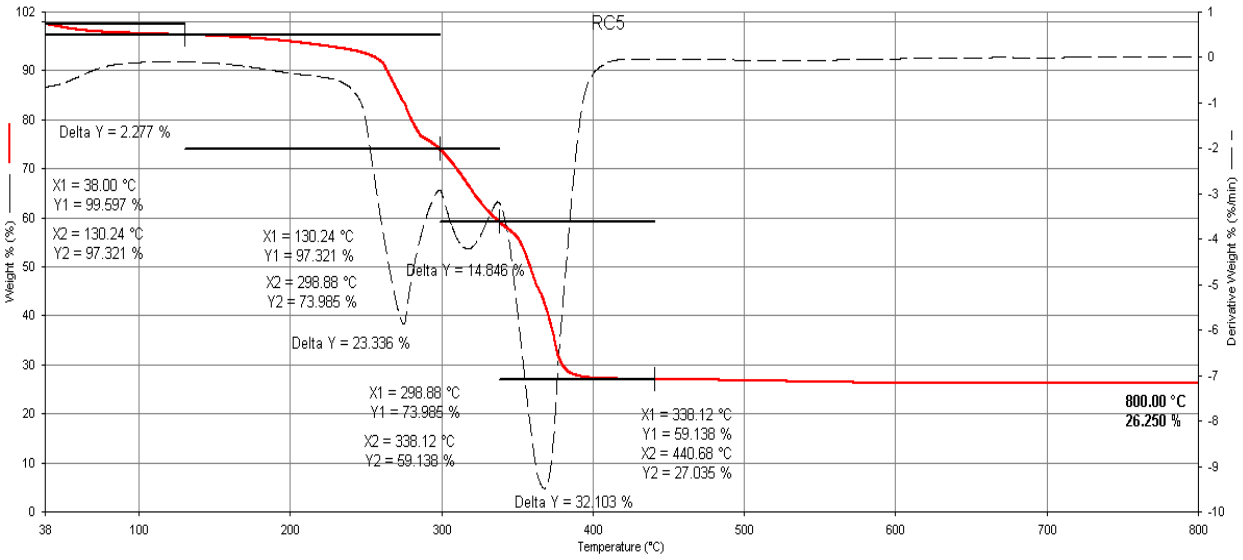

Figure 3.3 TGA curve (continuous red lines) and their first derivatives (dashed lines) for Cu-YBDC.

In Fig. 3.4 the TGA plot for the Au(I)-containing Cu-MOF (FG130a, MeOH 1h, 65 °C) is shown. Also in this case the two decomposition steps occur in the range 200-450 °C range with a final residue of ≈ 30 wt% i.e. a 4 wt% higher than in the absence of gold.

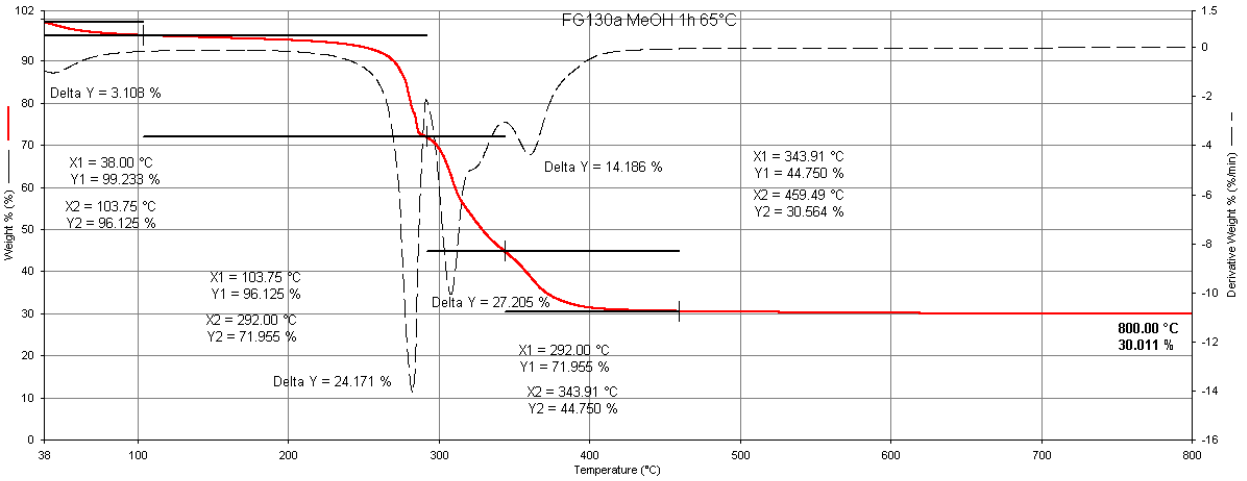

Figure 3.4. TGA curve (continuous red lines) and their first derivatives (dashed lines) for the Au(I) containing Cu-MOF FG130a (MeOH 1h, 65 °C).

2. The XRD patterns of Cu-YBDC (RC5) and Cu-MOF/Au(I) (FG130a, MeOH 1h, 65 °C) are compared in Fig 3.5. The two patterns are identical except for the fact that in Cu-MOF/Au(I) the peak at 12.82° (indicated by the green arrow), attributed to the $Cu_2(OH)_3(NO_3)$ contaminant species, is more intense.

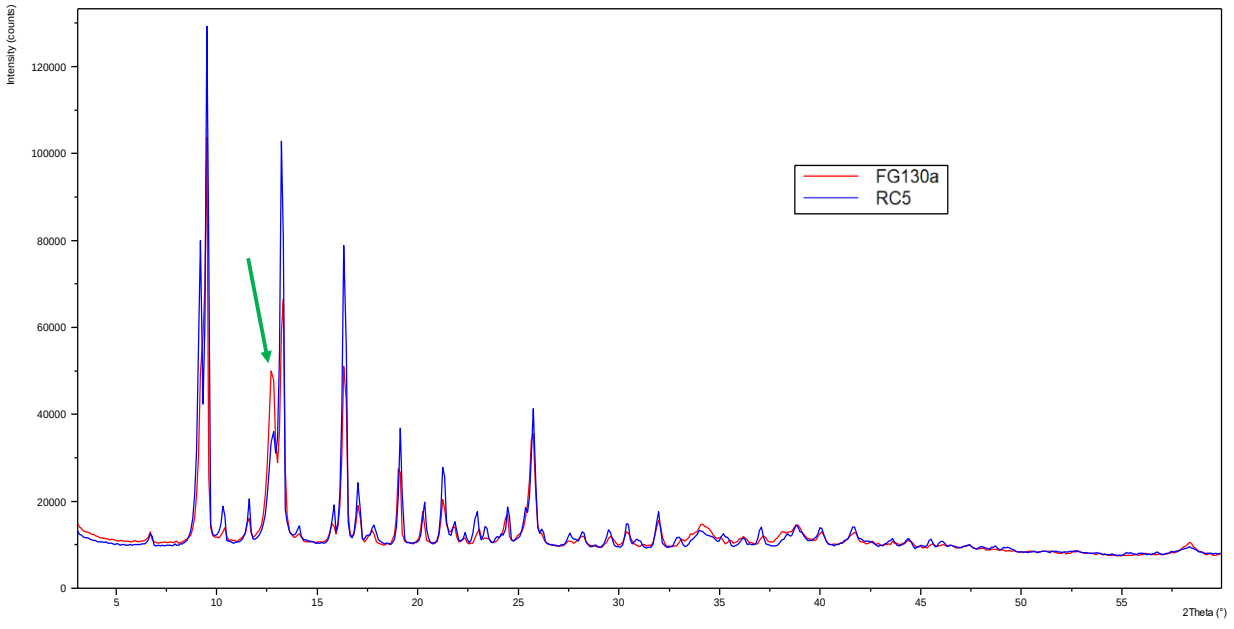

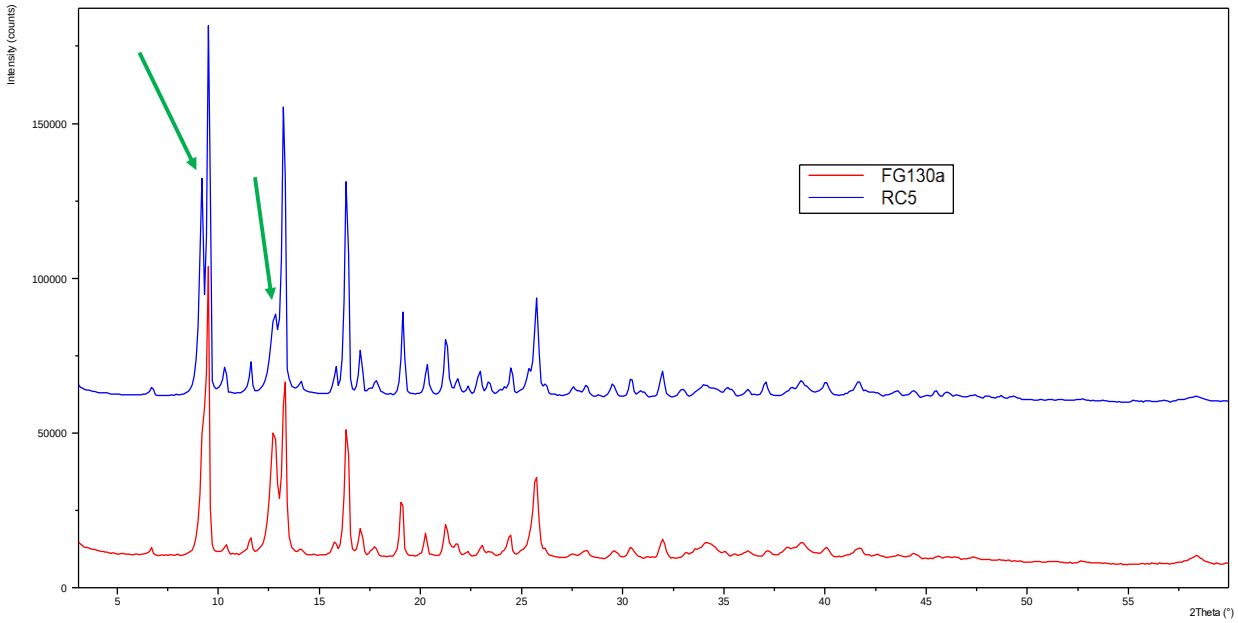

Figure 3.5 Full plot of diffraction for samples [Cu(1,3-YBDC)]·*x*h$_2$O (RC5) and Cu-MOF/Au(I) (FG130a, MeOH 1h, 65 °C).

3. In **Figure 3.6** the ATR-IR spectra of Cu-YBDC (FG74, red line) and Cu-MOF/Au(I) (FG130a, MeOH 1h, 65 °C, black line) are shown.

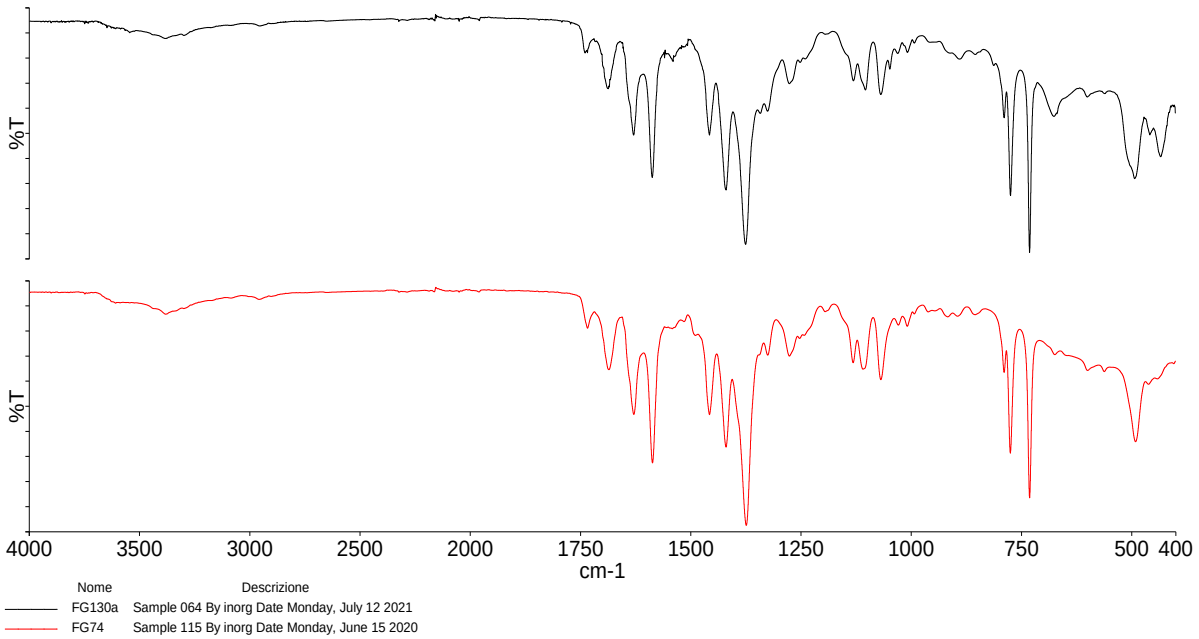

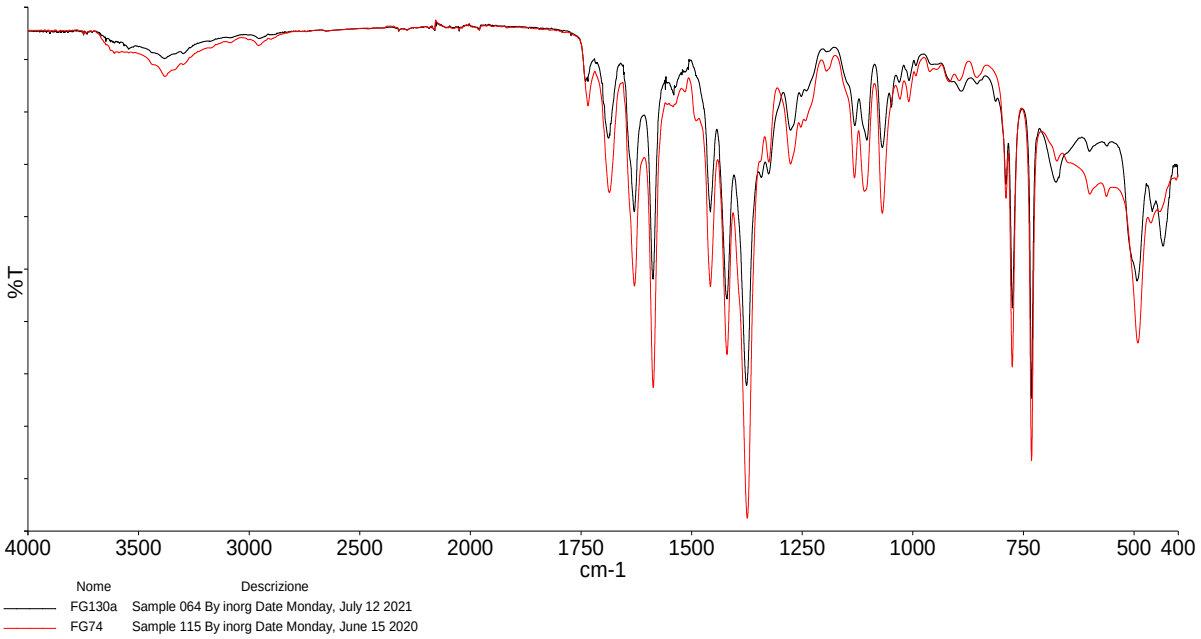

Figure 3.6. IR-ATR spectrum of Cu-YBDC (FG74, red line) and Cu-MOF/Au(I) (FG130a, MeOH 1h, 65 °C, black line).

4. The morphology of the powder was imaged by means of FE-SEM. In Fig. 3.7 SEM images of Cu-YBDC deposited on an electrode surface[15] after sonication in ethanol and Cu-YBDC/Au(I) are reported. The micrograph for Cu-YBDC (Figure 3.7A) revealed the predominant presence of large prismatic crystals with sub-micrometric dimensions while the micrograph for Cu-YBDC/Au(I) (Figure 3.7B) still showed the predominant presence of prisms although less defined and smaller of those observed with the sample not treated with $HAuCl_4$.

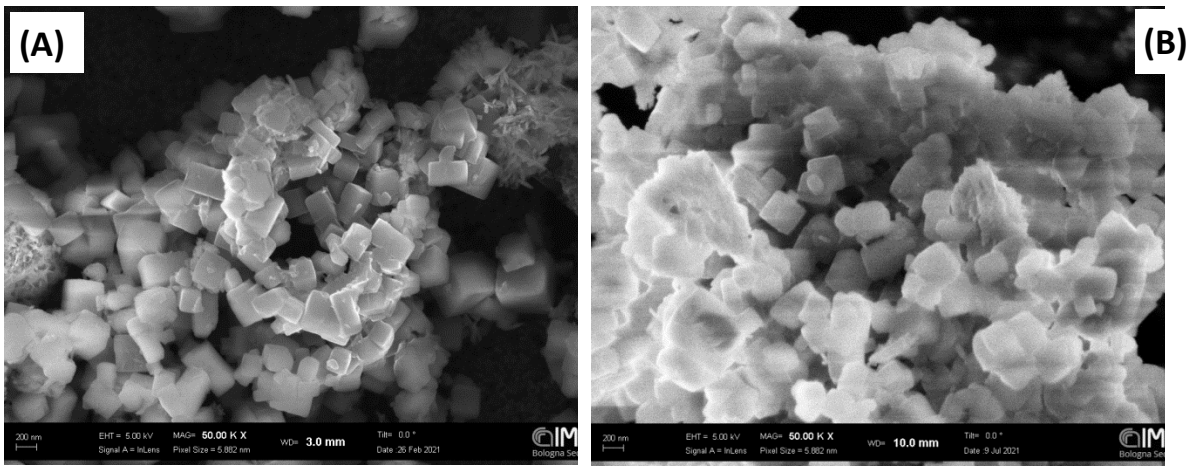

Figure 3.7 Representative FE-SEM images of Cu-YBDC (A) and Cu-YBDC/Au(I) (FG130a, B).

3.4 Conclusions

This thoroughly XPS study represents the evidence that the thermal treatment in alcohol of Cu-YBDC impregnated with $HAuCl_4$ leads to reduction of Au(III) to Au(0) and to Au(I), with the latter oxidation state as the predominant oxidation state, leaving the morphology of the starting Cu-MOF substantially unchanged. In fact, all the complementary characterizations (TGA, XRD, IR-ATR, SEM) done and compared with the Cu-MOF confirmed the stability of the material during the tests of reactivity with $HAuCl_4$.

The future work will focus on the following issues:

- to continue the search for the best optimized conditions for reduction of Au(III) to Au(I) or Au(0), possibly with the predomination of only one oxidation state as a fundamental requirement for realizing an efficient catalyst;
- to repeat the XPS characterization and confirm the stability of the material;
- to explore viable applications of the optimized material as a catalyst or, for example, as an adsorbent for dyes, as already partially explored in this work (see **Chapter 4**).

3.5 Experimental Section

3.5.1 Instrumental characterization

Field emission-scanning electron microscopy (FE-SEM) analysis was carried out by means of a Zeiss SUPRA 40VP instrument equipped with an INCAx-act PentaFET Precision spectrometer (Oxford Instruments) for energy dispersive X-ray spectroscopy (EDXS) characterization. The used primary beam acceleration voltages were comprised between 1 kV (for imaging) and 20 kV (for EDXS analyses).

X-ray photoelectron (XPS) studies were carried out by means of a Specs EnviroESCA instrument using a monochromated AlKα excitation source ($h\upsilon$ = 1486.6 eV), at an operating pressure of *ca*. 10^{-6} mbar. Survey scans were performed with 100 eV pass energy, every 1.0 eV·step^{-1}, and for 0.1 sec·step^{-1}. High resolution spectra were acquired with 50 eV pass energy, every 0.1 eV·step^{-1}, and for 0.1 s·step^{-1}. In agreement with the literature,[16] binding energy values (BEs; uncertainty = ± 0.2 eV) were corrected for charging assigning to the adventitious C 1s peak, attributed to adventitious hydrocarbons, the value of 284.8 eV. XPS curves were analyzed using the Specs Keystone software, applying a Shirley-type background substruction.[18] The sensitivity factors of integrated peak areas used for atomic percentages (at. %) quantification were supplied by Specs.

Thermogravimetric analyses were carried out using a Perkin Elmer TGA-7. The samples (ca. 10 mg) were heated in air (20 cm^3/min) in a platinum crucible at a rate of 10 °C min^{-1} from 38 °C to 800 °C.

XRD was performed by a Philips X'Pert Pro instrument equipped with a fast X'Celerator detector, working at 40 mA and 40 kV and using Cu Kα radiation.

3.5.2 Reactivity of [Cu(1,3-YBDC)]·xH_2O towards $HAuCl_4$

MeOH, 65 °C, 10 wt% w_{Au}/w_{MOF}

To a suspension of [Cu(1,3-YBDC)]·xH_2O (0.250 g) in MeOH (120 mL), $HAuCl_4 \cdot 3H_2O$ (0.050 g, 0.127 mmol) was added. The reaction mixture was stirred for 1 h at r.t. and the solid was successively separated from the supernatant by centrifugation at 5400 rpm for 15 min. After three cycles of washings with MeOH (3x20 mL) and centrifugations the product was divided in two parts: one half was placed in MeOH (30 mL) at 65 °C for 1 h under stirring (FG130a). The second half was placed in MeOH (30 mL) at 65 °C for 24 h under stirring (FG130b). After that, the solid was again separated by centrifugation and washed with MeOH.

Butanol, 118 °C, 10 wt% w_{Au}/w_{MOF}

To a suspension of [Cu(1,3-YBDC)]·xH_2O (0.250 g) in MeOH (120 mL), $HAuCl_4 \cdot 3H_2O$ (0.050 g, 0.127 mmol) was added. The reaction mixture was stirred for 1 h at r.t. and the solid successively was separated from the supernatant by centrifugation at 5400 rpm for 15 min. After three cycles of washings with MeOH (3x20 mL) and centrifugations the product was divided in two parts: one half was placed in butanol (30 mL) at 118 °C for 1 h under stirring (FG131a). The second half was placed in butanol (30 mL) at 118 °C for 24 h under stirring (FG131b). After that, the solid was again separated by centrifugation and washed with MeOH.

References

(1) Parise, C.; Ballarin, B.; Barreca, D.; Cassani, M. C.; Dambruoso, P.; Nanni, D.; Ragazzini, I.; Boanini, E. Gold Nanoparticles Supported on Functionalized Silica as Catalysts for Alkyne Hydroamination: A Chemico-Physical Insight. *Appl. Surf. Sci.* **2019**, *492*, 45–54. https://doi.org/10.1016/J.APSUSC.2019.05.192.

(2) Ballarin, B.; Barreca, D.; Boanini, E.; Cassani, M. C.; Dambruoso, P.; Massi, A.; Mignani, A.; Nanni, D.; Parise, C.; Zaghi, A. Supported Gold Nanoparticles for Alcohols Oxidation in Continuous-Flow Heterogeneous Systems. *ACS Sustain. Chem. Eng.* **2017**, *5* (6), 4746–4756. https://doi.org/10.1021/acssuschemeng.7b00133.

(3) Zhong, R.-Y.; Sun, K.-Q.; Hong, Y.-C.; Xu, B.-Q. Impacts of Organic Stabilizers on Catalysis of Au Nanoparticles from Colloidal Preparation. *ACS Catal.* **2014**, *4* (11), 3982–3993. https://doi.org/10.1021/cs501161c.

(4) Fazzini, S.; Cassani, M. C.; Ballarin, B.; Boanini, E.; Girardon, J. S.; Mamede, A. S.; Mignani, A.; Nanni, D. Novel Synthesis of Gold Nanoparticles Supported on Alkyne-Functionalized Nanosilica. *J. Phys. Chem. C* **2014**, *118* (42), 24538–24547. https://doi.org/10.1021/jp507637m.

(5) Cassani, M.; Gambassi, F.; Ballarin, B.; Nanni, D.; Ragazzini, I.; Barreca, D.; Maccato, C.; Guagliardi, A.; Masciocchi, N.; Kovtun, A.; Rubini, K.; Boanini, E. A Cu(Ii)-MOF Based on a Propargyl Carbamate-Functionalized Isophthalate Ligand. *RSC Adv.* **2021**, *11*, 20429–20438. https://doi.org/10.1039/D1RA02686K.

(6) Azhar, M. R.; Hussain, G.; Tadé, M. O.; Silvester, D. S.; Wang, S. Electrodeposited Metal Organic Framework toward Excellent Hydrogen Sensing in an Ionic Liquid, *ACS Appl. Nano Mater.* **2020**, *3* (5), 4376–4385. https://doi.org/10.1021/acsanm.0c00503.

(7) Barreca, D.; Gasparotto, A.; Tondello, E. CVD Cu2O and CuO Nanosystems Characterized by XPS. *Surf. Sci. Spectra* **2007**, *14* (1), 41–51. https://doi.org/10.1116/11.20080701.

(8) Barreca, D.; Gasparotto, A.; Maccato, C.; Tondello, E.; Lebedev, O. I.; van Tendeloo, G. CVD of Copper Oxides from a β-Diketonate Diamine Precursor: Tailoring the

Nano-Organization. *Cryst. Growth Des.*, **2009**, *9* (5), 2470–2480. https://doi.org/10.1021/CG801378X.

(10) Taher, A.; Wook Kim, D.; Lee, I.-M. Highly Efficient Metal Organic Framework (MOF)-Based Copper Catalysts for the Base-Free Aerobic Oxidation of Various Alcohols. *RSC Adv.* **2017**, *7* (29), 17806–17812. https://doi.org/10.1039/C6RA28743C.

(11) Azhar, M. R.; Hussain, G.; Tade, M. O.; Silvester, D. S.; Wang, S. Electrodeposited Metal Organic Framework toward Excellent Hydrogen Sensing in an Ionic Liquid. *ACS Appl. Nano Mater.* **2020**, *3* (5), 4376–4385.

(12) Chen, C.; Wu, T.; Yang, D.; Zhang, P.; Liu, H.; Yang, Y.; Yang, G.; Han, B. Catalysis of Photooxidation Reactions through Transformation between Cu2+ and Cu+ in TiO2-Cu-MOF Composites. *Chem. Commun. Camb. Engl.* **2018**, *54* (47), 5984–5987. https://doi.org/10.1039/c8cc03505a.

(13) Ballarin, B.; Barreca, D.; Boanini, E.; Cassani, M. C.; Dambruoso, P.; Massi, A.; Mignani, A.; Nanni, D.; Parise, C.; Zaghi, A. Supported Gold Nanoparticles for Alcohols Oxidation in Continuous-Flow Heterogeneous Systems. *ACS Sustain. Chem. Eng.* **2017**, *5* (6), 4746–4756. https://doi.org/10.1021/acssuschemeng.7b00133.

(14) Cassani, M. C.; Castagnoli, R.; Gambassi, F.; Nanni, D.; Ragazzini, I.; Masciocchi, N.; Boanini, E.; Ballarin, B. A Cu(II)-MOF Based on a Propargyl Carbamate-Functionalized Isophthalate Ligand as Nitrite Electrochemical Sensor. *Sensors* **2021**, *21* (14), 4922. https://doi.org/10.3390/s21144922.

(15) Taylor, A. Practical Surface Analysis, 2nd Edn., Vol I, Auger and X-Ray Photoelectron Spectroscopy. Edited by D. Briggs & M. P. Seah, John Wiley, New York, 1990, 657 Pp., Price: £86.50. ISBN 0471 92081 9. *J. Chem. Technol. Biotechnol.* **1992**, *53* (2), 215–215. https://doi.org/10.1002/jctb.280530219.

(16) Shirley, D. A. High-Resolution X-Ray Photoemission Spectrum of the Valence Bands of Gold. *Phys. Rev. B* **1972**, *5*, 4709.

CHAPTER 4

4. Exploring the Cu-YBDC and Cu-YBDC/Au environmental applications

4.1 Aim of the chapter

This part of the work investigates the possible environmental applications of the Cu-YBDC MOF (Figure 4.1) in the field of water remediation, exploring its properties in two kinds of possible future use:

1) A modified electrode was realized with [Cu(1,3-YBDC)]·xH2O containing the propargyl carbamate functionality and immobilized on glassy carbon by drop-casting (GC/Cu-YBDC). Afterwards, GC/Cu-YBDC was treated with $HAuCl_4$ and the direct electro-deposition of Au nanoparticles (GC/Au/Cu-YBDC) was achieved. The performance of both electrodes (with and without AuNPs) towards nitrite oxidation was tested and it was found that GC/Au/Cu-YBDC exhibited a better electrocatalytic behavior toward the oxidation of nitrite than GC/Cu-YBDC, with enhanced catalytic currents and a reduced nitrite overpotential. Additionally, GC/Au/Cu-YBDC showed a low limit of detection, an ultrafast response time, and a wide linear range.[1]

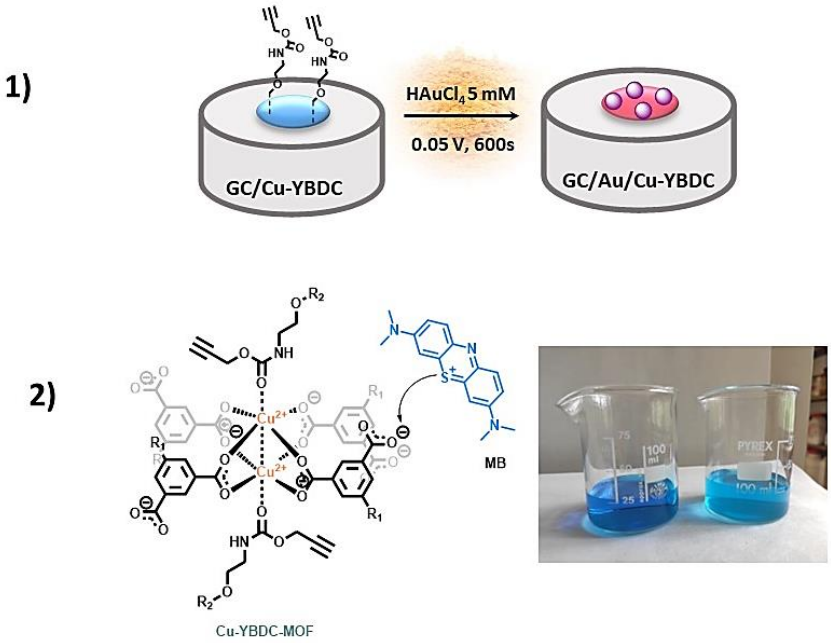

Figure 4.1. Schematic representation of Cu-YBDC applications. **1)** GC-CuMOF decorated electrode with AuNPs **2)** MB adsorption on Cu-YBDC surface thanks different charge interactions.

2) [Cu(1,3-YBDC)]·xH_2O was studied also as an adsorbent material for organic dyes by testing it with Methylene Blue (MB). The experimental determination of the adsorption kinetics of MB in different conditions was explored. The preliminary data suggest that the adsorption performances of the new material are limited, most likely due to the low porosity and surface area of the material, but they also highlight numerous potential issues with the experimental procedure.

4.2 Introduction

4.2.1 MOF and environmental applications

Freshwater harvesting from groundwater and desalination of seawater appear, *a priori*, as the natural options to circumvent the world's water crisis. However, the technologies needed to perform it in an efficient manner are not affordable all over the world. It is mandatory to raise awareness of the paramount importance of developing technologies for efficient removal of contaminants from water,[2,3] which will allow wastewater reclamation and reuse and consequently, help the re-establishment of the planet's environmental balance.

Existing technologies for water remediation (Figure 4.2) include precipitation, membrane technology, coagulation/flocculation, and biological processes: the latter have advantages and inconveniences and, in some of them, there are decontamination protocols implemented in sequence to mitigate its drawback. Currently used conventional decontamination and disinfection methods suffer from high operating cost and generation of secondary pollutants and, even more importantly, are not able to completely eliminate the waste of contaminated waters.[4] Adsorption of pollutants with porous materials is a suitable alternative to remove contaminants from our water ecosystems in an efficient manner. Mesoporous clay materials, zeolites, bioadsorbents, polymeric resins, and carbonaceous materials have all demonstrated, to some extent, good performances towards different contaminants present in aqueous media.[5]

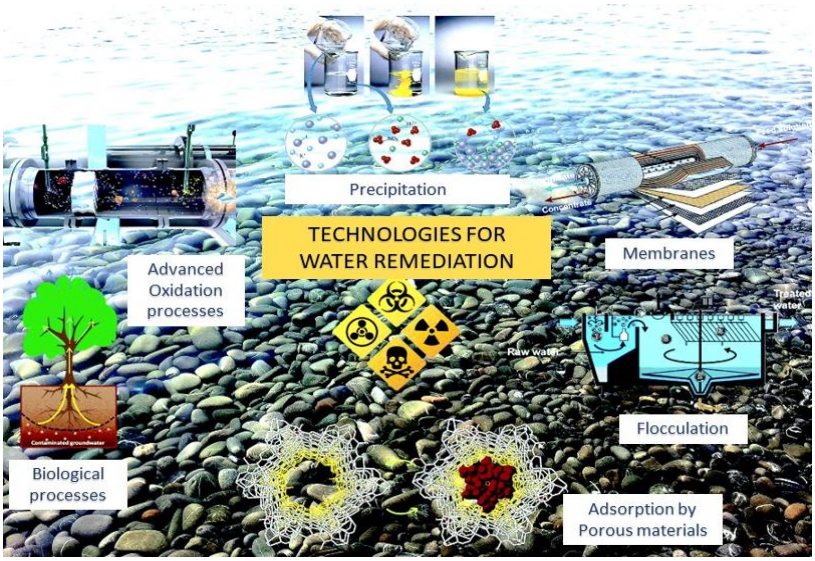

Figure 4.2. Panoramic of technologies for water remediation.

Among the currently investigated materials for water treatment, metal organic frameworks (MOFs) have provided excellent platforms for the separation of several

pollutants from water. The structural modularity and the striking chemical/physical properties of MOFs have provided more room for target-specific environmental applications.[6] Overall, they could be summarized based on:

(i) the hard/soft acid-base principle, using either high-valence metal ions with carboxylate-type ligands or divalent metal ions with nitrogen-containing ligands;

(ii) the introduction of hydrophobic groups on the ligand;

(iii) the minimization of the number of open metal sites (OMSs);

(iv) the use of biocompatible ligands.

To show an overview, **Table 4.1** reports in summary the possible uses of MOFs as adsorbents of inorganic and organic contaminants present in water.

Table 4.1. Example and reference of use of MOFs as adsorbent for different kinds of contaminants.

Type of contaminants	Example of contaminant	Example of MOF	Reference
Metal cations	Cadmium(II)	PCN-100	([7])
Inorganic acid	Boronic Acid	UiO-66, MIL-96	([8])
Pharmaceuticals	Anti-inflammatory	MIL-101	([9])
Agricultural products	Herbicides	UiO-66	([10])
Industrial products	caffeine	UiO-66-COOH	([11])
Organic dyes	Methylene Blue	MIL-100	([12])

4.2.2 Metal Organic Frameworks as electro sensor for water pollutants

Metal-Organic Frameworks (MOFs) have received enormous attention in these last years. Although the main research studies based on MOFs are driven by catalysis,[13] pollutants absorption, or gas storage,[14] potential uses were also proposed for electrochemical applications.[15] Due to the high porosity and surface area, MOF films can concentrate analytes near the surface of the electrode amplifying the signal response and improving the detection sensitivity.[16,17] Because MOFs suffer from low conductivity, to further increase the sensibility of the sensors in which they are employed, they are usually modified with highly conductive nanomaterials like metallic nanoparticles and carbon nanomaterials.[18]

Nitrite is extensively present in environmental, food, industrial, and physiological systems and due to its dangerousness, several analytical techniques were developed for its accurate, reliable quantification. Among them, electrochemical sensors have received great attention for being easy to use and for presenting outstanding features such as high sensitivity, low detection limits, and good selectivity. With the aim of decreasing the high oxidation potential that nitrites show at the traditional electrodes and of lowering the detection limit, several materials with good catalytic activity have been used as electrode modifiers, e.g., graphene, carbon nanotubes, and gold nanoparticles.[19] A few interesting applications of functionalized MOFs for the electrochemical determination of nitrite have recently appeared: in this context, electrodes based on MOFs have been recently employed to load or encapsulate catalytically active metal nanoparticles with high catalytic efficiency.

4.2.3 MOFs as adsorbent materials for dyes

At the same time, MOFs are receiving great attention in the studies of adsorbent materials for wastewaters treatment. Among the classes of polluting agents whose removal is being studied with MOFs, the most important are organic dyes: they are produced in large quantities (800000 tons per year), around 10-15% of which directly reaches the environment as effluent or during losses that occur in drying processes. Many of the released dyes and their breakdown products are toxic, carcinogenic, or mutagenic to life forms. Additionally, many of them remain in the environment for a long period of time. They are often divided in three main categories (Scheme 1.1): cationic dyes (e.g., Methylene Blue [MB]), anionic dyes (e.g., Methyl Orange [MO]), and neutral dyes (e.g., Dimethyl Yellow [DY]).

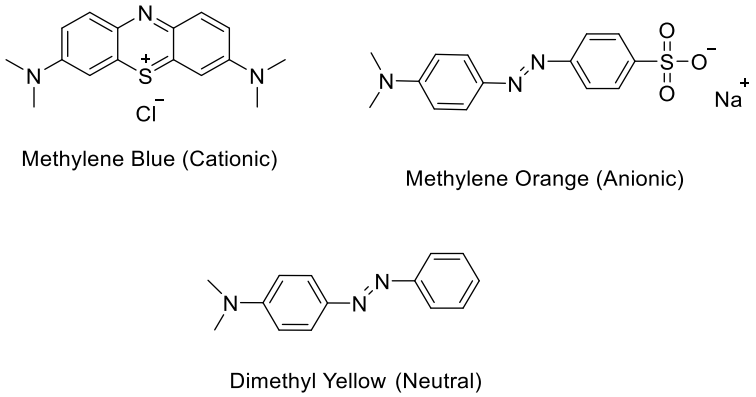

Scheme 4.1: examples of the three main categories of organic dyes.

Many molecules with diverse shapes, dimensions, and properties belong to these classes, so the possibility to easily tune the pore shapes and size and the superficial

functionalities of the MOFs represents the main strength of these materials for specific applications. Both the morphology of the pores and the MOF-adsorbate interaction can play a fundamental role in the adsorption performances of MOFs. Obviously, high porosities and surface areas are usually preferred, but there are reported cases where the positive interactions between the adsorbate molecules and the surface of a MOF lead to high adsorption capacities despite the low surface area available.

As stated in previous pages, one of the objectives of this work is to study the possible uses of the Cu-YBDC MOF as an adsorbent material for dyes. For that purpose, we tested its performances for the adsorption of Methylene Blue (MB). The low porosity and specific surface area of the tested material surely represent a disadvantage when it comes to adsorption efficacy, due to the difficulties that the dye molecules will face when entering the pores. In fact, according to the literature, the MB molecule can be regarded as a rectangular volume of dimensions 17.0 × 6.7 × 3.3 Å,[20] corresponding to a volume of 426.36 $Å^3$ and to an area of 129.2 $Å^2$ (if we discard the thickness and treat the molecule as planar). Considering that the size of the cavities of [Cu(1,3-YBDC)] is only 141 $Å^3$, it is clear that all the adsorption phenomena must take place on the external surface of the MOF. On the other hand, in literature there are already reported cases of MOFs with low surface area and porosity which showed nevertheless high adsorption capacities.[21] The different functional groups present upon the external surface of [Cu(1,3-YBDC)]·$x$$H_2O$ could provide an interesting substrate, due to the number of different adsorption mechanisms that can take place (hydrogen bonds between the dyes and the -NH- orthe C=O group of the carbamate, π-π interactions between the dyes and the aromatic rings, π-πinteractions between the dyes and the propargyl group), so, in our opinion, this idea was worthy the try.[22]

4.3 Result and discussion

4.3.1 Electrochemical applications of [Cu(1,3-YBDC)]·xH_2O

A Glassy Carbon (GC) electrode coated with [Cu(1,3-YBDC)]·xH_2O (hereafter abbreviated **GC/Cu-MOF**) was characterized electrochemically through cyclic voltammetry in different electrolyte solutions. Successively, such modified electrode was employed as a nitrite sensor. Due to the affinity of gold to the alkyne group of the MOF's linker, the GC/Cu-MOF electrode was successively modified through AuNPs incorporation. The electrode named **GC/Cu-MOF/Au** was prepared by making the MOF deposited on the electrode surface to adsorb Au(III) from a $HAuCl_4$ solution and then, after washing the electrode with ethanol, the Au(III) retained by the MOF was reduced to Au(0) through the application of a potential of 0.05 V. The GC/Cu-MOF/Au electrode was also characterized and tested for nitrite detection.

GC/Cu-MOF Characterizations

A SEM analysis was performed on modified SPEs before the electrochemical characterization. Figure 4.1 shows the SEM images of Cu-MOF deposited on a glassy carbon surface in which the lamellar structure of [Cu(1,3-YBDC)]·xH_2O is barely distinguishable (**Figure 4.3**).

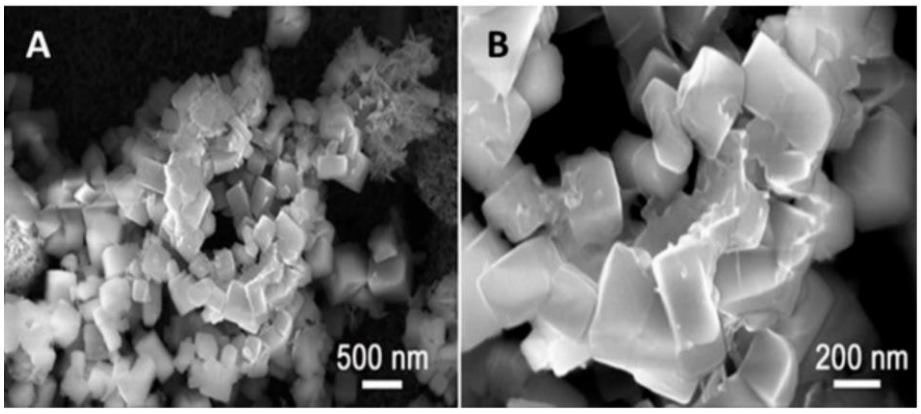

Figure 4.3. SEM images of GC/Cu-YBDC; magnified (**A**) 50 KX and (**B**) 150 KX.

The obtained micrographs showed no changes in the morphology of the deposited Cu-MOF, with the presence of large prismatic crystals with sub-micrometric dimensions.
The elemental mapping shows the uniform presence of copper and oxygen. (**Figure 4.4**)

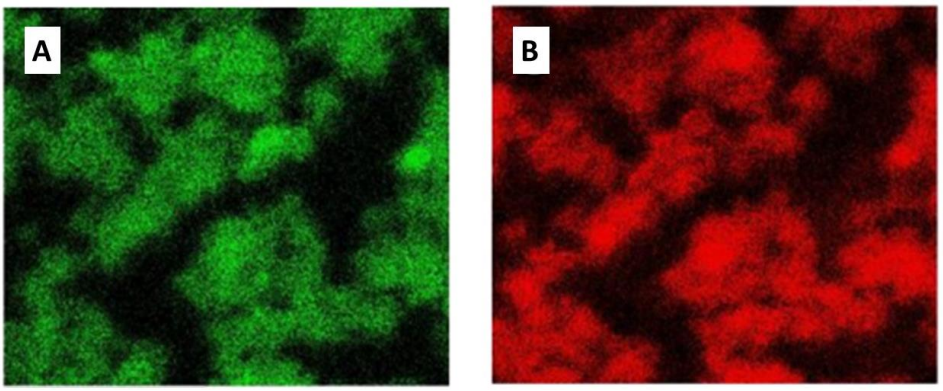

Figure 4.4 elemental mapping of Cu-YBDC deposited on a SPE showing the uniform presence of: O (A) and Cu (B).

Moreover, considering (as shown in the EDX analysis) the homogeneity of the Cu-YBDC suspension used in drop-coating the electrodes, the amount of Cu-YBDC deposited should be 1.25×10^{-2} mg, and considering that from the elemental analysis Cu is the 15.7% of MOF,[23] the amount of copper deposited on the electrodes is 1.96×10^{-3} mg. The overall amount of copper present was determined by means of flame atomic absorption spectroscopy (AAS, Thermo Scientific iCE 3300 AA01124707, Waltham, MA, USA) in an air-acetylene flame ($\lambda = 324.8$ nm; spectral bandwidth = 0.5 nm). The analyses were conducted by comparison with five calibration standards (2.0, 4.0, 6.0, 8.0, 10.0 ppm) prepared by dilution to 25 mL of different amounts of a 100 ppm standard solution prepared by diluting 1 mL of FIXANAL (03372-1EA Fluka, copper atomic spectroscopy standard concentrate 10.00 g/L) in 0.5 M HNO_3 (Normatom®, 67%–69%, d = 1.41 g/cm^3, MW 63.01, VWR Chemicals, Radnor, PA, USA,). The samples were prepared by first heating the solid (5.3 mg) with concentrated nitric acid until complete dissolution and subsequently diluted with HNO_3 0.5 M up to a volume of 100 mL.

Moreover, XRD spectrum of Cu-YBDC deposited on the electrode surface was recorded. Figure 4.5 reports raw diffraction data for GC/Cu-YBDC (in red) and simulated powder diffraction data from the known structure of the Cu-YBDC MOF (in blue).

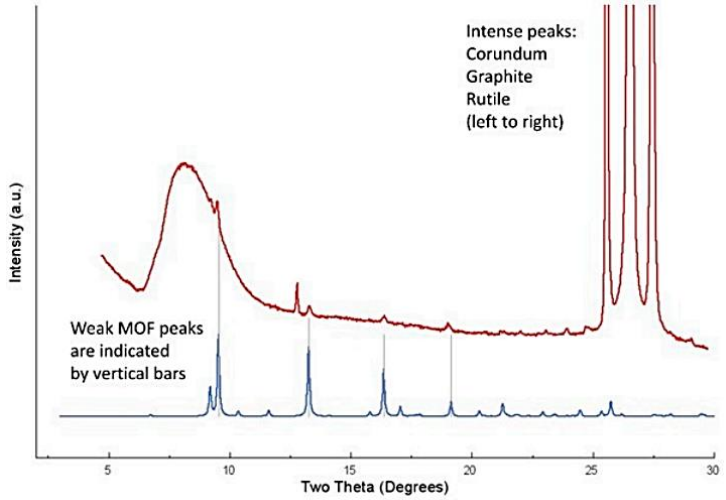

Figure 4.5. Comparison of XRD Cu-YBDC (in blue) and GC/Cu-YBDC spectra (in red).

Vertical bars indicate the angular location of the most intense diffraction peaks of the latter. The large hump in the 7–11◦ 2θ range and the triplet of peaks falling above 25◦ 2θ stem from the sample holder (amorphous plastics and crystalline substrate, respectively).

GC/Cu-MOF electrochemical characterization

The electrochemical behavior of GC/Cu-MOF was preliminary studied in different electrolyte solutions: (i) NaCl 0.1 M; (ii) Tris(hydroxymethyl)aminomethane (TRIS) buffer (pH 7.2) 0.1 M; (iii) PBS buffer (pH 7.2) 0.1 M. The cyclic voltammogram of the GC/Cu MOF electrode in NaCl 0.1 M electrolyte solution is shown in Figure 4.6.

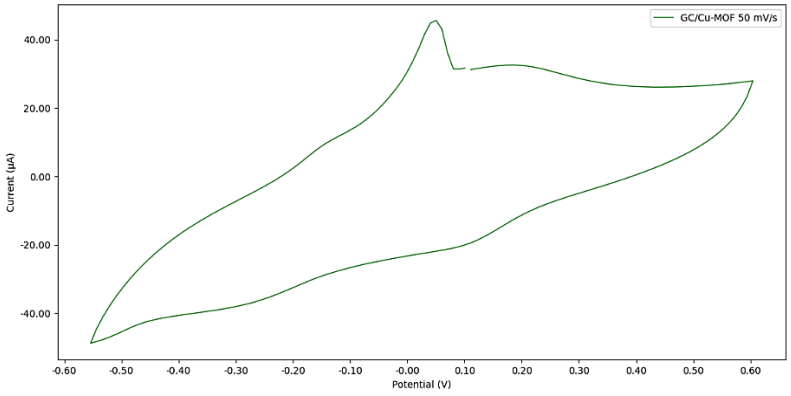

Figure 4.6: CV of GC/Cu-MOF at a scan-rate of 50 mV/s in NaCl 0.1 M electrolyte solution.

A table containing peak potentials is showed below (Table 4.2):

Table 4.2: peaks table for GC/Cu-MOF in NaCl 0.1M electrolyte solution at 50 mV/s.

Potential (V)	Description
Oxidation peaks	
-0.15	Cu(0)-Cu(I)
0.05	Cu(0)-Cu(II), stripping
0.20	Cu(I)-Cu(II)
Reduction peaks	
0.10	Cu(II)-Cu(I)
-0.27	Cu(I)-Cu(0)

In the cathodic part of the voltametric path two peaks at 0.10 and -0.27 V are visible, attributable to the reduction of Cu(II) to Cu(I) and Cu(I) to Cu(0), respectively. The Cu(I) redox peak at 0.10 V is due to the ability of chloride ions to stabilize copper in the +1 oxidation state through complexation. In the anodic part of the voltametric path a sharp oxidation peak at 0.05 V due to the oxidation of Cu(0) is well evident.

A cyclic voltammogram of the GC/Cu-MOF electrode in TRIS buffer 0.1 M (pH 7.2) is shown in Figure 4.7.

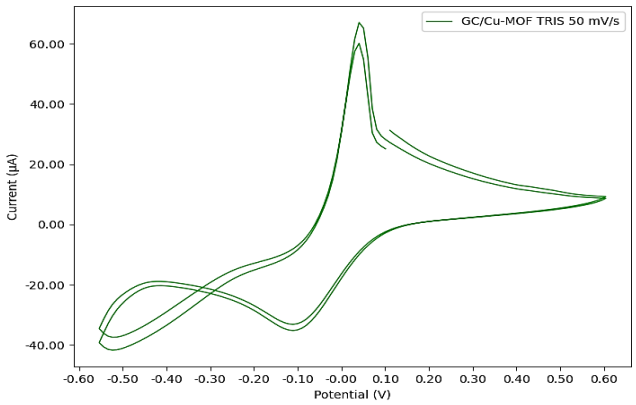

Figure 4.7: CV of GC/Cu-MOF at a scan-rate of 50 mV/s in TRIS buffer 0.1 M (pH 7.2).

Even in this case, the presence of Cl^- ions stabilized the Cu(I) redox peaks at a potential of -0.10 V. In table 4.3 are reported the peak potentials.

Table 4.3: peaks table for GC/Cu-MOF in TRIS buffer 0.1M (pH 7.2) at 50 mV/s.

Potential (V)	Description
Oxidation peaks	
-0.24	Cu(0)-Cu(I)
0.05	Cu(0)-Cu(II), stripping
Reduction peaks	
-0.10	Cu(II)-Cu(I)
-0.52 during anodic scan	Cu(I)-Cu(0)

The main difference between the CVs recorded in NaCl and in TRIS buffer is in the cathodic peak positions. In TRIS buffer, both reduction peaks are shifted toward higher cathodic potentials and this could be explained by the slow diffusion of the counter-ion $TRIS^+$ within the small pores of the MOF during copper reduction.

Nitrite oxidation

Three different sensors for nitrite, realized with three different kinds of glassy carbon systems are studied:

1. glassy carbone electrode (GC);
2. glassy carbone electrode decorated with Cu-MOF (GC/Cu-MOF);
3. glassy carbone electrode with Cu-MOf and AuNPs (GC/Cu-MOF/Au).

The CVs are performed with the aim to obtain a detailed comparison between differents electrode system devices an to understand the electrochemical performance of the Cu-MOF.

1. Nitrite oxidation on a glassy carbon electrode

The performance of the GC electrode towards nitrite oxidation was studied through cyclic voltammetry at a scan-rate of 50 mV/s in a PBS 0.1M (pH 7.2) electrolyte solution. As shown in Figure 4.8, the nitrite oxidation peak reaches a maximum at 0.997 V at a scan-rate of 50 mV/s.

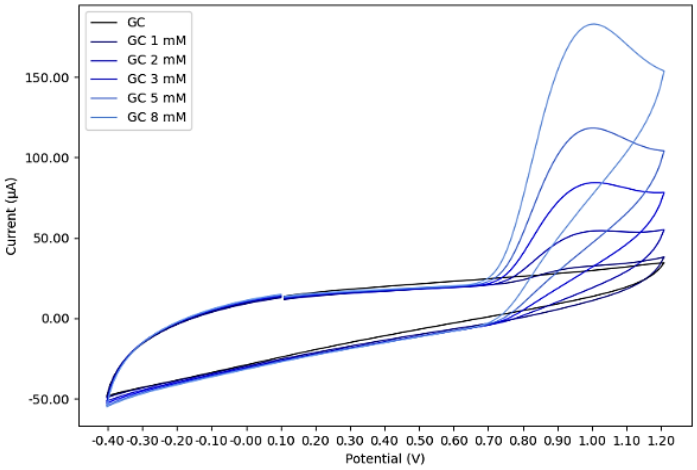

Figure 4.8: CV of GC electrode at different nitrite concentrations, from 0 to 8 mM.

No reduction peak was observed. Kozub et al.[24] reported that the nitrite oxidation is a one-electron reaction that leads to nitrogen dioxide formation, which rapidly disproportionate in water to yield nitrite and nitrate ions. The E-C mechanism (eq. 4.1 and 4.2),[24] with a fast chemical reaction, could explain the absence of a reduction peak in the CVs.

$$E) \quad NO_2^- - e^- \rightleftharpoons NO_2 \tag{4.1}$$

$$C) \quad NO_2 + H_2O \rightarrow 2H^+ + NO_2^- + NO_3^- \tag{4.2}$$

The need for a buffer solution is justified by the release of H^+ ions from the disproportion reaction, as a change of pH during the analysis could affect its reproducibility.

In order to acquire more information on the nitrite oxidation reaction at the GC electrode, CVs at different scan-rate were performed while nitrite 5 mM was present in the electrolyte solution (Figure 4.9).

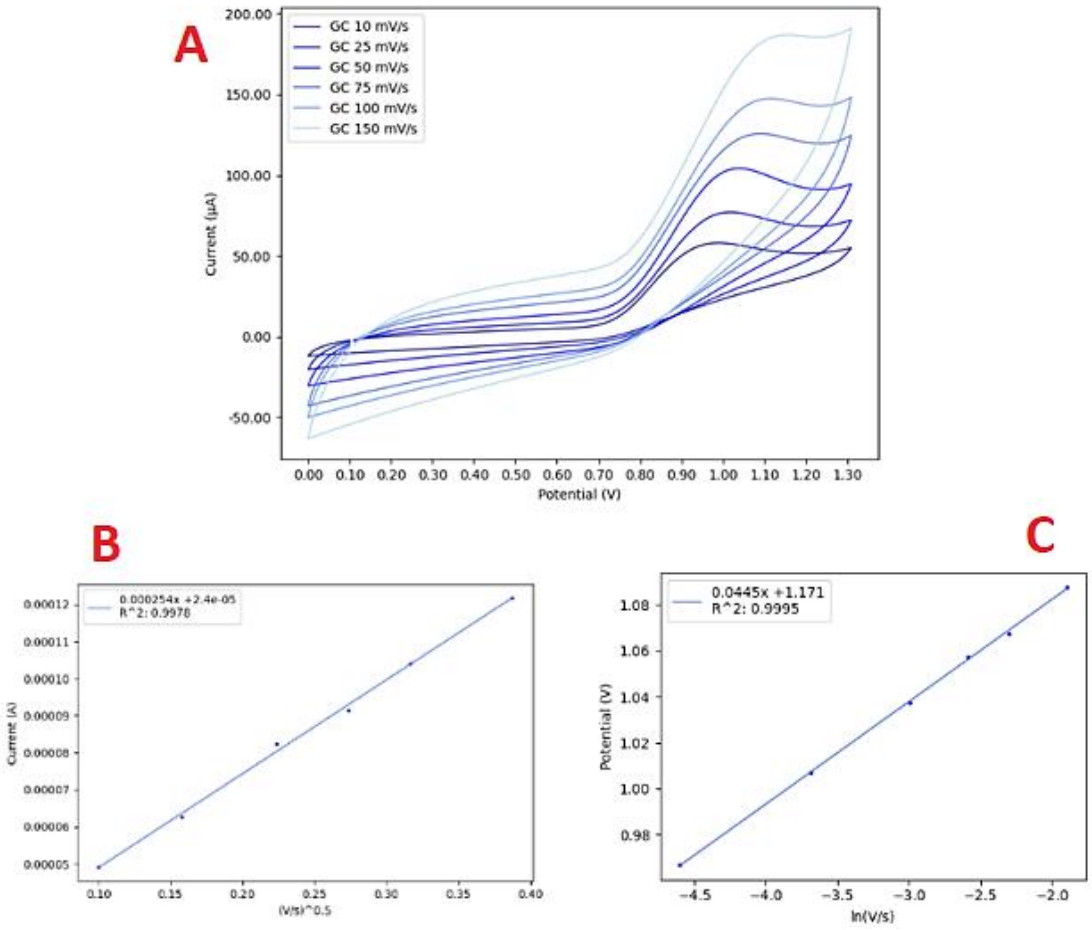

Figure 4.9: (A) CVs at different scan-rates from 10 mV/s to 150 mV/s, nitrite 5 mM, PBS 0.1M (pH 7.2);
(B) correlation between peak current and square root of the scan-rate;
(C) correlation between peak potential and natural logarithm of the scan-rate.

Equations 4.3 and 4.4 describe the effect of the scan rate on peak potential (Epa) and peak current (Ipa) for an irreversible reaction[25]

$$Epa = E0' + \frac{RT}{\beta F}\left[0.780 + ln\left(\frac{\sqrt{Dr}}{k0}\right) + ln\ ln\left(\sqrt{\frac{\beta F}{RT}}\right)\right] + \frac{RT}{2\beta F} ln(v) \quad (4.3)$$

$$Ipa = 0.4958\sqrt{\frac{\beta F}{RT}} FAC_r^* \sqrt{D_r}\ \sqrt{v} \quad (4.4)$$

where E0' is the formal potential of the redox couple, R is the gas constant, T is the temperature, D_r is the diffusion coefficient of the reduced species, C_r^* is the concentration of the reduced species in the bulk of the solution, v is the scan-rate, and A is the area of the electrode.

The peak potential of nitrite oxidation on the GC electrode is a linear function of the natural logarithm of the scan-rate (R^2 = 0.9995, slope = 0.0445 V/ln(V/s), intercept = 1.171

V). For this reason, the reaction appears to be irreversible, meaning that the electron transfer process is the limiting step, being way slower than nitrite diffusion. The peak current shows a linear correlation with the square root of the scan-rate (R^2 = 0.9978, slope = 2.54x10^{-4} $A/\sqrt{V/s}$, intercept = 2.4x10^{-5} A). This means that nitrite ions were freely diffusing species. They were not adsorbed on the GC electrode surface before exchanging electrons.[26,24,27]

2. Nitrite oxidation on GC/Cu-MOF and GC/Cu-MOF/Au

Both GC/Cu-MOF and GC/Cu-MOF/Au electrodes were tested as sensors in PBS 0.1M (pH 7.2) solution, at 50 mV/s in presence of nitrite 5 mM. The CVs paths are reported in Figure 4.10 and compared with those obtained with bare GC electrodes.

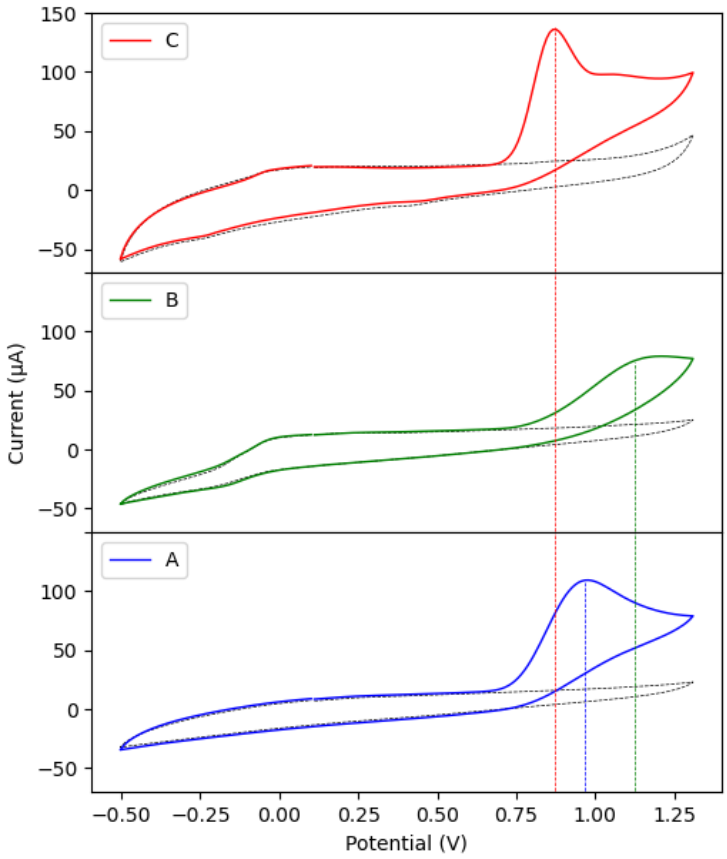

Figure 4.10: CVs at 50 mV/s in 0.1 M PBS (pH 7.2) contains 5 mM nitrite on: C) GC/Cu-MOF/Au; B) GC/Cu-MOF; A) bare GC electrode.

In table 4.4 the nitrite oxidation peak potential is reported for each electrode.

Table 4.4: nitrite oxidation peak potentials.

Electrode	Nitrite oxidation peak potential (V)
GC	0.97
GC/Cu-MOF	1.13
GC/Cu-MOF/Au	0.87

The higher peak potential for nitrite oxidation, observed with GC/Cu-MOF, is probably due to the low conductibility and low pore volume of our MOF. On the contrary, the presence of Au nanoparticles gives a shift of the oxidative potential towards lower value.

As a blank test (Figure 4.11), we compared the CV of a GC electrode modified with Au nanoparticles (GC/Au) following the procedure reported in Section 2.8.2.

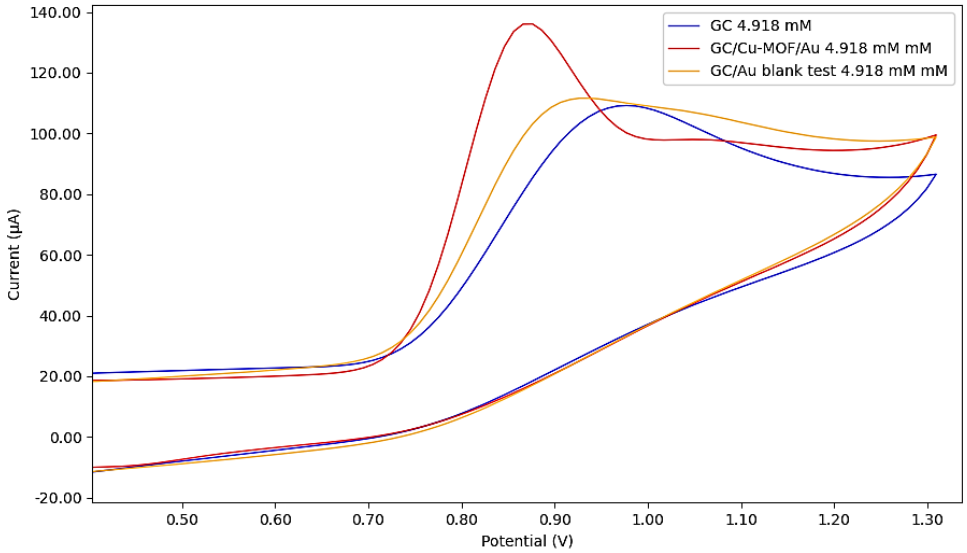

Figure 4.11: 50 mV/s in PBS 0.1M (pH 7.2) in the presence of nitrite 5 mM; (red) GC/Cu-MOF/Au; bare GC (blue); glassy carbon electrode modified for the blank test (orange).

In respect with GC, the GC/Au electrode shows a lower nitrite oxidation peak. However, only when GC/Cu-MOF/Au was used, an increase in the current and a significant shift in the potential became evident. This suggest a synergic effect between the Cu-MOF and the AuNPs.

CVs at different scan-rates were performed in PBS buffer electrolyte solution with 5 mM nitrite concentration. The results are reported in Figure 4.12.

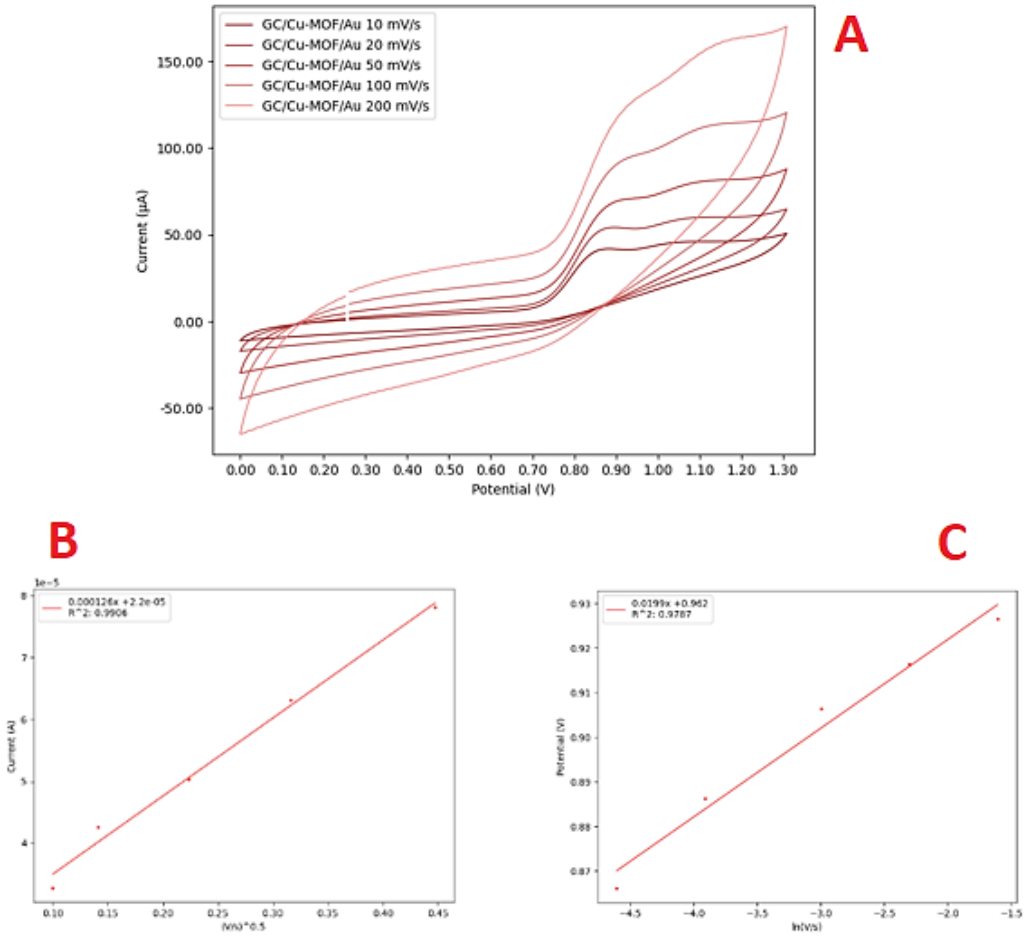

Figure 4.12 (A) CVs of GC/Cu-MOF/Au electrode at different scan-rates from 10 to 200 mV/s in PBS 0.1M (pH 7.2) with nitrite 5mM; (B) correlation between peak current and square root of the scan-rate; (C) correlation between peak potential and natural logarithm of the scan-rate.

The peak current for the oxidation of nitrite shows a linear correlation with the square root of the scan rate (R^2 = 0.9906, slope = 0.000126 A/$\sqrt{V/s}$, intercept = 2.2x10^{-5} A), confirming a diffusive process. The peak potential for nitrite oxidation slightly shifts toward higher oxidation potentials with the increase of the scan rate. The correlation of the peak potential is linear with the natural logarithm of the scan rate (R^2 = 0.9787, slope = 0.0191 V/ln(V/s), intercept = 0.962 V), meaning that the electron transfer step is still the slowest step. The shift of the oxidation peak towards lower anodic potentials found for the GC/Cu-MOF/Au electrode can be attributed to the acceleration of the charge transfer caused by the AuNPs.

Chronoamperometric tests were performed with different nitrite addition in PBS 0.1M (pH 7.2), at an applied potential of 0.9 V under stirring on GC, GC/Cu-MOF and GC/Cu-MOF/Au electrodes. The results are reported in Figures 4.13 and 4.14 and Table 4.5.

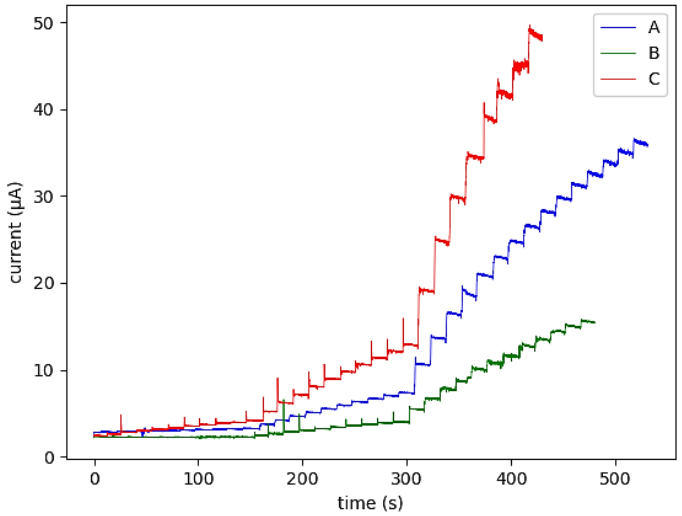

Figure 4.13. Chronoamperometric response of A) GC (blue), B) GC/Cu-MOF (green), C) GC/Cu-MOF/Au (red).

Table 4.5: Slopes, intercepts, R^2, linearity ranges and LODs of the different electrodes.

Electrode	Slope ($\mu A\ mM^{-1}\ cm^{-2}$)	Intercept (µA)	R^2	Linearity range (µM)	LOD (µM)
GC	(2) 59.59 (3) 44.12	(2) 2.50 (3) 4.73	(2) 0.9975 (3) 0.9916	(2) 160-1200 (3) 1200-8000	36
GC/Cu-MOF	(2) 24.92 (3) 20.18	(2) 1.98 (3) 2.66	(2) 0.9929 (3) 0.9932	(2) 160-1200 (3) 1200-8000	67
GC/Cu-MOF/Au	(1) 129.58 (2) 126.46 (3) 96.63	(1) 2.42 (2) 2.56 (3) 5.49	(1) 0.9986 (2) 0.9953 (3) 0.9955	(1) 20-160 (2) 160-1200 (3) 1200-5000	5

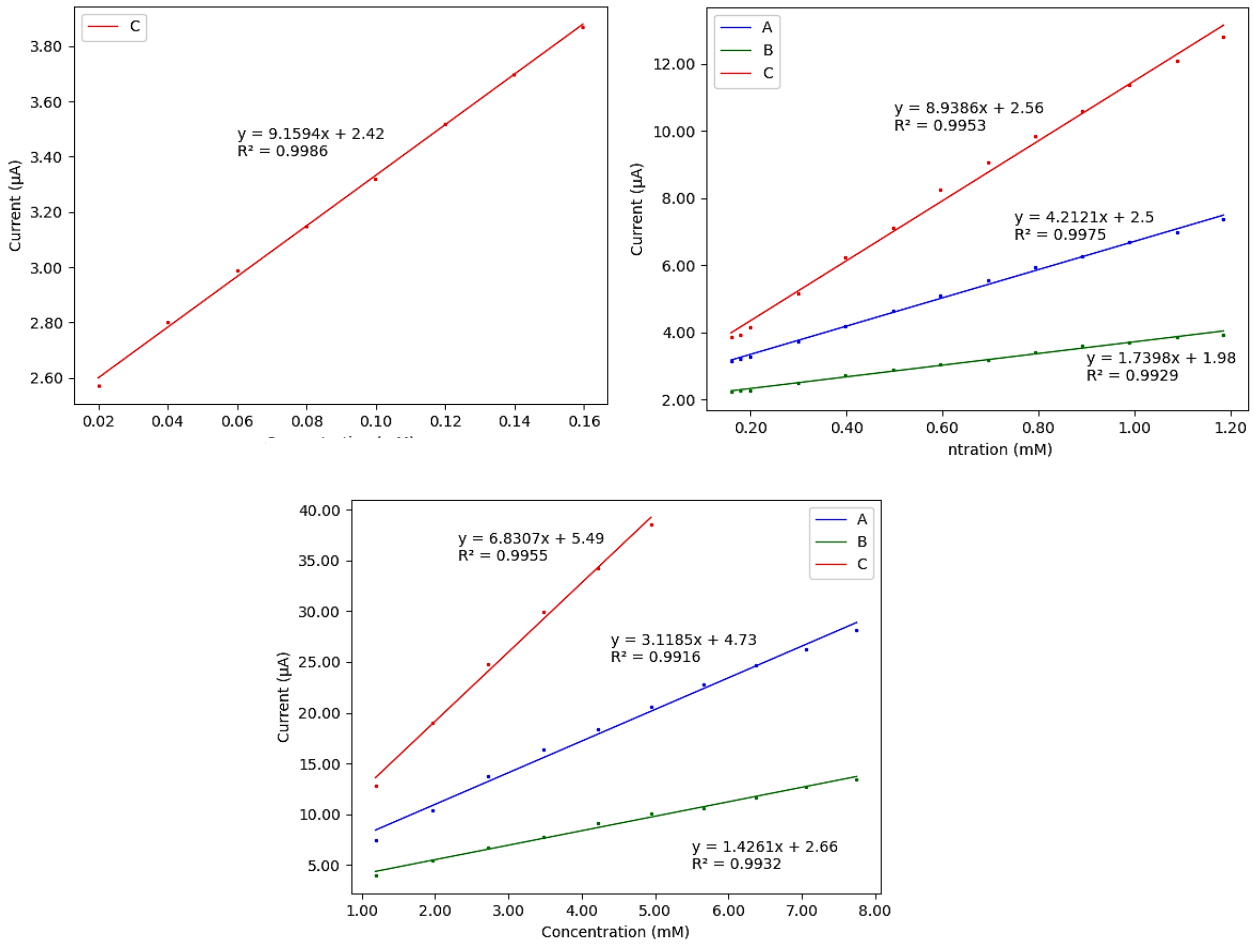

Figure 4.14: Calibration curves: GC/Cu-MOF/Au (red, C); GC/Cu-MOF (green, B); bare GC (blue, A).

**(1) linear regression performed in the 20-160 μM concentration range; (2) linear regression performed in the 160-1200 μM concentration range; (3) linear regression performed for concentrations higher than 1200 μM*

The results agree with the ones observed with cyclic voltammetry. The sensitivity of the GC/Cu-MOF/Au electrode toward nitrite is higher (more than double) than both the GC and GC/Cu-MOF electrode. Moreover, a lower LOD (calculated as LOD = 3.3σ where σ is the standard deviation of the intercept)[28] is obtained with GC/Cu-MOF/Au electrode. The LOD value around one order of magnitude higher than those reported in literature for similar modified electrodes could be due to the lower porosity of this MOF.

4.3.2 EIS Characterization

To better understand the electrochemical behaviour of the electrodes, the impedance spectra of the GC, GC/Cu-MOF, GC/Cu-MOF/Au electrodes were acquired from 10^5 to 1 Hz at an equilibrium potential of 0.22 V. The potential amplitude applied to the electrodes was 10 mV. The electrolytic solution utilized was KCl 0.1 M containing $K_4Fe(CN)_6$ 2 mM. The choice of $K_4Fe(CN)_6$ as an electroactive species was based on its well-known reversible behaviour. The results and equivalent circuit are reported in Figure 4.15 and 4.16, respectively.

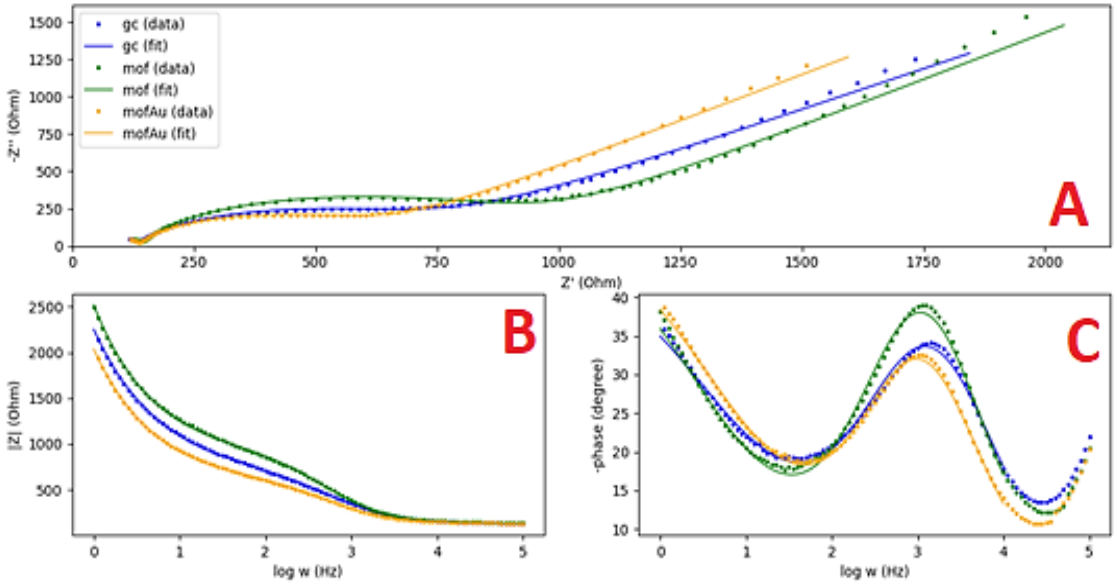

Figure 4.15. (A) Nysquist plot for the GC (blue), GC/Cu-MOF (green), GC/Cu-MOF/Au (orange) electrodes: dotted line = impedance data, continuous line = fitted model; (B) impedance module against the base 10 logarithm of the frequency; (C) phase plot.

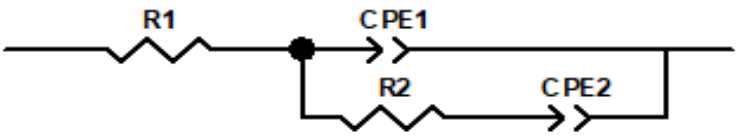

Figure 4.16. equivalent circuit used to fit impedance data.

Table 4.6: fitting parameters for the equivalent circuit.

	GC	GC/Cu-MOF	GC/Cu-MOF/Au
R1 (Ω)	123.5	137.3	131.1
CPE1 T(s^P/Ω)	3.4668 x 10^{-6}	2.0871 x 10^{-6}	3.2246 x 10^{-6}
CPE1 P	0.77744	0.82918	0.81755
R2 (Ω)	625	800.1	502
CPE2 T(s^P/Ω)	2.1531 x 10^{-4}	1.8424 x 10^{-4}	2.148 x 10^{-4}
CPE2 P	0.53352	0.57721	0.57099

The equation 4.5 shows the impedance for a constant phase element (CPE).

$$Z = \frac{1}{T(iw)^P} \quad (4.5)$$

Where i = $\sqrt{-1}$, w = frequency of the AC current (s^{-1}), T (s^P/Ω) and P are parameters. The resistance R1 is attributable to the resistance of the electrolyte solution. The resistance R2 is the resistance to the electron transfer process. The constant phase element CPE1 was used instead of a pure capacitor to take into account the deviation from an ideal double layer capacitor. This deviation is caused by the roughness of the surface of the electrodes.[29] The Chi-squared values for the fits are 2.3 10^{-4}, 6.6 10^{-4}, and 2.3 10^{-4} for the GC, GC/Cu-MOF and GC/Cu-MOF/Au electrodes respectively, indicating good fitting procedures. As expected from the electrochemical results, the resistance to the electron transfer process (R2) follows the order:

GC/Cu-MOF > GC > GC/Cu-MOF/Au

The MOF acts as a semi-conductor, lowering the rate of electron transfer, while the incorporation of AuNPs on the electrode makes the charge transfer faster. This finding agrees with what the CVs and chronoamperometries previously showed.

4.3.2 Reproducibility studies

Reproducibility on GC/Cu-MOF electrode preparation

Assuming the homogeneity of the [Cu(1,3-YBDC)]·xH_2O suspension used for drop-coating the electrodes, the amount of [Cu(1,3-YBDC)]·xH_2O deposited should be 1.25×10^{-2} mg, so that the theoretical amount of copper deposited is 1.96×10^{-3} mg (considering copper being 15.70% of the MOF weight). In order to investigate the reproducibility of the electrode drop-casting, four cyclic voltammetries of the GC/Cu-MOF electrode were performed in TRIS buffer 0.1 M (pH 7.2). This electrolytic solution was chosen because of the stabilizing effect of chloride ions on Cu (I), so that the amount of electrons exchanged in the first reduction peak at 0.08 V was known and from the area of this peak the determination of the amount of reduced Cu was possible through equation 4.6:

$$m_{Cu} = \frac{\text{reduction peak area (C)}}{\text{n(mol) F(C/mol)}} \, AW_{Cu} \, (g/mol) \qquad (4.6)$$

where the reduction peak area is the area of the peak at 0.08 V in the cyclic voltammetry (see Figure 4.17), n is the number of exchanged electrons which is equal to one, F is the Faraday constant, and AW_{Cu} is the atomic weight of copper.

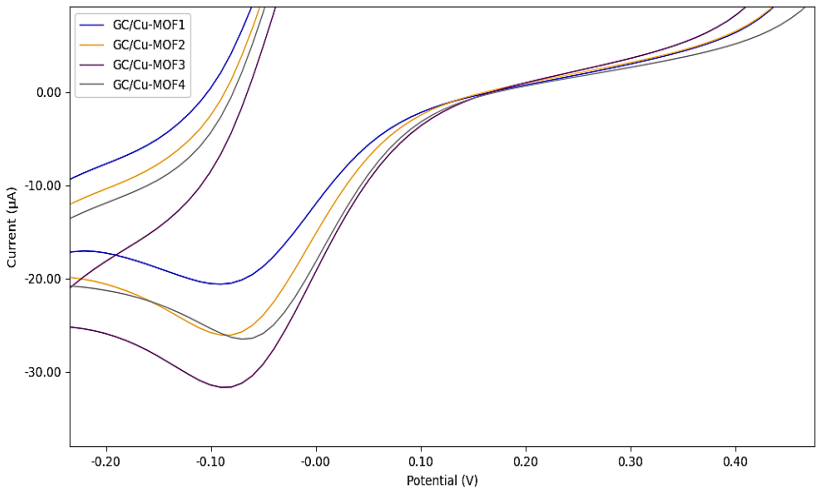

Figure 4.17: Reduction peak at 0.08V in the CV of the GC/Cu-MOF electrode in TRIS 0.1M (pH 7.2).

The mean area of the peak is 5.02×10^{-2} C so the amount of reduced Cu(II) is 3.31×10^{-5} mg, with an RSD% of 23.27. The discrepancy between the amount of reduced copper and the theoretical amount of copper deposited could derive from the fact that only the copper atoms very close to the glassy carbon surface are reduced. The high value of RSD% obtained could be attributed to:

- the non-homogeneity of the [Cu(1,3-YBDC)]·xH_2O suspension used to modify the electrode;
- the non-homogeneity of the distribution of [Cu(1,3-YBDC)]·xH_2O particles on the glassy carbon surface, as evidenced by the SEM characterizations of the electrodes.

Reproducibility on GC/Cu-MOF/Au electrode preparation

The nitrite oxidation signal was used for investigation by cyclic voltammetry in PBS 0.1M (pH 7.2) of the reproducibility of GC/Cu-MOF/Au electrode preparation. Five different GC/Cu-MOF/Au electrodes were tested in the presence of nitrite 5 mM and the nitrite oxidation peak currents were compared (see Figure 4.18).

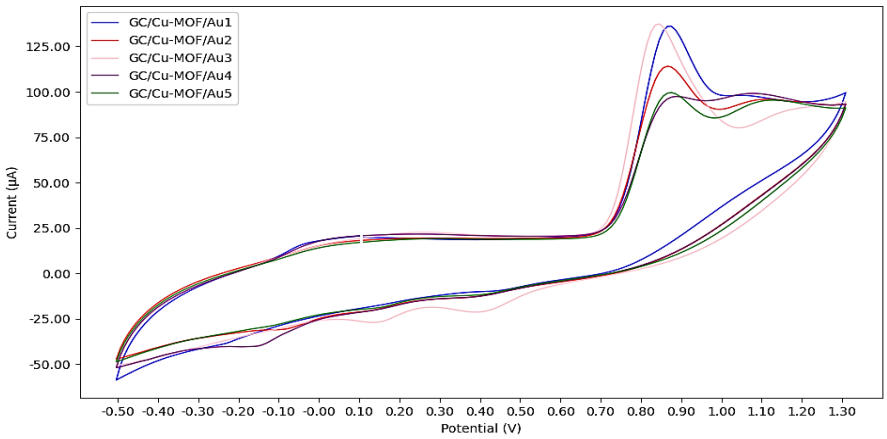

Figure 4.18: cyclic voltammetry of five different GC/Cu-MOF/Au electrodes in PBS 0.1M (pH 7.2) in the presence of nitrite 5 mM.

The average peak current for nitrite oxidation is 1.18×10^{-4} A with an RSD% value of 14.2%. The low reproducibility of the peak current for the oxidation of nitrite could be explained by the low reproducibility of the amount of gold electrodeposited on the electrode. As reported in the literature (2), the reproducibility of the modifications through the drop-coating technique is very low due to the non-homogeneity of the deposition itself. The AuNPs electrodeposition procedure can only further decrease the reproducibility of the electrode preparation.

4.3.3 Cu-YBDC as an adsorbent for Methylene Blue

To evaluate the dyes adsorption performances of MOFs, it is useful to perform kinetic studies, where the quantity of dye removed by the MOF is measured at different times, and then the data are elaborated to find the best-fitting kinetic model. The typical experimental procedure for kinetic studies consists in immersing a previously weighted quantity of adsorbent material in a sample of aqueous solution with a known concentration of dye and putting the mixture under stirring. At given periods of time, small samples of the mixture are taken out, centrifuged to separate the solid material from the solution, and finally the concentration of the solution is measured via UV-Vis spectroscopy measurements.[30,31]

The quantity of dye removed is commonly expressed with the parameter q, also known as *adsorption capacity*. It is often indicated as q_t when it is calculated at a precise time t, or q_e when it is calculated at equilibrium.[32] The adsorption capacity at equilibrium q_e is calculated with the following equation:

$$q_e = (C_0 - C_e)\frac{V}{m} \qquad (4.7)$$

where C_0 and Ce represent the dye concentration measured at t = 0 and at equilibrium respectively, V is the volume of the initial solution and m is the mass of adsorbent material used. Clearly, q_t is calculated with the same formula, using the concentration at t = t Ct instead of Ce. The variation of q over time can have different trends, depending on the adsorption mechanisms involved.

The adsorption of MB over Cu-YBDC was studied with a series of experiments described in the experimental section. All the experiments showed a similar trend in the variation of the absorbance (and therefore the concentration) over time, exemplified by the following graph (Figure 4.19), reporting an experiment with 50 mg of Cu-YBDC in a starting solution of MB 40 ppm.

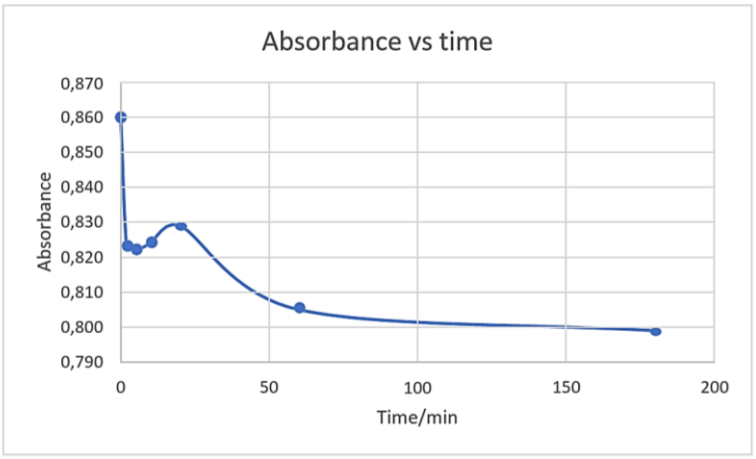

Figure 4.19: Absorbance vs time graph of a 40 ppm Methylene Blue solution put in contact with 50 mg of Cu-MOF.

In the graph tt is clearly visible that in the first minutes a fast decreasing in the absorbance occurs, followed by a small resurgence usually around 10 or 20 minutes. Finally, the absorbance settles down to a plateau, that fluctuates around the 90% of the starting value.

Usually, for short contact times the dye removal occurs fast due to the availability of numerous unoccupied active sites on the surface of the MOF, resulting in a rapid growth of q_t values. Commonly, the growth of q_t slows down significantly after a while, due to the increasingsaturation of the active sites.[45] Obviously, the starting availability of active sites is related to the load of adsorbent used. The starting adsorption capacity is also connected with the initial concentration of dye in the solution. Increasing the starting dye concentration results in an increasing of the initial value of q_t due to the higher solute concentration gradient,[46] until the point in which the adsorption capacity assumes a stable value, meaning that the adsorbent has reached its saturation point. From this point, any further increase in the starting dye concentration does not modify the adsorption capacity. The minimum starting concentration needed to instantly get to the saturation point is a parameter that can be used to compare different adsorbent materials. With the same starting load, the material which requires a higher starting concentration to get to the saturation point is considered the best adsorbent (more active sites available).[45]

The graphs in Figure 4.20 show the variation of q_t over time for the five experiments,obtained with equation (4.7).

The trend seems to be the same seen for the Absorbance/Time graphs, with a fast adsorption in the first minutes, a small drop around the 10-20 minutes mark, and then a second increasing, which sometimes ends in a plateau (Fig. 4.19, panels A and C), and sometimes followsmore irregular routes. Such unexpected results can be due to several reasons that are listed below.

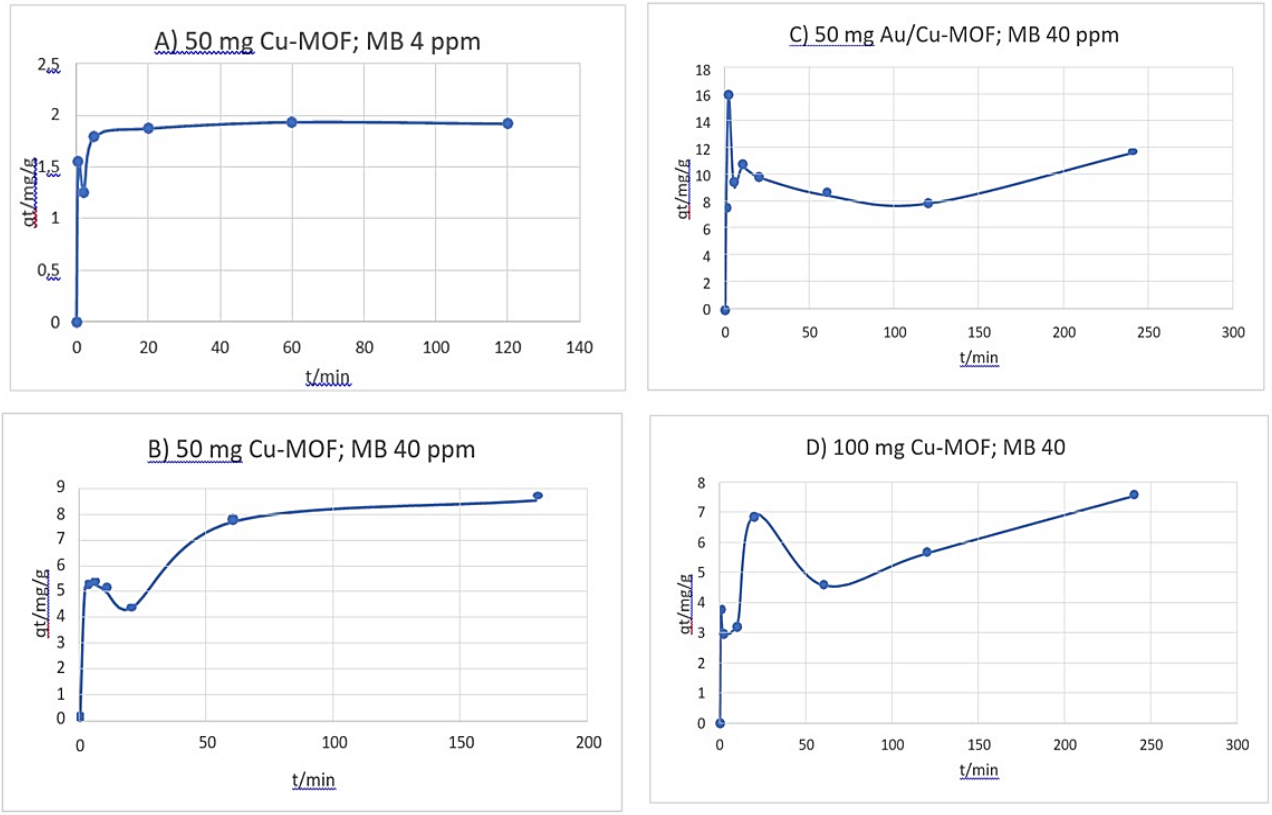

Figure 4.20: Trends of qt over time for the adsorption of MB under different conditions

The first possibility is that the methodology employed for the experiments contains some biases. The use of equation (1) to calculate the values of q_t could be the first issue. Seeing that the adsorption capacity of the material is low, the value of (C_0-C_t) represents a small percentage of the initial C_0 value (especially for short time intervals), therefore even if the uncertainties on the measures of C_t and C_0 is small, the propagation of the uncertainties makes the value of (C_0-C_t) susceptible of greater errors. This hypothesis could explain the peculiar data obtained, especially the drop in the adsorption capacity observed in the first 10-20 minutes.To verify this hypothesis, each experiment should be repeated numerous times, in order to ascertain if any significant changes are present in the average curve. Other biases in the methodology could reside in the sample collection step. Even if we overlook the fact that it is quite difficult to collect samples with a homogeneous composition, due to the

heterogeneity of the system, there is still the need to centrifugate the samples before analyzing them, which requires a non-negligible time consumption. Due to the fast nature of the phenomena involved in the adsorption process, this time lapse could alter the results of the measurements, which could be no more representative of the actual characteristics of the system at the time of the extraction of the sample. This issue could be avoided by employing a different set-up for the experiment, which should allow to measure the absorbance of the solution *in situ*, for example by using an optical fibre spectrometer.

Another way to avoid the centrifugation step would be to separate the MOF from the solution through filtration. This method would be undeniably faster, but the drawback is that most of the commonly available filters tend to adsorb high quantities of MB, which leads to significant alteration of the measured absorbance values. Different recovery tests were performed with diverse types of filters (common filter paper, cellulose acetate filters with 0.45μm pore size, polyamides filters with 0.45 μm pore size, polypropylene filters with 0.45 μm pore size, PES filters with 0.45 μm pore size), but all of them retained high quantities of MB (from the 15% to the 78% of the starting concentration) (an example of a recovery test is reported in Figure 4.21). Should we find a different filter with more suitable properties, it could bea valid substitute for centrifugation. In alternative, the possibility to saturate the filters with MB before the filtering of the samples, in order to eliminate the recovery could be taken into account.

Figure 4.21: A 4 ppm solution of MB (cuvette on the left) was filtered with (from left to right): PES filter (green), Nylon (polyamide) filter (blue), and Polypropylene filter (white). The recovery values are 78%, 14%, and 55%, respectively.

Finally, the tests should be repeated with different stirring speeds, to verify if this parameter influences the adsorption performance.

Should these experiments confirm that the trend observed is representative of the adsorption mechanism (second scenario), we have to explain the peculiar shape of the graphs. The most unsettling aspect is the drop in the adsorption capacity that occurs after the first 10- 20 minutes, and the following increasing that takes place after, that seems to indicate the presence of two or more subsequential adsorption phenomena. Considering that all the adsorption phenomena must take place on the external surface of the MOF, we can hypothesise the following sequence of events:

1. in the first minutes, MB is adsorbed on the active sites of the external surface, and thesystem rapidly gets to the equilibrium;
2. the adsorption causes some kind of modification in the nature of the active sites, therefore changing the equilibrium criteria and causing the temporary expulsion of part of the adsorbed MB;
3. the new active sites begin to adsorb MB with different mechanisms and/or kinetics. In this hypothetical model, the uncommon shape of the graphs could be described as the combination of two or more curves, corresponding to the number of different adsorptionmechanisms that take place. The changes in the equilibrium criteria that ideally happen during the switching from an adsorption mechanism to another, eventually causing the expulsion of part of the adsorbed MB, could explain the decreasing in the adsorption capacity that happens after 10-20 minutes.

To verify the validity of this model, the key point is to characterize the surface of the materials after the various steps of the adsorption process (after the 10-20 minutes mark and afterthe final equilibrium is reached) and check if there is any difference between them and the surface of the material before the adsorption. Considering the complexity of the surface of the MOF, it is not unlikely to imagine that the adsorption of MB could cause some structural changes on it. Different hypothesizes have been proposed about the nature of those modifications, among which there are the conformational rearrangement of the propargyl-carbamate chain and a redox reaction between the carbamate group and the molecules of Methylene Blue.

4.3.4 Comparison with literature

Due to the uncertainties concerning the experimental data, it is pointless to try any kind of curve-fitting with the kinetic models seen in chapter 1.5.7, therefore the only possible comparison with the literature data is the experimental adsorption capacity at equilibrium ($q_{e,Exp}$). In fact, the values of $q_{e,Exp}$ are the most reliable data, because they are the ones which are less touched by the possible methodological biases. In conditions of equilibrium, the difference between C_0 and C_t is larger, so the statistical error induced by the propagation of the uncertainties is less relevant compared to the measures taken at shorter time intervals. Also, in conditions of equilibrium the time lapse between the collection of the sample and the analysis should not significantly alter the results, because the adsorption process in the sample should not advance further compared to the bulk solution. In Table 4.7 we report the values of $q_{e,Exp}$obtained for the five experiments.

Table 4.7: Values of $q_{e,Exp}$ obtained for the adsorption of MB over Cu-[YBDC] under different conditions.

Experiment	**$q_{e,Exp}$/mg g^{-1}**
Cu-MOF (mg)/MB solution ppm	
A) 50/4	1.919
B) 50/20	6.109
C) 50/40	8.560
D) 50Au/Cu-MOF/40	11.759
E) 100/40	7.538

The performances of [Cu(1,3-YBDC)]·xH$_2$O in the adsorption of MB are quite low, compared to the examples from the literature. The best results in terms of $q_{e,Exp}$ were obtained in experiment C, where $q_{e,Exp}$ = 8.560 mg/g. This value is surpassed by almost every MOF considered from our analytical bibliography research in except for Zn-MOF.[33] The $q_{e,Exp}$ increases a bit with the encapsulation of AuNPs (Experiment D). In this case we obtained $q_{e,Exp}$ = 11.759 mg/g, surpassing also another MOF for MB adsorption, ZJU-71.[34] This value is still not exceptional, considering that most of the otherMOFs in the list possess $q_{e,Exp}$ values

of two or three orders of magnitude higher. Those results are coherent with the starting observation that the pores of the material cannot participate in the adsorption process. Apparently, the functionalities that characterize the external surface of the MOF compensate only partially the lack of availability of the cavities of the material. Nevertheless, considering the problematics highlighted in the previous paragraph, further investigation is necessary.

4.4. Conclusions and Future work

The main results for the applications in water remediation of the new Cu-MOF described in this Chapter are summarized below.

- ✓ The electrochemical properties and nitrite sensing performance of [Cu(1,3-YBDC)]·xH_2O were tested through the modification of a glassy carbon electrode by drop-casting a MOF suspension directly onto the electrode (Figure 4.22).

Figure 4.22. GC/Cu-MOF electrode.

Due to the low surface area and pore volume of the Cu-MOF, the modified electrode showed a higher peak potential and a lower peak current for the nitrite oxidation reaction than the bare glassy carbon electrode. Upon incorporation of AuNPs within the MOF through electrodeposition, the nitrite sensing performance of the modified electrode improved beyond that of the glassy carbon electrode. Cyclic voltammetry and EIS characterization of the electrodes confirmed the semiconductor behavior of the MOF and the ability of AuNPs to compensate for that by increasing the charge transfer rate. However, due to the drop-casting technique employed in the electrode modification, they showed poor reproducibility in terms of nitrite sensing performance.

- ✓ [Cu(1,3-YBDC)]·xH_2O was also tested as an adsorbent material for the adsorption of Methylene Blue (MB) under different conditions. The preliminary data suggest that the adsorption performances of the MOF are limited, most likely due to the low porosity and surface area of the material, but they also highlight numerous potential issues related to the experimental procedure.

Based on the results summarized above, the future work will focus on the following issues:

- improvement of the MOF-modified electrodes reproducibility by means of new modification techniques involving the in-situ growth of MOFs onto the electrode surface.
- to test the new material for possible applications, including the ones studied for Cu-(1,3-YBDC)]·*x*H2O (support of AuNPs and adsorption of MB);
- to improve the experimental procedure for the study of the adsorption of MB with Cu-(1,3-YBDC)]·*x*H2O.

4.5 Experimental Section

4.5.1 Materials

All reagents and solvents were purchased from commercial vendors and used as received; ultrapure water purified with the Milli-Q plus system (Millipore Co, resistivity over 18 MΩ cm) was used in all cases. The reactions were monitored by thin-layer chromatography (TLC) on highly purified Silica on TLC-PET foils (with fluorescent indicator 254 nm, Fluka). The chemicals 2-bromoethylamine hydrobromide, propargyl chloroformate, dimethyl 5-hydroxyisophthalate, tetrahydrofuran (THF), ethyl acetate, petroleum ether, diethyl ether, butanone, ethanol (EtOH), dichloromethane, deuterated chloroform ($CDCl_3$), sulphuric acid (H_2SO_4, 98%), hydrochloric acid (HCl, 37 wt%), nitric acid (HNO_3, 65 wt%), $NaHCO_3$, magnesium sulphate, and sodium hydroxide (NaOH, 50 wt%) were purchased from Sigma-Aldrich (analytical reagent grade). $HAuCl_4$ was synthetized by dissolving a gold wire (BASF, 99.9999%, 1.4 mm diameter) in hot aqua regia.[35]

4.5.2 Electrochemical cell setup

The electrochemical cell is composed by three electrodes: a glassy carbon (GC) working electrode (modified or not-modified), a platinum wire counter electrode, and a saturated calomel electrode (SCE) as the reference electrode. The electrolyte solutions were purged with N_2 for 10 min to eliminate the dissolved O_2.

SEM images of the modified electrodes were acquired using screen-printed electrodes (SPE) C110, purchased from Metrohm, composed by an Ag/AgCl reference electrode, a platinum counter electrode and a glassy carbon working electrode.

The electrolyte solutions employed in the electrochemical experiments were tris(hydroxymethyl)aminomethane (TRIS) buffer 0.1 M (pH 7.2), phosphate buffer (PBS) 0.1 M (pH 7.2) and NaCl 0.1 M. TRIS buffer 1.0 M (pH 7.2) was purchased from SIGMA ALDRICH and diluted with distilled water, while PBS buffer was made solubilizing $NaH_2PO_4 \cdot H_2O$ (7,159 g) and Na_2HPO_4 (6.839 g), both purchased from Merck Chemicals, in distilled water (1 L) adjusting the pH with a NaOH solution.

4.5.3 Electrodes modification

GC/Cu-MOF

[Cu(1,3-YBDC)]·xH_2O (10 mg) was dispersed in 8 mL of EtOH and sonicated for 10 min; 10 μL of the suspension were deposited over the GC surface. Then, the electrode was dried at 70 °C for 10 minutes.

GC/Cu-MOF/Au

The GC/Cu-MOF electrode was placed inside an EtOH solution containing $HAuCl_4$ 5 mM for 10 min. The electrode was washed with ethanol to eliminate the excess of $HAuCl_4$ from the GC or GC/Cu-MOF surface. Successively, the electrode was placed inside a PBS 0.1 M (pH 7.2) electrolytic solution. After drying the electrode at 70 °C for 10 min, the electro-deposition was carried at 0.05 V for 600 s to selectively reduce Au(III) to Au(0).

4.5.4 Adsorption kinetics of Methylene Blue (MB) over [Cu(1,3-YBDC)]·xH_2O

All the experiments were carried by following the same general set-up:

- 150 mL of a standard solution of MB are put in a flask under magnetic stirring;
- a weighted quantity of the MOF is added to the solution; at the same time, a chronometer is started;
- at fixed time intervals, a 4 mL sample of the suspension is taken, and put under centrifugation at 6000 rpm for 5 min, to separate the MOF from the solution;
- the supernatant is taken, and its absorbance is measured at the UV-Vis spectrophotometer (scan range: 800-320 nm, absorbance peak for MB at 664 nm); in some cases, if the predicted concentration of the sample is too high (outside the interval of linearity for the Absorbance/Concentration relationship), a 1000 μL sample is taken with a micropipette, put in a 10 mL matrass and make up to mark (1:10 dilution).

Most of the experiments were carried by using 50 mg of [Cu(1,3-YBDC)]·xH_2O and varying the initial concentration of MB in the standard solution (4 ppm, 20 ppm and 40 ppm). One additional experiment was carried out by adding 100 mg of [Cu(1,3-YBDC)]·xH_2O to a 40 ppm solution of MB. Another experiment was performed by adding 50 mg of [Cu(1,3-YBDC)]·xH_2O/Au (0.85% of Au, measured with AAS, see chapter 2.6) to a 40 ppm solution of MB, to see if the presence of gold nanoparticles on the adsorbent material could influence

the adsorption. All the experiments were performed at room temperature and pressure. The conditions employed in each experiment are reported in table 4.8.

Table 4.8: Conditions employed for the experimental determination of the adsorption kinetics of MB over [Cu(1,3-YBDC)]·xH_2O.

	MOF type	**MOF quantity**	**MB starting concentration**
A)	[Cu(1,3-YBDC)]·xH_2O	50 mg	4 ppm
B)	[Cu(1,3-YBDC)]·xH_2O	50 mg	20 ppm
C)	[Cu(1,3-YBDC)]·xH_2O	50 mg	40 ppm
D)	[Cu(1,3-YBDC)]·xH_2O/Au	50 mg	40 ppm
E)	[Cu(1,3-YBDC)]·xH_2O	100 mg	40 ppm

All the experiments were performed at room temperature and atmospheric pressure, under constant magnetic stirring. The volume of the starting MB solution was 150 mL.

References

(1) Cassani, M. C.; Castagnoli, R.; Gambassi, F.; Nanni, D.; Ragazzini, I.; Masciocchi, N.; Boanini, E.; Ballarin, B. A Cu(II)-MOF Based on a Propargyl Carbamate-Functionalized Isophthalate Ligand as Nitrite Electrochemical Sensor. *Sensors* **2021**, *21* (14), 4922. https://doi.org/10.3390/s21144922.

(2) Xu, Y.; Liu, T.; Zhang, Y.; Ge, F.; Steel, R. M.; Sun, L. Advances in Technologies for Pharmaceuticals and Personal Care Products Removal. *J. Mater. Chem. A* **2017**, *5* (24), 12001–12014. https://doi.org/10.1039/C7TA03698A.

(3) Richmond, E. K.; Grace, M. R.; Kelly, J. J.; Reisinger, A. J.; Rosi, E. J.; Walters, D. M. Pharmaceuticals and Personal Care Products (PPCPs) Are Ecological Disrupting Compounds (EcoDC). *Elem. Sci. Anthr.* **2017**, *5*, 66. https://doi.org/10.1525/elementa.252.

(4) Gupta, V. K.; Ali, I.; Saleh, T. A.; Nayak, A.; Agarwal, S. Chemical Treatment Technologies for Waste-Water Recycling—an Overview. *RSC Adv.* **2012**, *2* (16), 6380–6388. https://doi.org/10.1039/C2RA20340E.

(5) Saleh, T. A.; Gupta, V. K. Processing Methods, Characteristics and Adsorption Behavior of Tire Derived Carbons: A Review. *Adv. Colloid Interface Sci.* **2014**, *211*, 93–101. https://doi.org/10.1016/j.cis.2014.06.006.

(6) DeCoste, J. B.; Peterson, G. W.; Schindler, B. J.; Killops, K. L.; Browe, M. A.; Mahle, J. J. The Effect of Water Adsorption on the Structure of the Carboxylate Containing Metal–Organic Frameworks Cu-BTC, Mg-MOF-74, and UiO-66. *J. Mater. Chem. A* **2013**, *1* (38), 11922–11932. https://doi.org/10.1039/C3TA12497E.

(7) Fang, Q.-R.; Yuan, D.-Q.; Sculley, J.; Li, J.-R.; Han, Z.-B.; Zhou, H.-C. Functional Mesoporous Metal−Organic Frameworks for the Capture of Heavy Metal Ions and Size-Selective Catalysis. *Inorg. Chem.* **2010**, *49* (24), 11637–11642. https://doi.org/10.1021/ic101935f.

(8) Lyu, J.; Liu, H.; Zhang, J.; Zeng, Z.; Bai, P.; Guo, X. Metal–Organic Frameworks (MOFs) as Highly Efficient Agents for Boron Removal and Boron Isotope Separation. *RSC Adv.* **2017**, *7* (26), 16022–16026. https://doi.org/10.1039/C6RA26588J.

(9) Sarker, M.; Song, J. Y.; Jhung, S. H. Adsorptive Removal of Anti-Inflammatory Drugs from Water Using Graphene Oxide/Metal-Organic Framework Composites. *Chem. Eng. J.* **2018**, *335*, 74–81. https://doi.org/10.1016/j.cej.2017.10.138.

(10) Hasan, Z.; Khan, N. A.; Jhung, S. H. Adsorptive Removal of Diclofenac Sodium from Water with Zr-Based Metal–Organic Frameworks. *Chem. Eng. J.* **2016**, *284*, 1406–1413. https://doi.org/10.1016/j.cej.2015.08.087.

(11) Sarker, M.; Jhung, S. H. Zr-MOF with Free Carboxylic Acid for Storage and Controlled Release of Caffeine. *J. Mol. Liq.* **2019**, *296*, 112060. https://doi.org/10.1016/j.molliq.2019.112060.

(12) Tong, M.; Liu, D.; Yang, Q.; Devautour-Vinot, S.; Maurin, G.; Zhong, C. Influence of Framework Metal Ions on the Dye Capture Behavior of MIL-100 (Fe, Cr) MOF Type Solids. *J. Mater. Chem. A* **2013**, *1* (30), 8534–8537. https://doi.org/10.1039/C3TA11807J.

(13) Cirujano, F. G.; Martín, N.; Wee, L. H. Design of Hierarchical Architectures in Metal–Oganic Frameworks for Catalysis and Adsorption. **2020**. https://doi.org/10.1021/acs.chemmater.0c02973.

(14) Sumida, K.; Rogow, D. L.; Mason, J. A.; McDonald, T. M.; Bloch, E. D.; Herm, Z. R.; Bae, T.-H.; Long, J. R. Carbon Dioxide Capture in Metal-Organic Frameworks. *Chem. Rev.* **2012**, *112* (2), 724–781. https://doi.org/10.1021/cr2003272.

(15) Shahrokhian, S.; Ezzati, M.; Hosseini, H. Fabrication of a Sensitive and Fast Response Electrochemical Glucose Sensing Platform Based on Co-Based Metal-Organic Frameworks Obtained from Rapid in Situ Conversion of Electrodeposited Cobalt Hydroxide Intermediates. *Talanta* **2020**. https://doi.org/10.1016/j.talanta.2019.120696.

(16) Liu, C.-S.; Li, J.; Pang, H. Metal-Organic Framework-Based Materials as an Emerging Platform for Advanced Electrochemical Sensing. *Coord. Chem. Rev.* **2020**, *410*, 213222. https://doi.org/10.1016/j.ccr.2020.213222.

(17) Sun, Y.; Li, Y.; Wang, N.; Xu, Q. Q.; Xu, L.; Lin, M. Copper-Based Metal-Organic Framework for Non-Enzymatic Electrochemical Detection of Glucose. *Electroanalysis* **2018**, *30* (3), 474–478. https://doi.org/10.1002/elan.201700629.

(18) Yadav, D. K.; Ganesan, V.; Sonkar, P. K.; Gupta, R.; Rastogi, P. K. Electrochemical Investigation of Gold Nanoparticles Incorporated Zinc Based Metal-Organic Framework for Selective Recognition of Nitrite and Nitrobenzene. *Electrochimica Acta* **2016**, *200*, 276–282. https://doi.org/10.1016/j.electacta.2016.03.092.

(19) Zhang, Y.; Yin, J.; Wang, K.; Chen, P.; Ji, L. Electrocatalysis and Detection of Nitrite on a Polyaniline-Cu Nanocomposite-Modified Glassy Carbon Electrode. *J. Appl. Polym. Sci.* **2013**, *128* (5), 2971–2976. https://doi.org/10.1002/app.38466.

(22) Iman, K.; Shahid, M.; Khan, M. S.; Ahmad, M.; Sama, F. Topology, Magnetism and Dye Adsorption Properties of Metal Organic Frameworks (MOFs) Synthesized from Bench Chemicals. *CrystEngComm* **2019**, *21* (35), 5299–5309. https://doi.org/10.1039/C9CE01041F.

(23) Tchinsa, A.; Hossain, M. F.; Wang, T.; Zhou, Y. Removal of Organic Pollutants from Aqueous Solution Using Metal Organic Frameworks (MOFs)-Based Adsorbents: A Review. *Chemosphere* **2021**, *284*, 131393. https://doi.org/10.1016/j.chemosphere.2021.131393.

(24) Cassani, M.; Gambassi, F.; Ballarin, B.; Nanni, D.; Ragazzini, I.; Barreca, D.; Maccato, C.; Guagliardi, A.; Masciocchi, N.; Kovtun, A.; Rubini, K.; Boanini, E. A Cu(Ii)-MOF Based on a Propargyl Carbamate-Functionalized Isophthalate Ligand. *RSC Adv.* **2021**, *11*, 20429–20438. https://doi.org/10.1039/D1RA02686K.

(25) Kozub, B. R.; Rees, N. V.; Compton, R. G. Electrochemical Determination of Nitrite at a Bare Glassy Carbon Electrode; Why Chemically Modify Electrodes? *Sens. Actuators B Chem.* **2010**, *143* (2), 539–546. https://doi.org/10.1016/j.snb.2009.09.065.

(26) Faulkner, A. J. B. and L. R. *Electrochemical Methods: Fundamentals and Applications*; Wiley, 2001. https://doi.org/10.1023/A:1021637209564.

(27) Elgrishi, N.; Rountree, K. J.; McCarthy, B. D.; Rountree, E. S.; Eisenhart, T. T.; Dempsey, J. L. A Practical Beginner's Guide to Cyclic Voltammetry. *J. Chem. Educ.* **2018**, *95* (2), 197–206. https://doi.org/10.1021/acs.jchemed.7b00361.

(28) Alam, M. S.; Rahman, M. M.; Marwani, H. M.; Hasnat, M. A. Insights of Temperature Dependent Catalysis and Kinetics of Electro-Oxidation of Nitrite Ions

on a Glassy Carbon Electrode. *Electrochimica Acta* **2020**, *362*, 137102. https://doi.org/10.1016/j.electacta.2020.137102.

(29) Brunetti B, D. E. About Estimating the Limit of Detection by the Signal to Noise Approach. *Pharm. Anal. Acta* **2015**, *06* (04). https://doi.org/10.4172/2153-2435.1000355.

(30) Zhang, Y.; Li, X.; Li, D.; Wei, Q. A Laccase Based Biosensor on AuNPs-MoS2 Modified Glassy Carbon Electrode for Catechol Detection. *Colloids Surf. B Biointerfaces* **2020**, *186* (November 2019), 110683. https://doi.org/10.1016/j.colsurfb.2019.110683.

(31) Wu, W.-P.; Wu, J.; Liu, J.-Q.; Trivedi, M.; Kumar, A. Fabrication of a New Metal–Organic Framework for Sensitive Sensing of Nitroaromatics and Efficient Dye Adsorption. *RSC Adv.* **2017**, *7* (86), 54522–54531. https://doi.org/10.1039/C7RA11221A.

(32) Khan, M. S.; Khalid, M.; Ahmad, M. S.; Shahid, M.; Ahmad, M. Three-in-One Is Really Better: Exploring the Sensing and Adsorption Properties in a Newly Designed Metal-Organic System Incorporating a Copper(Ii) Ion. *Dalton Trans. Camb. Engl.* **2019**, *48* (34), 12918–12932. https://doi.org/10.1039/c9dt02578b.

(33) Ma, X.; Wang, W.; Sun, C.; Li, H.; Sun, J.; Liu, X. Adsorption Performance and Kinetic Study of Hierarchical Porous Fe-Based MOFs for Toluene Removal. *Sci. Total Environ.* **2021**, *793*, 148622. https://doi.org/10.1016/j.scitotenv.2021.148622.

(34) *Rapid and selective adsorption of cationic dyes by a unique metal-organic framework with decorated pore surface - ScienceDirect*. https://www.sciencedirect.com/science/article/pii/S0169433218302770 (accessed 2022-10-12).

(35) Hoskins, B. F.; Robson, R. Design and Construction of a New Class of Scaffolding-like Materials Comprising Infinite Polymeric Frameworks of 3D-Linked Molecular Rods. A Reappraisal of the Zinc Cyanide and Cadmium Cyanide Structures and the Synthesis and Structure of the Diamond-Related Frameworks [N(CH3)4][CuIZnII(CN)4] and CuI[4,4',4'',4'''-Tetracyanotetraphenylmethane]BF4.XC6H5NO2. *J. Am. Chem. Soc.* **1990**, *112* (4), 1546–1554. https://doi.org/10.1021/ja00160a038.

CHAPTER 5

5. Synthesis and characterization of H_2YL_{80} and Cu-[YL_{80}]

5.1 Aim of the chapter

The main task of this part of the work has been the design, synthesis, and characterization of a new organic ligand, named H_2YL_{80}, (where Y stands for the pendant alkyne and L_{80} indicates the similarity of the aromatic moiety of the ligand with the one of the ligand H_3L_{80} found in literature[1]) and the corresponding Cu-[YL_{80}] MOF. The new organic linker maintains the propargylcarbamate functionality and the two carboxylic acid groups of 1,3-H_2YBDC but provides a larger spacer between the carboxylic acid groups by adding two benzene rings on the aromatic moiety of the molecule (Fig. 5.1). This new design of the ligand was chosen envisaging that the larger, more rigid and more hindered spacer could prevent the coordination of the propargylcarbamate chains to the Cu(II) ions, in the hope of achieving a new MOF with higher porosity.

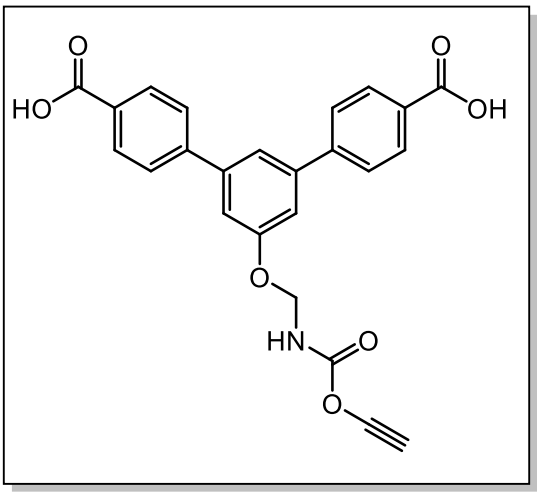

Figure 5.1. Structure of the new H_2YL_{80} ligand.

5.2. Introduction

The structure, pore size, and surface functionalities of MOFs can be tailored by judicious choices of the building blocks, thus leading to suitable diverse applications, such as in selective gas separation, gas storage, chemical sensing, biomedical applications, and catalysis. Generally, the functionalization of MOF interiors has relied on the preinstallation of ligands with desired functional groups or post modification of ligands bearing reactive groups such as alkynes or amines.[2] However, it is worth noting that all common methods for functionalization (including pre- and post-synthetic modifications) of the internal surface of a MOF tend to reduce the pore size of the MOF because the additional functional groups fill up the pores.[3]

Even in our case, the use of a propargylcarbamate-functionalized isophthalate ligand in the solvothermal preparation of a new copper(II)-based metal organic framework named [Cu(1,3-YBDC)]·xH$_2$O brought to a low porosity (46 mm^3/g) and surface area (14.5 ± 0.8 m^2/g). In that particular case, this was also due the extra coordination by the propargylcarbamate groups in the paddlewheel structure of the Cu-MOF, as seen in the synchrotron X-ray diffraction analysis.[4] Of course, these results may limit the application of the material, such as its use as support for nanoparticles. In fact, despite the latest positive results of the XPS analyses regarding the reduction of Au(III) within the Cu-MOF, the load of gold inserted inside the pores is still too low.[5]

Since one of the most important properties of metal organic frameworks is their high porosity and high specific area for maximizing the number of adsorptive sites within the given material, one of the simplest ways to accomplish this is to expand the organic linker to lead to MOFs with ultrahigh porosity.[6] However, one has to consider that expanded linkers can often yield fragile frameworks and the large void space within the crystal framework makes it generally susceptible to self-interpenetration (**Fig. 5.2**), precluding the desired high porosity.[7]

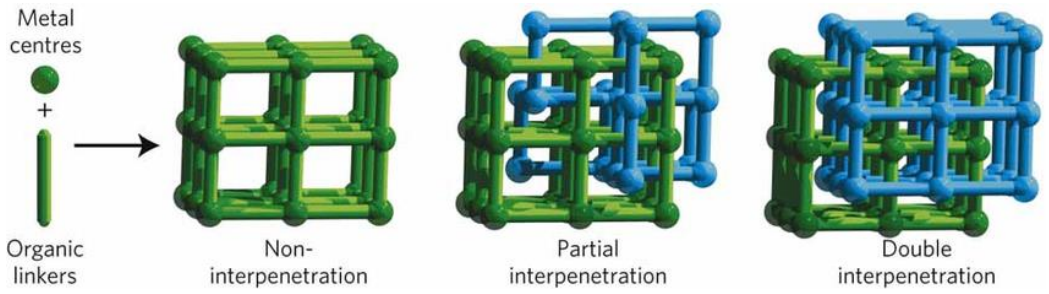

Figure 5.2. Interpenetration phenomena [8].

In fact, linkage between metal centers and long organic linkers can actually lead to the formation of a framework with open spaces, but these can be filled with another framework with identical composition and topology. This interpenetration phenomenon leads to frameworks mechanically entangled rather than chemically linked. Interpenetration is very common when using long flexible linkers. While interpenetration increases the density and mechanical properties of the material, it also negatively affects porosity and surface area. For this reason, this kind of phenomena must be avoided.

These assumptions led to the search for more sterically cluttered linkers to increase the size of the channels in the eventual MOF, with the idea of building a binder with a similar geometry and a MOF with a similar crystallinity to the one previously synthesized (Figure 5.3).

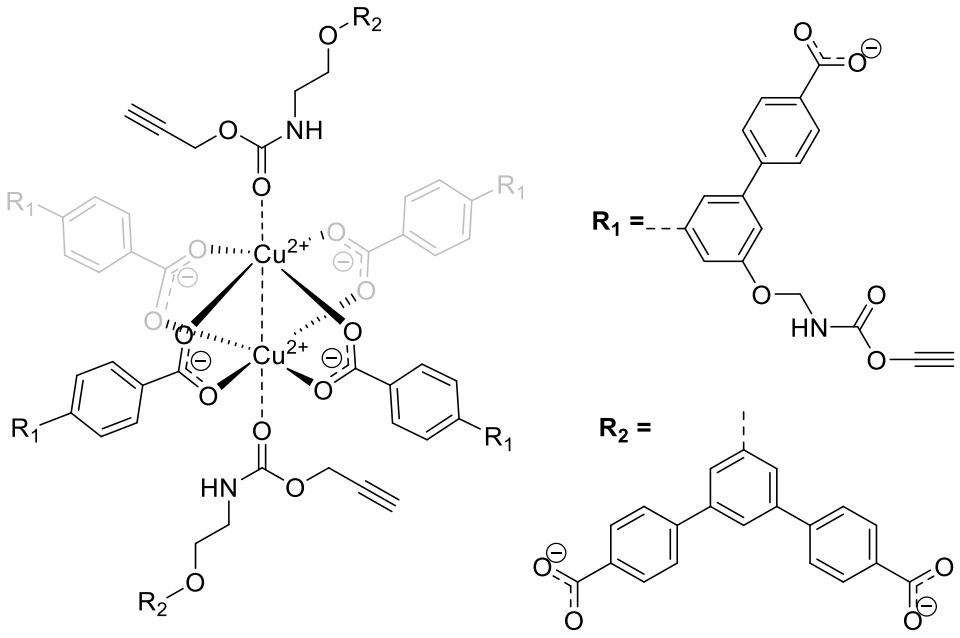

Figure 5.3. Hypothetical structure of the new Cu-[YL_{80}] ligand.

5.3 Result and Discussion

5.3.1 New Linker synthesis

5.3.2 New Linker synthesis first approach

The first synthetic path proposed for the synthesis of the new ligand H_2YL_{80} is illustrated in Scheme 5.1. It is a three-step synthesis. The first step consists in the condensation of commercially available propargyl chloroformate (1) with bromoethylamine (2), yielding carbamate (3). The second step is the nuclephilic substitution of the Br atom of (3) with the oxygen atom of commercially available 3,5-dibromophenol (4) to obtain the substituted carbamate (5). The final step involves a Suzuki reaction between the substrate (5) and two equivalents of 4- boronobenzoic acid (6), to obtain the new ligand (10).

The first step was already used in the synthesis of H_2YBDC, so the procedure was already mostly optimized. The only additional precautions that were taken were to stir the mixture during the final concentration under high vacuum (10-2 mmHg), to favour the evaporation of ethyl acetate, and to store the product under nitrogen at 4 °C.

The second step did not present any issue; Cs_2CO_3 was used to deprotonate the -OH group of the 3,5-dibromophenol in order to make it more electrophilic. NaI was used to exchange the bromide on the carbamate with a iodide, a better leaving group.

The third step, unfortunately, represented an insurmountable obstacle to the success of this synthetic route. The main issue is the difference in the solubility of the two reagents involved in this step. To overcome this problem, numerous expedients were used, such as employing different mixtures of solvents (water/toluene, water/acetonitrile, etc.) and the use of additives like CPME to favor the passage of the hydrophilic boronic acid from the aqueous phase to the organic phase. Despite several attempts under different reaction conditions (an example is reported in the § Experimental Section 5.5), in most cases the reagents remained segregated in separate layers and did not come in contact with each other. In addition to that, we suspect that the carbamate group present in 5 could have some undesired interaction with the Pd(II) catalyst used for the Suzuki reaction, in particular due to the presence of the terminal alkyne group.[9]

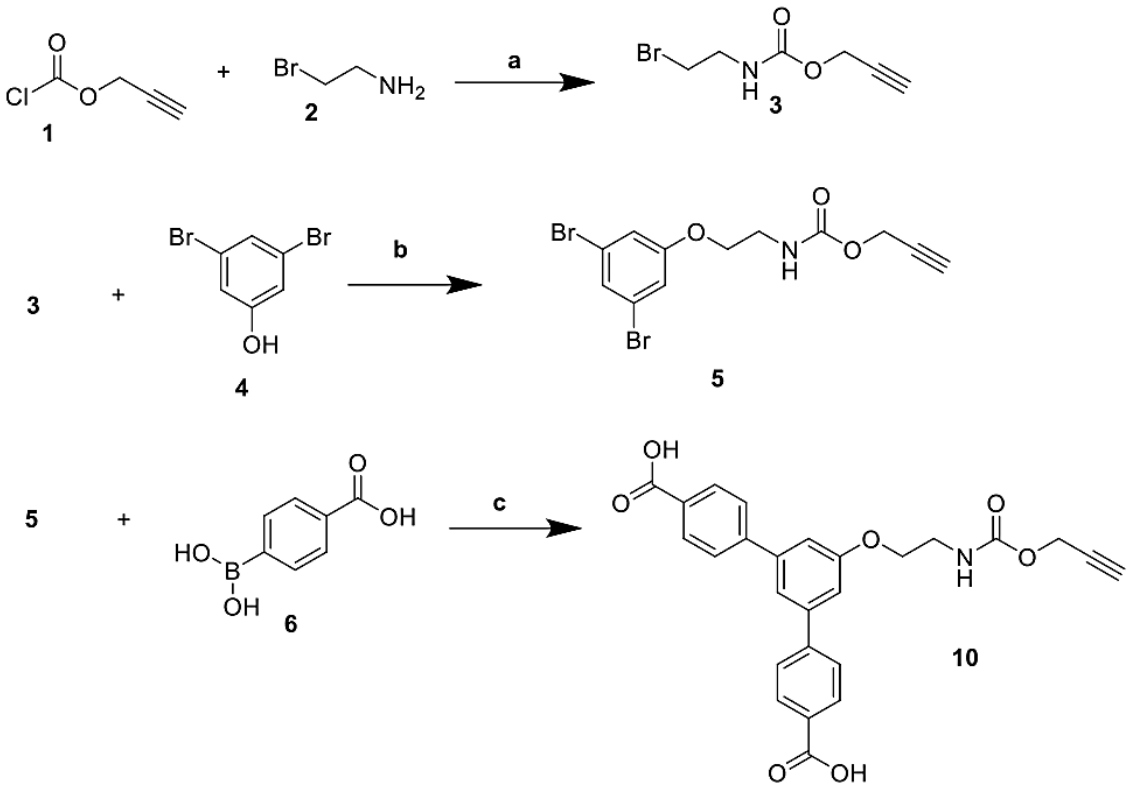

Scheme 5.1. First synthetic route proposed for the new ligand H_2YL80 synthesis. Reagents and conditions: a) $NaHCO_3$ 3 eq, THF/H_2O 1.25:1, overnight; b) Cs_2CO_3 1.5 eq, NaI 1.5 eq, 2-butanone, 80 °C, overnight; c) K_2CO_3 1 M 9.4 eq, Toluene/CPME 19:1, cat. $PdCl_2(PPh_3)_2$, 110 °C, 4 hours.

5.3.3 New Linker synthesis second approach

The second proposed synthetic path for the new ligand synthesis is reported in Scheme 5.2. In this new approach the Suzuki reaction is performed on the unsubstituted 3,5-dibromophenol, and the propargyl carbamate is added subsequently. This method brings two main benefits. First, it removes the possible interference with the Pd(II) catalyst by the pendant alkyne of the carbamate during the Suzuki reaction. Second, the aromatic rings that undergo the coupling reaction are much more similar to each other compared to the ones involved in the Suzuki reaction of the first approach, therefore their solubility is also similar, and it is easier for the reagents to come into contact.

Nevertheless, also this route presents a drawback. In fact, due to the presence of the carboxylic acid groups on the diacid (7), the nucleophilic substitution reaction on the bromo-propargyl carbamate (3) cannot be performed without having the carboxylic -OH groups to compete with the phenolic -OH group. Considering that carboxylic acid usually possess a pKa of ~5 and phenols have a pKa of ~10, the acid groups are actually favoured as

nucleophiles for the substitution. Therefore, this process requires two additional steps (protection of the carboxylic acid groups via esterification, and the following deprotection by basic hydrolysis) in order to successfully yield the desired product.

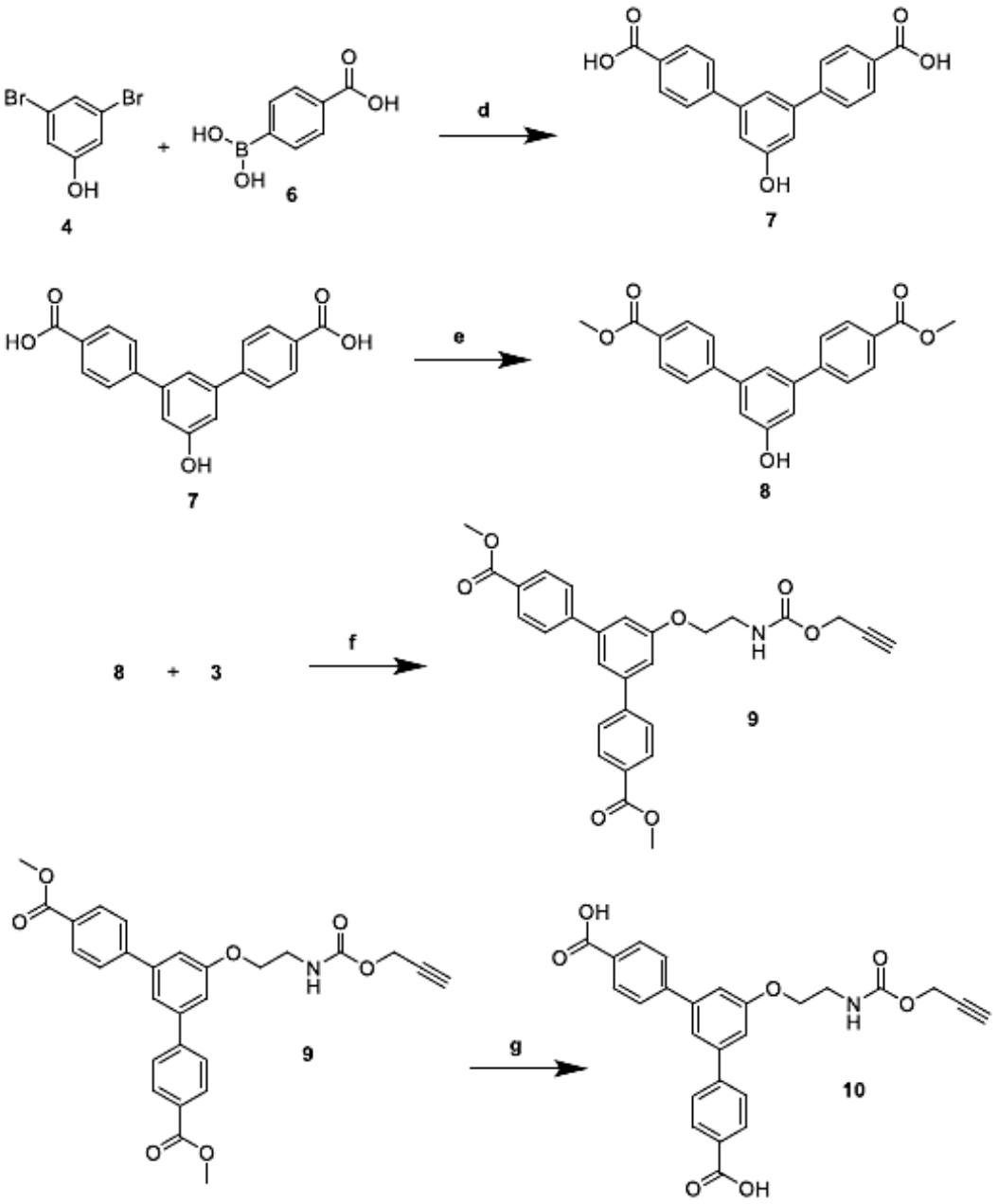

Scheme 5.2. Second synthetic route proposed for the new ligand H2YL80 synthesis. Reagents and conditions: d) K_2CO_3 1 M 7.4 eq, $PdCl_2(PPh_3)_2$ 0.02 eq, CH_3CN, 100 °C, overnight; e) MeOH, H_2SO_4 conc. 10 eq, 65 °C, 24 hours; f) Cs_2CO_3 1.5 eq, NaI 1.5 eq, 2-butanone, 80 °C, 24 hours; g) LiOH 2 M 5 eq, MeOH/THF 1:1, r.t., overnight.

For the first step we modified a procedure taken from the literature.[10] The original procedure used a 10% catalytic load and a reaction time of 48 hours. After numerous attempts

we managed to optimise the process using a 2% catalytic load (smaller catalytic loads result in lower yields) and carrying out the reaction overnight.

From the same literary source, we also took the procedure for the second step. In this case, there was no need to further modify the process.

For the third step we based our procedure on the analogue substitution reaction that was used for the synthesis of the ligand H_2YBDC. It required numerous attempts to find the optimal reaction conditions to give the desired product in satisfying yields. Each time, we modified some of the following parameters:

- Solvent: different solvents were tried (DMF, 2-butanone, 2-pentanone). We carried each reaction in reflux conditions, so the different boiling points of the solvent influenced the reaction temperature.

- Carbamate/diester ratio: the unreacted carbamate is quite difficult to remove during the work-up, so we opted for the use of an excess of diester. Seeing that the diester is obtained through an expensive procedure, we tried to use the minimum possible excess. The optimal carbamate/diester millimolar ratio was found to be 1:1.5.

- Inorganic salts: as for the second step of the first synthetic approach (see experimental data) we used Cs_2CO_3 to deprotonate the phenolic -OH in the diester and NaI to exchange the Br atom of the carbamate with a iodine atom, which is a better leaving group. Though, the presence of those salts requires numerous aqueous washings during the work-up, and hence we tried to use the smallest possible quantity of those reagents. For the definitive procedure we opted for 1.5 equivalents of each salt.

For the final step (base-catalysed hydrolysis), the critical parameter was the reaction time. The main issue is that, if the reaction is carried on for too long, the carbamate chain hydrolyses as well as the ester groups, and part of the desired product is converted in 5'-(2-aminoethoxy)-[1,1':3',1''-terphenyl]-4,4''-dicarboxylic acid via the hydrolysis of the N-C(O) bond in the carbamate chain resulting in a pendant amine group (**Figure 5.4**)

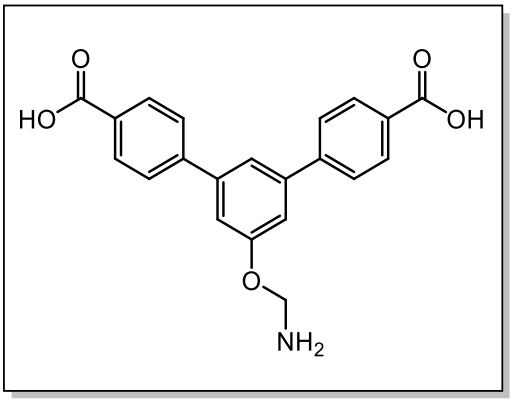

Figure 5.4. structure of 5'-(2-aminoethoxy)-[1,1':3',1"-terphenyl]-4,4"-dicarboxylic acid.

Indeed, if the reaction is carried for 24 h, after the work-up we found that the aqueous washings contained both the desired product and the amine product. This is particular evident from the ^{1}H-NMR spectra (Figure 5.5), where is clearly visible the presence of two distinct sets of signals in the aromatic phase. The nature of the by-product is confirmed by the ESI-MR spectrum (Figure 5.6) where we observe the presence of a signal at 378 m/z corresponding to the mass of 5'-(2-aminoethoxy)-[1,1':3',1"-terphenyl]-4,4"-dicarboxylic acid. We found that the optimal reaction time to obtain a satisfying yield and to keep the amine formation at minimum was around 12 hours (generally the reaction was carried overnight).

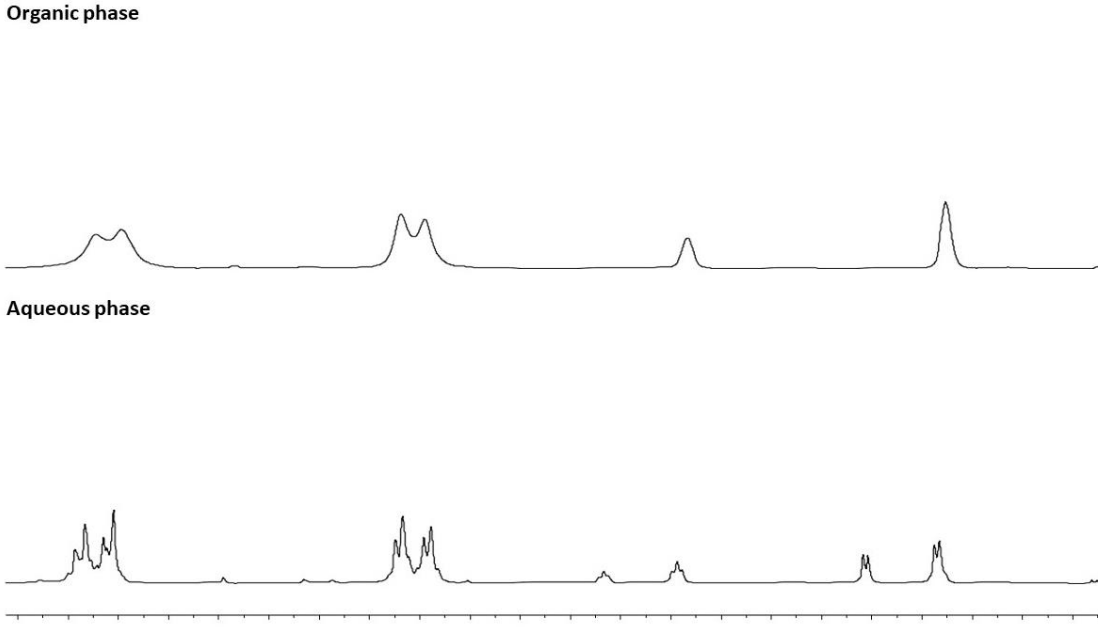

Figure 5.5. ^{1}H-NMR spectra of the organic phase (top) and the aqueous phase (bottom) after the work-up of the final step carried for 24 hours. The zoom on the aromatic zone of the spectrum shows that in the aqueous phase there are two distinct sets of signals, belonging to the desired product and the amine product.

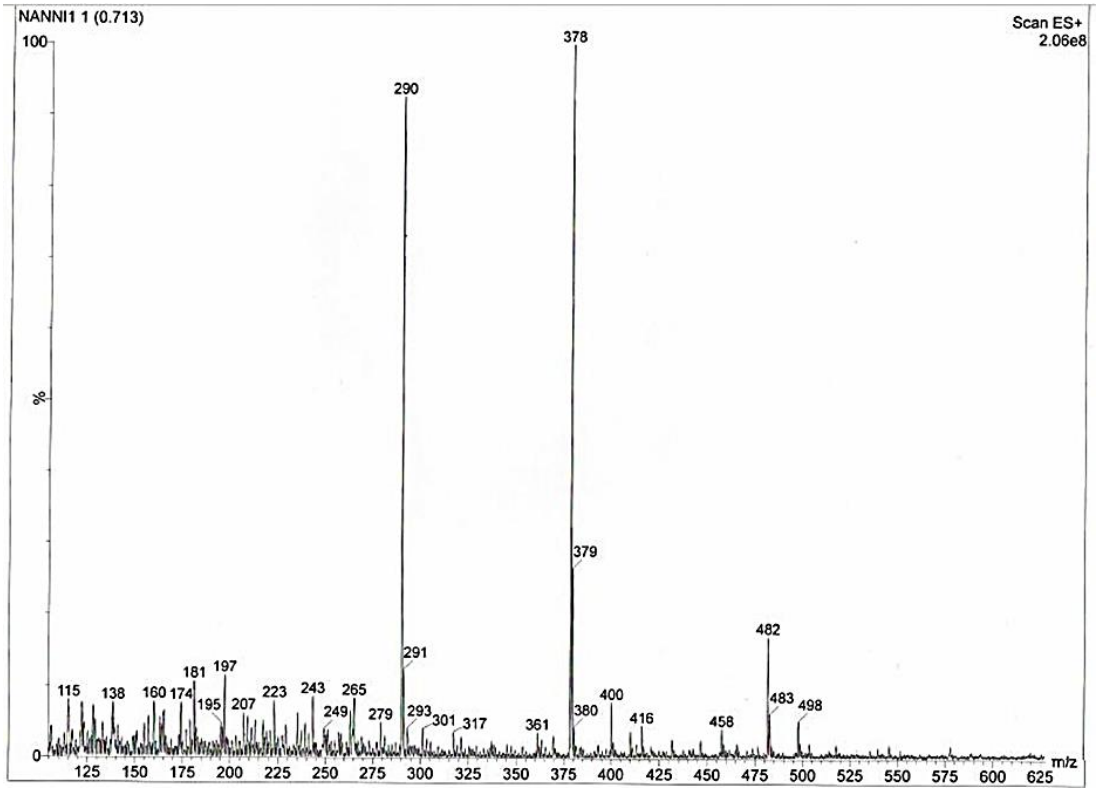

Figure 5.6. ESI-MS(+) of the aqueous phase (bottom) after the work-up of the final step carried for 24 hours. Both the signal of the desired product (482 m/z, $C_{26}H_{21}NO_7Na^+$) and the amine product (378 m/z, $C_{22}H_{20}NO^+$).

The TGA analysis of the ligand (Figure 5.7) shows four weight losses. The first three are attributed to the decomposition of the propargyl carbamate groups [obs. 32.45% (7.322+12.077+13.051), calc. for $C_6H_8NO_3$, mw 142,13 g mol-1 30.94%]. At 800 °C there is a 5% residual, probably consisting in LiCl from the last reaction step.

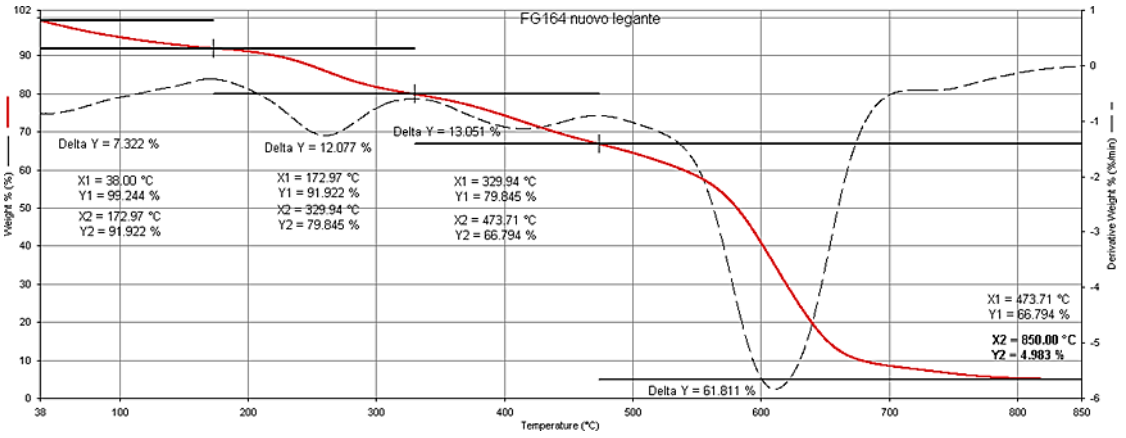

1st loss (%)	2nd loss (%)	3rd loss (%)	4th loss (%)	Residual 800°C (%)
7.3	12.1	13.1	61.8	5.0

Figure 5.7: TGA curve (continuous red line) and first derivative (dashed line) of the weight loss of H2YL80.

The presence of LiCl in the ligand could lead to the formation of $Cu(OH)_2$ and/or $CuCl_2$ during the synthesis of the new MOF, therefore we tried to purify the ligand through crystallization (see Experimental Section for the procedure). In Table 5.1 we report the yields for every crystallization cycle and the solid residual at 800 °C checked with TGA analysis.

Table 5.1: Yields (%) and inorganic residual at 800 °C of the purified H2L80

Crystallization	Yield (%)	Residual at 800 °C (%)
1st	84	4.3
2nd	22	3.9

The results show that the first crystallization, although having high yields, only reduces the inorganic residuals of 0.7 percentage points (Figure 5.8). Considering that the instrument uncertainty is about 1% it is a negligible result.

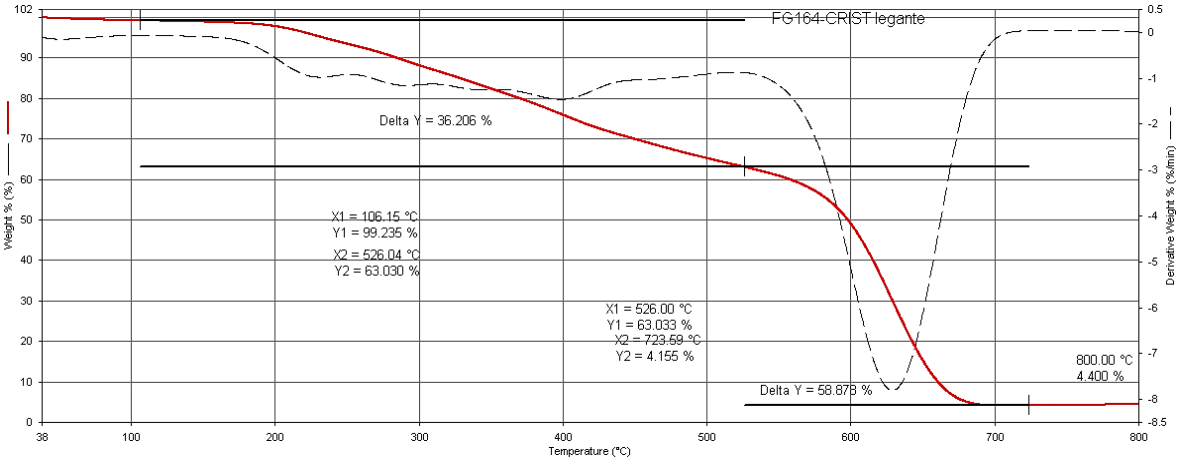

1st loss (%)	2nd loss (%)	Residual 800°C (%)
36.2	58.88	4.4

Figure 5.8. TGA curve (continuous red line) and first derivative (dashed line) of the weight loss of H2YL80 after the first crystallisation.

The second crystallisation gave slightly better results in terms of inorganic residual at 800 °C, reducing it to 3.9% (Figure 5.9), but the yield decreased by almost four times (22%).

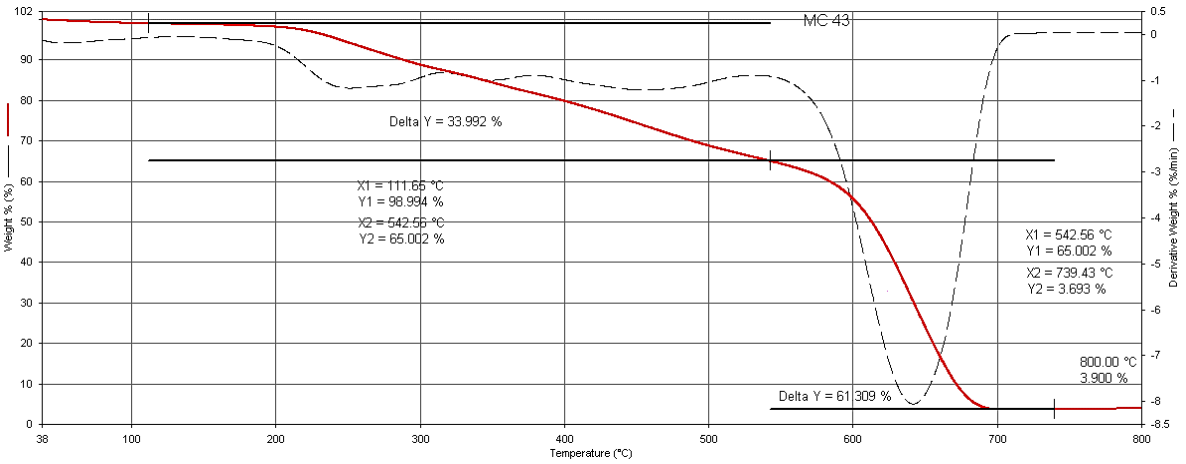

1st loss (%)	2nd loss (%)	Residual 800°C (%)
34.0	61.31	3.0

Figure 5.9. TGA curve (continuous red line) and first derivative (dashed line) of the weight loss of H2YL80 after the second crystallization.

Those results brought to the conclusion that, taking into consideration the long and complex process needed to synthesise H_2YL_{80}, the material loss caused by the purification process is too high compared to the small removal of inorganic impurities. Therefore, for the synthesis of the new MOF, the ligand was used without any purification.

5.3.4 New Cu-MOF synthesis

The new organic ligand H_2YL_{80} was used to attempt the synthesis of a new Cu-based MOF. As for the synthesis of [Cu(1,3-YBDC)]·xH_2O, the copper salt the organic ligand is reacted with $Cu(NO_3)_2 \cdot 2.5H_2O$. Ideally, this new MOF should be structurally similar to [Cu(1,3- YBDC)]·xH_2O, but hopefully, the larger organic moiety of the ligand will prevent the extra coordination of the carbonylic oxygen of the propargyl carbamate chain to the apical positions of the paddlewheel unit.

The characterization of MOFs is typically accomplished through X-ray spectroscopy techniques. In order to successfully perform those measurements, it is necessary to obtain the material in a crystalline form. It follows that the reaction conditions have to be carefully chosen, so we attempted numerous synthesis processes, each time modifying different reaction parameters (Metal:Ligand ratio, reagents concentration, solvents, temperature, stirring, atmosphere, reaction time). In table 5.2 are reported the reaction conditions used in all different attempts.

Table 5.2: Reaction conditions for the different attempts for the new MOF synthesis.

Reaction	M:L; Ligand concentration	DMF:H_2O: 2-propanol	T/°C	Stirring	Atm.	Time/h	Results
MC35	1.8:1 0.026 M	0:0:1	85	Yes	Air	24	Amorphous solid (green). 70% yield.
MC44	2:1 0.016 M	3:1:0	80	Yes	Air	24	Amorphous solid (green), presence of Cu-oxides. 78.4% yield.
MC45	2:1 0.016 M	3:1:0	r.t (starting) 50 (after 24 h)	Yes	Air	48	At r.t the reaction does not happen, so the temperature is increased after 24 hours. The final product is an amorphous green solid; when washed with water the precipitation of a white inorganic residue is observed (contains traces of the ligand).
MC46	2:1 0.016 M	3:1:0	50	No	Air	168	Green solid mixed with traces of white solid; higher crystallinity compared to MC44 (polycrystalline). 46% yield.
MC49	2:1 0.016 M	1:9:0 (starting) *After 48 hours DMF is added, the new rate becomes* 1:1:0	50 (starting) 80 (after 48 h)	No	N_2	168	With the starting solvent composition, the ligand is not completely soluble. After 120 h at 80°C the product is decomposed (mostly brown Cu-oxides).
MC50	2:1 0.016 M	1:0:0	50 (starting) 80 (after 48 h)	No	N_2	168	After 48 h at 50 °C no solid is formed. After 120 h at 80°C the product is decomposed (mostly brown Cu-oxides).
MC51	2:1 0.016 M	4:1:0	50	No	N_2	168	Polycrystalline green solid. 70% yield.
MC52	2:1 0.016 M	2:1:1	50	No	N_2	168	Polycrystalline green solid. 61% yield.
MC53	2:1 0.008 M	4:1:0	50	No	N_2	168	Polycrystalline green solid. 30.5% yield.

The choice of the solvents is one of the most delicate points. The combination of solvents in different ratios not only determines the solubility of the reagents, but it also influences the rate of the various reaction steps, and therefore the characteristics of the final product (Fig. 5.10). For example, if the organic ligand has a low solubility in water, the use of a high rate of water in the solvent combination leads to a slow ligand dissolution, making it the rate-determining step in the crystallization process.[11] It is often observed that the use of high ratios of water and/or alcohols leads to the formation of larger crystals but with generally low yields, while on the other hand the use of organic solvents such as DMF increases the solubility of the organic ligands and consequentially the nucleation rate.[12]

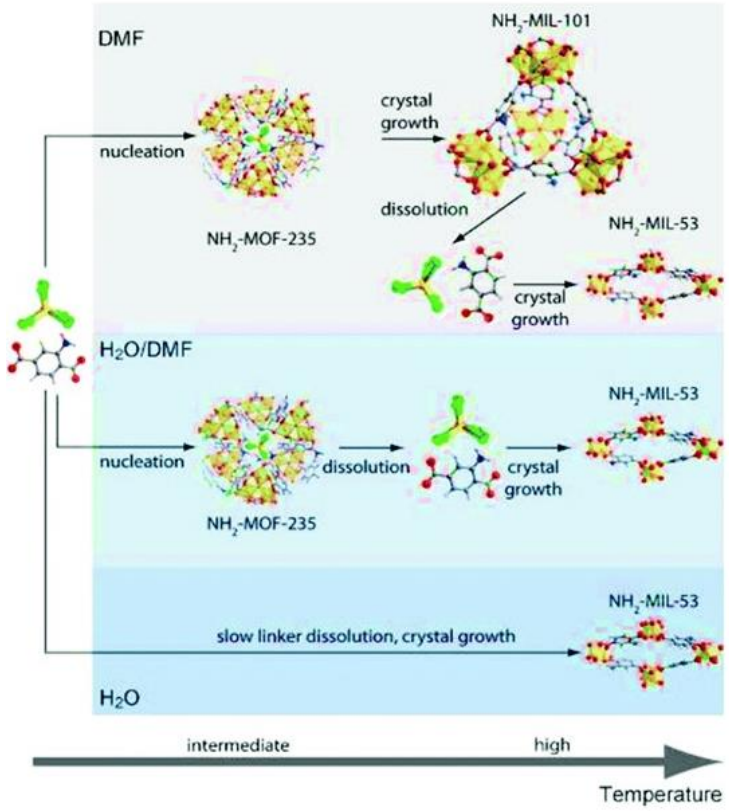

Figure 5.10. Sequence of events taking place during the NH_2-MIL-53(Al) and NH_2-MIL-101(Al) crystallization processes under different synthesis conditions.
C: grey, H: white, N: blue, O: red, Al: yellow, Cl: green.[11]

Due to the similarity of the reagents used, in the first attempt of the synthesis of the new Cu-MOF we employed the same conditions as those of the synthesis of [Cu(1,3-YBDC)]·$x$$H_2O$[4] (see MC35 in Table 5.2). In these conditions the reagents reacted fast, yielding a light-green solid, but the XRD analysis on the product showed that the solid was almost completely amorphous (Fig 5.11).

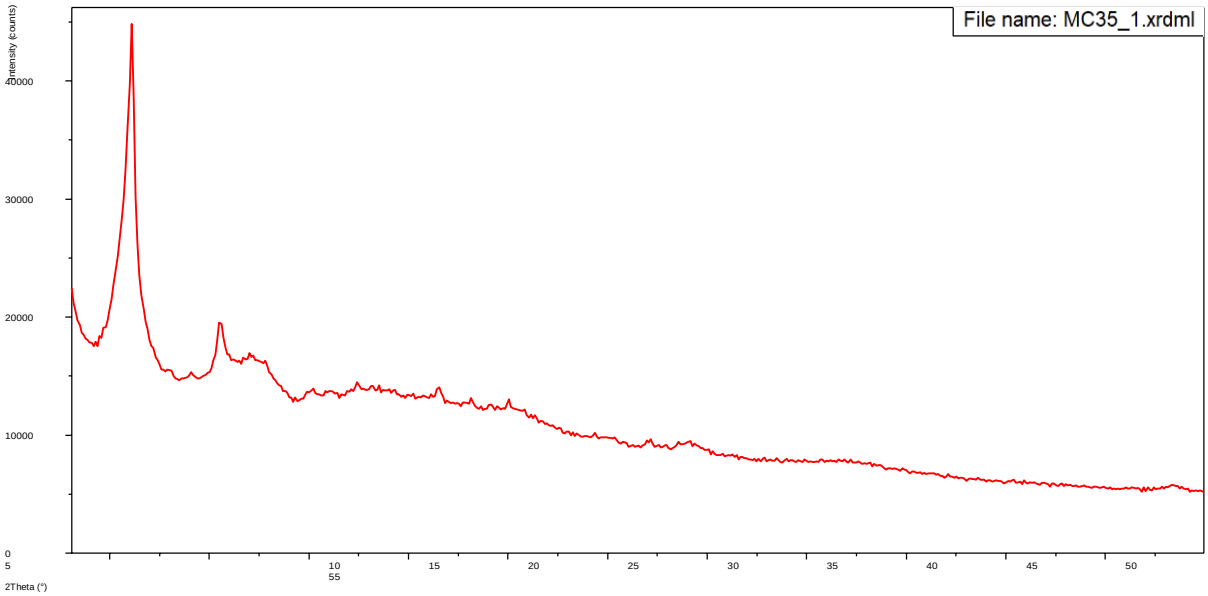

Figure 5.11. XRD analysis of the product of MC35, showing the almost completely amorphous nature of the material.

The FTIR spectrum of the product was compared to the one of the neat ligand (Fig 5.12). The comparison highlighted the loss of the carboxylic acid protons of the ligand. This, together with some other difference in the spectrum area below 2000 cm^{-1}, showed that H_2YL80 effectively coordinated the Cu ions. Having verified that the ligand and the copper salt react successfully with each other, the successive attempts were aimed to the search for optimal conditions to increase the crystallinity of the final product.

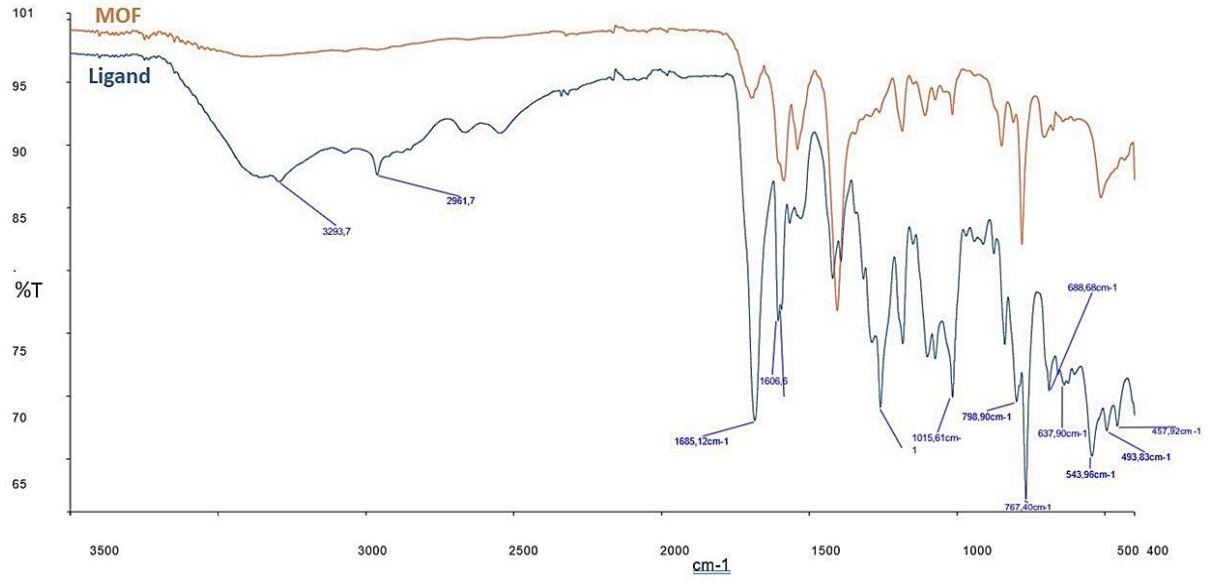

Figure 5.12. Comparison between the FTIR spectra of H_2YL80 (blue line) and the product of MC35 (red line), showing the disappearance of the carboxylic O-H peaks at 3294 cm^{-1}. The differences in the region below 2000 cm^{-1} couldbe attributed to the formation of Cu-O bonds.

Different solvent compositions were tried, modifying the DMF:H_2O:2-propanol ratio. 2-propanol was chosen instead of the more common ethanol[12] because during the synthesis of [Cu(1,3-YBDC)]·$x$$H_2O$ it was found that the presence of ethanol could lead to the esterification of the ligand.[5] The experiments led to the conclusion that for the new Cu-MOF synthesis, the presence of at least a 50% of DMF in the solvent composition is necessary to dissolute effectively the organic ligand, but also that the presence of H_2O and/or 2-propanol is mandatory to have the correct precipitation of the final product (see MC50 in Table 5.2).

The choice of the temperature was made in order to avoid the decomposition of the reagents and the formation of copper oxides. The optimal temperature was found to be 50 °C. Higher temperatures led to the formation of Cu-oxides in almost all cases, while at room temperature the reaction does not take place (see MC45 in table 5.2). By keeping the temperature at 50 °C we were able to avoid the decomposition even for long reaction times (one week), and, at the same time, to have acceptable reaction rates (formation of the first crystals within the first 24-30 hours).

The first four syntheses (MC35, MC44, MC45 and MC46 in table 5.2) were carried in air atmosphere, then for the following ones we switched to N_2 atmosphere, hoping that it could prevent the decomposition of the reagents and the consequent formation of copper oxides. Unfortunately, it appears that even with the inert atmosphere, at high temperatures (80 °C) the decomposition occurs anyway (see MC49 and MC50 in table 5.2). On the other hand, none of the reactions carried in N_2 showed the formation of the white inorganic residue that had been observed in MC45 and MC46 (see Table 5.2), but it is not clear if this phenomenon is related to the atmosphere.

The first three syntheses (MC35, MC44, and MC45 in table 5.2) were carried under magnetic stirring. After those unsuccessful attempts, the magnetic stirring was not employed for the following reactions, to see if keeping the system still could help to slow down the nucleation and give a more crystalline product. Apparently, this precaution seems effective, seeing that the products that were obtained without magnetic stirring showed higher crystallinity (polycrystalline materials) compared to the previous ones (see MC46, MC51 and MC52 in Table 5.2 and the relative XRD spectra in Fig. 5.12).

The last parameter that was taken into account was the concentration of the reagents. For the first reaction (MC35), a concentration of 0.026 M for the ligand and 0.046 M for the copper salt were employed. For the subsequent reactions up to MC52, the concentration of the ligand was lowered to 0.016 M and to 0.031 M for the copper salt. After the encouraging results

obtained with the reaction MC51, we decided to repeat the reaction in the same conditions but halving the concentration of the reagents (see MC53 in table 5.2). This way, we hoped to slow down the nucleation process, allowing an easier crystallization of the product. We confirmed that the formation of the solid was actually slower compared to MC51 (the first formation of the solid was only observed after 96 hours). Unfortunately, the product of MC53 was also polycrystalline (Fig. 5.13), plus the yield was exactly half compared to MC5: this is obviously a result far from being satisfying.

Comparing the XRD spectra of the products of MC51, MC52 and MC53 (Fig. 5.14), it appears that the crystalline phases are slightly different in each case. In MC51 we observe the presence of two main crystalline phases, one predominant at $2\theta = 5.25°$ and the other at $2\theta = 5.58°$. In MC52 we observe the same two phases but this time they are present in an almost equal proportion. In MC53 we have the disappearance of the phase at $2\theta = 5.25°$, but a new phase at $2\theta = 6.40°$ appears, in lower proportion compared to the one at $2\theta = 5.58°$.

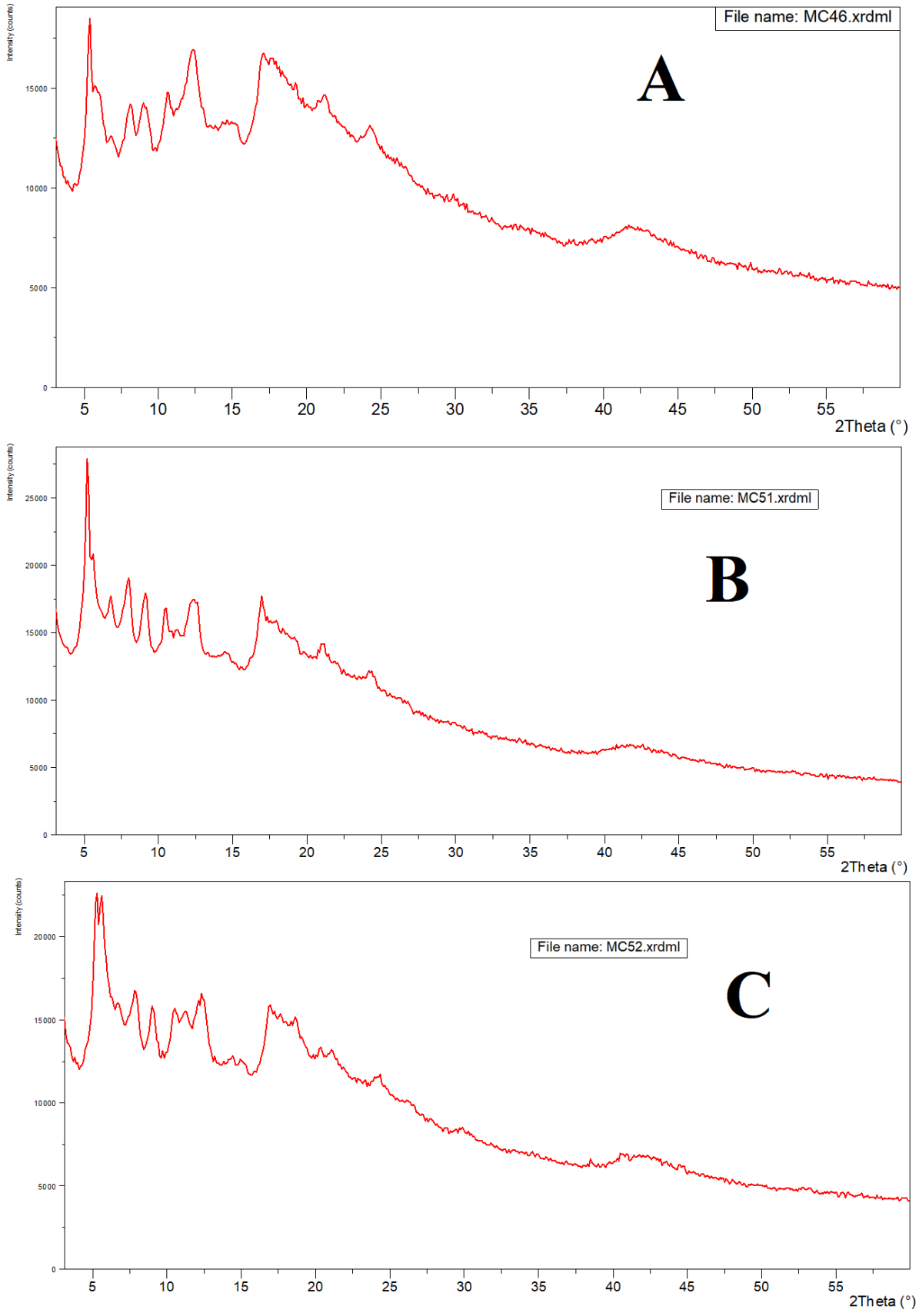

Figure 5.13. XRD spectra of the products of the reactions MC46 (panel A), MC51 (panel B) and MC51 (panel C).The materials show higher crystallinities compared to MC35 (see Fig. 5.11).

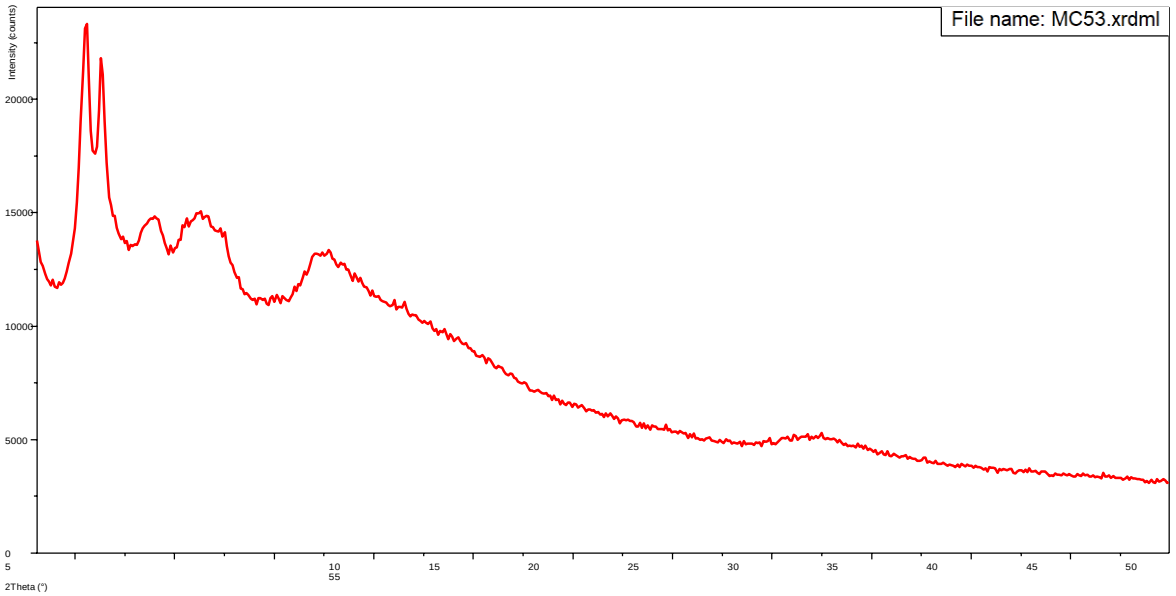

Fig. 5.14. XRD spectrum of the product of the reaction MC53.

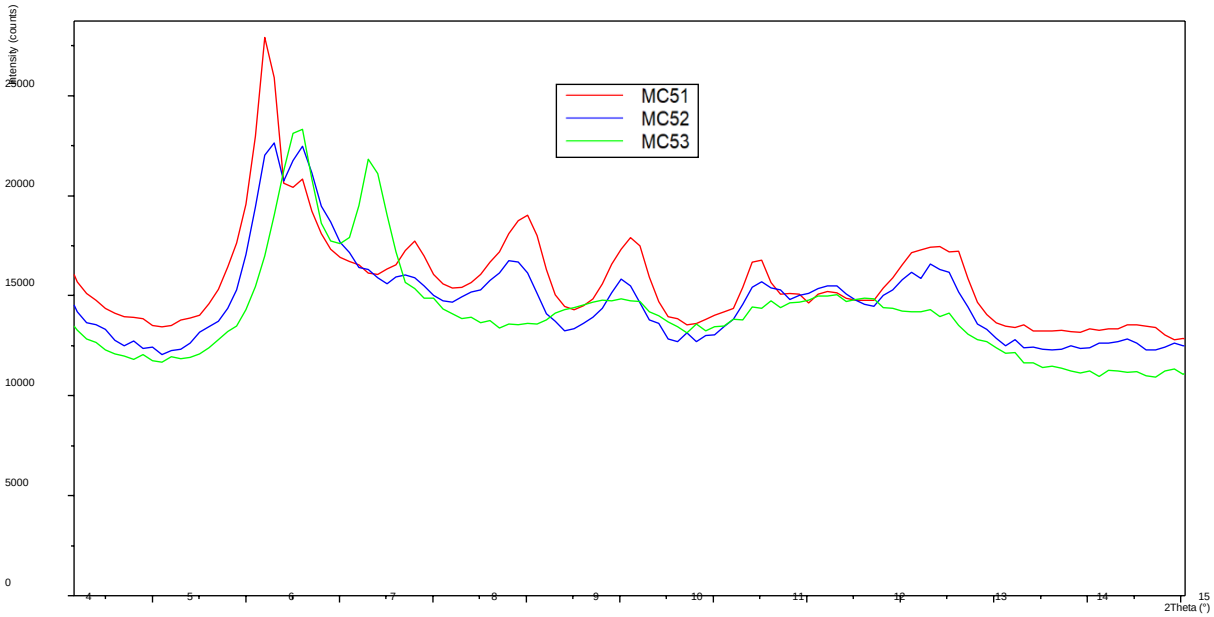

Figure 5.15. Comparison of the XRD spectra of the products of reactions MC52 (red line), MC52 (blue line) andMC53 (green line).

5.4 Conclusions

The main results described in this chapter of the thesis can be summarized as follows.

- ✓ The new organic ligand 5'-(2-(((prop-2-yn-1-yloxy)carbonyl)amino)ethoxy)-[1,1':3',1"-terphenyl]-4,4"-dicarboxylic acid, abbreviated as H2YL80, was designed, synthesized and fully characterized;
- ✓ The new ligand was reacted with Cu(NO3)2·2.5H2O, in order to obtain a new Cu-based MOF. Having verified that the ligand and the Cu-salt react effectively with each other, different reaction conditions have been studied in order to obtain the desired product in satisfying yield and crystallinity. Currently, the best result obtained was a polycrystalline solid with a 70% yield.

Based on these results, the future work will focus on studying new reaction conditions to obtain a novel MOF from the new ligand and $Cu(NO_3)_2 \cdot 2.5H_2O$ in high yield and crystallinity, and fully characterize the new material.

5.5 Experimental Part

5.5.1 Materials

All reagents and solvents were used as received, ultrapure water purified with the Milli-Q plus system (Millipore Co, resistivity over 18 MΩ cm) was used in all cases. Reagents were purchased from Sigma-Aldrich (analytical reagent grade). The reactions were monitored by thin-layer chromatography (TLC) on highly purified Silica on TLC-PET foils (with fluorescent indicator 254 nm, Fluka). ESI-MS analyses were performed by direct injection of methanol solutions using a WATERS ZQ 4000 mass spectrometer; working temperature: 80 ÷ 100 °C; working concentrations: ca. 10^{-8} g/L; Cone Voltage: 10 ÷ 30 V; working flow: 10 μL/min. The NMR spectra were recorded at 298 K using a Varian Gemini XL 300 (1H 300.1 MHz, 13C 75.5 MHz) and a Varian MercuryPlus VX 400 (^{1}H, 399.9; ^{13}C, 100.6 MHz); spectra were referenced internally to residual solvent resonances and were recorded at 298 K for characterization purposes; full ^{1}H and ^{13}C NMR assignments were done using standard Varian pulse sequences. Spectra have been edited with the software MestReNova Version: 12.0.1-20212, 2017 Mestrelab Research S.L. Abbreviations: s = singlet, d = doublet, t = triplet, m = multiplet, bs = broad singlet. ATR-FTIR analyses were performed with a Perkin Elmer Spectrum Two spectrophotometer, equipped with a Universal ATR accessory, in the range 4000-600 cm^{-1} with a resolution of 0.5 cm^{-1}. Abbreviations: ν = stretching, δ = bending. Thermogravimetric analyses were carried out using a Perkin Elmer TGA-7. The samples (initial weight ≈10 mg) were heated in air in a platinum crucible at a rate of 10 °C min^{-1} from room temperature to 900 °C. UV-Vis spectra were recorded with a Agilent Cary 3500 multicell spectrophotometer. The atomic adsorption spectroscopy (AAS) measurements were performed with a Thermo Scientific iCE 3300 AA01124707 spectrometer in air-acetylene flame (λ = 242.8 nm; spectral bandwidth = 0.5 nm). XRD was performed by a Philips X'Pert Pro instrument equipped with a fast X'Celerator detector, working at 40 mA and 40 kV and using Cu Kα radiation. Field emission-scanning electron microscopy (FE-SEM) analysis was carried out by means of a Zeiss SUPRA 40VP instrument equipped with an INCAx-act PentaFET Precision spectrometer (Oxford Instruments) for energy dispersive X-ray spectroscopy (EDXS) characterization. The used primary beam acceleration voltages were comprised between 1 kV (for imaging) and 20 kV (for EDXS analyses). X-ray photoelectron (XPS) studies were carried out by means of a Specs EnviroESCA instrument using a monochromated AlKα excitation source ($h\upsilon$ = 1486.6 eV), at

an operating pressure of *ca*. 10^{-6} mbar. Survey scans were performed with 100 eV pass energy, every 1.0 eV·step^{-1}, and for 0.1 sec·step^{-1}. High resolution spectra were acquired with 50 eV pass energy, every 0.1 eV·step^{-1}, and for 0.1 s·step^{-1}. In agreement with the literature,[13] binding energy values (BEs; uncertainty = ± 0.2 eV) were corrected for charging assigning to the adventitious C 1s peak, attributed to adventitious hydrocarbons, the value of 284.8 eV. XPS curves were analyzed using the Specs Keystone software, applying a Shirley-type background substraction.[13] The sensitivity factors of integrated peak areas used for atomic percentages (at. %) quantification were supplied by Specs.

5.5.2 Ligand synthesis

First approach

- **Synthesis of prop-2-yn-1-yl (2-bromoethyl)carbamate (3)**

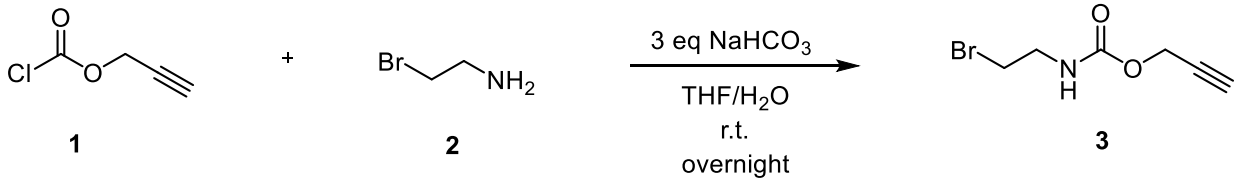

Scheme 5.3. synthesis of **(3)**

A solution of 2-bromoethylamine hydrobromide (**2**, 9.138 g, 44.6 mmol) and $NaHCO_3$ (11.239 g, 133.8 mmol, 3 eq) was prepared in THF/H_2O (107 mL/85 mL) and cooled to 0 °C. Propargyl chloroformate (**1**, 6.075 g, 5 mL, 1.15 eq) was added dropwise. The mixture is kept in the ice-bath under magnetic stirring overnight. THF was then evaporated. The aqueous phase was extracted with ethyl acetate (3 x 20 mL). The organic layer is then washed with HCl 1 M (2 x 10 mL) and Brine (2 x 10 mL) and dried with Mg_2SO_4. The solution was filtered and concentrated under vacuum (first at the rotary evaporator and then for 3 hours at the mechanical pump) under magnetic stirring to favour the evaporation of residual ethyl-acetate. The final product is a colourless oil (6.608 g, 32.2 mmol, 72% yield), that has been used without further purification and stored under Nitrogen at 4 °C.
Rf (in Petroleum Ether/ Ethyl Ether 1:2): 0.48.

ESI-MS(+): (MeOH, m/z): 228 (100) $[C_6H_8NO_2Br + Na]^+$

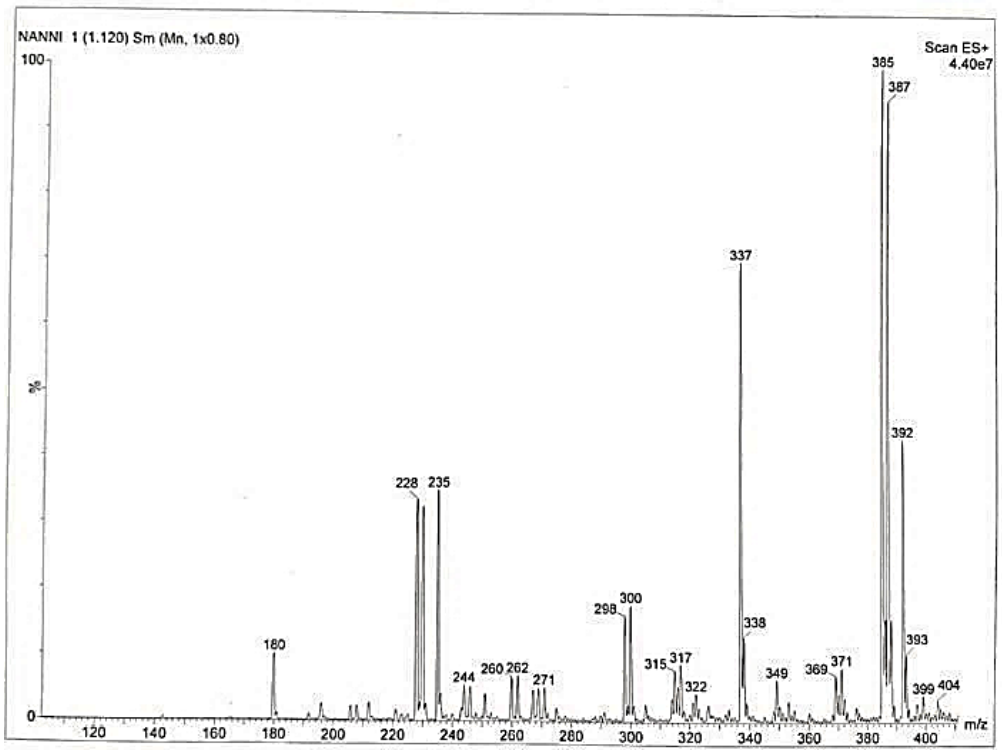

Figure 5.16. ESI-MS(+) spectrum of **3**. Note the presence of an unknown co-product at 385 with the typical Br pattern.

^{1}H-NMR (300 MHz, CDCl3): δ 5.24 (bs, N*H*^{3}), 4.69 (d, ^{4}J=2.4, 2H, O-C*H*$_2$^{4}), 3.60 (m, 2H, NH-C*H*$_2$^{2}), 3.46 (t, ^{3}J=5.7, 2H, Br-C*H*$_2$^{1}), 2.48 (t, ^{4}J= 2.4, 1H, C≡C*H*^{5})

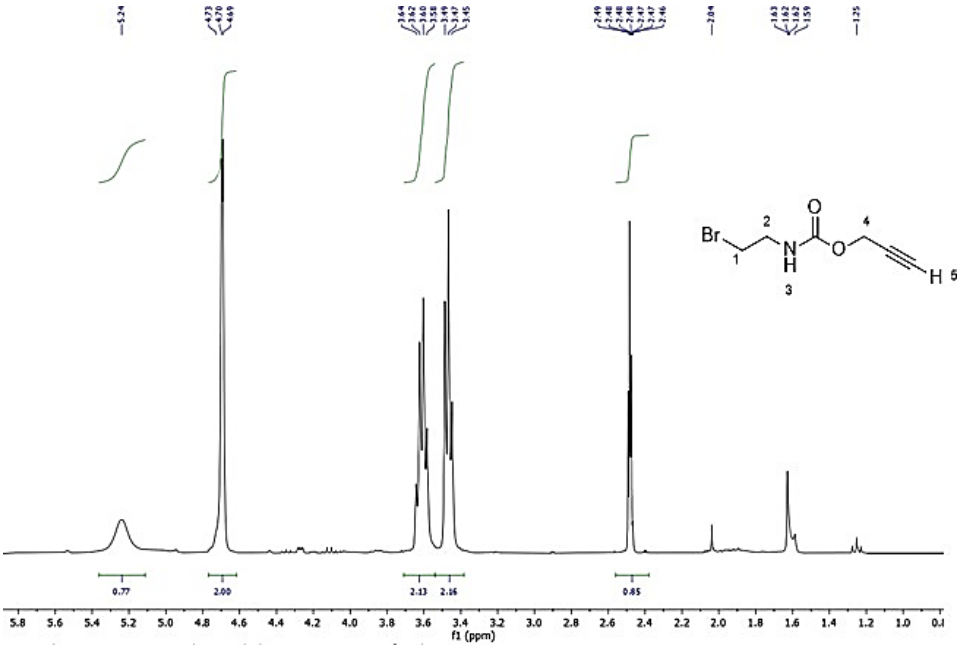

Figure 5.17. ^{1}H-NMR spectrum of **3**.

^{13}C-NMR (75 MHz, CDCl3): δ 155.22 (Cq, *C*^{3}=O), 77.94 (Cq, *C*^{5}≡CH), 74.80 (C≡*C*^{6}H), 52.70 (-*C*^{4}H$_2$C≡CH), 42.77 (-*C*^{2}H$_2$NH-), 32.20 (-*C*^{1}H$_2$Br) ppm

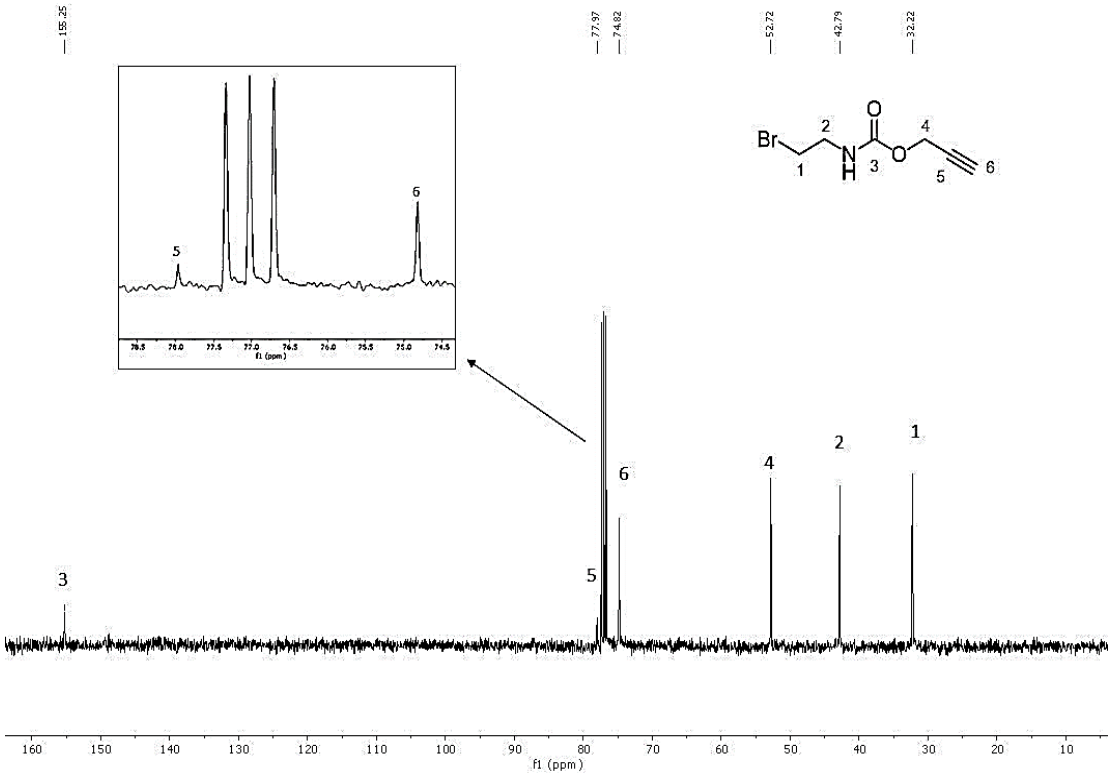

Figure 5.18. ^{13}C-NMR spectrum of **3**.

- **Synthesis of prop-2-yn-1-yl (2-(3,5-dibromophenoxy)ethyl)carbamate (5)**

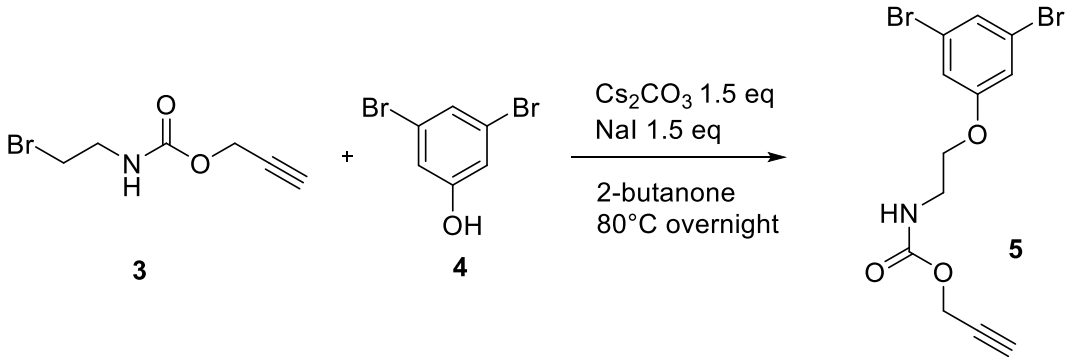

Scheme 5.4. Synthesis of **5**.

A solution of crude **3** (1 g, 2.63 mmol due to the presence of ethyl acetate) and 3,5-dibromophenol (**4**, 1.911 g, 7.59 mmol, 2.88 eq) was prepared in 2-butanone (90 mL). Cs_2CO_3 (2.472 g, 7.59 mmol, 2.88 eq) and NaI (1.137 g, 7.59 mmol, 2.88 eq) were added. The rection

is kept overnight at reflux temperature (80 °C) under magnetic stirring. The solution is then cooled at room temperature and concentrated under vacuum. The solid residual is dissolved in CH_2Cl_2 (20 mL) and NaOH 10% w/w (20 mL) and stirred for ten minutes. The organic layer and the aqueous layer are divided with a separating funnel. The aqueous phase is washed with CH_2Cl_2 (3 x 10 mL), and the washings are added to the organic phase. The organic phase is washed with NaOH 10% w/w (3 x 10 mL), dried with Mg_2SO_4, filtered, and concentrated under vacuum. The final product is a yellow solid (1.043 g, 2.27 mmol, 86% yield). Rf (in Petroleum Ether/ Ethyl Ether 1:2): 0.35.

^{1}H-NMR (300 MHz; DMSO): δ =7.55 (t, ^{3}J=5.4, N*H*$^{\mathbf{5}}$); 7.36 (t, ^{4}J=1.64, 1H, Ar-*H*$^{\mathbf{1}}$); 7.20 (d,^{4}J=1.64, 2H, Ar-*H*$^{\mathbf{2}}$); 4.63 (d, ^{4}J=2.4, 2H, O-C*H*$_2^{\mathbf{6}}$); 4.04 (t; ^{3}J=5.2, 2H, O-C*H*$_2^{\mathbf{3}}$); 3.47 (t, ^{4}J=2.4,1H, C≡C*H*$^{\mathbf{7}}$), 3.34 (d, ^{3}J=5.7, 2H; NH-C*H*$_2^{\mathbf{4}}$, partially covered by the water peak).

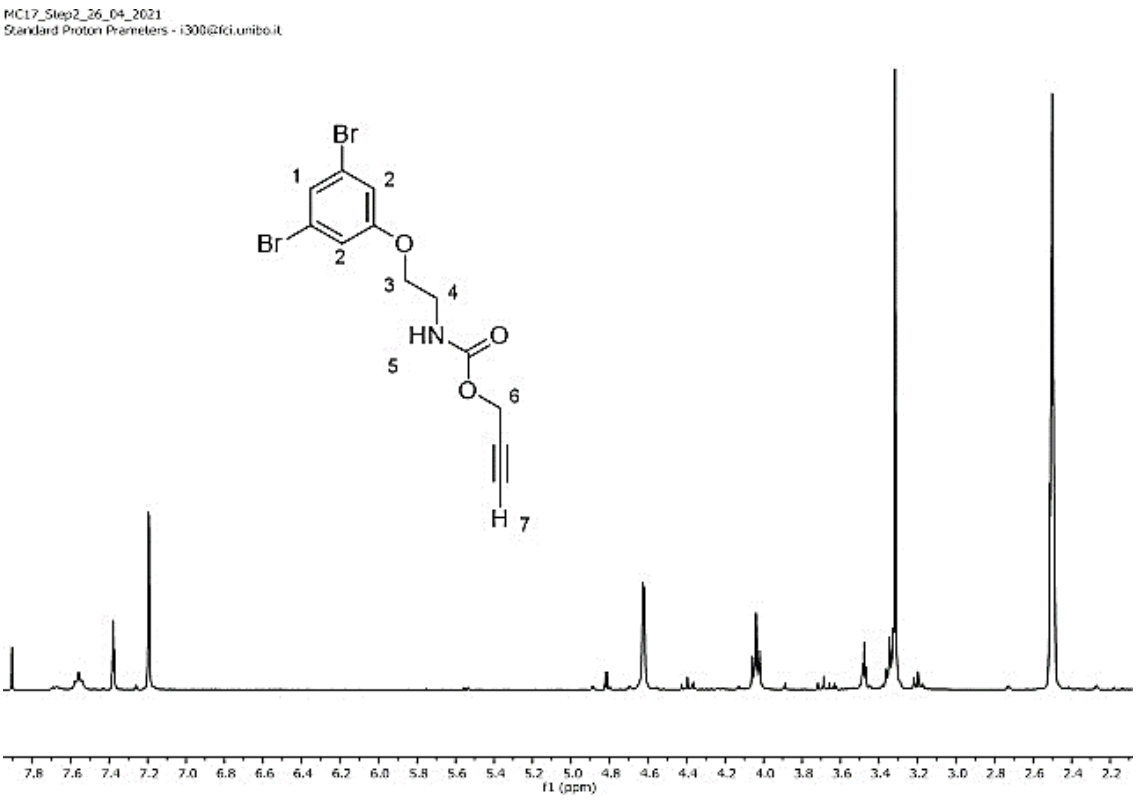

Figure 5.19. ^{1}H-NMR spectrum of **5**.

^{13}C-NMR (75 MHz; DMSO): δ = 159.95 (Cq, Ar-*C*^{4}-OH), 155.46 (Cq, *C*^{7}=O); 132.91 (Ar-*C*^{1}-H); 125.79 (Ar-*C*^{2}-Br); 122.82 (Ar-*C*^{3}-H); 117.17 (NH-*C*^{6}H$_2$); 79.31 (Cq, *C*^{9}≡CH); 77.14 (C≡*C*^{10}H); 67.11 (O-*C*^{5}H$_2$); 51.63 (O-*C*^{8}H$_2$).

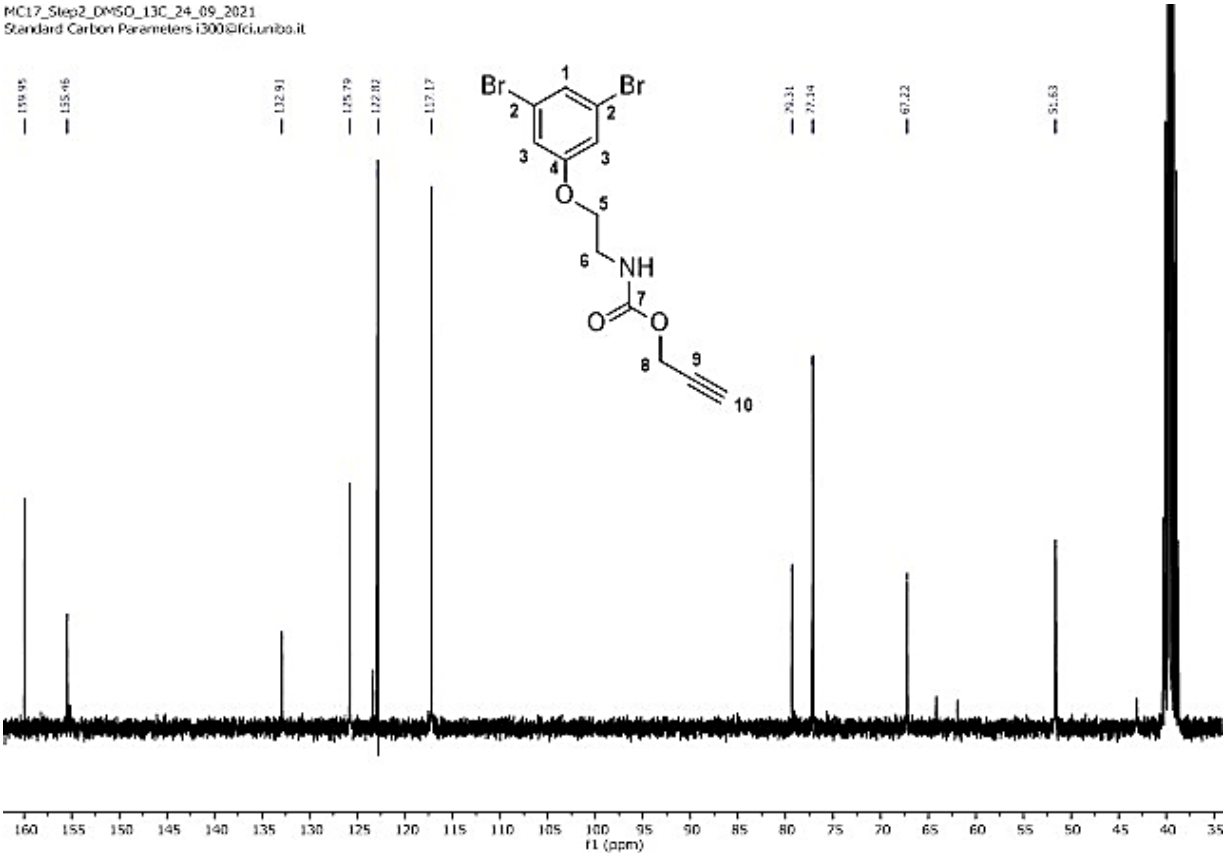

Figure 5.20. ^{13}C-NMR spectrum of **5**.

ATR-FTIR spectra of neat 5 (cm^{-1}): 3331 (ν NH, m), 3293 (ν ≡C-H, m), 2949 (ν C-H aliphatic, w), 2131 (ν -C≡C-, w), 1703 (ν -C(O)NH- carbamate, s), 1520 (δ NH, s), 1245 (ν C-O,

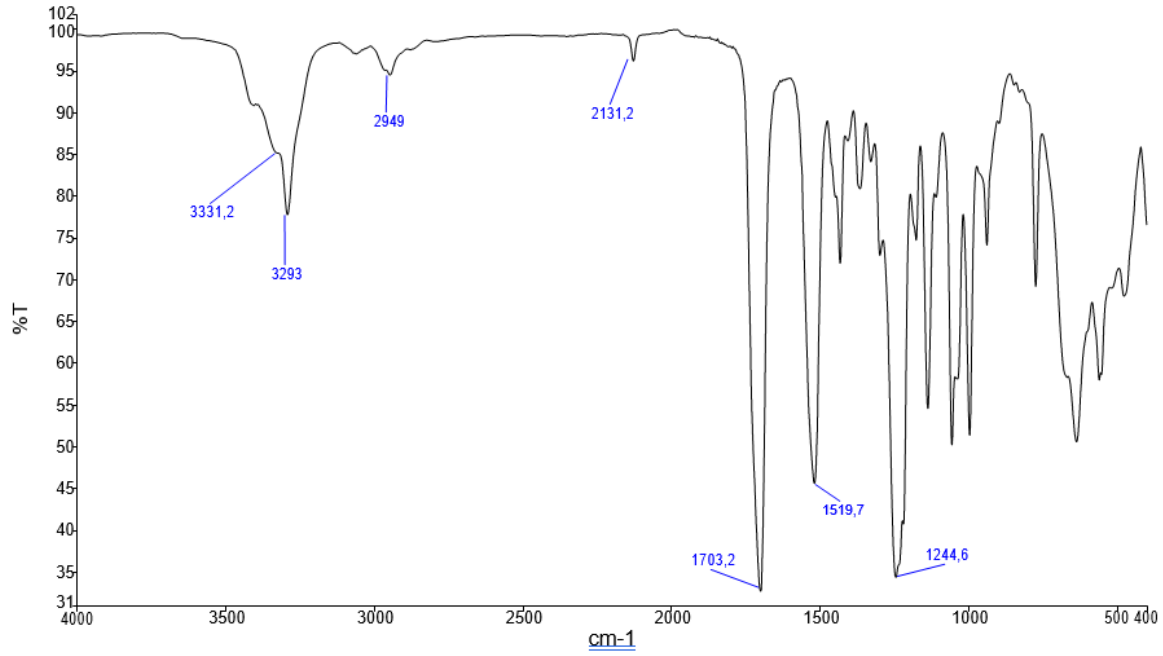

Figure 5.21. IR-ATR Spectrum of **5**.

- **Attempted synthesis of 5'-(2-(((prop-2-yn-1-loxy)carbonyl)amino)ethoxy)-[1,1':3',1''-terphenyl]-4,4''-dicarboxylic acid (H2YL80) (first approach)**

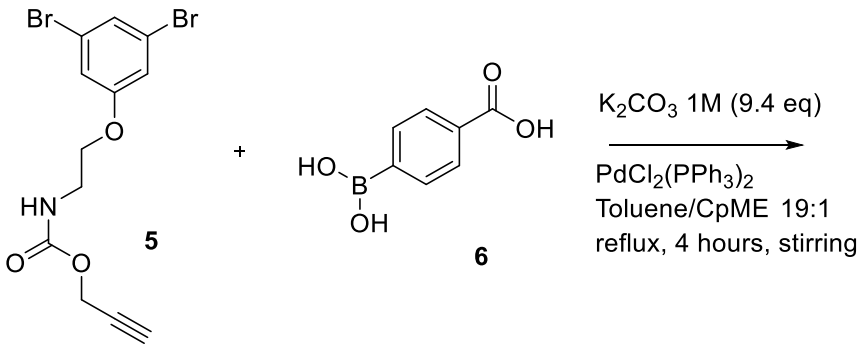

Scheme 5.5. Attempted synthesis of 5'-(2-(((prop-2-yn-1-yloxy)carbonyl)amino)ethoxy)-[1,1':3',1''-terphenyl]-4,4''-dicarboxylic acid [first approach].

In a two-necked round flask, crude **5** (0.2 g, 0.53 mmol) and 4-boronobenzoic acid (**6**, 0.29 g, 1.75 mmol, 3.3 eq) are dissolved in a mixture of toluene/Cyclopenthyl Methyl Ether (CPME) 19:1 (10 mL). A solution of K_2CO_3 1 M (5 mL, 5 mmol, 9.4 eq) is added, then the flask undergoes 3 vacuum/nitrogen cycles. While fluxing nitrogen, a spatula of the catalyst $PdCl_2(PPh_3)_2$ is added. The system is stirred at reflux temperature (110 °C) for 4 hours, keeping the flask wrapped in tin foil. The solution is then filtered on celite and washed with toluene (10 mL) and water (10 ml). The solution is extracted with a mixture of Ethyl Acetate/Hexane 1:1 (2 x 20 mL). The aqueous and the organic phases are separated. The aqueous layer is diluted with water (15 mL) and then 10 mL of HCl 1 M are added. The formation of a white precipitate is observed. The solid is filtered and dried in the oven. The organic layer is dried with Mg_2SO_4, filtered, and concentrated under vacuum. The ^{1}H-NMR analysis showed that the products found in the organic phase and in the aqueous phase are respectively the unreacted reagents **5** and **6** (Fig. 5.22 and 5.23).

^{1}H-NMR organic phase (400 MHz, DMSO) : δ =7.55 (t, ^{3}J=5.4, N*H*^{5}); 7.36 (t, ^{4}J=1.64, 1H, Ar-*H*^{1}); 7.20 (d, ^{4}J=1.64, 2H, Ar-*H*^{2}); 4.89 (d, ^{4}J=2.4, 2H, O-C*H*2^{6}); 4.04 (t; ^{3}J=5.2, 2H, O-C*H*2^{3}); 3.47 (t, ^{4}J=2.4, 1H, C≡C*H*^{7} partially covered by the water peak).

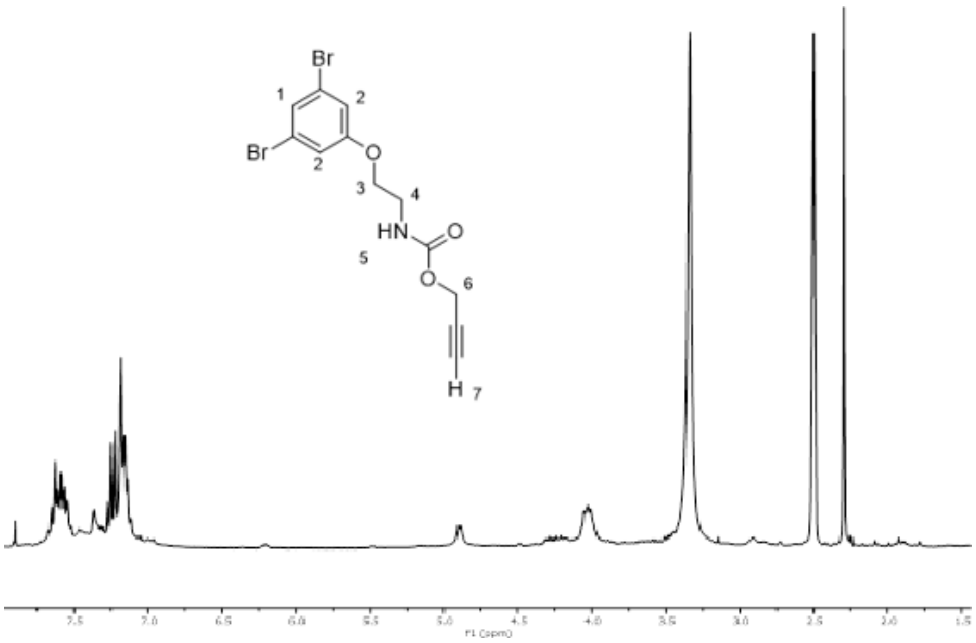

Figure 5.22. ^{1}H-NMR spectrum of the organic phase, showing the presence of reagent **5** with some impurities.

^{1}H-NMR aqueous phase (400 MHz, DMSO) : δ = 8.24 (s, 1H, O*H*^{3}), 7.87 (s, 2H, Ar-*H*^{1}), 7.87 (s, 2H, Ar-*H*^{2}) (the aromatic protons 1 and 2 are different but their signals fall at thesame chemical shift).

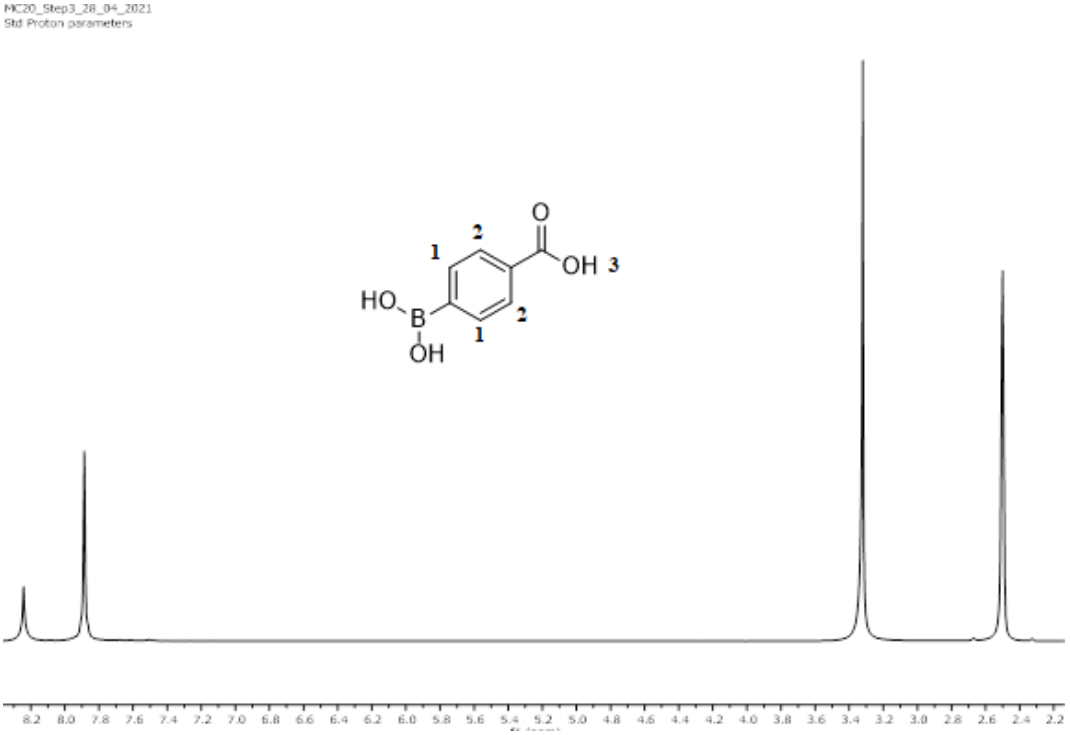

Figure 5.23. ^{1}H-NMR spectrum of the product found in the organic phase, showing the presence of reagent **6**.

Second approach

- **Synthesis of 3,5-Bis(4-carboxyphenyl)-1-hydroxybenzene (7)**

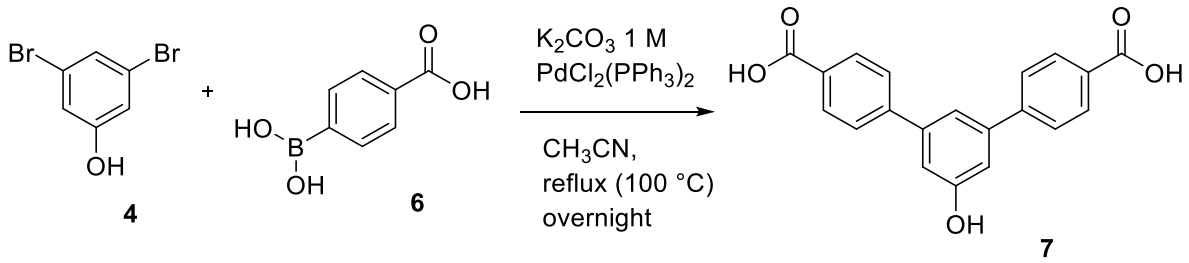

Scheme 5.6. synthesis of **(7)**.

In a two-necked round flask, a solution of **4** (1.8 g, 7.15 mmol) and **6** (2.373 g, 14.3 mmol, 2 eq) is prepared in CH_3CN (60 mL). A solution of K_2CO_3 1 M (57.2 mL, 52.7 mmol, 7.4 eq) is added, and the system undergoes 3 vacuum/nitrogen cycles. The catalyst $PdCl_2(PPh_3)_2$ (0.1 g,

0.143 mmol, 2% catalytic load) is added while fluxing nitrogen, then the flask is wrapped in tin foil, and the system is put at reflux temperature (100 °C) under magnetic stirring overnight. Then the solution is cooled down to room temperature, filtered on celite, washed with DI water (3 x 10 mL) and extracted with a mixture of Ethyl acetate/hexane 1:1 (3 x 50 mL). The organic layer is treated with HCl 2 M (55 mL), and the formation of a dark precipitate is observed. The solution is filtered and the solid is dried in the oven overnight. The final product **7** weights 2.213 g (6.62 mmol, 92.6% yield).

ESI-MS(-) (MeOH, m/z): 333(100) $[C_{20}H_{13}O_5]^-$.

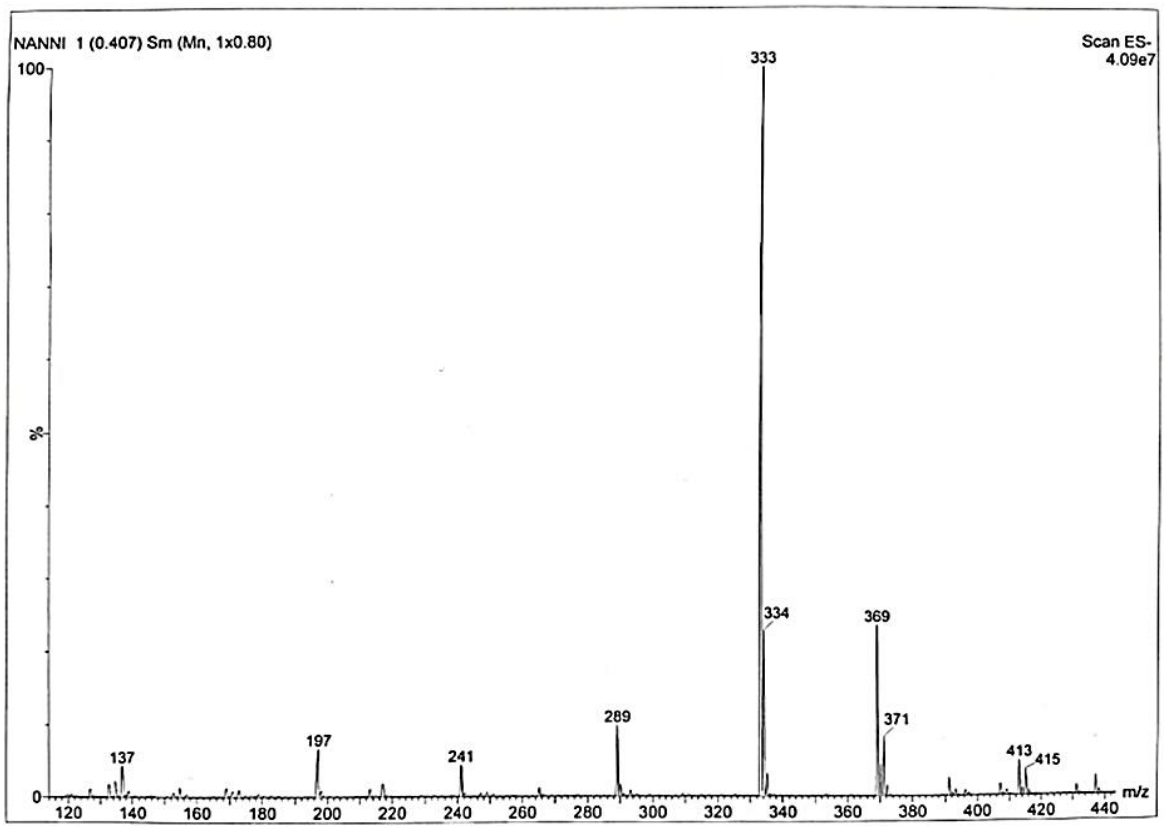

Figure 5.24. ESI-MS(-) spectrum of **7**.

^{1}H-NMR (300 MHz, DMSO): δ= 12.97 (s, 2H) 9.91 (s, 1H), 8.03 (d, 4H, ^{3}J= 8.41 Hz), 7.85 (d, 4H, ^{3}J= 8.41 Hz), 7.46 (t, 1H, ^{4}J= 1.88 Hz), 7.15 (d, 2H, ^{4}J=1.88 Hz).

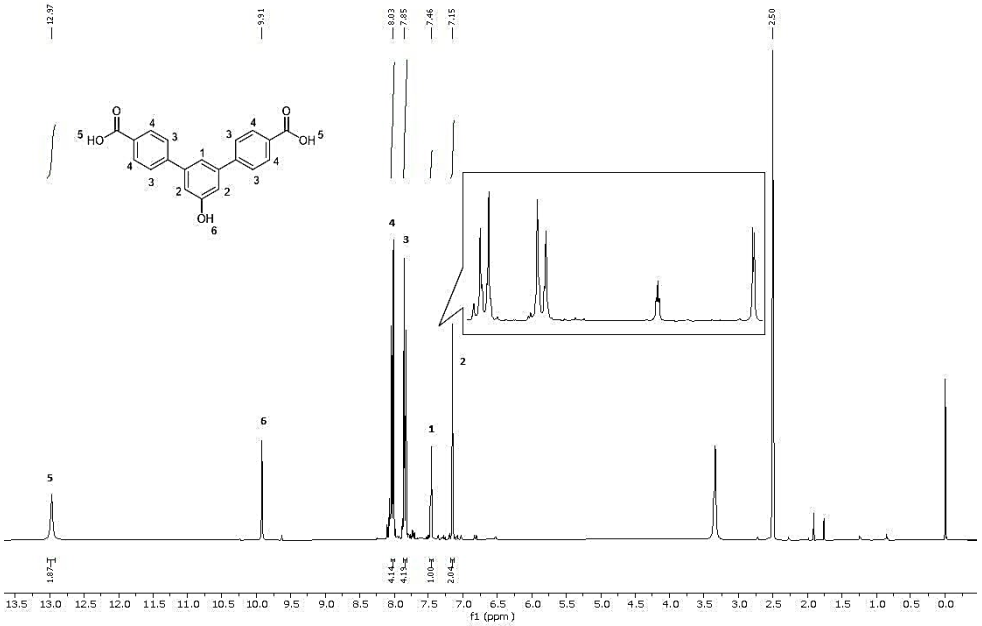

Figure 5.25. ^{1}H-NMR spectrum of **7**.

^{13}C-NMR (100.6 MHz, DMSO): 167.13 (Cq; C^{9}(O)OH); 158.56 (Cq; Ar-C^{4}-OH); 144.26 (Cq; Ar-C^{5}-Ar); 141.19 (Cq; Ar-C^{2}-Ar); 129.93 (Cq; Ar-C^{8}-C(O)OH); 129.82 (Ar-C^{6}H);127.00 (Ar-C^{7}H);116.64 (Ar-C^{1}H); 113.15 (Ar-C^{3}H).

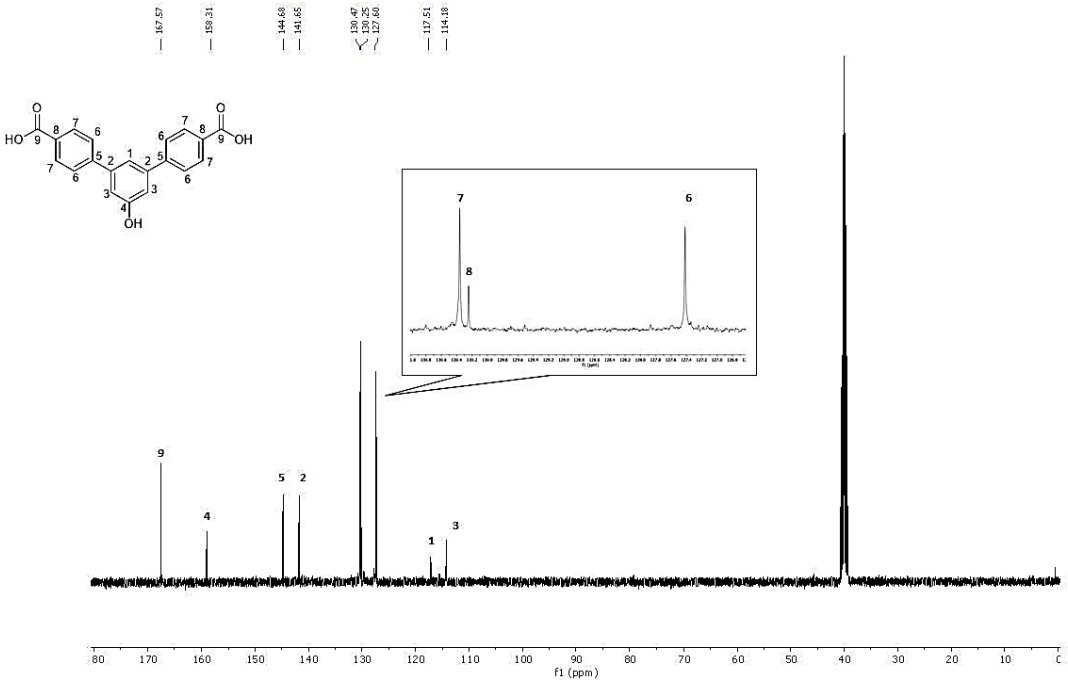

Fig. 5.26. ^{13}C-NMR spectrum of **7**.

ATR-FTIR spectra of neat 7 (cm^{-1}): 3398 (ν O-H alcol, m), 3196 (ν O-H acid, m), 2984 (ν C-H aliphatic, w), 1676 (ν C(O)OH, s), 1285 (ν C-O acid, s), 1181 (ν C-O alcol, s), 839 (δ C-H aromatic), 767 (δ C-H aromatic).

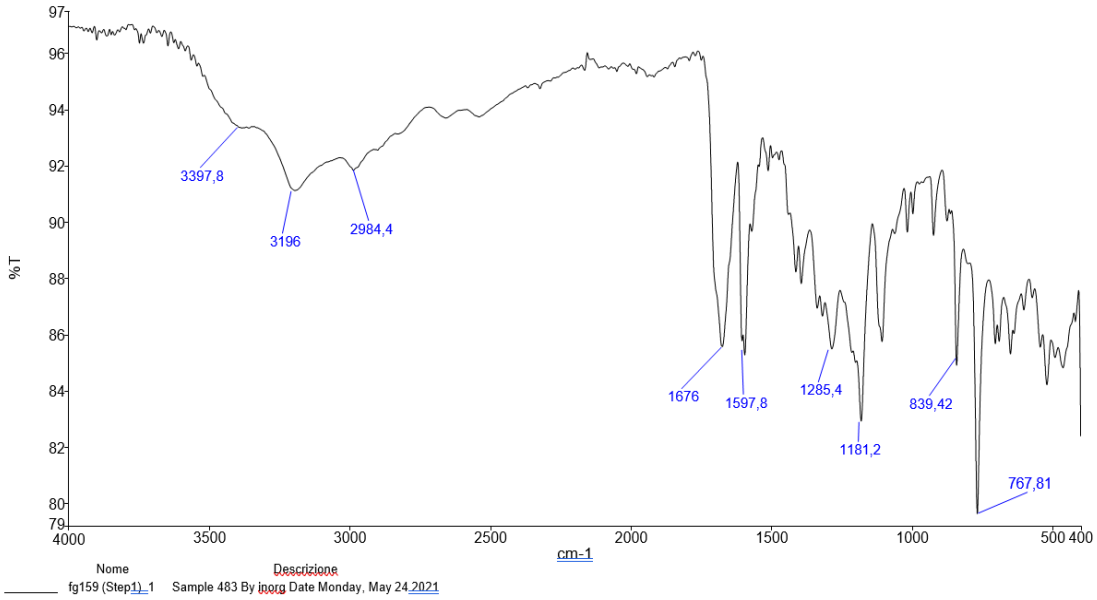

Figure 5.27. IR-ATR spectrum of **7**.

- **Synthesis of dimethyl 5'-hydroxy-[1,1':3',1''-terphenyl]-4,4''-dicarboxylate (8)**

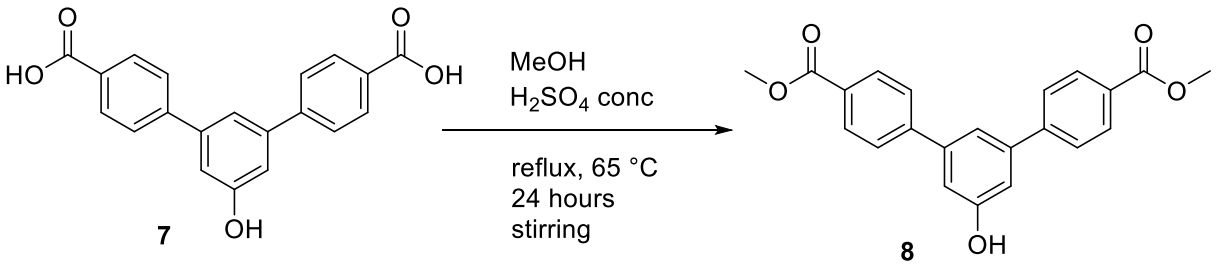

Scheme 5.7. synthesis of **8**.

A solution of **7** (0.779 g, 2.33 mmol) in methanol (80 mL) is prepared. Concentrated H_2SO_4 (1.30 mL, 23.6 mmol, ~10 eq) is added while keeping the solution stirred. The system is stirred for 24 hours at reflux temperature (65 °C). The solution is then cooled down to 0 °C, and 200 mL of DI water are slowly added. The formation of a pink-orange precipitate is observed. The solution is filtered and the solid is dried in the oven overnight. The final product is a pink solid (0.668 g, 2.06 mmol, 88% yield). Rf (in Petroleum Ether/ Ethyl Ether 1:2): 0.32.

ESI-MS(-) (MeOH, m/z): 361(100) $[C_{22}H_{17}O_5]^-$.

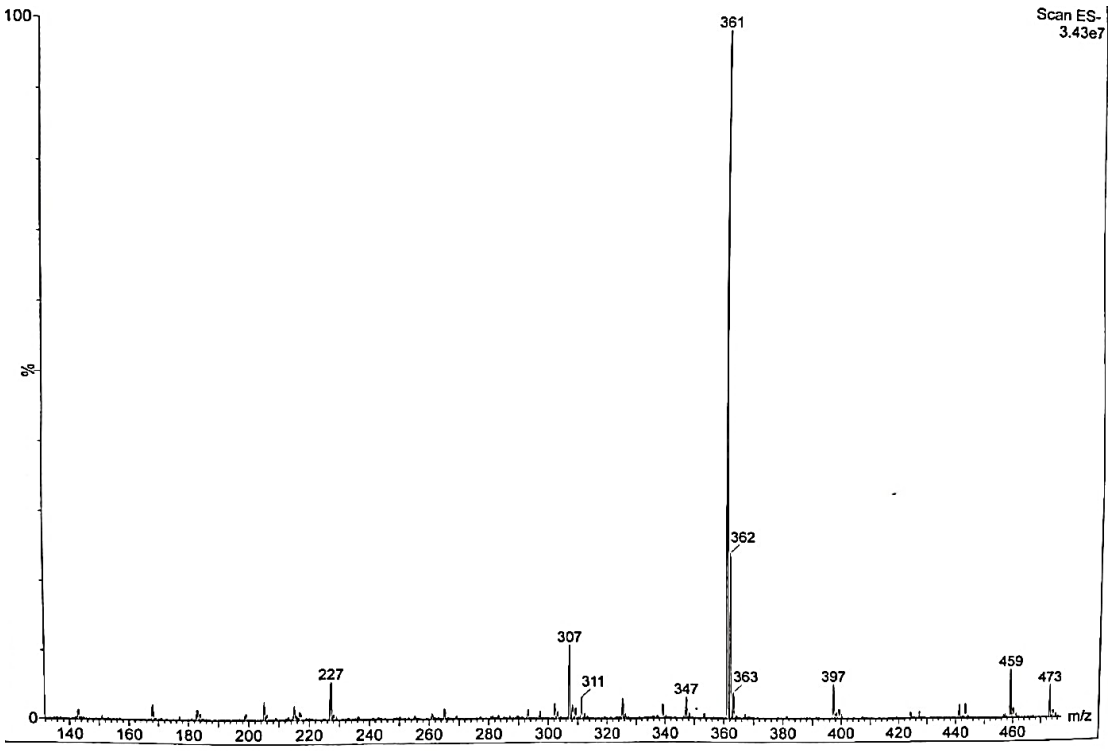

Figure 5.28. ESI-MS(-) spectrum of **8**.

^{1}H-NMR (300 MHz, DMSO): δ= 9.92 (s, 1 H, -O*H*^{6}); 8.03 (d, ^{3}J=9.00, 4H; Ar-*H*^{2}); 7.89 (d, ^{3}J=9.00, 4H; Ar-*H*^{3}); 7.48 (t, ^{4}J=1.50, 1H; Ar-*H*^{4}); 7.16 (d; ^{4}J=1.50, 2H; Ar-*H*^{5}); 3.88 (s; 6H; O-C*H*3^{1}).

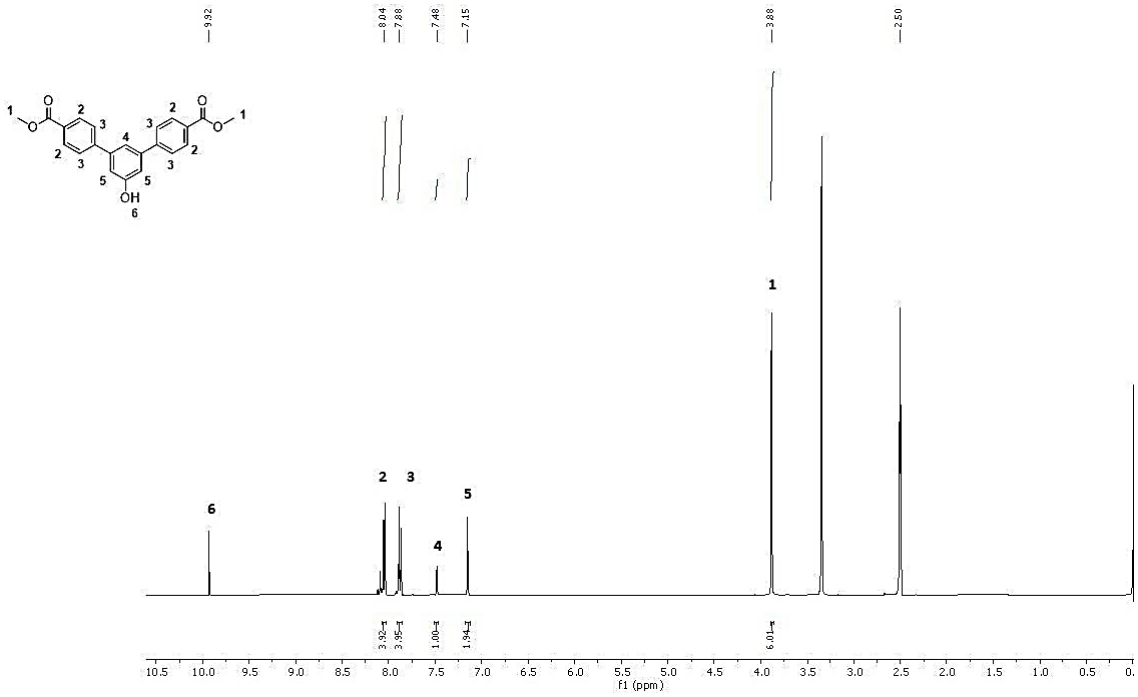

Figure 5.29. ^{1}H-NMR spectrum of **8**.

^{13}C-NMR (DMSO, 100.6 MHz): δ= 166.51 (Cq; C^{9}(O)OH); 158.98 (Cq; Ar-C^{4}-OH); 144.54(Cq; Ar-C^{5}-Ar); 140.02 (Cq; Ar-C^{2}-Ar); 130.23 (Cq; Ar-C^{8}-C(O)OCH3); 129.10 (Ar-C^{6}H); 127.60 (Ar-C^{7}H); 117.15 (Ar-C^{1}H); 114.31 (Ar-C^{3}H); 52.62 (O-C^{10}H3).

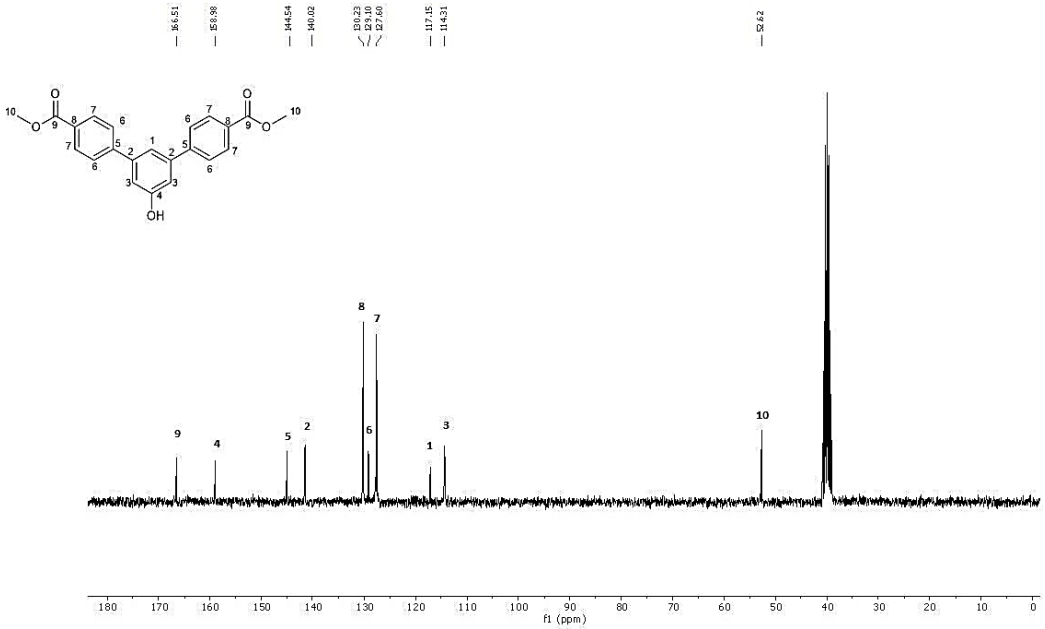

Figure 5.30. ^{13}C-NMR spectrum of **8**.

ATR-FTIR spectra of neat 8 (cm^{-1}): 3361 (ν O-H alcol, m), 1696 (ν C(O)OH, s), 1276 (ν C-O acid, s), 1192 (ν C-O alcol, s), 845 (δ C-H aromatic), 766 (δ C-H aromatic).

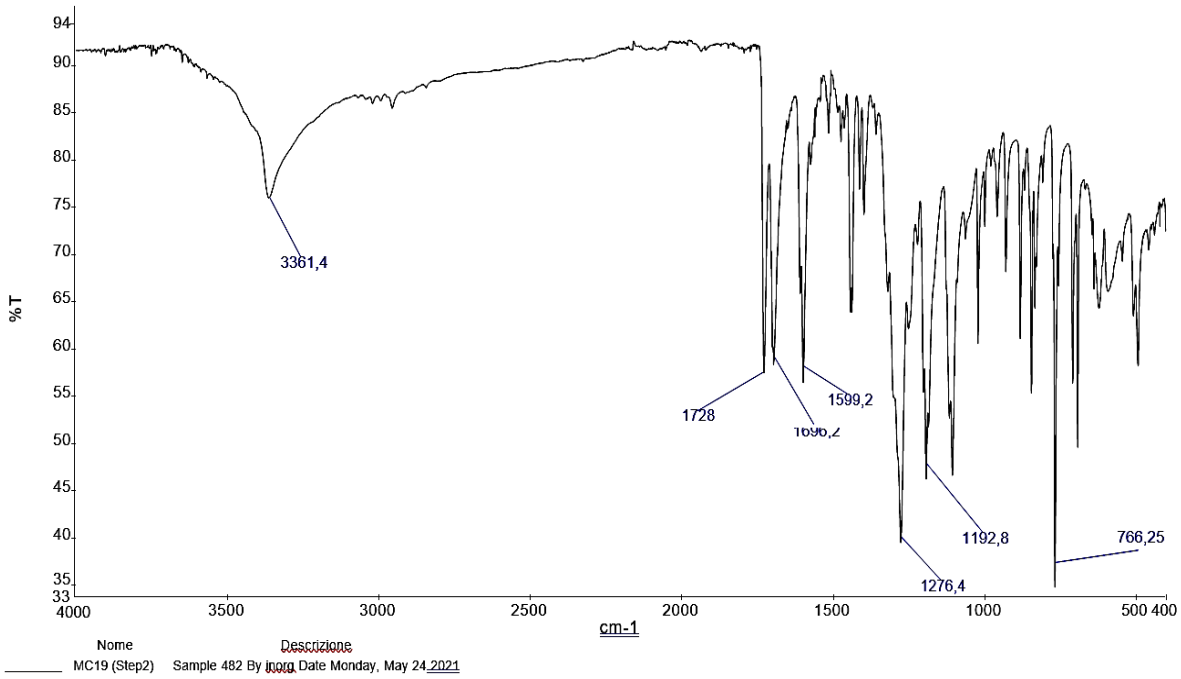

Figure 5.31. IR-ATR spectrum of **8**.

- **Synthesis of dimethyl 5'-(2-(((prop-2-yn-1-yloxy)carbonyl)amino)ethoxy)-[1,1':3',1''-terphenyl]-4,4''-dicarboxylate (9)**

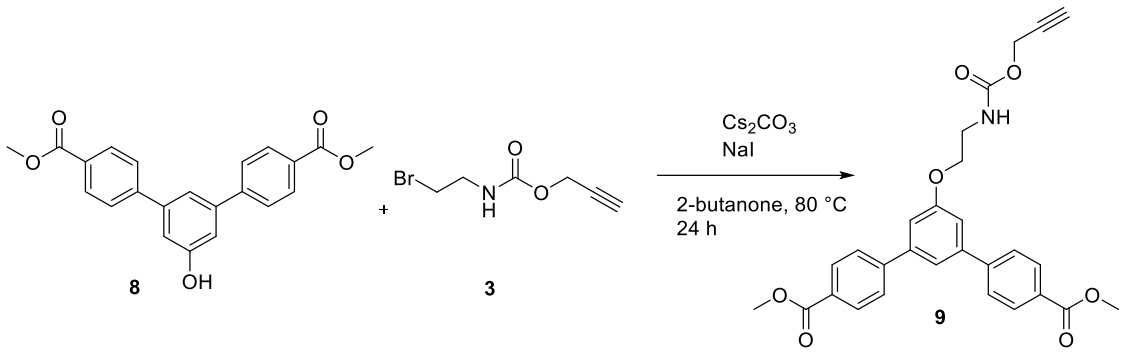

Scheme 5.8: synthesis of **(9)**.

A solution of **8** (1.208 g, 3.3 mmol, 1.5 eq) and **3** 0.451 g, 2.2 mmol) in 2-butanone (30 mL) is treated with Cs_2CO_3 (1.075 g, 3.3 mmol, 1.5 eq) and NaI (0.494 g, 3.3 mmol, 1.5 eq). The solution is stirred at reflux temperature (80 °C) for 24 hours. The solution is then cooled down at room temperature, concentrated in vacuum and diluted with CH_2Cl_2 (25 mL) and NaOH 10% w/w (25 mL). With a separating funnel the aqueous layer and the organic layer are divided. The aqueous layer is washed with CH_2Cl_2 (3 x 20 mL) and the washings are added to the organic phase. The organic layer is washed with NaOH 10% w/w (3 x 20 mL), then dried with Mg_2SO_4, filtered, and dried under vacuum overnight. The final product is a light-brown sticky solid (0.86 g, 1.76 mmol, 80% yield). Rf (in Petroleum Ether/ Ethyl Ether 1:2): 0.32.

ESI-MS(-) (MeOH, m/z): 510 (100) $[C_{28}H_{25}NO_7+Na]^+$.

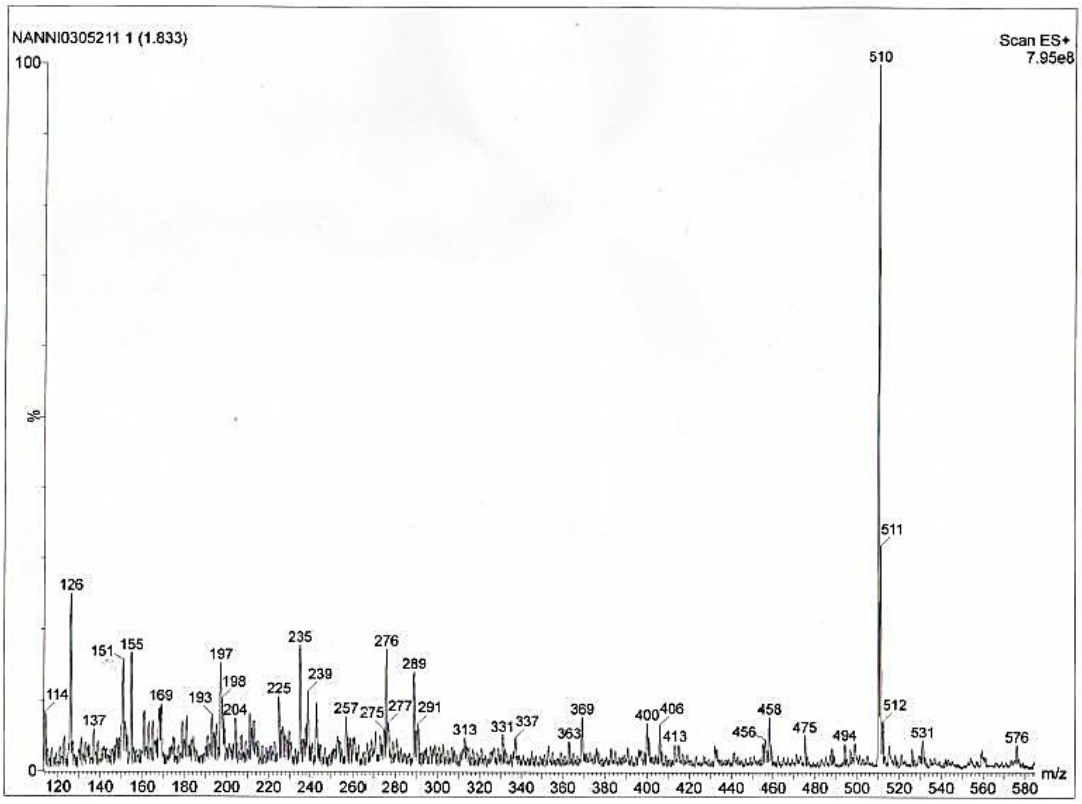

Figure 5.32. ESI-MS(+) spectrum of **9**.

^{1}H-NMR (300 MHz, DMSO): δ= 8.04 (d, ^{3}J=8.55, 4H; Ar-*H*$^{\mathbf{4}}$);7.93 (d, ^{3}J=8.55, 4H; Ar-*H*$^{\mathbf{3}}$); 7.63 (t, ^{4}J=1.50, 1H; Ar-*H*$^{\mathbf{1}}$); 7.32 (d; ^{4}J=1.50, 2H; Ar-*H*$^{\mathbf{2}}$); 4.62 (d; ^{4}J=2.4; 2H; O-*C*H2$^{\mathbf{9}}$); 4.16 (t; ^{3}J=5.4, 2H; O-*C*H2$^{\mathbf{6}}$); 3.89 (s; 6H; O-C*H*3$^{\mathbf{5}}$) 3.46 (t, ^{4}J=2.4; 1H, C≡C*H*$^{\mathbf{10}}$); 3.42 (t, ^{3}J=5.4, 2H; NH-C*H*2$^{\mathbf{7}}$).

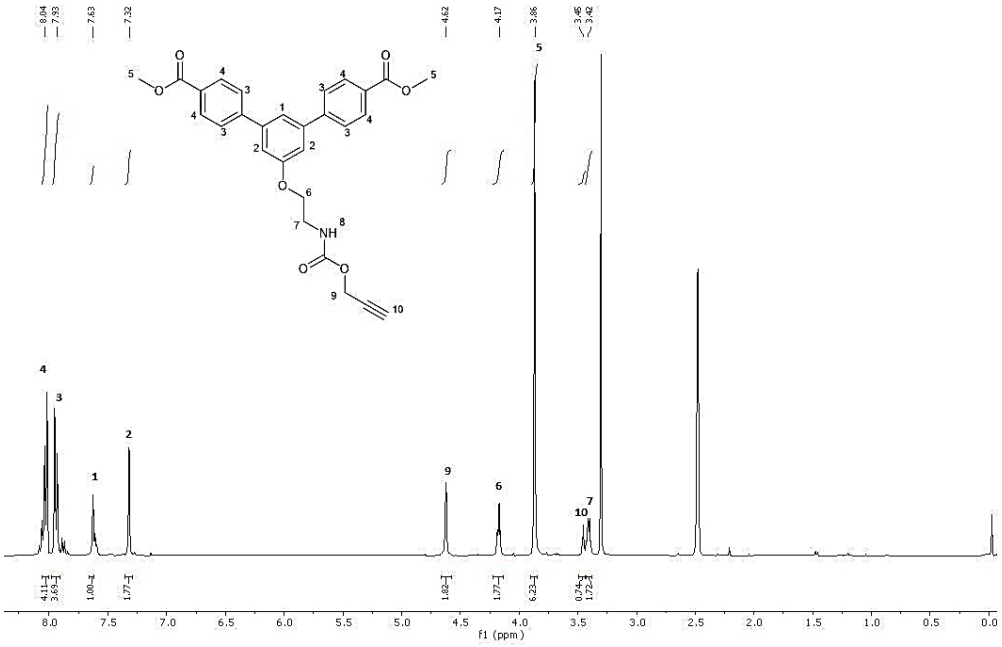

Figure 5.33. ^{1}H-NMR spectrum of **9**.

^{13}C-NMR (DMSO, 100.6 MHz): δ= 166.49 (Cq; *C*^{9}(O)OCH3); 159.93 (Cq; Ar-*C*^{4}-OCH2);155.94 (Cq; NH-*C*^{13}(O)O); 144.57 (Cq; Ar-*C*^{5}-Ar); 141.51 (Cq; Ar-*C*^{3}-Ar); 130.32 (Cq; Ar-*C*^{6}-C(O)OCH3); 129.22 (Ar-*C*^{8}H); 127.80 (Ar-*C*^{7}H); 118.31 (Ar-*C*^{1}H); 113.67 (Ar-*C*^{2}H); 79.77 (-CH2-*C*^{15}≡CH); 77.58 (-C≡*C*^{16}H); 67.15 (-O-*C*^{11}H2-); 52.63 (-O-*C*^{14}H2-); 52.05 (-O-*C*^{10}H3);

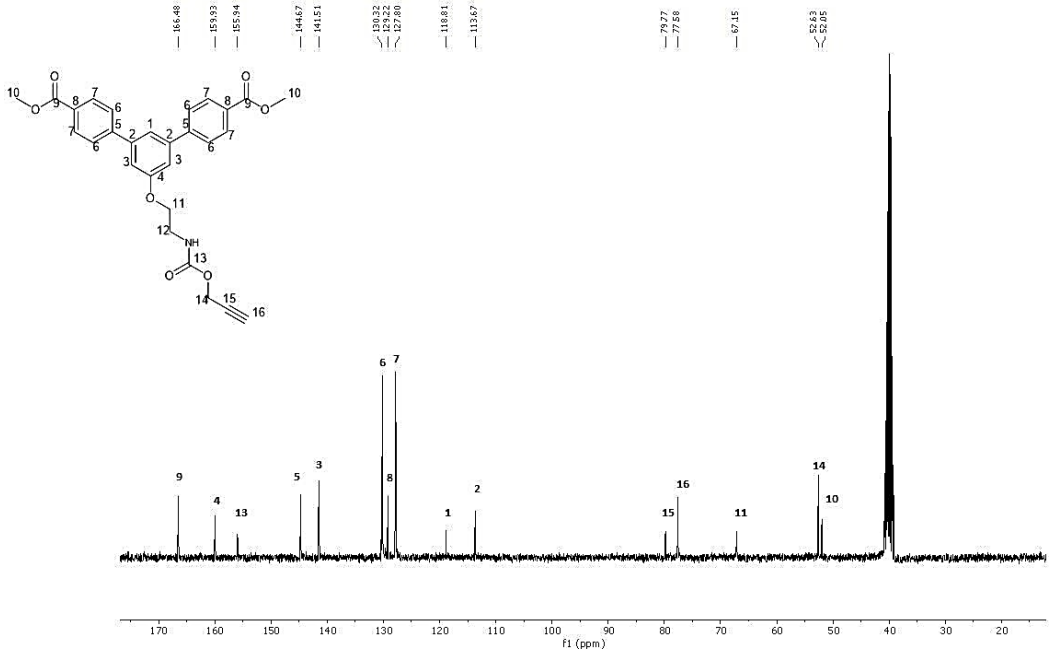

Figure 5.34. ^{13}C-NMR spectrum of **9**.

ATR-FTIR spectra of neat (10) (cm^{-1}): 3298 (ν ≡C-H), 2958 (ν C-H aliphatic, w), 2130 (ν C≡C), 1713 (ν C(O)OCH3, s), 1606 (ν C=O, s), 1535 (ν N-H, s), 1281(ν -C(O)O-), 808 (δ bending), 767 (δ bending).

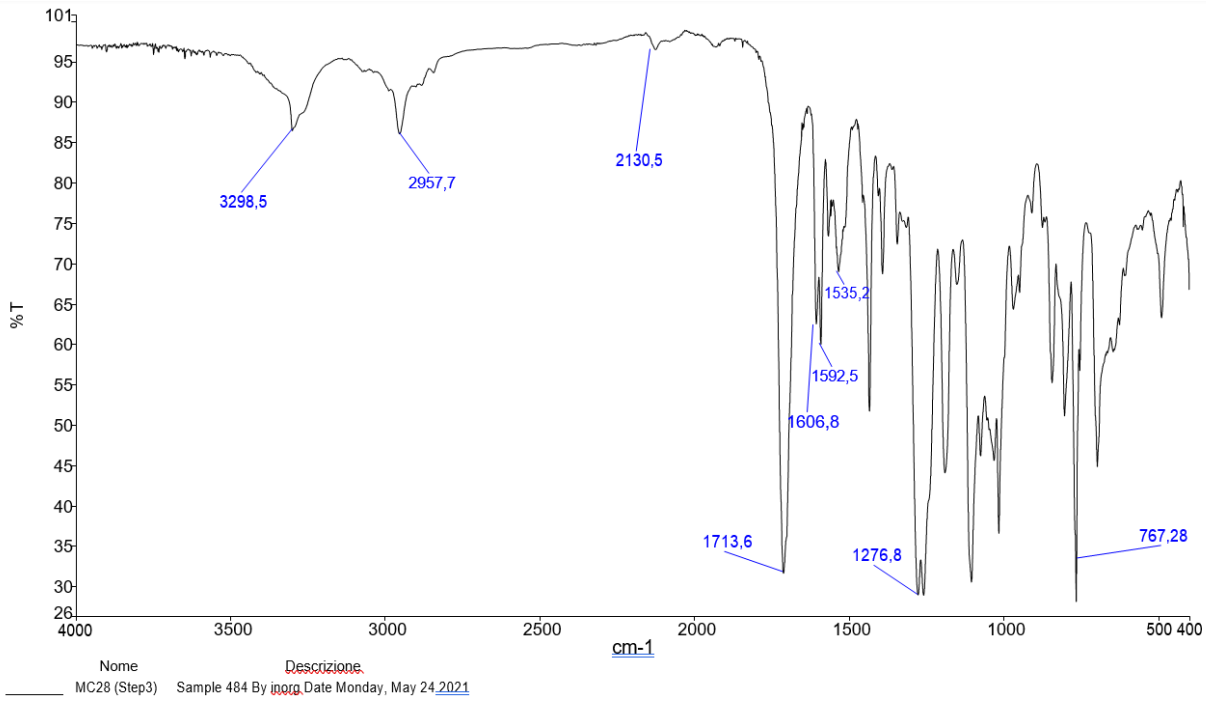

Figure 5.35. IR-ATR spectrum of **9**.

- **Synthesis of 5'-(2-(((prop-2-yn-1-yloxy)carbonyl)amino)ethoxy)-[1,1':3',1''-terphenyl]-4,4''-dicarboxylic acid (10, H_2YL_{80})**

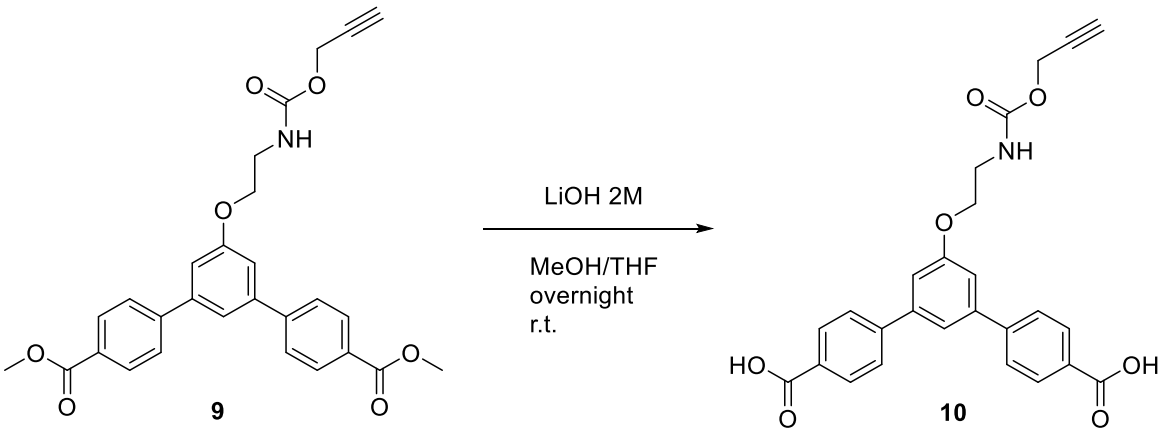

Scheme 5.8: synthesis of **10**.

A solution of **9** (0.82 g, 1.68 mmol) is prepared using a mixture of Methanol/THF 1:1 (20 mL). The system is put under magnetic stirring, and a solution of LiOH 2 M is added (4.2 mL, 8.4 mmol, 5 eq). The solution is stirred overnight at room temperature, then is concentrated under vacuum, and diluted with DI water (10 mL). The system is then treated with HCl 1 M (15 x 1 mL) and the formation of a white precipitate is observed. The solution is filtered and the solid is washed with DI water (50 mL) and dried in the oven overnight. The resulting product is a white solid (0.588 g, 1,28 mmol, 76% yield). Rf (in Petroleum Ether/ Ethyl Ether 1:2): 0.15.

ESI-MS(-) (MeOH, m/z): 482 (100) $[C_{26}H_{21}NO_7 + Na]^+$.

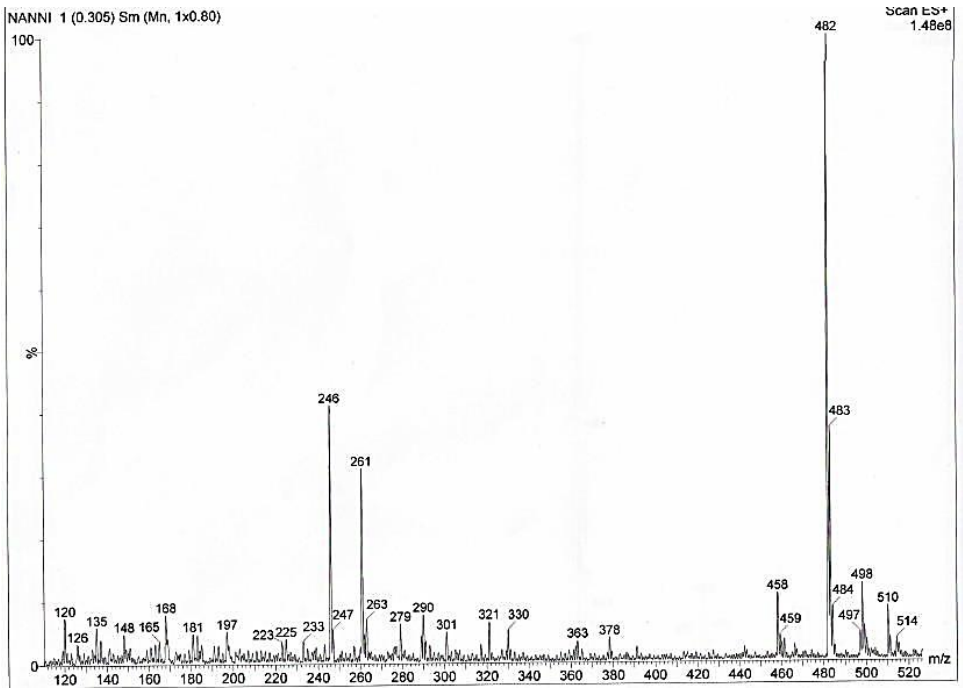

Figure 5.36. ESI-MS(+) spectrum of **(10)**.

^{1}H-NMR (300 MHz, DMSO): δ= 8.02 (d, ^{3}J=8.55, 4H; Ar-*H*$^{\mathbf{4}}$); 7.92 (d, ^{3}J=8.55, 4H; Ar-*H*$^{\mathbf{3}}$);7.62 (t, ^{4}J=1.50, 1H; Ar-*H*$^{\mathbf{1}}$); 7.31 (d; ^{4}J=1.50, 2H; Ar-*H*$^{\mathbf{2}}$); 4.62 (d; ^{4}J=2.4; 2H; O-*C*H$_2^{\mathbf{9}}$); 4.18(t; ^{3}J=5.4, 2H; O-*C*H$_2^{\mathbf{6}}$); 3.48 (t, ^{4}J=2.4; 1H, C≡C*H*$^{\mathbf{10}}$); 3.42 (t, ^{3}J=5.4, 2H; NH-C*H*$_2^{\mathbf{7}}$).

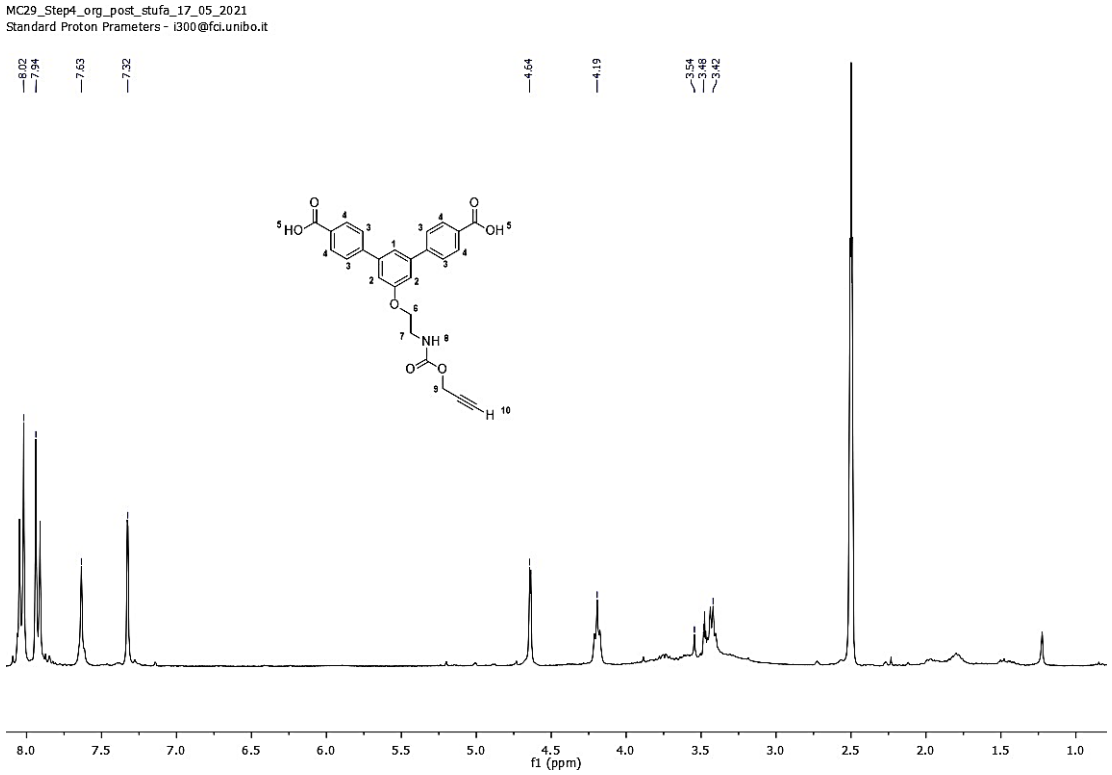

Figure 5.37. ^{1}H-NMR spectrum of **10** in DMSO.

^{1}H-NMR (300 MHz, MeOH): δ=8.10 (d, ^{3}J=7.80, 4H; Ar-*H*^{4}); 7.82 (d, ^{3}J=7.80, 4H; Ar-*H*^{3});7.55 (t, ^{4}J=1.45, 1H; Ar-*H*^{1}); 7.28 (d; ^{4}J=1.50, 2H; Ar-*H*^{2}); 4.67 (d; ^{4}J=2.4; 2H; O-*C*H ^{9}); 4.20 (t; ^{3}J=5.4, 2H; O-*C*H2^{6}); 3.57 (t, ^{3}J=5.4, 2H; NH-C*H*2^{7}) 2.86 (t, ^{4}J=2.4; 1H, C≡C*H*^{10}).

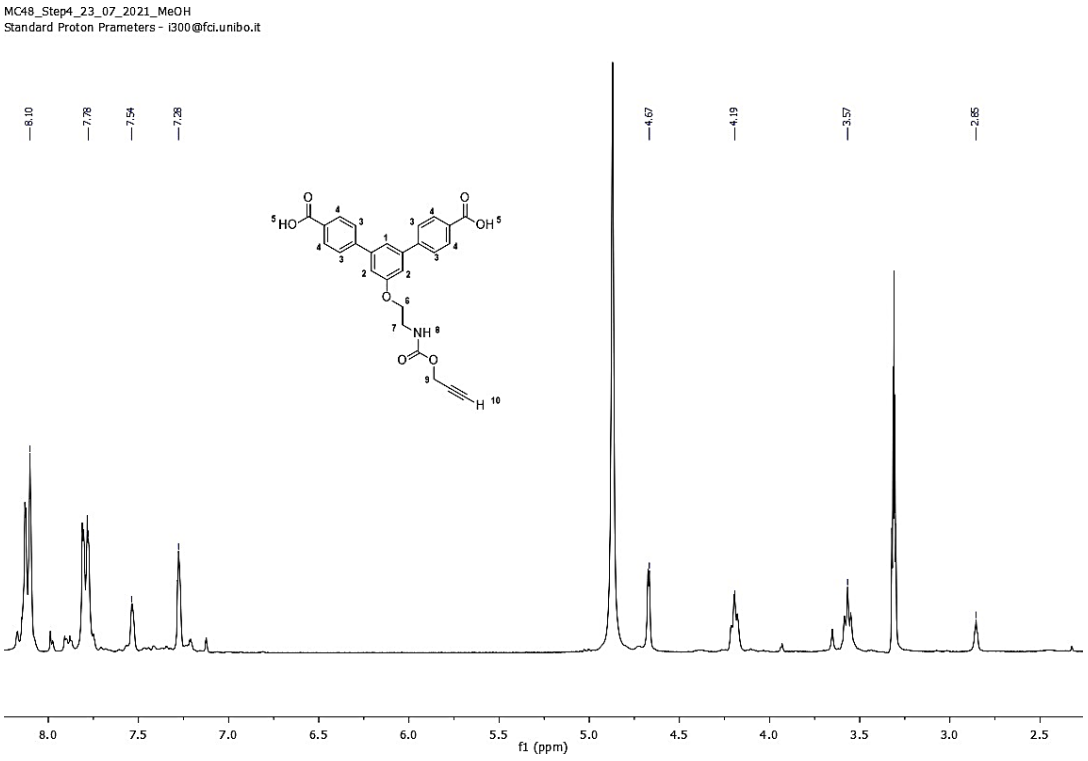

Figure 5.38. ^{1}H-NMR spectrum of **10** in MeOH.

^{13}C-NMR DMSO, 100.6 MHz) δ: 167.16 (Cq, *C*^{9}(O)OH); 159.48 (Cq; Ar-*C*^{4}-OCH2); 155.51 (Cq; NH-*C*^{12}(O)O); 143.36 (Cq; Ar-*C*^{5}-Ar); 141.27 (Cq; Ar-*C*^{2}-Ar); 129.88 (Cq; Ar-*C*^{8}-C(O)OCH3); 127.20 (Ar-*C*^{6}H); 122.83 (Ar-*C*^{7}H); 118.37 (Ar-*C*^{1}H); 113.09 (Ar-*C*^{3}H); 79.35 (-CH2-*C*^{14}≡CH); 77.14 (-C≡*C*^{15}H).

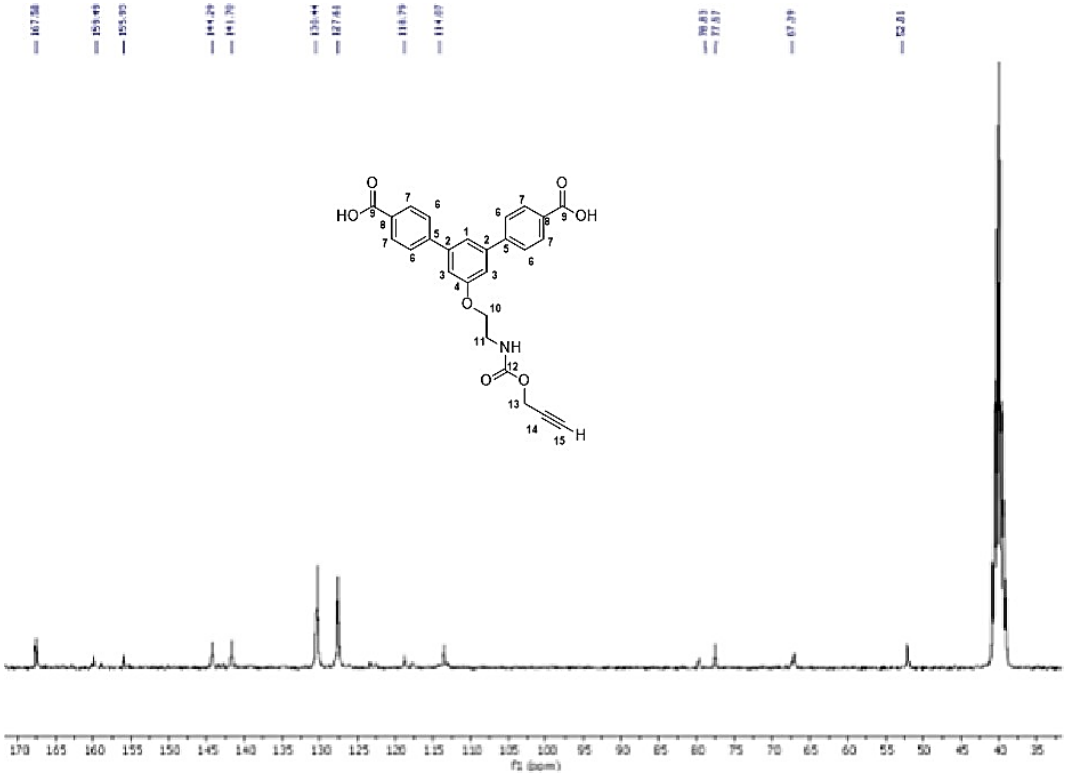

Figure 5.39. ^{13}C-NMR spectrum of **10**.

ATR FTR Spectra of neat 10 (cm^{-1}): 3294 (ν O-H), 2960 (ν C-H aliphatic, w), 1687 (ν C(O)OCH3, s), 1606 (ν C=O, s), 1528 (ν N-H, s), 1292 (ν -C(O)O-), 768 (δ bending).

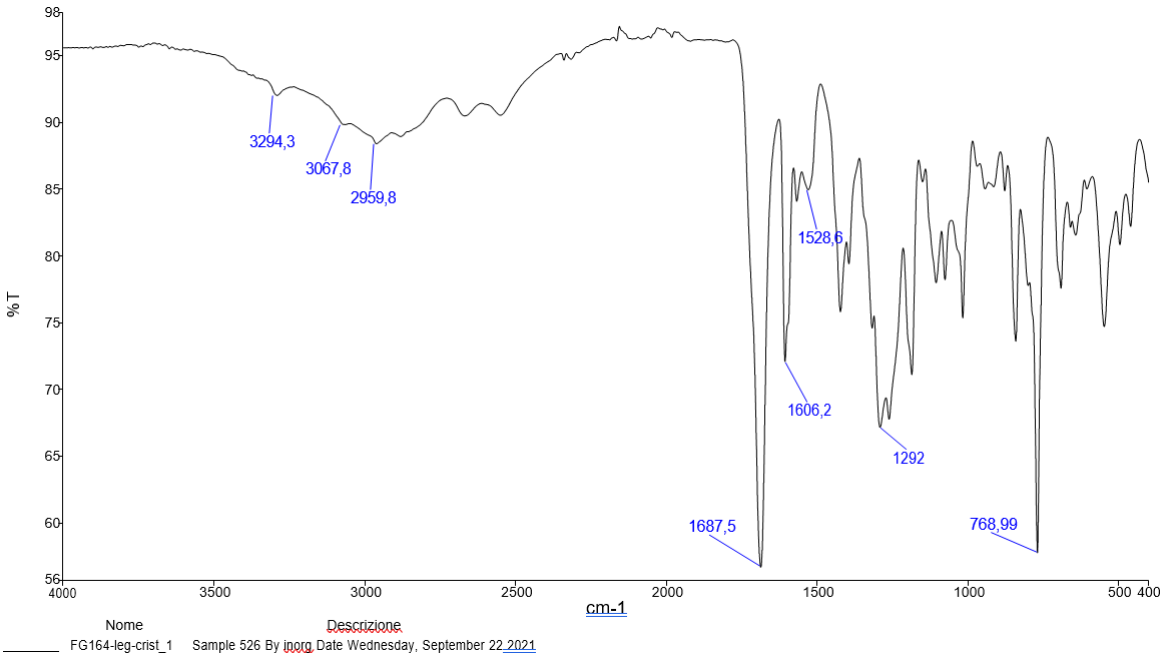

Figure 5.40. ATR-IR spectrum of **10**.

5.5.3 Crystallization of H_2YL_{80}

H_2YL80 (0.414 g, 0.9 mmol) is put in 20 mL of ethanol. At room temperature it appears mostly insoluble in this solvent. The solvent is heated to its boiling point (78 °C) and most of H_2YL80 dissolves. After 5 minutes, the solution is cooled down to 0 °C and the flask is left in an ice bath for 30 minutes. No precipitation is observed, so the solution is put at -18 °C overnight. The following day, seeing that no precipitate has still formed, the flask is put again in the ice bath and DI water (4 x 10 mL) is added, causing the formation of a white precipitate. The precipitate is filtered and washed with DI water. Keeping the mother solution in the ice bath, additional DI water (4 x 10 mL) is added, and further precipitation of a white solid is observed. This new precipitated is also filtered and washed with DI water. The process is repeated two other times, with the additional precaution of filtering the boiling ethanol solution to remove the insoluble residuals.

5.5.4 Synthesis of the new Cu-MOF

- **Synthesis in 2-propanol (MC35)**

A solution of H_2YL80 (0.176 g, 0.390 mmol) and $Cu(NO_3)_2 \cdot 2.5H_2O$ (0.163 g, 0.701 mmol, 1.8 eq) is prepared in 2-propanol (15 mL). The reaction is carried at reflux temperature (85 °C), under magnetic stirring (300 rpm). The formation of a light-green solid is observed soon at the beginning of the reaction. After 24 h the reaction is cooled at room temperature, and the product is filtered and washed with 2-propanol (Fig 5.41). The product is dried in the oven overnight. The final product is a light green solid, weighting 0.143 g. Assuming that Cu atoms and the ligand are present in 1:1 stoichiometric rate, we can calculate a 70% yield for the reaction.

Figure 5.41. The product of the MOF synthesis in 2-propanol after the washing with 2-propanol.

- **Synthesis in DMF/H2O 3:1 (MC46)**

A solution of H_2YL80 (0.057 g, 0.125 mmol) and $Cu(NO_3)_2 \cdot 2.5H_2O$ (0.058 g, 0.250 mmol, 2 eq) is prepared in DMF/H_2O 3:1 (8 mL) in a closed vial. The solution was heated at 50 °C without stirring for a total of 168 h (1 week). After the first 24 h a green-blue solid starts appearing at the interface of the solution. After 48 h on the bottom of the vial a white solid starts forming, while the presence of the green-blue solid increases. At the end of the 168 h the solution is cooled down to room temperature and the product (Fig. 5.42) is filtered, washed withH_2O, and dried in the oven overnight. The final product is a light green solid, mixed with tracesof the white solid. The total weight is 0.030 g. Assuming that Cu atoms and the ligand are present in 1:1 stoichiometric rate, we can calculate a 46% yield for the reaction.

Figure 5.42. Synthesis in DMF/H2O 3:1 of the new Cu-MOF, after 168 hours, before the work-up.

- **Synthesis in DMF/H2O 4:1 under inert atmosphere (MC51)**

A solution of H_2YL80 (0.057 g, 0.125 mmol) and $Cu(NO_3)_2 \cdot 2.5H_2O$ (0.058 g, 0.250 mmol, 2 eq) is prepared in DMF/H_2O 4:1 (8 mL) in a closed vial previously put under N_2 atmosphere. The solution is put under magnetic stirring for 10 minutes until the ligand is completely dissolved. The solution is then heated at 50 °C without stirring for a total of 168 h (1 week). After 24 h the formation of a green solid in small quantities at the interface of the solution is observed. After 48 h the green solid starts growing also on the walls and the bottom of the vial. Neither the formation of white solid nor brown oxides is observed during the whole time (Fig. 5.43). After 168 h, the reaction is cooled down at room temperature. The product is put in a Petri capsule, and the solvent is removed by decantation using a Pasteur pipette. The product iswashed with DI water directly in the capsule and the washings are removed by decantation using a

Pasteur pipette (filtration was avoided to minimise the material loss). The final product(Fig. 5.44) is dried in the oven overnight. The final product is a green solid, weighting 0.046 g. Assuming that Cu atoms and the ligand are present in 1:1 stoichiometric rate, we can calculate a 70% yield for the reaction.

Figure 5.43. Synthesis in DMF/H_2O 4:1 of the new Cu-MOF after 168 hours, before the work-up.

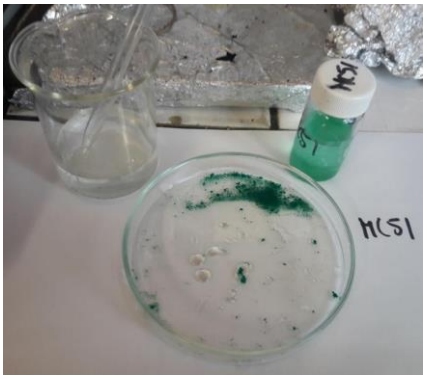

Figure 5.44. The product of MC51 after the washings in the Petri capsule.

- **Synthesis in DMF/H2O/2-propanol 2:1:1 under inert atmosphere**

A solution of H_2YL80 (0.057 g, 0.125 mmol) and $Cu(NO_3)_2 \cdot 2.5H_2O$ (0.058 g, 0.250 mmol, 2 eq) is prepared in DMF/H_2O/2-propanol 2:1:1 (8 mL) in a closed vial previously put under N_2 atmosphere. The solution is put under magnetic stirring for 10 min until the ligand is completely dissolved. The solution is then heated at 50 °C without stirring for a total of 168 h (1 week). After 48 h on the bottom of the vial begins the formation of a green solid, whose quantity increases slowly during the following days (Fig. 5.45). After 168 h the reaction is cooled down

to room temperature. The product is put in a Petri capsule, and the solvent is removed by decantation using a Pasteur pipette. The product is washed with DI water directly in the capsule and the washings are removed by decantation using a Pasteur pipette (filtration was avoided to minimise the material loss). The final product (Fig. 5.46) is dried in the oven overnight. The final product is a green solid, weighting 0.040 g. Assuming that Cu atoms and the ligand are present in 1:1 stoichiometric rate, we can calculate a 61% yield for the reaction.

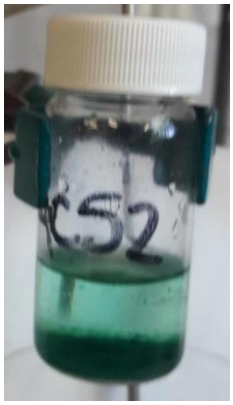

Figure 5.45. Synthesis in DMF/H_2O/2-propanol 2:1:1 of the new Cu-MOF after 168 h, before the work-up. Notice that the solid is almost all deposited on the bottom of the vial, while in MC51 it also grew on the walls and at the interface of the solution.

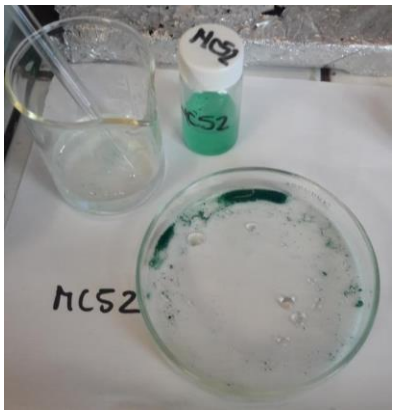

Figure 5.46. The product of MC52 after the washings in the Petri capsule.

- **Synthesis in DMF/H2O 4:1 under inert atmosphere at reduced ligand concentration(MC53)**

A solution of H_2YL80 (0.057 g, 0.125 mmol) and $Cu(NO_3)_2 \cdot 2.5H_2O$ (0.058 g, 0.250 mmol, 2 eq) is prepared in DMF/H_2O 4:1 (16 mL) in a closed vial previously put under N_2 atmosphere. The solution is heated at 50 °C without stirring for a total of 168 h. After 24 h no formation of solid is observed. After 96 h the formation of a turquoise-green solid at the interface of the solution is observed, with the precipitation of the heavier crystals to the bottom of the vial (Fig. 5.44).

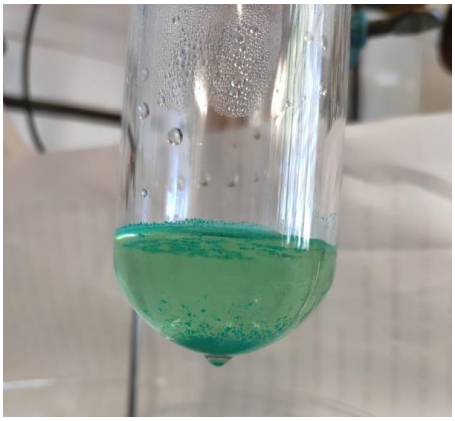

Figure 5.46. Formation of solid during the synthesis of the new Cu-MOF in DMF/H2O 4:1 under inert atmosphere at reduced ligand concentration after 96 h.

After 168 h the reaction is cooled down to room temperature and the solvents are separated through decantation. The solid product is washed with DI water (3 x 20 mL). The washings are separated through decantation, and the washings result do be turbid due to the presence of traces of white solid, maybe containing part of the unreacted ligand. The product is then washed with ethanol (20 mL), and this time the washings appear to be clear. The washings are removed through decantation and the resulting solid is dried in the oven for 24 hours. The final product is a green solid, weighting 0.023 g. Assuming that Cu atoms and the ligand are present in 1:1 stoichiometric rate, we can calculate a 35% yield for the reaction.

References

(1) Ghasempour, H.; Wang, K.-Y.; Powell, J. A.; Zarekarizi, F.; Lv, X.-L.; Morsali, A.; Zhou, H.-C. Metal–Organic Frameworks Based on Multicarboxylate Linkers. *Coord. Chem. Rev.* **2021**, *426*, 213542.

(2) Eddaoudi, M.; Kim, J.; Rosi, N.; Vodak, D.; Wachter, J.; O'Keeffe, M.; Yaghi, O. M. Systematic Design of Pore Size and Functionality in Isoreticular MOFs and Their Application in Methane Storage. *Science* **2002**, *295* (5554), 469–472. https://doi.org/10.1126/science.1067208.

(3) Mohideen, M. I. H.; Xiao, B.; Wheatley, P. S.; McKinlay, A. C.; Li, Y.; Slawin, A. M. Z.; Aldous, D. W.; Cessford, N.; Duren, T.; Zhao, X.; Gill, R.; Thomas, K. M.; Griffin, J. M.; Ashbrook, S. E.; Morris, R. E. Protecting Group and Switchable Pore-Discriminating Adsorption Properties of a Hydrophilic–Hydrophobic Metal–Organic Framework. *Nat. Chem.* **2011**, *3* (4), 304–310. https://doi.org/10.1038/NCHEM.1003.

(4) Cassani, M.; Gambassi, F.; Ballarin, B.; Nanni, D.; Ragazzini, I.; Barreca, D.; Maccato, C.; Guagliardi, A.; Masciocchi, N.; Kovtun, A.; Rubini, K.; Boanini, E. A Cu(Ii)-MOF Based on a Propargyl Carbamate-Functionalized Isophthalate Ligand. *RSC Adv.* **2021**, *11*, 20429–20438. https://doi.org/10.1039/D1RA02686K.

(5) Pagot, G.; Cassani, M. C.; Gambassi, F.; Ballarin, B.; Nanni, D.; Coi, M.; Barreca, D.; Boanini, E.; Di Noto, V. Propargyl Carbamate-Functionalized Cu(II)-Metal Organic Framework after Reaction with Chloroauric Acid: An x-Ray Photoelectron Spectroscopy Data Record. *Surf. Sci. Spectra* **2022**, *29* (2), 024007. https://doi.org/10.1116/6.0001950.

(6) Barin, G.; Krungleviciute, V.; Gutov, O.; Hupp, J. T.; Yildirim, T.; Farha, O. K. Defect Creation by Linker Fragmentation in Metal-Organic Frameworks and Its Effects on Gas Uptake Properties. *Inorg. Chem.* **2014**, *53* (13), 6914–6919. https://doi.org/10.1021/ic500722n.

(7) Jiang, H.-L.; Makal, T. A.; Zhou, H.-C. Interpenetration Control in Metal–Organic Frameworks for Functional Applications. *Coord. Chem. Rev.* **2013**, *257*, 2232–2249. https://doi.org/10.1016/J.CCR.2013.03.017.

(8) Chan, H.-K.; B Lindgren, E. B.; Stace, A. J.; Bitchouskaia, E. A General Geometric Representation of Sphere-Sphere Interactions. *Frontiers in Quantum Methods and*

Applications in Chemistry and Physics, Progress in Theoretical Chemistry and Physics **2015**, 29–36. https://doi.org/10.1007/978-3-319-14397-2_2.

(9) L'Hermite, N.; Giraud, A.; Provot, O.; Peyrat, J.-F.; Alami, M.; Brion, J.-D. Disproportionation Reaction of Diarylmethylisopropyl Ethers: A Versatile Access to Diarylmethanes from Diarylcarbinols Speeded up by the Use of Microwave Irradiation. *Tetrahedron* **2006**, *62* (51), 11994–12002. https://doi.org/10.1016/j.tet.2006.09.083.

(10) Chen, Z.; Weseliński, Ł. J.; Adil, K.; Belmabkhout, Y.; Shkurenko, A.; Jiang, H.; Bhatt, P. M.; Guillerm, V.; Dauzon, E.; Xue, D.-X.; O'Keeffe, M.; Eddaoudi, M. Applying the Power of Reticular Chemistry to Finding the Missing Alb-MOF Platform Based on the (6,12)-Coordinated Edge-Transitive Net. *J. Am. Chem. Soc.* **2017**, *139* (8), 3265–3274. https://doi.org/10.1021/jacs.7b00219.

(11) Rivera-Torrente, M.; Mandemaker, L. D. B.; Filez, M.; Delen, G.; Seoane, B.; Meirer, F.; Weckhuysen, B. M. Spectroscopy, Microscopy, Diffraction and Scattering of Archetypal MOFs: Formation, Metal Sites in Catalysis and Thin Films. *Chem. Soc. Rev.* **2020**, *49* (18), 6694–6732. https://doi.org/10.1039/d0cs00635a.

(12) Campbell, J.; Tokay, B. Controlling the Size and Shape of Mg-MOF-74 Crystals to Optimise Film Synthesis on Alumina Substrates. *Microporous Mesoporous Mater.* **2017**, *251*, 190–199. https://doi.org/10.1016/j.micromeso.2017.05.058.

(13) Shirley, D. A. High-Resolution X-Ray Photoemission Spectrum of the Valence Bands of Gold. *Phys. Rev. B*, **1972**, *5*, 4709.

CHAPTER 6

6. Synthesis and characterizations of a new chiral metal organic framework

6.1 Aim of the chapter

In this chapter the direct-method synthesis of a new Chiral MOF (CMOF) is explored as a promising way to synthesizes these materials for specific applications including, but not limited to, chiral recognition, separation, and catalysis. For the direct synthetic method approach, the first task was to find the most appropriate chiral linker for the synthesis of the chiral MOF. In fact the low number of suitable chiral linkers remains a challenge in this field, and for this reason the starting idea of this project was first the synthesis of a new chiral linker with two fundamental functionalities: the carboxylic one, to realize a bidentate linker for the metal node or cluster, and the chiral functionality, realized with a simple chiral molecule with low steric hindrance to avoid the constriction of the pores and the decrease of SSA of the new synthetized MOF.

Following these features, the proposed linker has been (*S*)-5-(2-methylbutoxy)isophtalic acid:

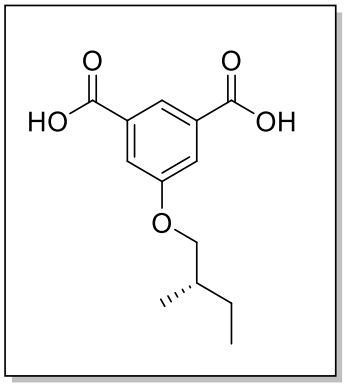

(*S*)-5-(2-methylbutoxy)isophthalic acid

This molecule already exists but its synthesis is covered by patent,[1] so the procedure proposed has been adapted from the synthesis of similar molecules found in the literature.[2] So, the first challenge of this work was to find the best procedure to synthesize this kind of molecule, and

then characterize it for the next step. Once the synthesis of the linker was done, the subsequent task was is to synthetize a chiral MOF of the MIP-206 type (see Section 6.3 for details on this class of MOFs) under optimized reaction conditions. Finally, the properties of the new CMOF, from the crystalline structure to the porosity, were investigates by means of complementary techniques as NMR, IR-ATR, XRD, TGA, and BET studies.

6.2 Introduction

6.2.1 Chiral Metal organic frameworks

Chiral metal−organic frameworks (CMOFs) are a captivating subgroup of the MOF family: they are usually constructed by metal nodes or metal clusters with organic ligands featured in chiral groups and have not yet been fully developed (Figure 6.1a). However, in the last years CMOFs have captured growing attention (Figure 6.1b), by virtue of their high modularity: in fact the interior surfaces of CMOFs can be systemically tailored with high accuracy for the benefit of suitable host−guest interactions. In this case, chemo-, regio-, and even enantioselectivity can be created and modulated at the atomic level, and such features have not been realized by conventional chiral materials.[3]

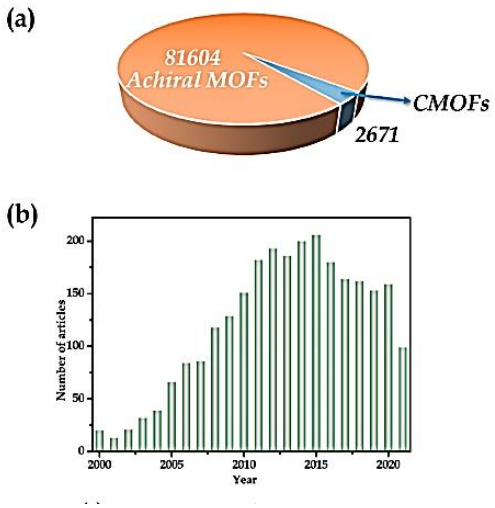

Figure 6.1 a) Statistical scheme of achiral MOFs and chiral MOFs published through August 2021. **b)** Number of published articles on CMOFs through 2000 to August 2021. The data was obtained from Web of Science.

This kind of materials offer great potential in heterogeneous asymmetric catalysis and selective separations (GC/HPLC) because of their periodic porous structure, high surface area, and adjustable chiral functionality. In fact, the highly modular toolkit offers a wealth of opportunity for the fabrication of novel chirality, making them suitable for diverse enantioselective applications that are unattainable by traditional materials. Moreover, the highly crystalline nature of these materials enables us to clearly reveal the enantioselective mechanism at the molecular level, which would greatly facilitate the further development of material design

methodology and preparation of high performing materials. Recently, CMOFs have been proved to be promising in some other cutting-edge applications such as circularly polarized luminescence (CPL), second order nonlinear optics (NLO) and drug delivery (DD). These intriguing potential applications further highlight the uniqueness of CMOFs in the respect of intrinsic asymmetricity, chiral pore environment, as well as tunability.

In 2000, Kim and co-workers first reported the direct synthesis of CMOFs with enantiopure building blocks and demonstrated their successful use in asymmetric catalysis.[4] Since then, examples of CMOFs based on mesoporous MOFs such as UiO-67, UiO-68, and MIL-101 have been reported,[5] but the introduction of chirality is often a challenge. In fact the chiral active molecules could lead to unforeseen covalent or coordinated bonds that would not only block the pores of MOFs but also reduce chiral degree of freedom. Therefore, the design principles for the synthesis of CMOFs are mainly concentrated on how, where, and when to introduce the chirality in a perfect way into the resultant frameworks, usually by employing similar synthetic techniques as achiral MOFs.

In principle, chirality can be introduced into MOFs by the two main following methods:

(1) the *direct method*, where enantiopure chiral linkers or co-linkers (auxiliaries) were used to ensure absolute chirality transition from molecules to the final frameworks;

(2) the *post modification method*, where achiral MOFs with appropriate functional groups reacted with chiral reagents to implant chirality within the entire framework.

It is quite clear that each method has its pros and cons. Specifically, the direct synthesis method is generally the preferred choice for assembling CMOFs because the "chirality conservation" process to achieve homochirality is well established and has already been thoroughly documented in dozens of studies. Nevertheless, the lack of inherently chiral functional linkers has greatly limited its further development.

Post-modification synthesis has been demonstrated to be a facile and efficient method to produce CMOFs as it does not require the multistep preparation of specific and intricate chiral building blocks and allows the divergent functionalization of parent MOFs for target-specific enantioselective applications. However, to realize successful chiral modification, the parent MOFs should exhibit certain properties, such as chemically stable and large internal surfaces with potentially active functional sites.

For these reasons the use of enantiopure and directional ligands as building blocks playing the role of bridged linkers to bind metal ions or metal clusters for the rational construction of CMOFs seems the most robust, encouraging, and widely employed strategy. So, the main challenge in this field lies on the judicious choice of the individual components for the construction of outstanding CMOFs bearing appropriate and stable chiral architectures and pore structures, luxuriant and powerful active sites, as well as accessible channels or apertures.

Anyway, the intrinsic chirality, high modularity and great designability of CMOF compared to traditional chiral solid materials (polymers, zeolites, carbons) allow for the ultrafine tuning of these new materials and an impressive development of rational synthetic methods with respect to implementation and maximization of versatile chiral functionalities.

6.2.2 Introduction to MTV-MOFs

Recently, an original approach, consisting basically of using different types of organic linkers, has emerged for the fabrication of MOFs with different and controlled functionalities within their channels. This type of sequence dependent material, so-called multicomponent or multivariate (MTV) MOFs, are capable of new functions without apparent loss of synthetic control. The first step in truly realizing the potential of introducing heterogeneity within MOF structures came with the discovery of multivariate (MTV) MOFs in 2010.[6] The MTV discovery had a profound implication: the resulting MTV-MOFs possessed properties that did not arise from linear combinations of the pure constituents.

In this context, the introduction of chirality in MOFs usually adopts the methods of chiral preliminary treatment of the ligands; anyway, the chiral active molecule suffered from such covalent or coordinated modification and would not only block the pores of MOFs but also reduce their chiral degree of freedom. The multivariate synthetic approach of MOFs might provide a new avenue for the rational synthesis of CMOFs with larger cavities. By the incorporation of missing linkers and missing node defects into MOFs, some bigger cavities can be generated in the defect sites without losing long-range-order MOFs, producing a larger adsorbent space. So, a simple and effective method is to use a mixed truncated ligand that would generate a linker defect and produce mesopores, leading to the formation of defective structures of the MOFs. The idea was to try different ratios of the simpler linker and the chiral one to find the optimizing conditions to have a crystalline solid (Fig. 6.2 and 6.3).

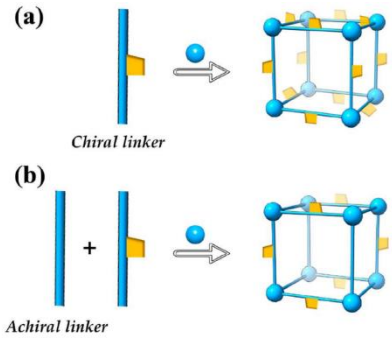

Figure 6.2. a) Scheme of a simple chiral MOF **b)** MTV chiral MOF with the introduction of achiral linker

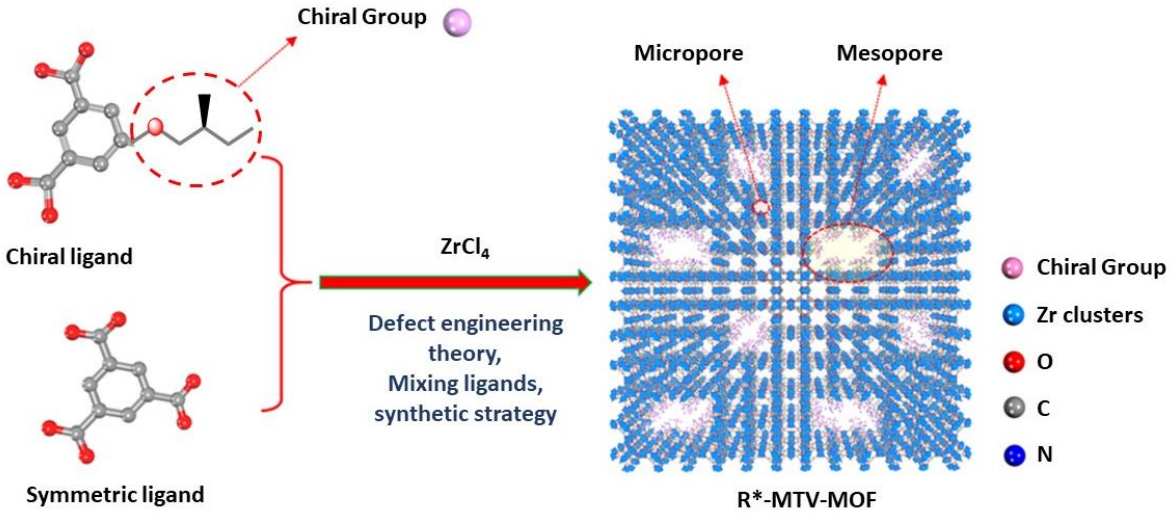

Figure 6.3. Representation of the synthesis of an MTV chiral MOF with a ratio of symmetric and chiral ligand

The attempts of involving more than one linker in the same structure have gain concern in a quest for complexity and heterogeneity. Complexity refers to the formation of new complex structures due to the implication of more than one network topology in one formulation, producing a totally distinct network. In contrast, heterogeneity implies the growth of the same structural type of the parent MOF (i.e., topology) but with comparable building units, preserving identical backbone.[7]

6.3 Result and discussion

6.3.1 Preliminary TESTs

To optimize the synthesis of the linker, several approaches have been studied. First, the possibility of obtaining a crystalline MOF starting directly from the methylated Br-isophthalic acid was studied, to avoid, in the synthesis of the functionalized ligand, the hydrolysis of the -COOMe groups into -COOH as an additional synthetic step.

Furthermore, some preliminary tests with reagents containing the same functionality of the chiral one were performed to check the best synthetic way and to choose the chiral reagent and the functionalized isophthalic acid more convenient to order. Considering as a starting point the *O-alkylation* reaction of isophthalic acid that gave the best results in the previous chapters on the synthesis of organic ligands of this work, two ways can be followed according to the electrophilic or nucleophilic nature of the isophthalic acid chosen.

Direct synthesis of MOFs from dimethyl 5-bromoisophtalate

- Synthesis of dimethyl 5-bromoisophthalate (Me-IPA-Br)

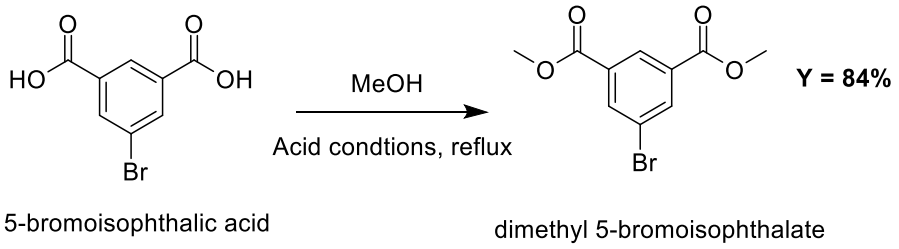

Scheme 6.1. Methylation of 5-bromoisophtalic acid in acid condition.

The methylated product was prepared with simple acid conditions in MeOH at reflux for 24 h. The work up led to a pink solid, with a good yield (**84%**), whose structure was confirmed by NMR analysis, in which it is possible to recognize the six protons signal of the two new -CH_3[1] (3.89 ppm).

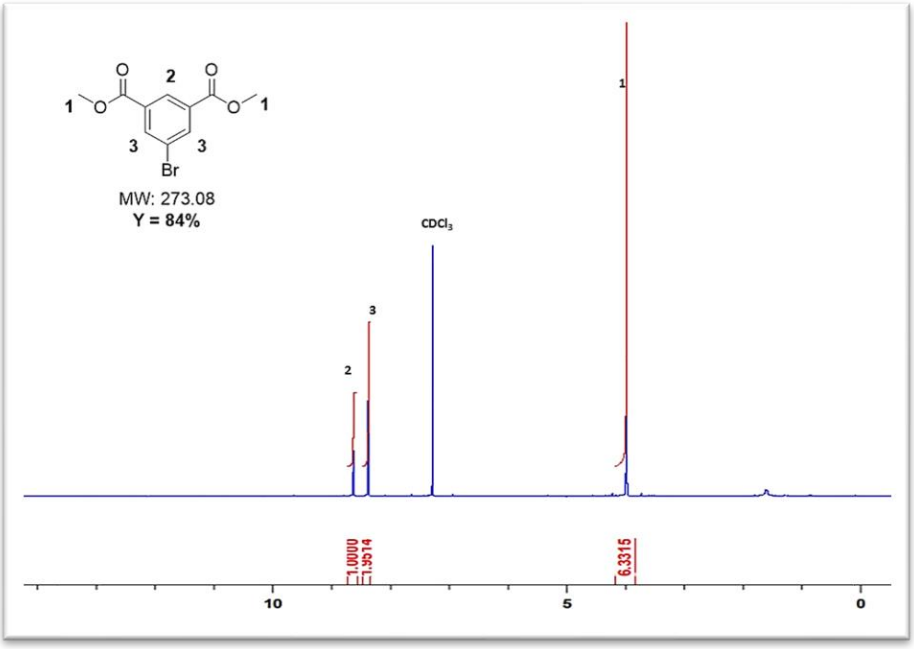

Figure 6.4. ^{1}H-NMR spectrum of the dimethyl bromoisophtalate. The signal **1** represents the proof of the reagent conversion

- Synthesis of a robust mesoporous MOF of the MIP-206 class from Me-IPA-Br

The association of non-toxic Zr-oxo clusters starting from $ZrCl_4$ as reagent and feedstock isophthalic acid through a simple solvothermal synthesis result in a robust crystalline mesoporous MOF, denoted as MIP-206, where MIP stands for the Materials of the Institute of Porous Materials of Paris.[8] That's why in this Chapter we are all around talking about "MOF of the MIP-206 class".

Due the use of acidic conditions in the MIP-206 synthesis, the idea is to start directly from the methylated compound (dimethyl 5-bromoisophtalate) for the synthesis of the subsequent (Scheme 6.2) MOF.

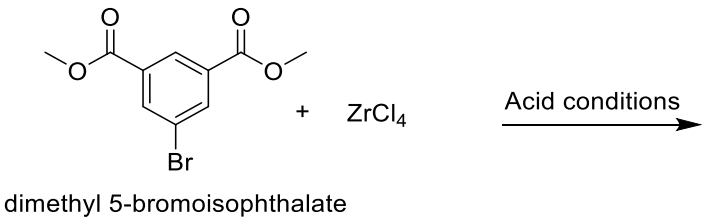

Scheme 6.2. direct synthesis of a MIP-206 MOF with a Br-functionalized linker

MIP-206 from IPA-Br was synthesized solvothermally by the reaction of $ZrCl_4$ and IPA-Br in formic acid. After cooling down to room temperature, the expected product was collected by centrifugation, washed with ethanol and dried in vacuum. The PXRD patterns (λCu ≈ 1.5406 Å) of the new MIP-206 with bromoisophthalate as linker shows that the use of the methylated compound leading to crystalline isostructural material analogous to the others previously synthesized MIP-206s (Figure 6.6b).

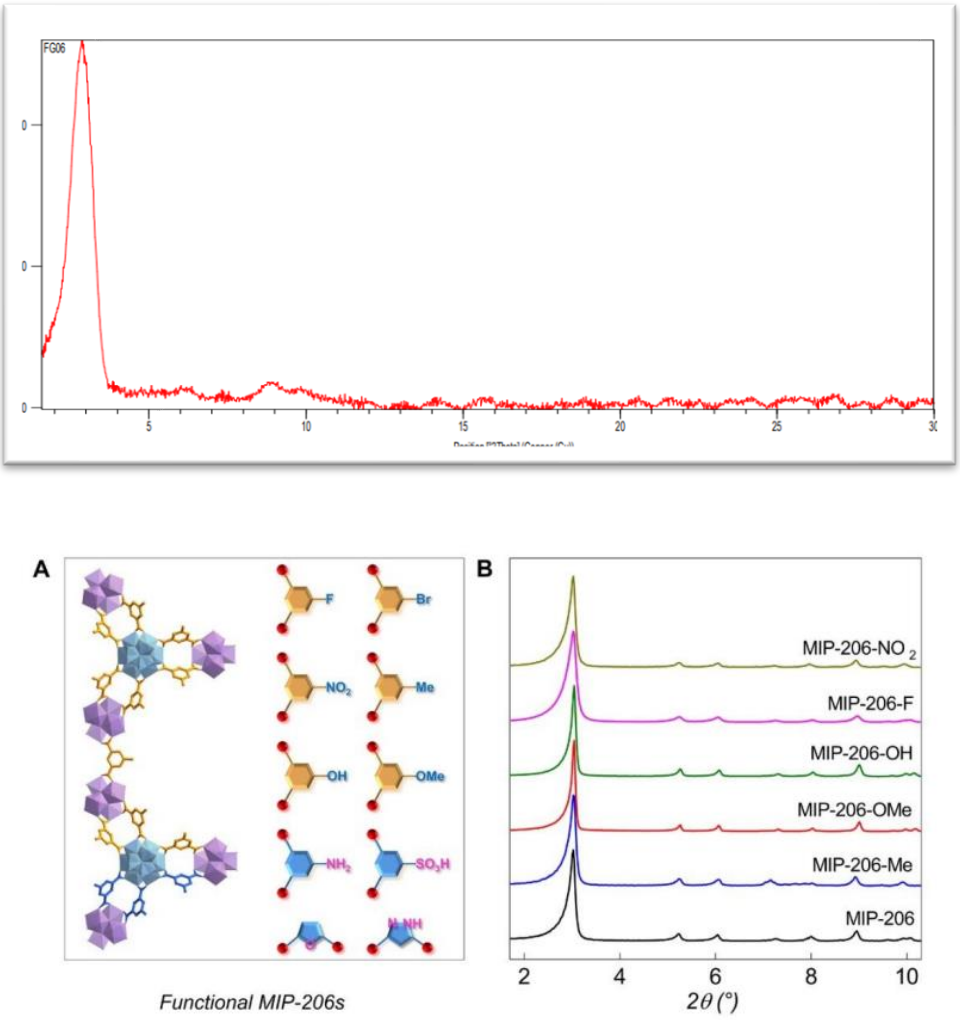

Figure 6.5. a) Simplified illustration of a structural segment of functional MIP-206s constructed with pure substituted IPA linkers. **B)** PXRD patterns (λCu ≈ 1.5406 Å) of selected MIP-206s with different functional groups.

So, according to the XRD data, there are two types of Zr oxo-cluster secondary building units (SBUs) in the structure, namely 8-connected Zr_6 and 12-connected Zr_{12} oxo-clusters. Each Zr_{12} oxo-cluster is centered between three adjacent Zr_6 oxo-clusters, through linkages formed by six pairs of bridging IPA molecules (Figure 6.6a). This preliminary result hence confirm that the synthesis conditions can be actually optimized avoiding the additional synthetic step of hydrolysis of the ester groups.

Alkoxylation of Bromo isophthalic acid

In these preliminary tests two different synthesis attempts were carried out: unfortunately, in both case the reaction did not afforded the expected results. The procedures proposed are adapted from the synthesis of similar molecules found in the literature.

- Synthesis in Acetone as solvent

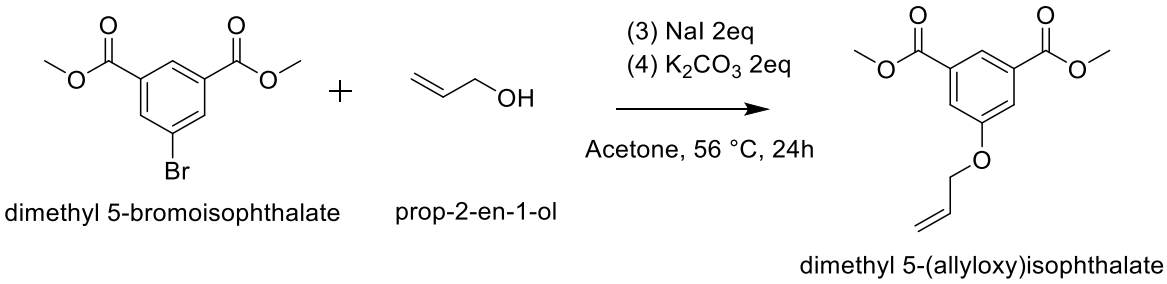

Scheme 6.3. Alkoxylation of dimethyl 5-bromoisophtalate with prop-2-en-1-ol in acetone

Despite the simple reaction conditions, the NMR analyses did not show the expected product but the starting reagent only.

- Synthesis in DMF as solvent

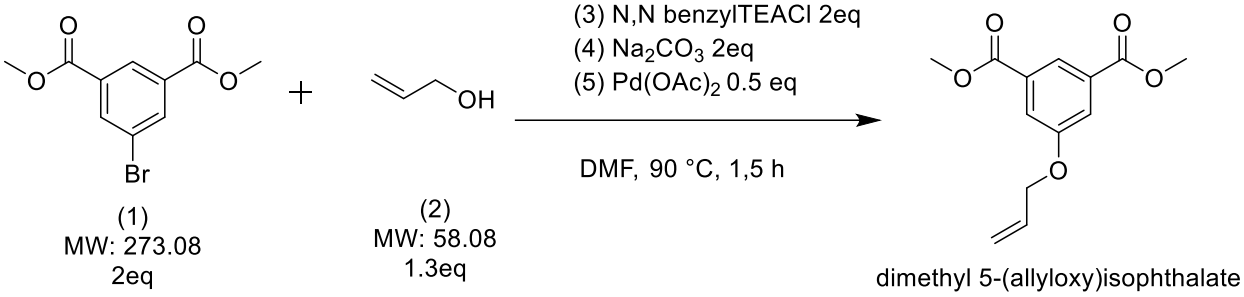

Scheme 6.4. Alkoxylation of dimethyl 5-bromoisophtalate with prop-2-en-1-ol in DMF.

Even in this case, NMR analyses did only show the starting reagent. Moreover, the reaction conditions are more complicated than the previous ones and the use of DMF as solvent is not the best choice, considering the toxicity of the solvent and its high boiling point, involving consequently complicated steps of purification.

O-Alkylation of dimethyl 5- hydroxyphthalate with allyl bromide

- Methylation of 5-hydroxyisophthalic acid

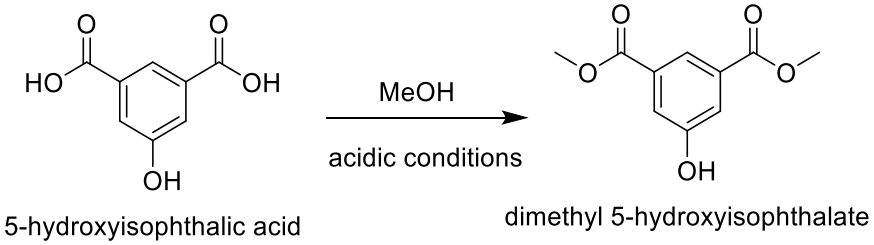

Scheme 6.5. Reaction of protection of 5-hydroxyisophthalic acid with MeOH

The methylation of 5-hydroxyisophthalic acid led to the formation of a pink-orange precipitate. The final product was isolated as a pink solid with a very good yield (89%); ^{1}H-NMR analysis clearly showed the six protons signal of the two new -CH_3 **1** (3.8 ppm).

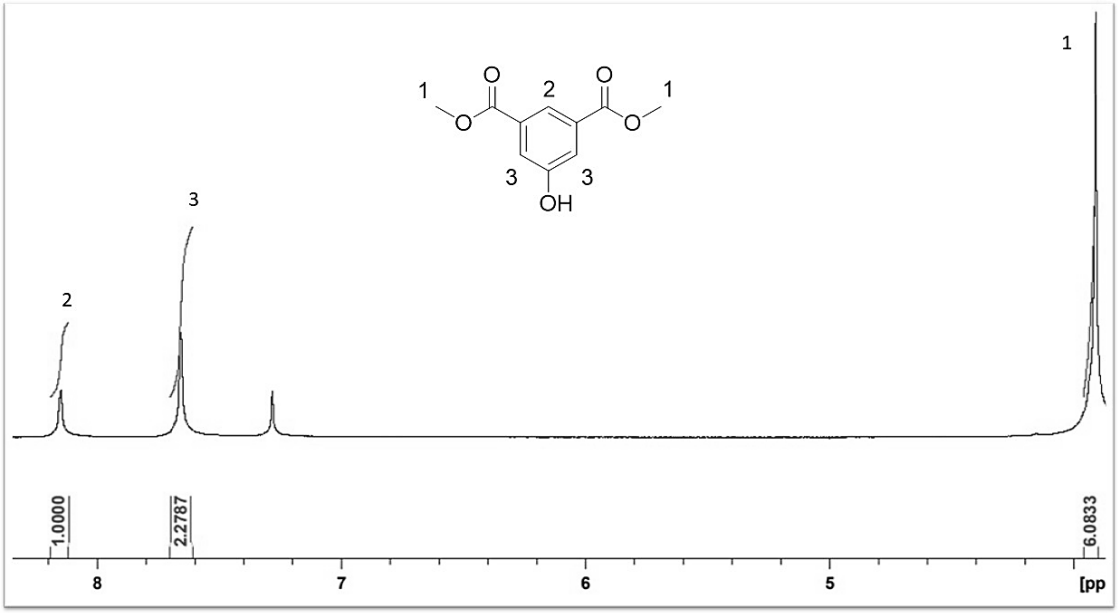

Figure 6.6. ^{1}H-NMR spectrum of dimethyl 5-hydroxyisophthalate. The signal **1** represents the proof of the reagent conversion.

- *O*-Alkylation of dimethyl 5-hydroxyisophthalate with allyl bromide

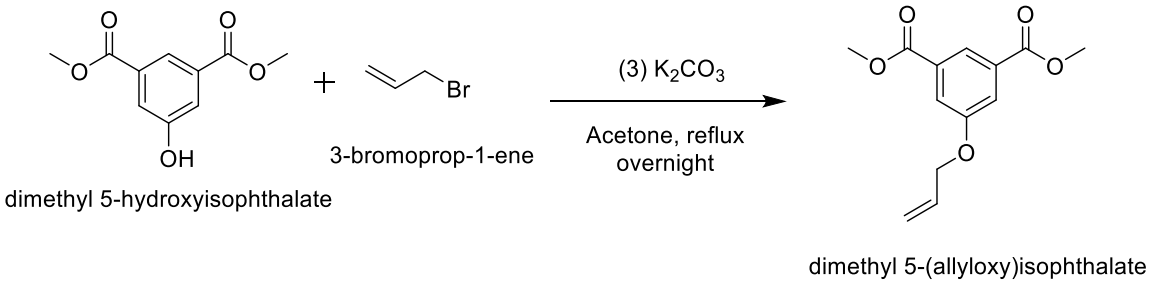

Scheme 6.6. O-Alkylation of dimethyl 5-hydroxyisophthalate with allyl bromide in Acetone

The *O*-alkylation of a nucleophilic hydroxyisophthalate and an electrophilic allyl halide led to an efficient result, with the complete conversion of the reagents and very good yields. The product (Me-IPA-O-allyl) as a white solid (yield = 89%) was analyzed by ^{1}H-NMR without further purification.

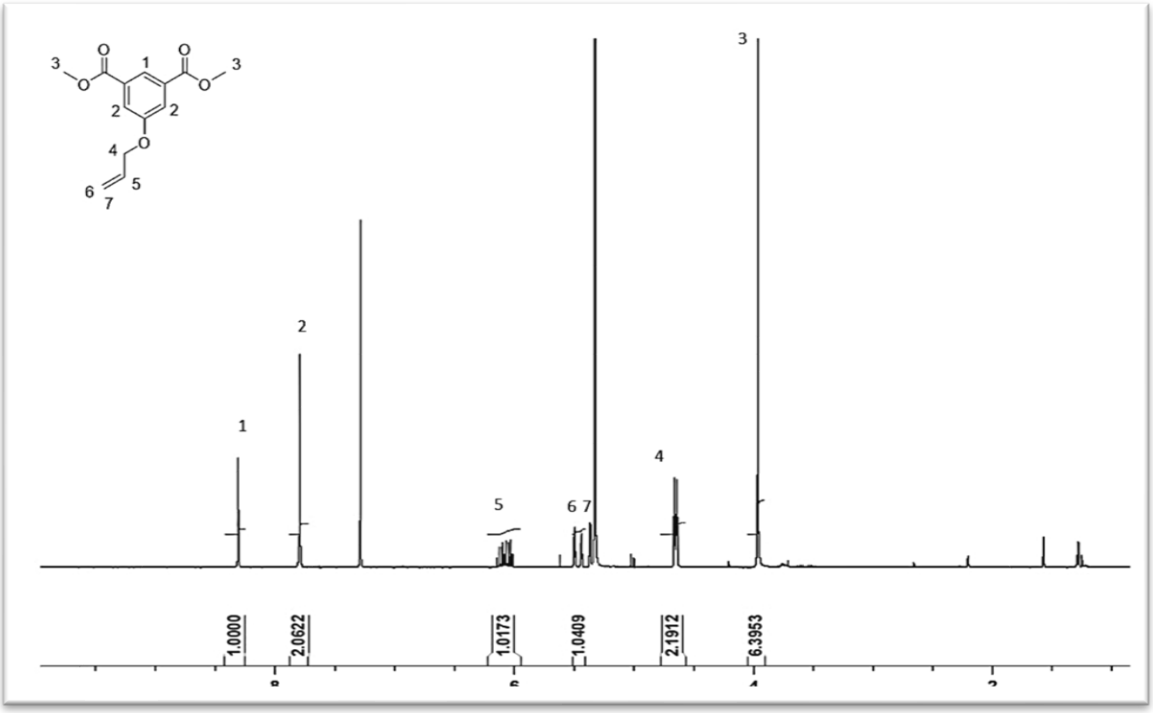

Figure 6.7. ^{1}H-NMR analysis of dimethyl 5-allyloxyisophthalate shows the complete conversion of the reagents and the presence of all the peaks of the desired product.

Synthesis of allyl MOF with $ZrCl_4$

Following the preliminary tests, the dimethyl allyloxyisophthalate was tested in a reaction with $ZrCl_4$ to check the possibility to obtain, through usual synthetic conditions, an isoreticular material to MIP-206 (Scheme 6.6).

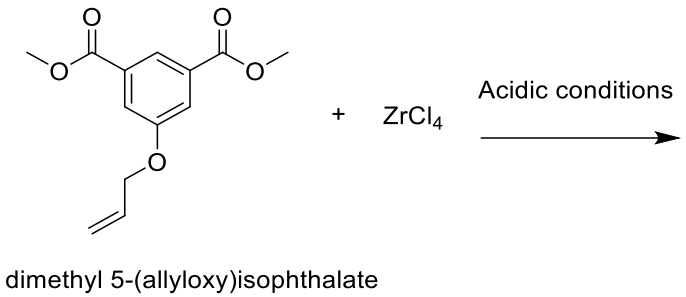

dimethyl 5-(allyloxy)isophthalate

Scheme 6.7. Synthesis of MIP206 allyl MOF.

So, the Allyl MIP-206 was synthesized solvothermally by the reaction of $ZrCl_4$ and Me-IPA-O-allyl with the same procedure of MIP-206 synthesis.

The PXRD patterns (λCu ≈ 1.5406 Å) of the new MIP-206 obtained from dimethyl 5-allyloxyisophthalate as linker shows (Figure 6.9) that the use of the allyl compound lead to a crystalline isostructural material analogous to the others previously synthesized MIP-206s.[8]

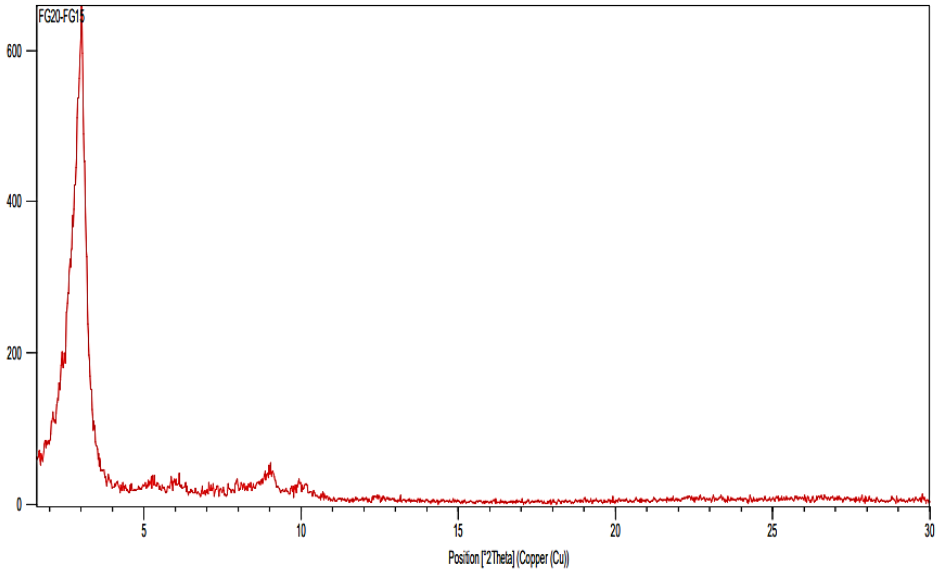

Figure 6.8. PXRD patterns (λCu ≈ 1.5406 Å) of the novel MOF.

For future work it could be interesting to continue the characterizations of this novel kind of allyloxy MOF in terms of porosity, SSA, and applications. In fact, in literature there is

only one example of a MOF (Al-CAU-10-OC_3H_5, with Al as metal node) constructed with this linker, used for aqueous-phase fluorescence recognition of Pd(II) ions.[9] Moreover, only a negligible surface area value (32 m^2g^{-1}) was obtained for the Al-CAU-MOF.

6.3.2 Synthesis of the chiral linker (*S*)-5-(2-methylbutoxy)isophtalic acid

The information acquired in the preliminary tests allowed to choose the most suitable reagents for this synthesis, that is a nucleophilic dimethyl isophthalate (a phenolic isophthalate) and an electrophilic alkylating reagent (an alkyl halide or sulphonate). The reagents of choice are shown in Scheme 6.7 and the reaction was carried out at 100 °C.

- Synthesis of dimethyl *(S)*-5-(2-methylbutoxy)isophthalate

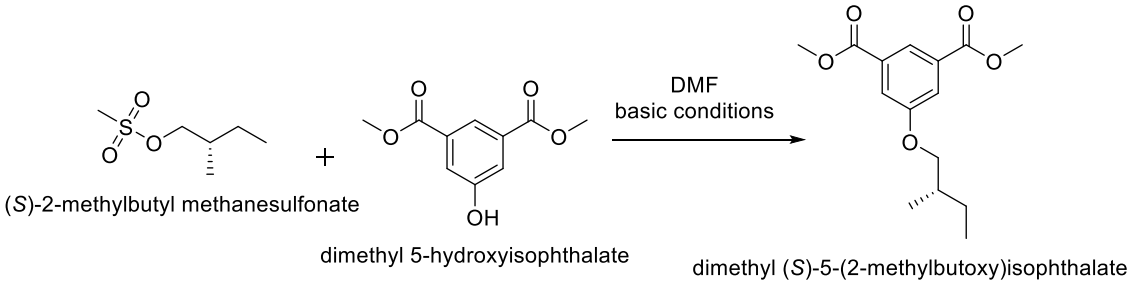

Scheme 6.8. Synthesis of the chiral linker.

For the purification of the reaction mixture three different work-ups were tried but the best yield (53%) was obtained under the conditions reported in the experimental part. Despite various attempts and various changes in work-up, yields remained quite low. Rather than increasing the reaction time, already quite long, it could be worthy trying to increase the temperature to reflux of solvent (DMF, 153 °C), an attempt that is underway.

The product was isolated in high purity and its ^{1}H-NMR spectrum shows all the predictable signals for the expected compound (Figure 6.10).

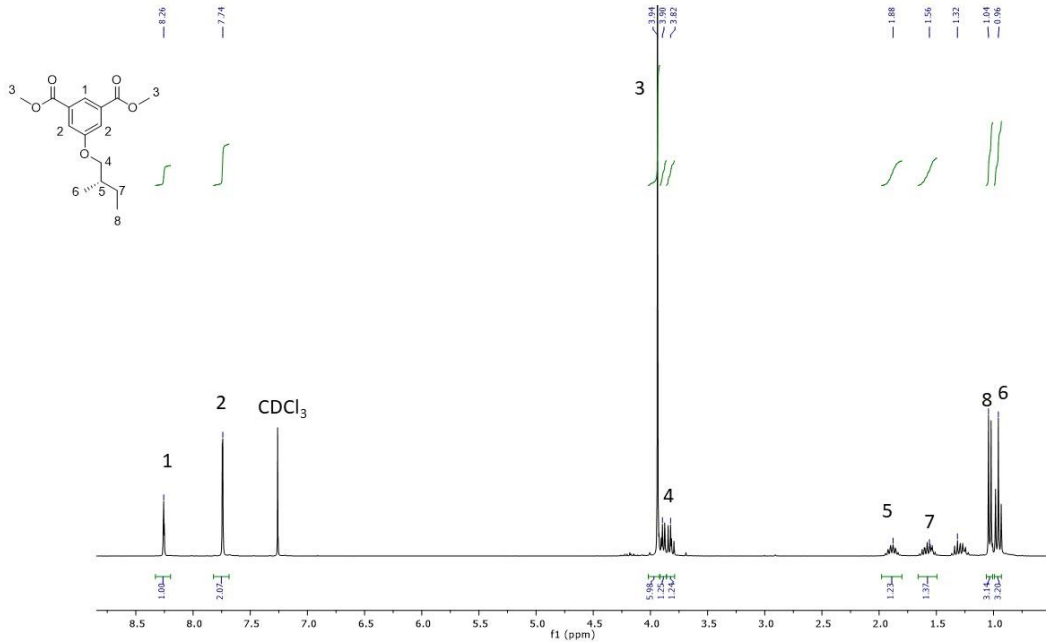

Figure 6.9. ^{1}H-NMR analysis of dimethyl allyl-(2-methylbutoxy)isophthalate shows the complete conversion of the reagents and the presence of all the peaks of the product wanted.

In the aromatic region, the Ar-H^{1} signal at 8.26 ppm is a singlet and its integral was set to be unitary while the Ar-H^{2} signal at 7.74 ppm is a singlet with a double integral. In the aliphatic region of the spectra, the -OCH$_3$^{3} signal at 3.94 ppm is a singlet that integrates the six protons of the methylated compound. The signals of -OCH$_2$^{3}-, located between 3.82 and 3.90 ppm results more deshielded due to its proximity to the more electronegative oxygen and is a multiplet coupling with the protons -CH$_2$CH^{5}CH$_2$- and -CHCH$_3$^{6}. The signal at 1.88 ppm is attributed to -CH$_2$CH^{5}CH$_2$-, it is a multiplet coupling with -CHCH$_3$^{6} and -CHCH$_2$^{7}CH$_3$ and in the same way the signal at 1.56 ppm is attributed to -CHCH$_2$^{7}CH$_3$, a multiplet too coupling with -CH$_2$CH^{5}CH$_2$- and -CH$_2$CH$_3$^{8}. Then is possible to recognize at 1.04 ppm the signal of -CHCH$_3$^{6}, a doublet that integrates three protons coupling with -CH$_2$CH^{5}CH$_2$-, and the signal of -CH$_2$CH$_3$^{8} at 0.96 ppm, a triplet that integrates three protons coupling with -CHCH$_2$^{7}CH$_3$.

- Synthesis of *(S)*-5-(2-methylbutoxy)isophthalic acid

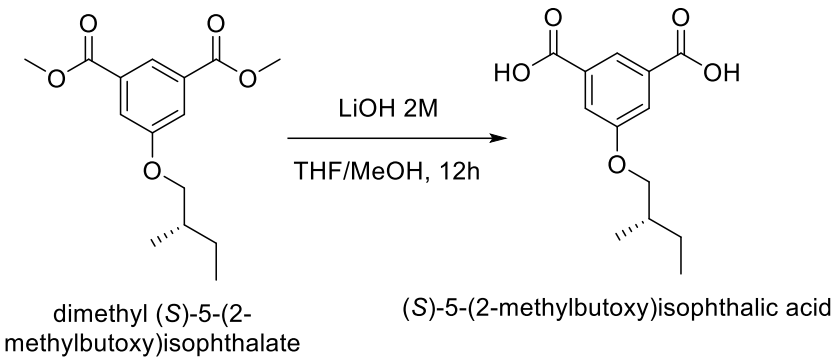

Scheme 6.9. Deprotection of the chiral linker.

Dimethyl *(S)*-5-(2-methylbutoxy)isophthalate was converted into the corresponding dicarboxylic acid by LiOH-promoted hydrolysis, to obtain the pure desired product as a white solid (yield = 76%). The reaction works thoroughly, as reported in the ^{1}H-NMR spectra, which clearly shows the absence of the signal of the -CH_3 ester groups (3.94 ppm, 6H) (Figure 6.11).

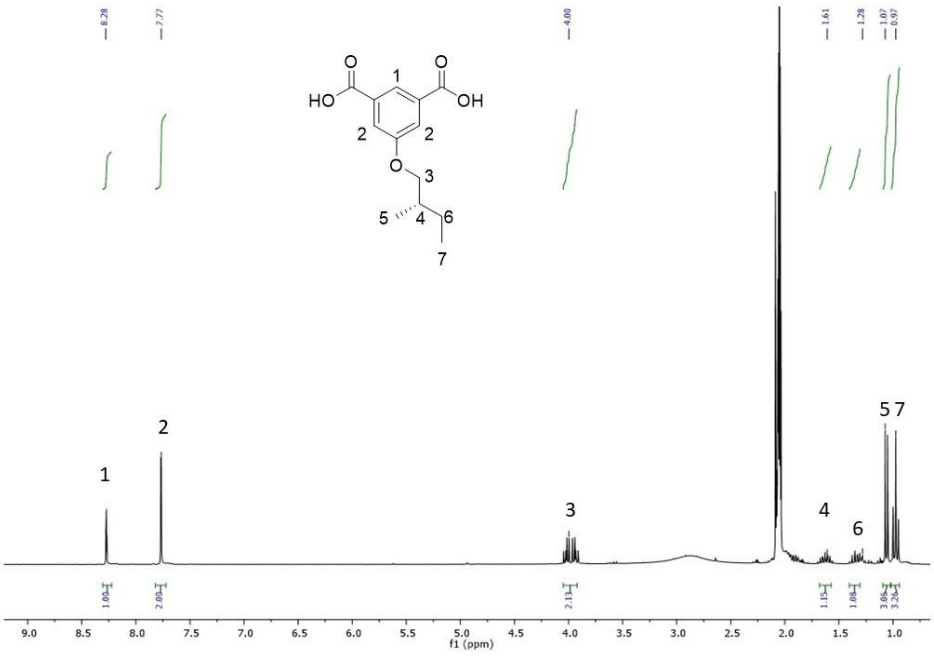

Figure 6.10. ^{1}H-NMR analysis of (S)-5-(2-methylbutoxy)isophthalic acid.

6.3.3 Characterization of the chiral linker *(S)*-5-(2-methylbutoxy)isophthalic acid

The best NMR spectra of this product are given when acetone-d_6 is used as a solvent: in fact the product is not completely soluble in $CDCl_3$.

Figure 6.11 shows the ^{1}H-NMR spectra of the (S)-5-(2-methylbutoxy)isophthalic acid, really similar to the isophthalate reagent. In the aromatic region, the Ar-H^1 signal at 8.28 ppm is a singlet and its integral was set to be unitary while the Ar-H^2 signal at 7.77 ppm is a singlet with a double integral. In the aliphatic region of the spectra, the signal of -OCH_2^3- is located at 4.00 ppm and results more deshielded due to its proximity to the more electronegative oxygen: it is a multiplet coupling with the protons -$CH_2CH^4CH_2$- and -$CHCH_3^5$. The signal at 1.61 ppm is attributed to -$CH_2CH^4CH_2$-: it is a multiplet coupling with -$CHCH_3^5$ and -$CHCH_2^6CH_3$ and in the same way the signal at 1.28 ppm is attributed to -$CHCH_2^6CH_3$, a multiplet too coupling with -$CH_2CH^4CH_2$- and -$CH_2CH_3^7$. Then is possible to recognize the signal of -$CHCH_3^7$ at 1.07, a doublet that integrates three protons coupling with -$CH_2CH^4CH_2$- and the signal of -$CH_2CH_3^7$ at 0.97, a triplet that integrates three protons coupling with -$CHCH_2^6CH_3$.

IR-ATR of the chiral linker

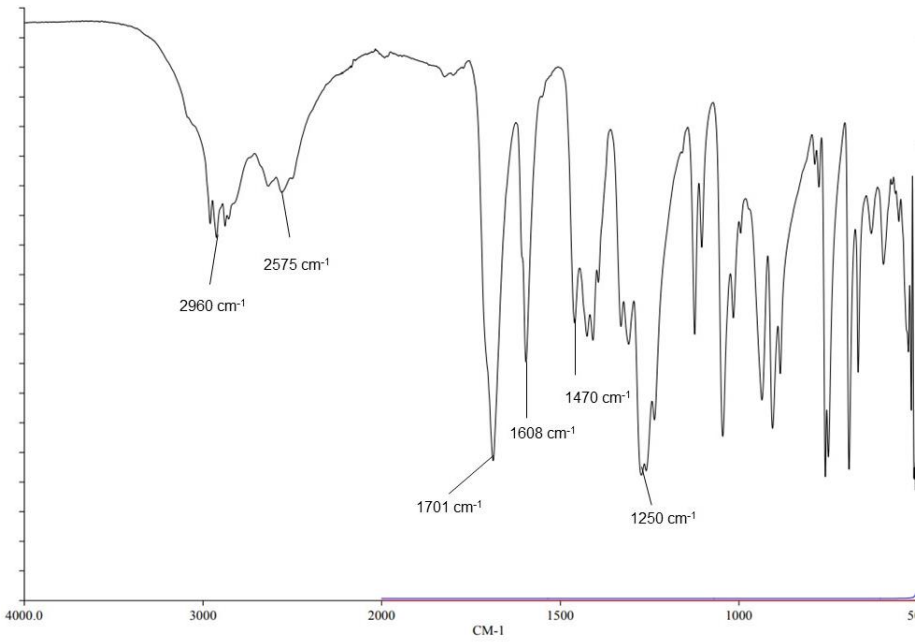

Figure 6.11. ATR-FTIR of (S)-5-(2-methylbutoxy)isophthalic acid.

Figure 6.12 shows the ATR-FTIR spectra of the chiral linker. It is possible to recognize the frequency of the major functional groups, i.e. the aliphatic stretching at 2960 cm^{-1} (ν C-H aliphatic, m) and at 2575 cm^{-1}, the peak at 1701 cm^{-1} attributed to the stretching of carboxilate (-C(O)O-), the 1608-1470 cm^{-1} band attributed to the aromatic stretching (ν C-H aromatic, s), and the peak at 1250 cm^{-1} of the aliphatic -CH_3.

6.3.4 Synthesis of Chiral MIP-206 MOF (R*-MOF)

- Synthesis of Chiral MOF with $ZrCl_4$ and *(S)*-5-(2-methylbutoxy)isophthalic acid

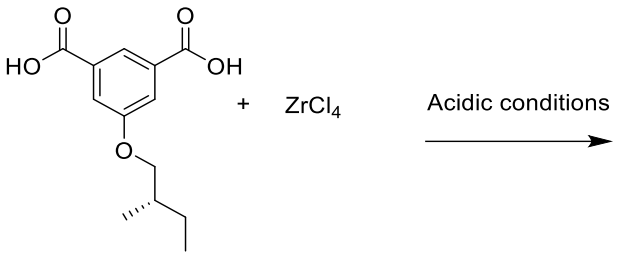

(*S*)-5-(2-methylbutoxy)isophthalic acid

Scheme 6.10. Synthesis of the chiral MOF (R*-MOF) in simple conditions.

This kind of chiral MIP-206 from IPA-*(S)*-methylbutoxy reagent was synthesized solvothermally by the reaction with $ZrCl_4$ under usual acidic conditions. After cooling down to room temperature, the expected product was collected by centrifugation, washed with ethanol, and dried under vacuum.

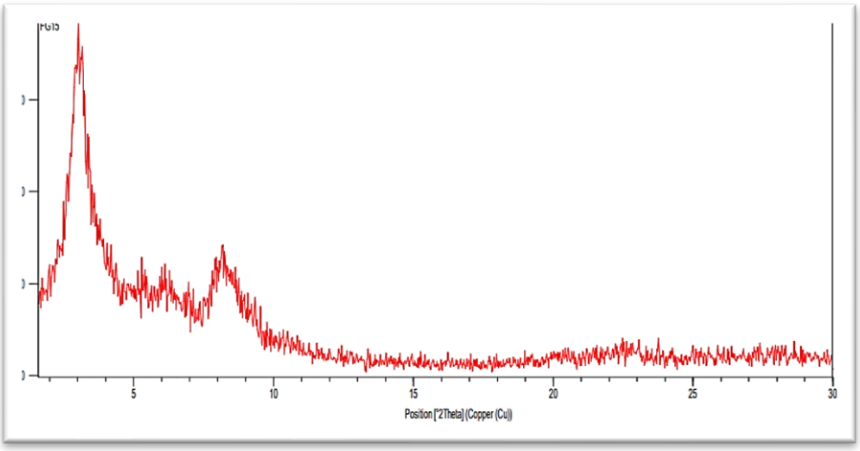

Figure 6.12. PXRD patterns of the new MIP-206 with the chiral linker

The PXRD patterns (λCu ≈ 1.5406 Å) of the new MIP-206 with the chiral linker (Figure 6.13) shows that the introduction of a chiral functional group led to a PXRD pattern similar to MIP-206 but with a bit lower crystallinity compared to the other materials previously synthesized (MIP-206).[8] This first result remains however interesting and for the next MOF synthesis attempts it could be worthy to try to modulate the linkers (50% of chiral linker and 50% of IPA-OH, for example) to improve the crystallinity of the material.

6.3.5 Functionalization Studies

To check if the linker is present in the MOF structure and remains stable inside the MOF a digestion procedure of the material was applied as follows:

1) a solution of 800 µL H_2O and 2 pellets of KOH was prepared;
2) 10 mg of R*-MOF was added, and the system was put in an Eppendorf for 48 hours under slow agitation;
3) after 48 hours the homogenization of the solution was obtained and a work-up to extract the linker was executed:
   - HCl addition to protonate the linker;
   - EtOAc addition to extract the organic part;
   - evaporation of the solvent.

^{1}H-NMR of the extracted linker

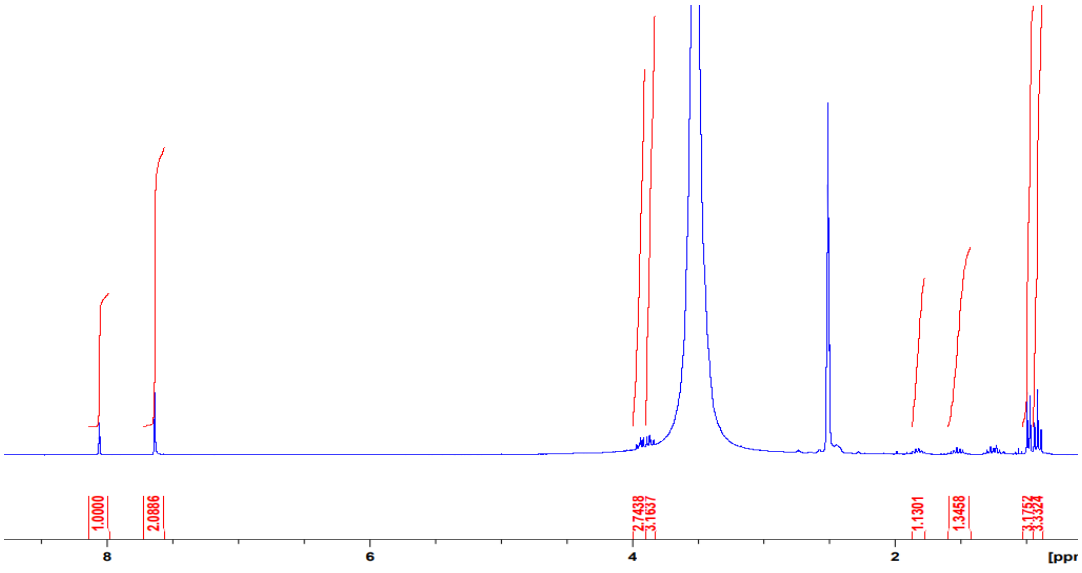

Figure 6.13. ^{1}H-NMR spectrum evidences the presence of the linker after the digestion procedure

All the signals of the linker are recognizable. The presence of water for MOFs digestion is the reasons of the peaks around 3.05 ppm.

6.3.6 Characterizations and applications of the new chiral MOF

The second part of this project was focused on the characterization and optimization of the new synthesized chiral MOF (R*-MOF). In the end, the specific properties of this new porous material for chiral applications were investigated with preliminary adsorption and catalytic tests.

1) TGA Analysis of the chiral MOF

Thermal stability of R*MOF was first tested by thermogravimetric analysis (TGA). TGA data were collected on Mettler Toledo TGA/DSC 2, STAR System apparatus with a heating rate of 5 °C/min under the oxygen flow until 600 °C.

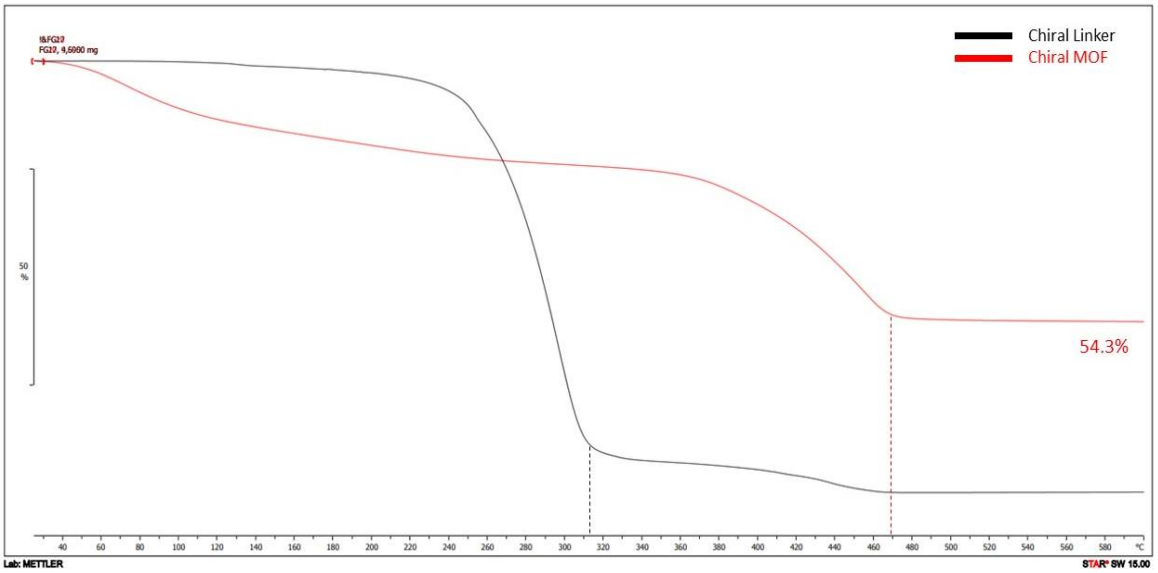

Figure 6.14. Comparison of the TGA curves of the chiral Zr-R*-MOF and the *(S)*-5-(2-methylbutoxy)isophthalic acid chiral linker.

TGA curves of the chiral Zr-R*-MOF were comparable to those of the *(S)*-5-(2-methylbutoxy)isophthalic acid chiral linker. An enhancement of the maximum temperature point before the sharp drop, from 310 °C for the linker to 450 °C for the MOF was observed.

The ZrO_2 content found in the experiment was 54.3%, which is in agreement with that of the theoretical one (54.7%).

2) Analysis of porosity and surface area of the Chiral MOF

After activation at 150 °C for 12 hours, the material surface area and porosity were characterized. The free space data, as Brunauer−Emmett−Teller (BET) and Langmuir surface areas and pore volumes, of the R*-MOF are presented in the following table:

SSA and Porosity	
BET Surface area (m^2/g)	563.29
Langmuir Surface area (m^2/g)	1,035.93
Pores volume adsorption (cm^3/g)	0.3749
Pores volume desorption (cm^3/g)	0.3763
Average Pore Size (Å)	26.73

The Accessible pore volume of 0.37 $cm^3\ g^{-1}$ results slightly lower than that measured for standard MIP-206 (0.45 $cm^3\ g^{-1}$). The Pore Size Distribution (PSD) analysis of chiral MIP-206 (Figure 6.16) suggests the presence of uniform meso-voids with a diameter of ca. 2.6 nm, exactly the same as the classic MIP-206.

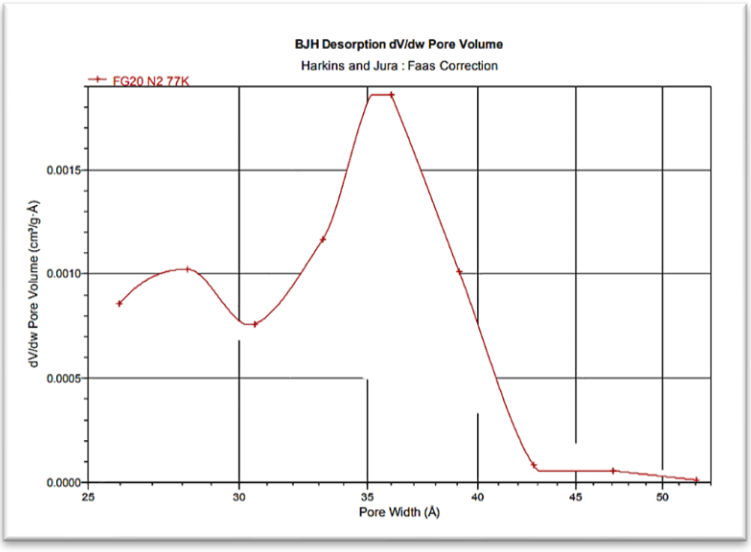

Figure 6.15. dV/dw Pore size distribution

As a result of the similar transition steps in the adsorption isotherms, samples tested for nitrogen sorption all possess similar mesopore diameters, within the range of 2.5-2.7 nm, which

further highlights the negligible influence of bulky substitutes on the dimensions of the MOF porosity.

The chiral active molecule suffered from coordinated modification that would not only block the pores of MOFs but also reduces their chiral degree of freedom. In fact, the chiral groups could block the windows of the cavities, resulting in a decrease in the Brunauer-Emmet-Teller (BET) surface area, from of the parent MOF without any functionalization to of the chiral MOF.[5] In fact, the BET surface area (563.29 m^2/g) of the synthesized chiral MOF decreases with respect to the BET surface area of MIP-206-OH or MIP-206.

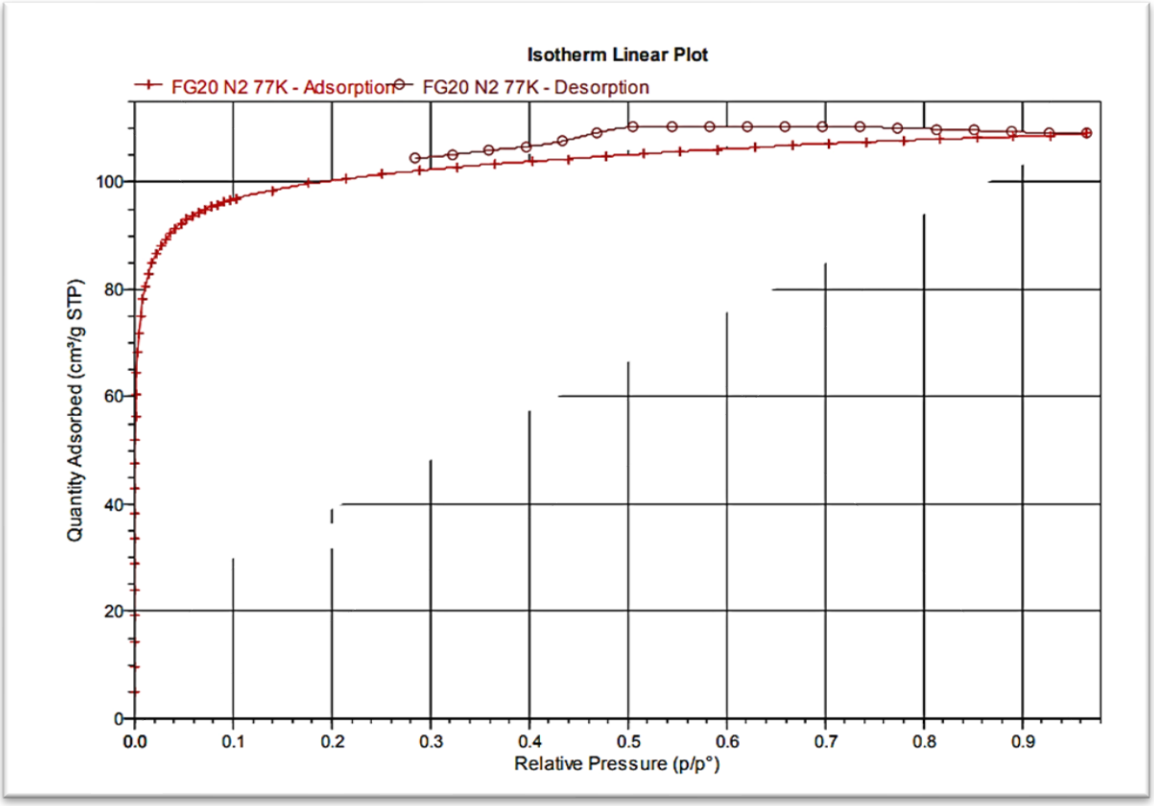

Figure 6.16. Isotherm linear plot (N2, 77K) of chiral MIP206

3) Chiral MOF stability under different conditions

Chemical stability is another important criterion to consider when selecting a MOF for any application. In our case, if we are planning to construct an enantioselective material exploitable for separation procedures, for example in a HPLC system, it is fundamental to test its stability in the solvents commonly used in the fields of application. Therefore, comparing the resulting patterns before and after the exposure to the environment under study gives a basic idea of the degree of the possible framework deterioration.

To check the chemical stability, the material was soaked in different solvent media, i.e. EtOH, H_2O, MeOH, and Acetone, for 24 h. After completing the stirring process, the material was centrifugated, dried under vacuum for 24 h, and its crystallinity was checked by carrying out P-XRD measurements. The powder XRD analysis after soaking experiments showed that the framework of the material was actually unaffected in various solvent systems.

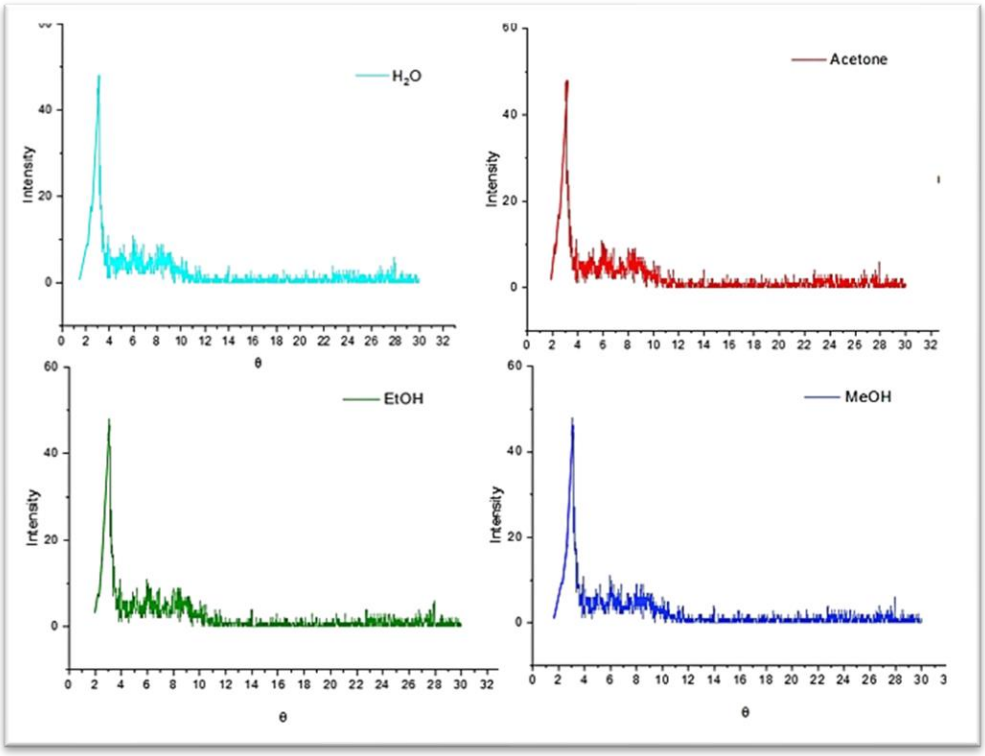

Figure 6.17. Powder XRD analysis of R*-MOF after soaking experiments.

6.3.7 Synthesis of MTV Chiral MIP-206 MOF

The following synthetic attempts were performed with the aim of increasing the surface area of the produced chiral MOF. The idea was to try different ratio of the simpler linker and the chiral one to find the optimized conditions that could lead to a highly crystalline solid. In fact, as already written in the introduction, by the incorporation of missing linker and missing node defects into MOFs, some bigger cavities can be generated in the defect sites without losing long-range-order MOFs, and hence producing a larger adsorbent space.

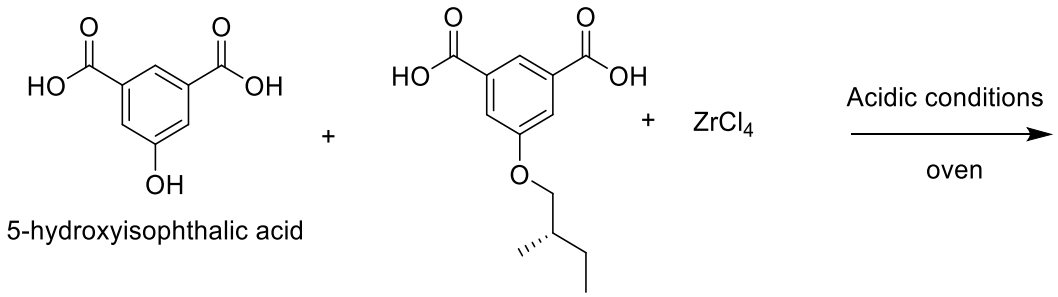

Scheme 6.11. Synthesis of R*-MOF with m MTV approach.

Chiral MIP-206 was synthesized solvothermically by the reaction of $ZrCl_4$ and a mixture of 5-hydroxyisophtalic acid (IPA-OH) and *(S)*-5-(2-methylbutoxy)isophtalic acid (IPA-R*) in formic acid varying the reagents ratio in three different test:

1. IPA-OH : IPA-R* **90:10**
2. IPA-OH : IPA-R* **80:20**
3. IPA-OH : IPA-R* **50:50**

The synthetic procedure and the work up of the reactions were tha same as those employed in the single reagent (the chiral one) reaction described above.

XRD Characterizations

The secondary building units of the DCMOFs (Defected Chiral MOFs) should be the same as those of parent MOFs but in reality the XRD analysis for the first test (90:10) revealed a crystalline solid but with a different XRD pattern of the synthesis of the chiral MOF or the synthesis of the IPA-OH MOF (Figure 6.19).

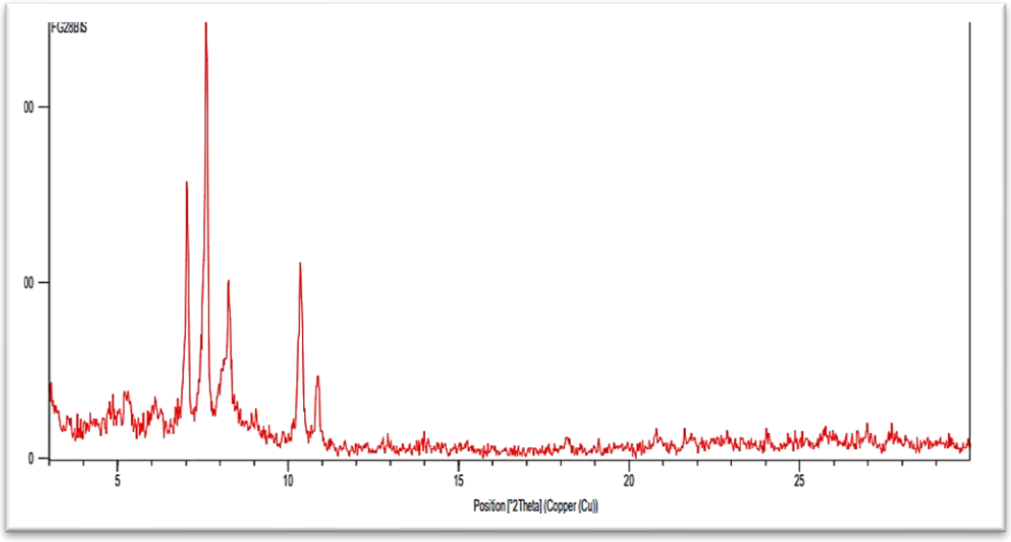

Figure 6.18. Powder XRD analysis for the first MTV-MOF test synthesis (90:10)

On the other hand, The XRD analysis revealed an amorphous solid in the case of both 80:20 and 50:50 ratios, but the results seems to be improving by changing the ratio IPA-OH:IPA-R* from 80:20 to 50:50 (Figure 6.20).

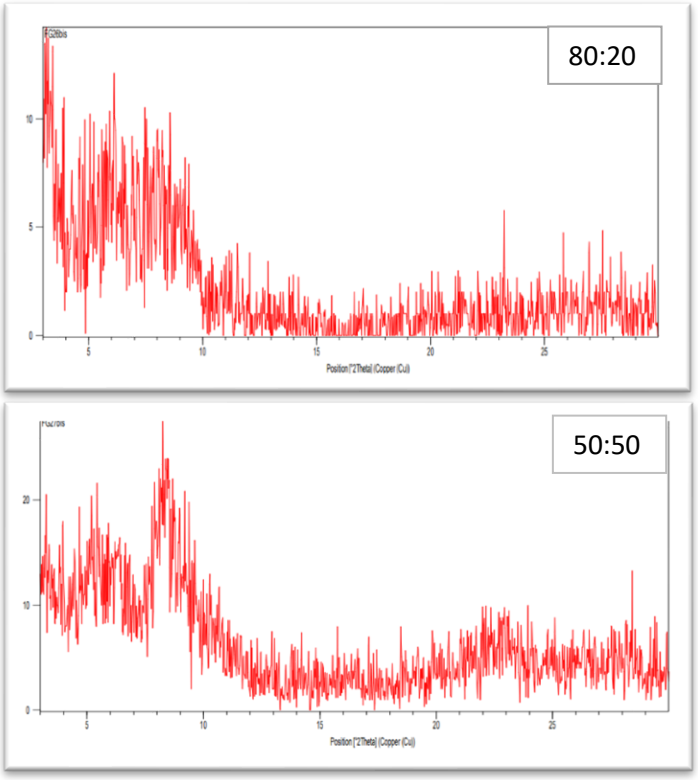

Figure 6.19. Powder XRD analysis for the MTV-MOF tests synthesis 80:20 and 50:50.

6.3.8 Preliminary tests of a chiral adsorption/catalysis activity

Although the new chiral MOF is not characterized by exceptional value of surface area, comparing the volume of the pores of the MIP206-R*-MOF and the average volume of the two chiral molecules selected for the tests, *(S)*- and *(R)*-1-phenylethan-1-amine, preliminary tests of a chiral adsorption or catalysis activity were attempted, to explore the possible applications of the new material.

Adsorptive separation approach

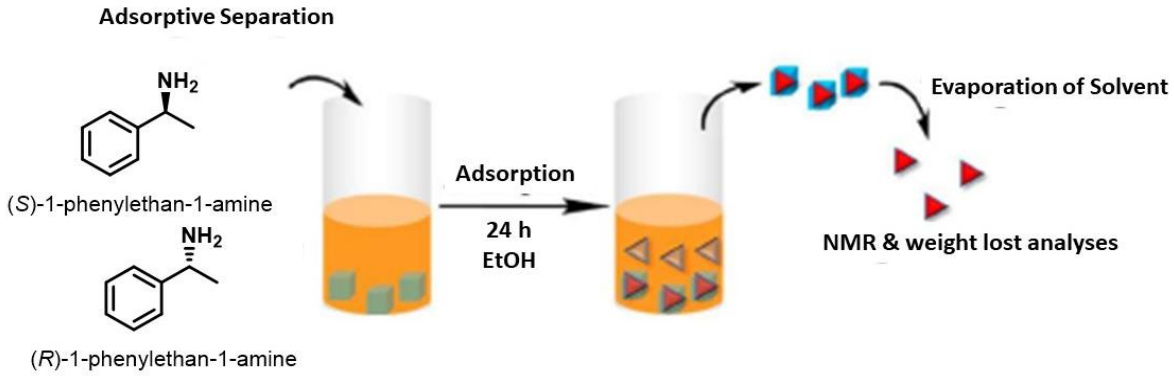

Figure 6.20. adsorptive chiral separation of two enantiomeric molecules by the chiral MOF.

For the preliminary tests the idea was to use the adsorptive separation approach, in the most simple way: in a solution of 10 mL of EtOH 30 mg of R*-MOF and 30 mg of *(R)*-1-phenylethan-1-amine were mixed a 500 rpm for 24 hours; after a simple deposition of the solid, the surnatant was concentrated to eliminate all the solvent and the weight loss data weree collected. The same system was used for the *(S)*-1-phenylethan-1-amine enantiomeric molecule.

First of all, it is worth noting that a different behaviour in the adsorption test was observed:

- *(S)*-1-phenylethan-1-amine % adsorbed = 60.5%
- *(R)*-1-phenylethan-1-amine % adsorbed = 15.7%

Then, from the ^{1}H-NMR spectrum of the surnatant of the first test, it was possible to detect the *(S)*-1-phenylethan-1-amine not adsorbed (39.5%), while in the case of the tesst carried out with the *(R)*-enantiomer, although the percentage of adsorbed material was very low, a change in the spectrum of the surnatant was observed (see below).

1) ^{1}H-NMR spectrum of the adsorption test with *(S)*-1-phenylethan-1-amine

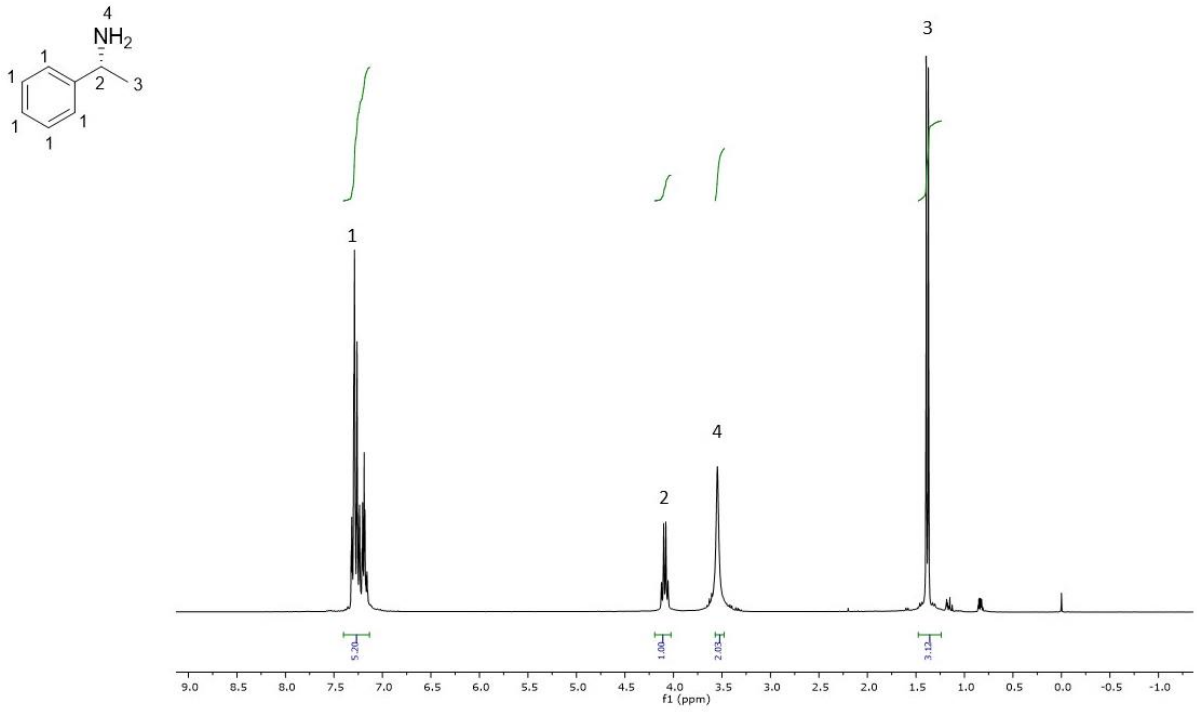

Figure 6.21. NMR analysis of adsorption test of *(S)*-1-phenylethan-1-amine.

The NMR analysis of adsorption test of *(S)*-1-phenylethan-1-amine (Figure 6.22) confirms the presence of 39.5% of the enantiomer (S) in the surnatant. Comparing this result with that obtained with the *(R)*-enantiomer, it is evident that different interactions are established between the chiral porous material and the chiral host molecules, according to the three-point attachment model (TPA) (Figure 6.23).

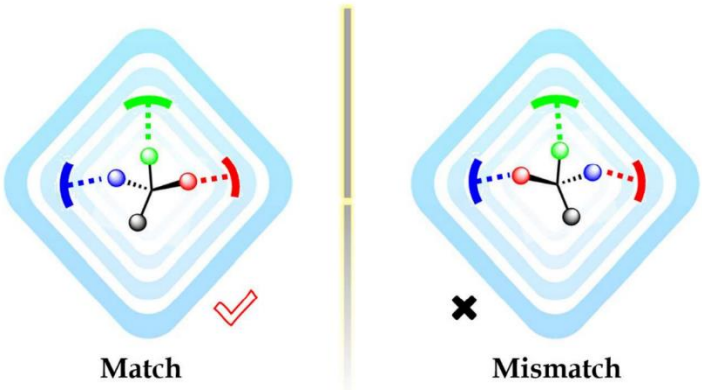

Figure 6.22. three-point attachment model (TPA) representing the close interactions between adsorbates and adsorbent

This model, where an interaction in at least three configuration-dependent points is needed for a chiral selector to recognize enantiomers, represents the key to effective separation on the close stereospecific interaction between adsorbates and adsorbent.

2) ^{1}H-NMR spectrum of adsorption test with *(R)*-1-phenylethan-1-amine

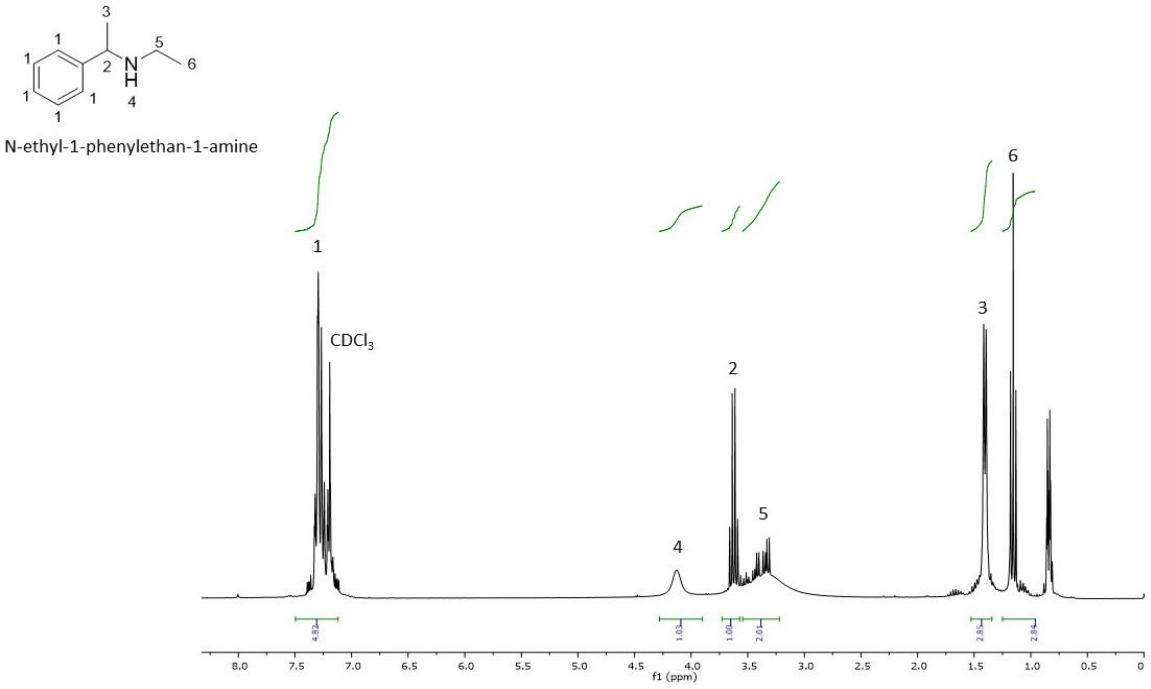

Figure 6.23. NMR analysis of adsorption test of *(R)*-1-phenylethan-1-amine.

The ^{1}H-NMR spectrum of the adsorption test carried out with *(R)*-1-phenylethan-1-amine shows different results compared to the spectrum of the previous experiment, particularly the occurrence of a unexpected, novel compound. A possible explanation could be that this chiral MOF catalyzes the reaction between *(R)*-1-phenylethan-1-amine and EtOH with the formation of the secondary amine, *N*-ethyl-1-phenylethan-1-amine (Scheme 6.11).

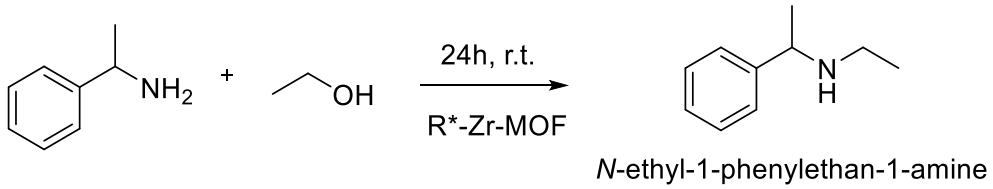

Scheme 6.12. Direct catalytic alkylation of primary amine with ethanol.

The direct alkylation of amines with alcohols would represent a brilliant, benign alternative to usual reactions with potentially genotoxic alkyl halides: unfortunately, this reaction does not work in the absence of any catalyst. An alcohol can be activated (oxidized) by temporary transfer of hydrogen to a metal catalyst, generating an aldehyde: the latter can form in situ an imine with a primary amine reagent; eventual reduction of the imine by the reduced catalyst would afford the amine in an overall process termed *borrowing hydrogen* (Scheme 6.12).[10]

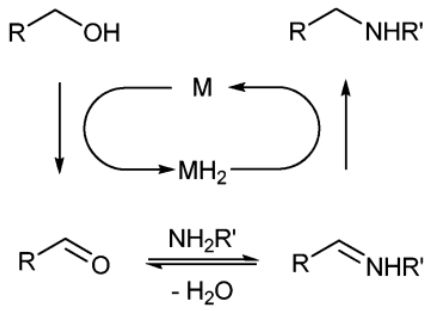

Scheme 6.13. catalytic cycle of the alkylation of amines through borrowing hydrogen processing.

There are only few examples of this reaction in the literature, the majority of them involving homogeneous catalysts: for example, several ruthenium complexes have been shown to be active for this transformation.[11] Iridium complexes have also proved to be successful,[12] but most of them need reflux and the presence of a base to activate the catalyst, conditions not required by our MOF. Therefore, this is a result that is certainly worth of being explored futher.

6.4 Conclusions

In this chapter the synthesis of a new zirconium chiral metal–organic framework (R*MOF) and a new linker, *(S)*-5-(2-methylbutoxy)isophthalic acid, have been presented. The novel material was prepared using the synthetic route of the known MIP-206 and was fully characterized by spectroscopic analyses of different kinds: XRD, FTIR, NMR, as well as by thermal and surface area measurements (TGA, BET). The resistance and stability of the new R*-MOF have been explored by resistance and functionalization study.

Moreover, the chiral properties of this new material were tested with preliminary enantiomeric separative application. In this case, interesting results were observed that have yet to be explored in more detail, both as far as the possibility of using the new R*MOF as a stationary phase for HPLC racemic mistures separation is concerned, but also, even more interesting, for carrying out *N*-alkylation enantioselective reactions.

6.5 Experimental Section

Materials

All reagents and solvents were purchased from commercial vendors and used as received; the chemicals anhydrous $ZrCl_4$, *(2S)*-2-methylbutyl methanesulfonate, 5-hydroxyisophthalate, K_2CO_3, ethyl acetate, lithium hydroxide, dimethylformamide, methanol (MeOH), tetrahydrofuran (THF), ethanol (EtOH), dichloromethane, deuterated chloroform ($CDCl_3$), sulphuric acid (H_2SO_4, 98%), hydrochloric acid (HCl, 37 wt%), $NaHCO_3$, magnesium sulphate, and sodium hydroxide (NaOH, 50 wt%) were purchased from Sigma-Aldrich (analytical reagent grade).

Instrumentation

All syntheses of the R*MOF were performed in oven with a 23 mL PTFE lined metal vessel model 4547 Parr® Instruments. The XRD spectra were recorded using a D8 Discovering Plus XRD equipped with a LynXEye detector, working at 40 mA and 40 kV and using Cu K radiation. The BET measurements were performed at 423 K using the Micromeritics® TriStar II Plus automated surface area and porosity analyzer and the results are analyzed by MicroActive Software for TriStar II Plus. The NMR spectra were recorded at 298 K using a Varian MercuryPlus VX 400 (^{1}H, 399.9); spectra were referenced internally to residual solvent resonances and were recorded at 298 K for characterization purposes; full ^{1}H assignments were done using standard Varian pulse sequences. Spectra have been edited with the software MestReNova Version: 14.1.0-24037, 2019 MestRelab Research S.L. Abbreviations: s = singlet, d = doublet, t = triplet, m = multiplet, bs = broad singlet. ATR-FTIR analyses were performed with a Perkin Elmer Spectrum Two spectrophotometer, equipped with a Universal ATR accessory, in the range 4000-600 cm^{-1} with a resolution of 0.5 cm^{-1}. The products were directly analysed performing 40 scans. Abbreviations: ν = stretching, δ = bending. Thermogravimetric analyses were carried out using a Perkin Elmer TGA-7. The samples (ca. 10 mg) were heated in a platinum crucible at a rate of 10 °C min^{-1} from 40 °C to 600 °C.

Linkers synthesis

- **Methylation of hydroxy isophthalic acid**

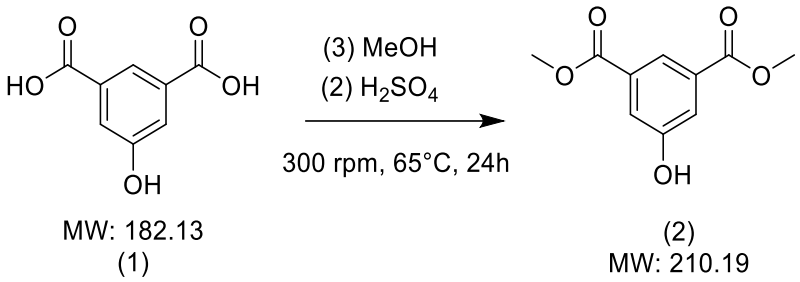

MW: 182.13
(1)

(2)
MW: 210.19

Scheme 6.14. Experimental condition of the methylation of hydroxy isophthalic acid.

A solution of 1 (0.728 g, 2.33 mmol) in methanol (80 mL) was prepared. Concentrated H_2SO_4 (1.30 mL, 23.6 mmol, ~10 eq) was added while keeping the solution stirred. The system was stirred for 24 hours at reflux temperature (65 °C). The solution was then cooled down to 0 °C, and 200 mL of DI water were slowly added. The formation of a pink-orange precipitate was observed. The solution was filtered and the solid dried in the oven overnight. The final product is a pink solid (0.668 g, 2.06 mmol, **89%** yield).

^{1}H-NMR analysis of dimethyl 5-hydroxyisophthalate

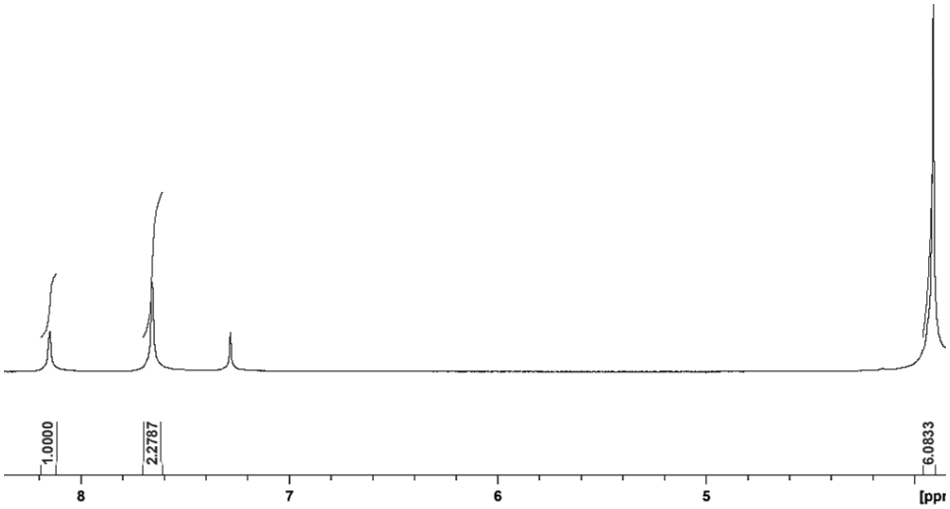

Figure 6.24. ^{1}H-NMR analysis of neat **2**.

^{1}H-NMR: (300 MHz, $CDCl_3$) δ = 8.26 (t, J=1.2 Hz, 1H), 7.74 (d, J=1.2 Hz, 1H), 3.98 (s, 6H).

- **Synthesis of dimethyl 5-(allyloxy)isophtalate**

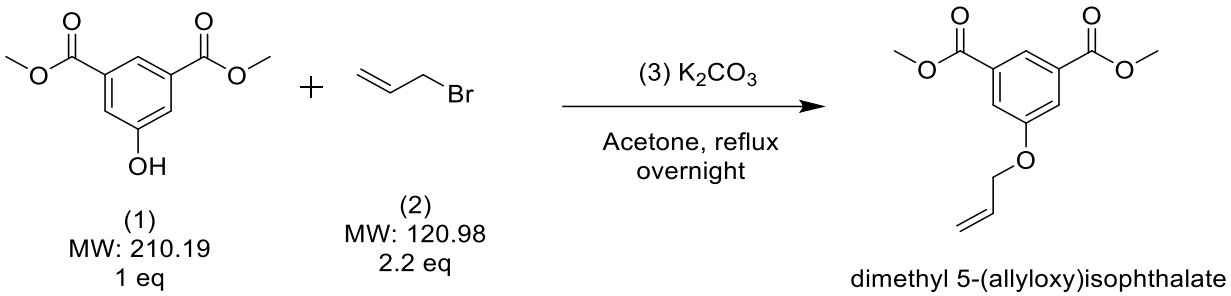

Scheme 6.15. Experimental condition of the synthesis of dimethyl 5-(allyloxy)isophtalate.

To a solution of 5-hydroxy-isophtalate (0.720 g) and allyl bromide (0.65 mL) in 15 mL acetone was added K_2CO_3 (1.00 g) The reaction mixture was stirred at reflux temperature overnight. The solid part was filtered and washed with acetone. The filtrate was evaporated at reduced pressure to give the product as a white solid (Yield=**89%**) without further purification.

NMR analysis of dimethyl allyl-(2-methylbutoxy)isophthalate

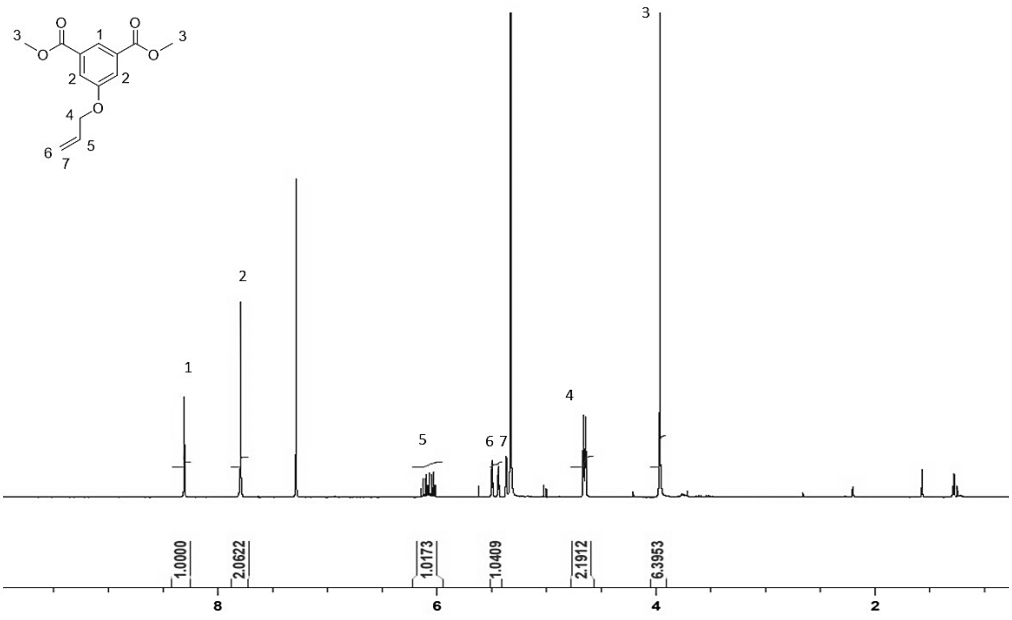

Figure 6.25. ^{1}H-NMR analysis of neat **2**.

^{1}H-NMR: (300 MHz, $CDCl_3$) δ = 8.26 (t, J=1.2 Hz, 1H), 7.74 (d, J=1.2 Hz, 1H), 6.26 (m, 1H), 5.52 (m, 1H), 5.48 (m, 1H), 4.68 (m, 2H), 1.32 (m, 1H), 3.98 (s, 6H).

- **Synthesis of dimethyl *(S)*-5-(2-methylbutoxy)isophthalate (3)**

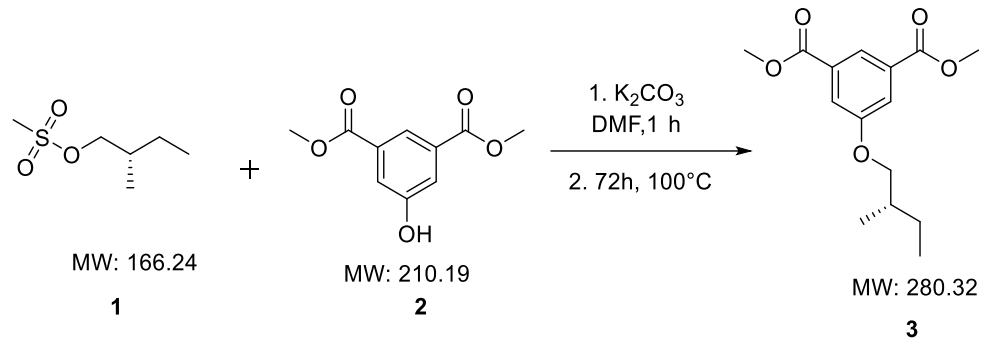

Scheme 6.16. Experimental condition of synthesis of the chiral linker.

To a flask containing 5-hydroxyisophthalate (27.2 mmol) and potassium carbonate (10.27 g, 74.3 mmol) was added DMF (300 mL) and the mixture was stirred for 1 h. *(S)*-2-methylbutyl methane sulfonate (9.5 g, 57.1 mmol) was added slowly and the reaction stirred at 100 °C for 72 h. After being allowed to cool to room temperature, the reaction mixture was concentrated on a rotary evaporator. Then etil acetate was added and the organic layer was washed with water (1 x 50 mL), 1M K_2CO_3 (1 x 50 mL), and brine (1 x 50 mL), and dried over anhydrous sodium sulfate. Removal of the solvent on a rotary evaporator provided the product as colorless oil (**Y**= 53.7%).

^{1}H-NMR of neat 3 (400 MHz, $CDCl_3$): δ 8.26 (t, J=1.2 Hz, 1H), 7.74 (d, J=1.2 Hz, 1H), 3.94 (s, 6H), 3.90-3.82 (m, 2H), 1.88 (m, 1H), 1.56 (m, 1H), 1.32 (m, 1H), 1.04 (d, J=6.6 Hz, 3H), 0.96 (t, J=7.4 Hz, 3H).

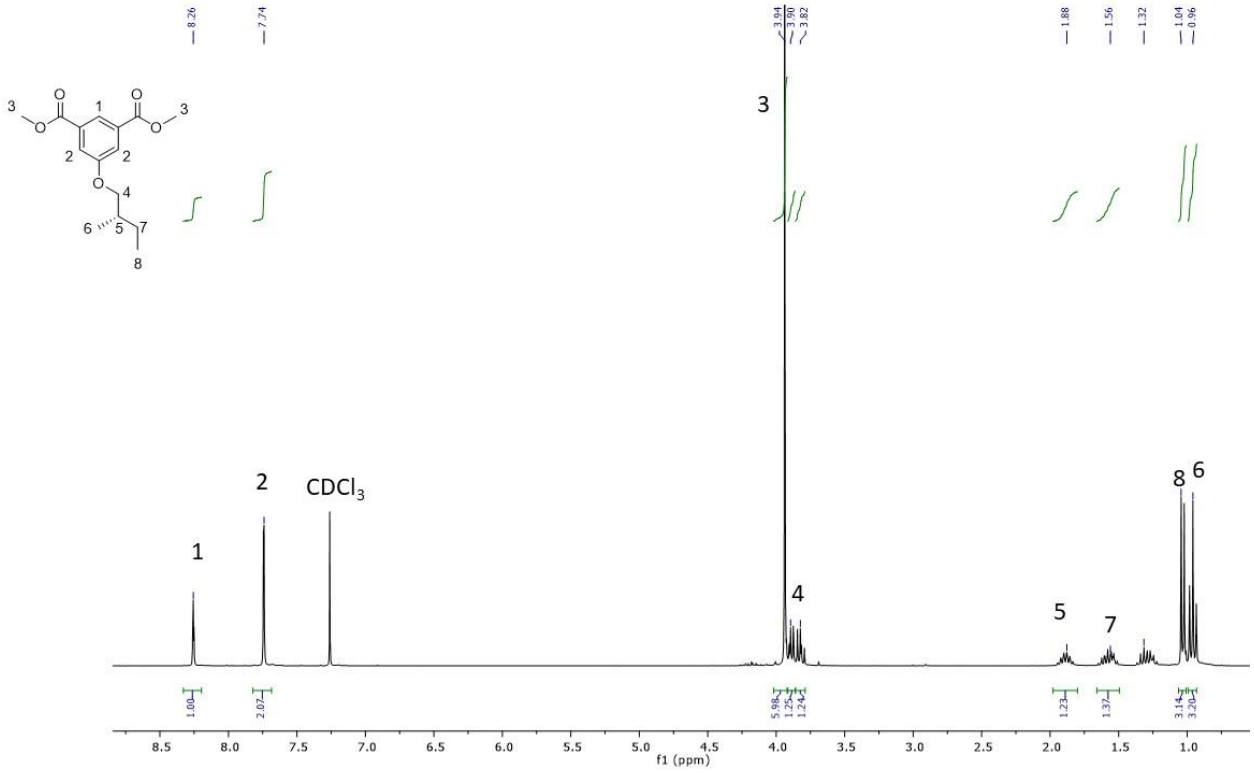

Figure 6.26: ^{1}H-NMR spectrum of **3.**

- **Synthesis of *(S)*-5-(2-methylbutoxy)isophthalic acid (4)**

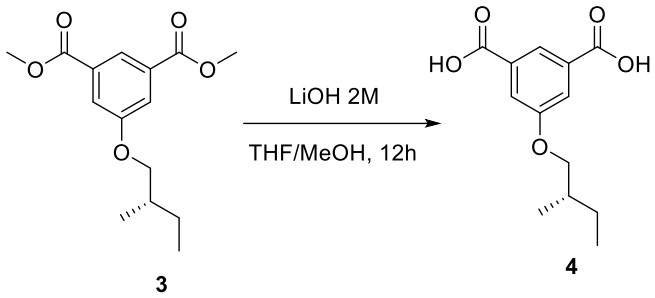

Scheme 6.17. Experimental condition of the deprotection of the chiral linker.

Dimethyl *(S)*-5-(2-methylbutoxy)isophthalate **(3**, 0.520 g, 1.54 mmol) was dissolved in a 1:1 v/v mixture of THF/methanol (15 mL) and treated with 4 mL of 2.0 M aqueous solution of LiOH. After stirring for 4 h, the solvents were concentrated and the residue was treated with 1.0

M aqueous HCl (20 mL) and extracted with ethyl acetate. The organic phase was dried with Na_2SO4 and concentrated to obtain the pure desired dicarboxylic acid derivative **4** as a white solid **(Y =** 76%**)**.

^{1}H-NMR of neat 4 (399.9 MHz, acetone-d$_6$) δ = 8.26 (t, J=1.2 Hz, 1H), 7.74 (d, J=1.2 Hz, 1H), 3.90-3.82 (m, 2H), 1.88 (m, 1H), 1.56 (m, 1H), 1.32 (m, 1H), 1.04 (d, J=6.6 Hz, 3H), 0.96 (t, J=7.4 Hz, 3H).

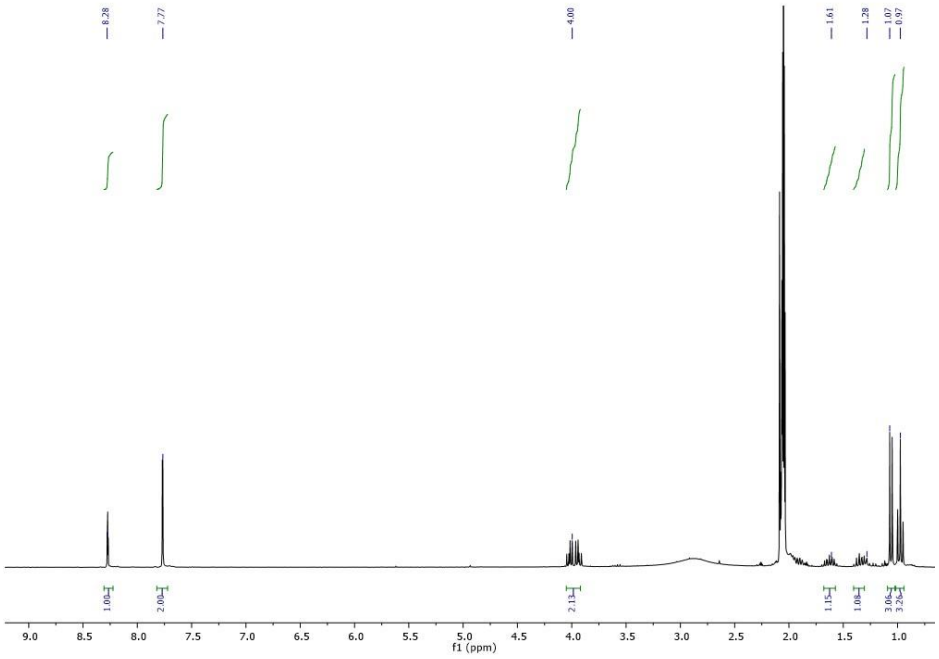

Figure 6.27: ^{1}H-NMR spectrum of 4.

ATR-FTIR spectrum of neat 4 (cm^{-1}): 2960 (ν C-H aliphatic, m), 2575 (ν C-H aliphatic), 1701 (ν C(O)O, s), 1608- 1470 (ν C-H aromatic, s), 1250 (ν -CH_3 aliphatic)

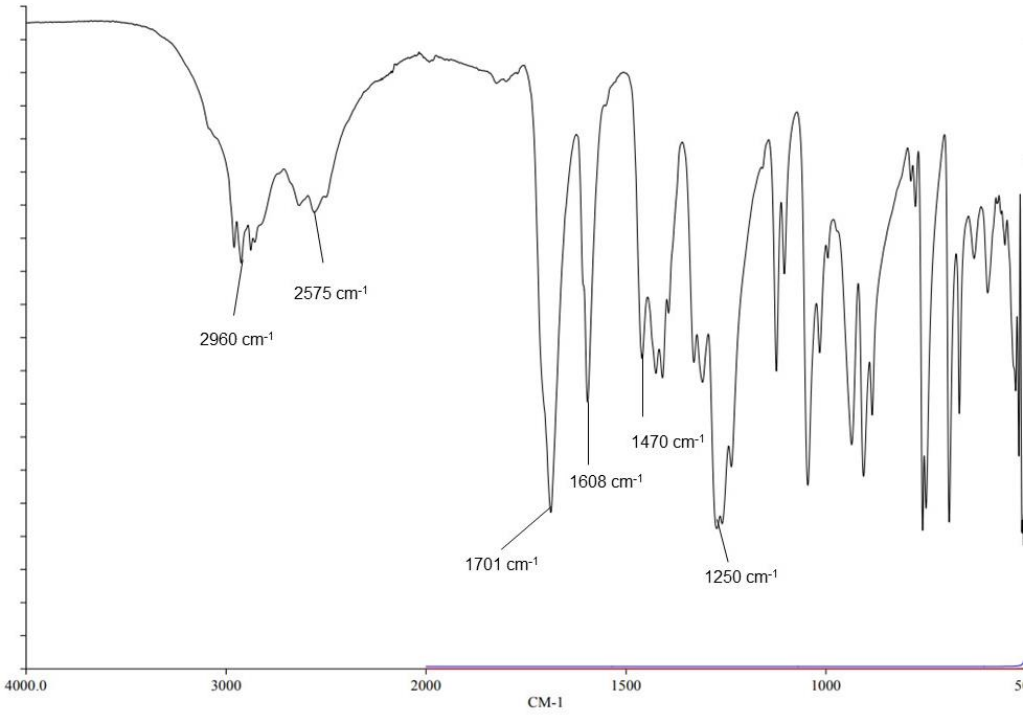

Figure 6.28: IR-ATR spectrum of **4**.

- **Synthesis of MIP-206 MOF**

Synthesis of allyl MOF with $ZrCl_4$

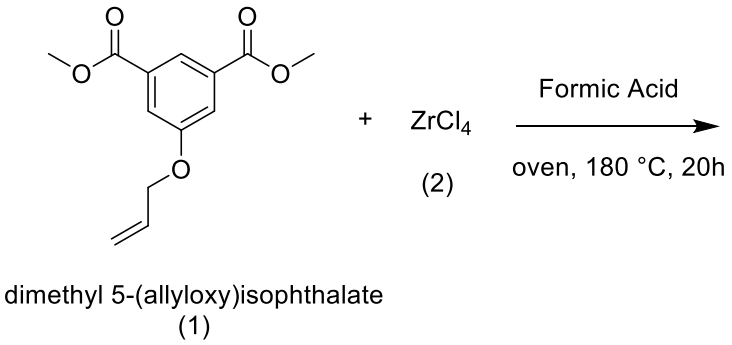

Scheme 6.18. Experimental condition of the synthesis of allyl MOF.

Allyl MIP-206 was synthesized solvothermally by the reaction of $ZrCl_4$ and IPA-O-allyl linker in formic acid. Dimethyl 5-allyloxy isophtlate (0.275 g, 1.15 mmol) was weighed into a 23 mL Teflon reactor, formic acid (0.83 mL) was added followed by stirring at room temperature for 5 minutes until a homogeneous suspension was formed. $ZrCl_4$ (0.333 g, 1.4 mmol) was added to the suspension followed by 10 minutes stirring at room temperature to disperse the reactants uniformly. Afterwards, the reaction was sealed in an autoclave at 180 °C for 24 hours. After cooling down to room temperature, the expected product (**0.320 g**) was collected by filtration, washed with Ethanol (at reflux for 24 h) and dried in vacuum oven for 24h at room temperature.

Synthesis of Chiral MOF with $ZrCl_4$ and (S)-5-(2-methylbutoxy)isophthalic acid

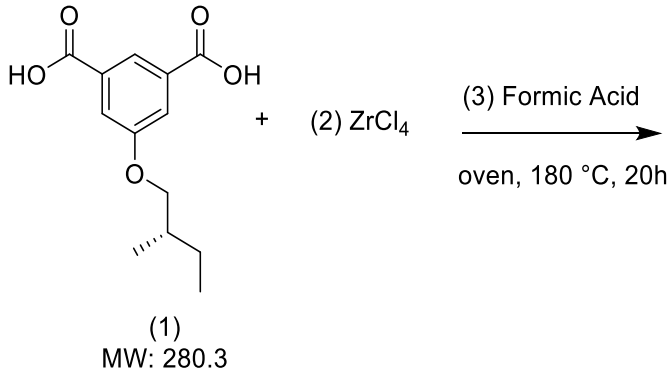

Scheme 6.19. Experimental condition of the synthesis of Chiral MOF (R*-MOF).

Chiral MIP-206 was synthesized solvothermally by the reaction of $ZrCl_4$ and *(S)*-5-(2-methylbutoxy)isophthalic acid in formic acid. IPA-OH was weighed into a 23 mL Teflon reactor, formic acid was added followed by stirring at room temperature for 5 minutes until a homogeneous suspension was formed. $ZrCl_4$ was added to the suspension followed by 10 minutes stirring at room temperature to disperse the reactants uniformly. Afterwards, the reaction was sealed in an autoclave at 180 °C for 24 hours. After cooling down to room temperature, the expected product was collected by centrifugation, washed with Etanol (at reflux for 24 h) and dried in vacuum oven for 24h at room temperature.

References

(1) *Thermoplastic Composition Comprising a Polyamide and a Polysiloxane - Patent US-2017267862-A1 - PubChem*. https://pubchem.ncbi.nlm.nih.gov/patent/US-2017267862-A1 (accessed 2022-09-06).

(2) Kline, M.; Wei, X.; Gong, B. Aromatic Oligoamide Macrocycles with a Backbone of Reduced Constraint. *Org. Lett.* **2013**, *15* (18), 4762–4765. https://doi.org/10.1021/ol4021207.

(3) Han, X.; Yuan, C.; Hou, B.; Liu, L.; Li, H.; Liu, Y.; Cui, Y. Chiral Covalent Organic Frameworks: Design, Synthesis and Property. *Chem. Soc. Rev.* **2020**, *49* (17), 6248–6272. https://doi.org/10.1039/d0cs00009d.

(4) Seo, J. S.; Whang, D.; Lee, H.; Jun, S. I.; Oh, J.; Jeon, Y. J.; Kim, K. A homochiral metal–organic porous material for enantioselective separation and catalysis. *Nature* **2000**, *404*, 982–986. https://doi.org/10.1038/35010088.

(5) Fang, Z.; Bueken, B.; De Vos, D. E.; Fischer, R. A. Defect-Engineered Metal–Organic Frameworks. *Angew. Chem. Int. Ed.* **2015**, *54* (25), 7234–7254. https://doi.org/10.1002/anie.201411540.

(6) Helal, H.; Yamani, Z. H.; Cordova, K. E.; Yaghi, O. M. Multivariate metal-organic frameworks. *National Sc. Rev.* **2017**, *4* (3), 296–298. https://doi.org/10.1093/nsr/nwx013.

(7) Yaghi, O. M.; Kalmutzki, M. J.; Diercks, C. S. *Introduction to Reticular Chemistry: Metal-Organic Frameworks and Covalent Organic Frameworks*, Wiley, **2019**. ISBN: 978-3-527-34502-1.

(8) Wang, S.; Chen, L.; Wahiduzzaman, M.; Tissot, A.; Zhou, L.; Ibarra, I. A.; Gutiérrez-Alejandre, A.; Lee, J. S.; Chang, J.-S.; Liu, Z.; Marrot, J.; Shepard, W.; Maurin, G.; Xu, Q.; Serre, C. A Mesoporous Zirconium-Isophthalate Multifunctional Platform. *Matter*, **2021**, *4* (1), 182–194. https://doi.org/10.1016/j.matt.2020.10.009.

(9) Míguez-Lago, S.; Gliemann, B. D.; Kivala, M.; Cid, M. M. A Chiral Molecular Cage Comprising Diethynylallenes and N-Heterotriangulenes for Enantioselective Recognition. *Chem. Eur. J.* **2021**, *27* (53), 13352–13357. https://doi.org/10.1002/chem.202101801.

(10) Nixon, T. D.; Whittlesey, M. K.; Williams, J. M. J. Transition metal catalysed reactions of alcohols using borrowing hydrogen methodology. *Dalton Trans.* **2009**, 753–762. https://doi.org/10.1039/B813383B.

(11) Jamil, Md. A. R.; Touchy, A. S.; Rashed, Md. N.; Ting, K. W.; Siddiki, S. M. A. H.; Toyao, T.; Maeno, Z.; Shimizu, K. *N*-Methylation of Amines and Nitroarenes with Methanol Using Heterogeneous Platinum Catalysts. *J. Catal.* **2019**, *371*, 47–56. https://doi.org/10.1016/j.jcat.2019.01.027.

(12) Cami-Kobeci, G.; Williams, J. M. J. Conversion of alcohols into *N*-alkyl anilines via an indirect aza-Wittig reaction. *Chem. Commun.* **2004**, 1072–1073. https://doi.org/10.1039/B402020K.